Yale University

EliScholar – A Digital Platform for Scholarly Publishing at Yale

Yale Graduate School of Arts and Sciences Dissertations

Spring 2021

Morphogenesis of Class IV Neurons in Drosophila melanogaster

Olivier Trottier
Yale University Graduate School of Arts and Sciences, olivier.trottier@yale.edu

Follow this and additional works at: https://elischolar.library.yale.edu/gsas_dissertations

Recommended Citation

Trottier, Olivier, "Morphogenesis of Class IV Neurons in Drosophila melanogaster" (2021). *Yale Graduate School of Arts and Sciences Dissertations*. 120.
https://elischolar.library.yale.edu/gsas_dissertations/120

This Dissertation is brought to you for free and open access by EliScholar – A Digital Platform for Scholarly Publishing at Yale. It has been accepted for inclusion in Yale Graduate School of Arts and Sciences Dissertations by an authorized administrator of EliScholar – A Digital Platform for Scholarly Publishing at Yale. For more information, please contact elischolar@yale.edu.

Abstract

Morphogenesis of Class IV Neurons in *Drosophila melanogaster*

Olivier Trottier

2021

The establishment of the neuron's morphology is essential to its function. The class IV neurons of the Drosophila melanogaster larva are two-dimensional sensory neurons that develop a complex dendritic arbor sensitive to mechanical stimuli. The fully-developed dendritic tree results from a multitude of stochastic processes including dendritic tip growth, branching and self-avoidance. However, it is yet unknown how the microscopic dendritic growth processes produce the macroscopic morphology of the class IV neurons. In this study, we aim to bridge this gap by formulating multi-scale models of neuronal dendritic morphogenesis. We begin by analyzing the tip dynamics and branching process of class IV dendritic trees. We find that the tip growth dynamics can be described by a Markov process that transitions between three velocity states: growing, paused and shrinking. Driven by the results of our analysis, we propose two types of model of morphogenesis. First, we use the mean-field approximation to formulate dendritic tree growth as a system of reaction-diffusion equations with two kinds of species, dendrites and tips. This coarse-grained approach predicts that the dendritic tree grows by the propagation of a density wave whose tail stabilizes to a steady-state. Second, we construct an agent-based model of morphogenesis that implements the stochastic rules of microscopic tip growth and branching whose combined effects lead to the development of the dendritic tree. Within the limitations of the model, this more fine-grained approach predicts morphometrics that agree with the measured values. In summary, our results characterize the development of class IV neurons and provide a framework to understand how the large-scale morphology of the class IV neuron dendritic tree emerges from the local stochastic growth of its branches.

Morphogenesis of Class IV Neurons in *Drosophila melanogaster*

A Dissertation
Presented to the Faculty of the Graduate School
of
Yale University
in Candidacy for the Degree of
Doctor of Philosophy

By
Olivier Trottier

Dissertation Director: Prof. Jonathon Howard

June 2021

©2021 by Olivier Trottier

All rights reserved.

Contents

Acknowledgements

While this thesis is conventionally meant to be a summary of my scientific inquiry, it really represents the accomplishments of many who have provided me with their advice, guidance, support and hard labor throughout my study. Let me acknowledge the contributions of the people without whom this written work would be nonexistent.

First, I thank my advisor Prof. Jonathon Howard. Since the beginning of my Ph.D. studies, Joe has given me complete freedom in my scientific thinking and encouraged my interests outside of academia. On the scientific side, my interaction with the diverse group of scientists assembled by Joe has broadened my knowledge and has taught me the value of collaboration across disciplines. In addition, Joe's rigor and scientific method has forever shaped my critical thinking and analytical mind. I will carry his lessons throughout the rest of my career. On the personal side, I feel grateful that Joe has supported the development of my interests, even when they were not necessarily related to my research. During graduate school, I was fortunate enough to take part in various formative experiences teaching students at the elementary and high-school levels. My participation in these extra-curricular activities would have been impossible without Joe's support.

I thank my co-advisor Prof. Yuhai Tu. Ever since we met at the Gordon conference in 2017, Yuhai has been instrumental in building the mean-field model. His proposal to use a mean-field approach and his guidance in simplifying the model

to its current elegant form has led us to many valuable insights in our understanding of the growth class IV neurons. His advice and intuition have taught me valuable techniques in model building and analysis. I wished we had met earlier so that his knowledge would have diffused more profusely into my brain.

I thank Sonal Shree and Sabyasachi Sutradhar for their essential contribution to my thesis research. Sonal maintained the fly lines, imaged the larva and performed some of the most painstaking image analysis. Sabya designed the tracking algorithm and analyzed the dendrites tip dynamics, which were foundational in shaping and constraining our models. I am tremendously grateful for the help that Sonal and Sabya has given me throughout my Ph.D. studies.

I also thank Qiwei Yu for his help in producing the mean-field model predictions. Although Qiwei and I collaborated at the end of my studies, his contribution was nonetheless invaluable. During our frequent remote conversations across the globe, Qiwei's insights into the mathematical derivations of the mean-field model propelled the project forward. I was certainly impressed by Qiwei's constructive criticisms and mathematical sharpness as he was completing his undergraduate studies.

I thank Hugo Bowne-Anderson and Sujoy Ganguly who introduced me to the complex and wonderful system of class IV neurons. Their guidance and advice laid out the foundations of the *in silico* model and morphometric analysis, which motivated me to continue my inquiry of the class IV neuron development.

I thank Ania Luchniak, Mohammed Mahamdeh, Yin-Wei Kuo, Qiwei Yu and Lamiya Mowla for their revisions and comments on the initial draft of this thesis.

I thank Prof. Corey O'Hern and Prof. Michael Murrell for taking part in my thesis committee. I am grateful that Corey has taken the time to advise me on the analysis of the tip dynamics while he was fulfilling many other academic responsibilities. I

am also grateful for Michael's scientific and career advice on pursuing academic and non-academic paths.

I thank the many members of the Howard lab with whom I have interacted: Sujoy, Hugo, Veikko, Josh, Fernando, Maria P., Anneke, Maria F., Mohammed, Ania, Kris, Ivy, Catherine, Raj, Jeremiah, Ross, Sabya, Sonal, Maijia, Wanyu, Ron and Carol. Your help, feedback, insights and smile have motivated me in times when I was hitting a roadblock in my research. Getting to know you in the many lab outings, lunches at the carts or impromptu scientific discussions has made my graduate school experience enjoyable and fulfilling.

I also thank my fellow classmates of the PEB program, Neal, Nandan and Curran. Our Sunday meetings discussing almost everything science-related have always invigorated me. I feel fortunate that you have imprinted your curiosity and passion for science on me.

I am infinitely grateful to my life companion Lamiya. Since our first meeting at HGS, your companionship has brought me joy and happiness whether it be during our walks in East Rock park or road trips on the East Coast or travels around the world. During times of hardship or sadness, your support and love have given me strength and resilience. Witnessing the many obstacles that you have overcome has given me the willpower to move forward in hope of a better day. Thank you Lami for being my private cheerleader.

It also goes without saying that my family has been a constant source of support. My parents, Maude et Marc, have given me their unconditional love ever since I was born into this world. They have constantly fueled my curiosity to discover the world through songs, books, documentaries or travels which has led me to pursue research in science. I have also been blessed to grow up with two cheerful siblings, Ludovic and Mireille, with whom I developed an undying camaraderie ever since my earliest

memory. Merci pour votre amour et je vous suis infiniment reconnaissant pour les valeurs que vous m'avez inculquées.

Finally, I want to thank all the friends that I have made throughout this journey. Thanks to my fellow physics classmates, Judy, Estella, Supraja, Tyler, Qing, Yuqi and Arpit for all the lunches and parties that we spent together. Thanks to Sebiha for the thoughtful gifts and food, and for being a good player in our scare contests. Thanks to Ania for being an excellent listener and for the helpful advice in navigating grad school. Thanks to Mohammed for all the fun nights that we spent together playing video games. Thanks to Nikita for your constant cheerfulness. Thanks to Nathan and Johannes for your zealous passion for board games, which have made our social gatherings even more enjoyable. Lastly, thanks to Meza and Anton for the many Hogwarts battles that we fought together.

1 Introduction

Neurons are the primary units of the nervous system allowing the majority of biological organisms to perceive and respond to their environment. They exhibit a variety of shapes and fulfill a multitude of functions by communicating information through synapses. Their proper development is therefore crucial for the survival of the organism. The class IV dendritic arborization neurons in the *Drosophila melanogaster* larva are an example of a cellular machinery that the larva uses to sense its surroundings. Their sensory function relies on the formation of a complex dendritic tree that is continuously refined over the larval development. In this chapter, I present a brief overview of the developmental biology of class IV neurons and introduce models of dendritic morphogenesis that aim to decipher their multi-scale developmental process.

1.1 Biology of class IV neurons in *Drosophila melanogaster*

1.1.1 Structure and function

The dendritic arborization neurons are sensory neurons that are found in all of the abdominal body segments of the *Drosophila melanogaster* larva. The larva's body

is separated into 11 body segments along the antero-posterior axis, including 3 thoracic and 8 abdominal segments. Each body segment is further divided into two hemisegments separating the left and right side of the larva. Within the body hemisegment, the territories of the dendritic aborization neurons are organized in a stereotypical manner that is repeated throughout all abdominal hemisegments (see fig. 1.1) [27]. Furthermore, along the anatomical frontal axis, i.e. the axis that traverses the larva from left to right, they are located between the cuticle and the epidermis of the larva (see fig. 1.2) [20].

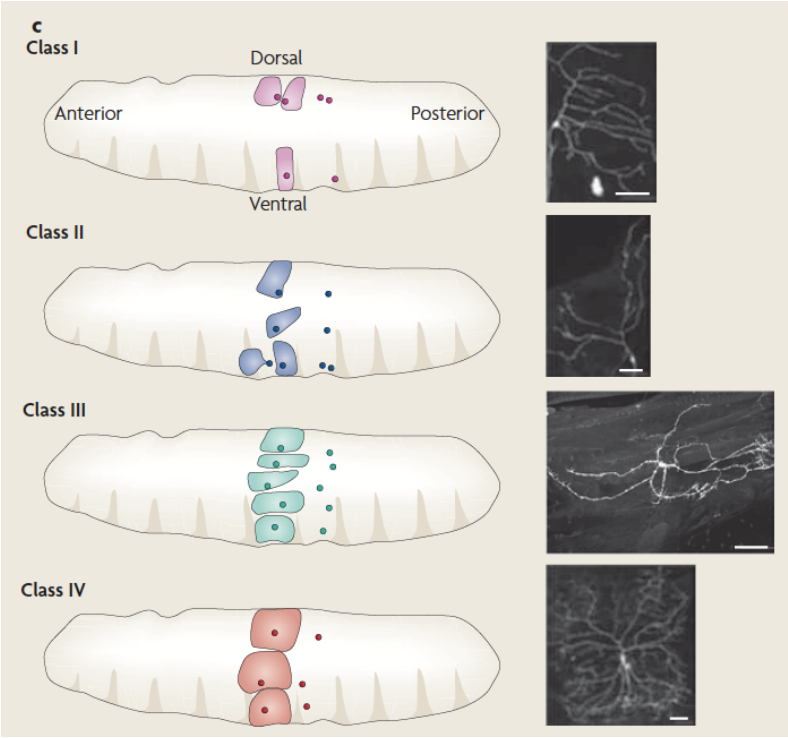

Figure 1.1 – The four classes of dendritic arborization neurons in Drosophila
Reproduced from box 2 of [27]. The shaded areas correspond to the receptive fields while the circles identify the cell bodies. The neuronal territories of two body segments only are drawn for simplicity. The same pattern repeats for other segments' boundary. Scale bars correspond to 50 μm.

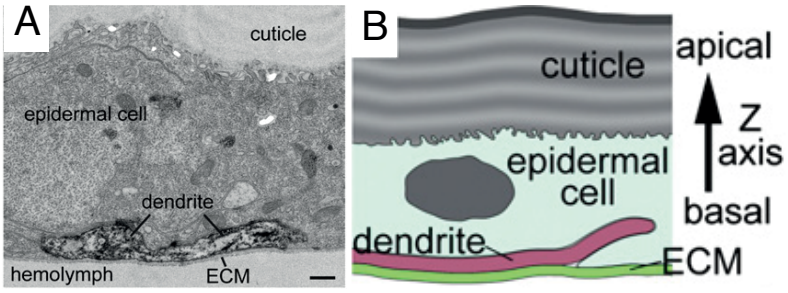

Figure 1.2 – Cross-sectional view of the *Drosophila* larva epidermis
Reproduced from figure 2D and 1B of [20]. **A.** Class IV neuron dendrites are located at the bottom of the epidermis surrounded by the extra-cellular matrix (ECM). The scale bar corresponds to $0.5\,\mu m$ **B.** Diagram of the anatomy shown in A.

As part of the peripheral nervous system, the dendritic arborization neurons are stimulated by physical contacts and relay their sensory information to the central nervous system through synaptic connections [26]. They are categorized by the complexity of their dendritic arbor into four classes as shown in fig. 1.1. Class I neurons exhibit a few dendritic branches while the dendritic arbor of class IV neurons has an abundance of branches that extend far beyond the range of other classes [19]. As such, understanding the development of the class IV neuron dendritic tree poses a difficult problem and is the subject of this thesis.

Endowed with an extensive dendritic arbor, class IV neurons are excellent nociceptors that respond to mechanical, thermal and light stimuli [26, 82, 91]. This function is crucial for the survival of the larva especially when attacked by one of its most dangerous predator, the parasitic wasp *Leptopilina boulardi*. During these attacks, the wasp punctures the larva with an ovipositor aiming to inject an egg that ultimately hatches inside the larva's body leading to its death. As a defense mechanism, the perforation of the larva's cuticle stimulates the dendrites of its class IV neurons, which subsequently initiates various escape behaviors that prevent the injection of the wasp egg [69]. In other words, the survival of the larva is intertwined with its ability to detect these attacks using its mechanosensory system. Moreover, recent studies have discovered that class IV neurons cover the entire epidermis of

the larva in a two-dimensional array, ensuring the detection of the ovipositor jab from all directions [19]. Therefore, class IV neurons have been evolutionarily driven to construct complex dendritic arbors that optimize the detection of external stimuli within their developmental constraints.

In fact, it has been suggested that the shape and size of dendritic arbors result from a general optimization principle whereby neurons balance the metabolic cost of their molecular components and the need to efficiently sample the information that reaches their receptive field [89]. In addition, this optimum is constantly changing as the organism develops, which incurs changes in size and metabolism. Therefore, dendrites must adapt to these changes by continuously remodeling their dendritic arbor while receiving synaptic or sensory inputs.

1.1.2 Development of the dendritic tree

The development of dendritic arborization neurons in *Drosophila* is the subject of intense research. Over the past decades, innovation in imaging and genetic techniques, such as the Mosaic Analysis with a Repressible Cell Marker (MARCM) [40], has opened new horizons in *Drosophila* studies. These novel tools have lead to the discovery of an extensive family of molecules that are involved in the growth of dendritic arborization neurons. A summary of these molecules and their function is given in [27, Table 1]. This section summarizes the role of some of these molecules within the dendritic growth process. The goal is not to be exhaustive, but to identify and describe the key growth mechanisms that motivate the analysis and modeling of the class IV neuron morphogenesis.

Under ideal temperature and humidity conditions, the *Drosophila* larva has a life cycle that spans ~ 4 days following an initial embryo stage that lasts ~ 20 hours after the egg is laid [3]. During this cycle, the larva grows almost 5-fold in size from a length of $\sim 0.5\,\text{mm}$ after hatching to $\sim 3\,\text{mm}$ in the adult stage. Following

this considerable anatomical change, the average diameter of class IV neurons also increases almost 5-fold from $\sim 75\,\mu m$ to $\sim 350\,\mu m$ (see fig. 1.3).

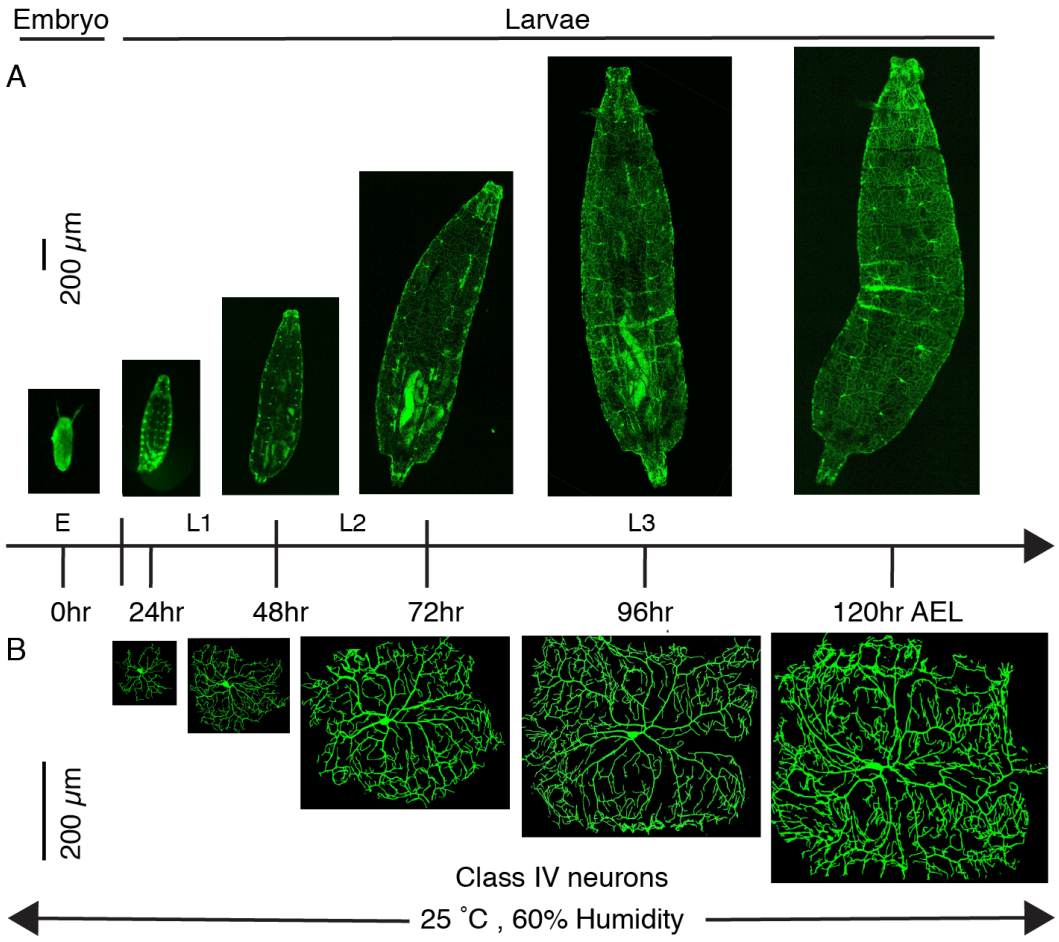

Figure 1.3 – Development of *Drosophila* class IV neurons
A. Development of the larva over the embryo (E) and the three larval stages (L1, L2, L3). **B.** Development of the class IV neurons over the embryo and larval stages. Figure provided by Sonal Shree.

To maintain coverage of its receptive field, the class IV dendritic tree must continuously grow in size and complexity. This large-scale growth is accomplished through several molecular processes: 1) dendritic branches elongate, 2) new dendritic branches are formed by lateral branching and 3) dendritic tips stop growing upon contact with other dendrites.

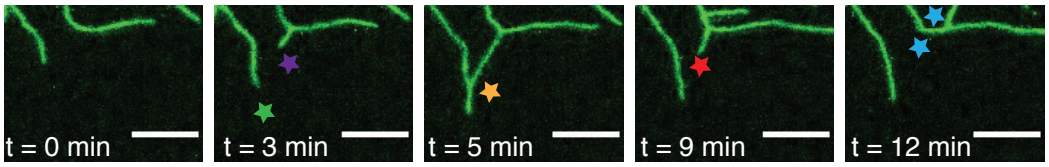

Figure 1.4 – Dynamical processes in class IV neuron development
The time-lapse images are recorded at 24 hr AEL over the course of 12 min. Growth, branching, contact, retraction and annihilation events are identified by green, magenta, yellow, red and blue stars, respectively. Scale bars correspond to 5 μm. Modified from a figure provided by Sonal Shree.

Growth

The growth of the dendritic arbor of class IV neurons is a complex machinery due to its enormous size in comparison to typical cellular scales that are $\sim 1 - 10\,\mu m$ [52]. Although the growth of axons have been studied extensively in the past, our knowledge of dendritic growth is still unfolding. Nonetheless, we have started uncovering a variety of molecules whose cooperative actions lead to the proper development of the class IV dendritic tree [8].

Throughout development, dendritic tips of class IV neuron elongate as depicted in fig. 1.4. At the molecular scale, tip growth is accompanied by the growth of the cytoskeleton, which is made of actin filaments and microtubules. Actin filaments (F-actin) are helical polymers [10] and microtubules (MTs) are rod-shaped polymers that exhibit a stochastic process of growth and shrinkage called *dynamic instability* [24, 53]. Sustaining tip growth with cellular building blocks poses a significant metabolic problem due to the large extension of the dendritic tree. To supply this demand, molecular-motors actively transport intracellular material by carrying cargoes along the cytoskeleton. For example, microtubule-associated molecular motors such as dynein and kinesin transport several kinds of cargo such as organelles, vesicles, neurotransmitter receptors, cell adhesion molecules, cell signaling molecules and mRNAs [23, 96]. The structure and maintenance of the microtubule meshwork is therefore paramount to enable cellular transport from and to the cell body, ensuring

proper development [30]. Several studies have reported that microtubules in the dendrites of class IV neuron have a mixed polarity early in their development (50% of MT minus-ends are oriented outward and 50% are oriented inward with respect to the cell-body), but the orientation of MTs uniformizes to outwardly-oriented minus-ends at the later developmental stages [22, 54, 76]. However, these studies utilize MT end-binding proteins (EB) to probe the MT polarity [1], which may be biased against stable outwardly-oriented plus-end MTs.

In addition to intracellular transport, class IV dendritic trees utilize a more local strategy to nucleate microtubules. Indeed, studies have discovered that pieces of the Golgi apparatus, called *Golgi outposts*, are found throughout the entire arbor, predominantly located near branch points [60, 94]. A positive correlation between the location of Golgi outposts and growing microtubules suggest that Golgi outposts contribute to dendritic tip growth by providing a local (acentrosomal) supply of microtubule nucleation sites. In fact, studies on mammalian neuronal dendrites suggest that Golgi outposts could play an important role in dendritic development by participating in the local synthesis of proteins [75].

Branching

In cooperation with dendritic tip growth, the formation of new branches also contributes to establishing coverage of the class IV neuron receptive field. As shown in fig. 1.4, *branching* occurs throughout the entire branch, and not only at the branch tip.

Several studies have started elucidating the molecular mechanisms that give rise to the branching process. As explained above, Golgi outposts have been found throughout the entire class IV dendritic arbor and their correlation with growing microtubules suggests that they may promote branch formation and stabilization by providing initial cellular building blocks (e.g. microtubule nucleation sites) [60].

However, other studies demonstrate that the regulation of microtubule nucleation sites is controlled by γ-tubulin, a nucleator of mictrobules, independently of Golgi outposts [57].

Remodeling of the cytoskeleton may also be a major molecular strategy for generating new branches. One study has found that actin filaments are enriched at the location of future branch points and hence precede their formation [58]. Moreover, several studies have observed that the severing activity of cytoskeletal elements significantly affects the complexity of the dendritic tree pattern. For example, reducing the expression of the actin-severing protein Tsr/cofilin or increasing the stability of F-actin decreases the formation of new dendrites [58]. Other investigations made similar observations for microtubules. One study shows that the transcription factor Knot regulates branching by controlling the expression of Spastin, an ATPase that severs microtubules [29]. Another study has found that axonal regeneration in *Drosophila* da neurons is strongly dependent on the expression of the *spastin* gene [77]. Furthermore, Katanin 60, another microtubule severing protein, is also required for the proper development of da neurons [48]. In addition, using a statistical approach, another study has shown that the density of microtubules and F-actin are strong determinants of the tree topology [56]. More specifically, the MT density is a strong predictor of arbor length and branch points are enriched with F-actin. Overall, these results indicate that cytoskeletal severing proteins play an important role by reshaping the dendritic tree and providing nucleation sites. This function is also consistent with our findings that Spastin acts as a nucleator by increasing the average number of MT growing ends [36, 37].

Conjointly with the cytoskeleton, there is also evidence that molecular motors and endosomes play an active role in branching. Indeed, mutations in genes encoding for motor-protein such as the dynein subunit gene (*dlic*) and the kinesin-1 heavy chain (*khc*) reduce the complexity of the dendritic arbors and shift the branch spatial distributions towards the cell body [72]. In addition, mutant arbors that do

not express Rab5, a small GTPase that regulates the early endocytic pathway, show a reduction in the number of branches. This phenotype indicates that Rab5-endosomes play a key role in the branching process by carrying an essential cargo for forming new branches. Another study showed that reducing the expression of the coiled-coil protein Shrub, which is a key component of the endosomal sorting complex required for transport, reduced the amount of branches in early-stage class IV neurons, but increased the number of terminal branches in third-instar larva [80].

Finally, another hypothesized mechanism of neurite branching worth mentioning is the extension of neurites by mechanical cytoskeleton forces. By analyzing axonal growth in *Drosophila* cultured primary neurons, one study has found that sliding of microtubules mediated by kinesin-1 was necessary and sufficient to extend the axon [46]. Subsequent studies by the same group, using kinesin-1 heavy chain (KHC) mutants, found that this outgrowth mechanism is also conserved in class IV neuron dendrites [59, 90].

Self-avoidance

Tip growth and branching are two mechanisms that promote coverage of the receptive field. To prevent excessive filling of the occupied area, the growth of dendritic tips in class IV neurons is inhibited after contacting other dendrites. This process is known as *self-avoidance* and is mediated by the Down Syndrome Cell Adhesion Molecule (DSCAM). Intense research on the molecular basis of self-avoidance has uncovered a novel strategy of dendritic pruning that warrants a brief foray into this mechanism [51, 73, 97].

Dscam1 is a cell adhesion molecule that is embedded across the cellular membrane of class IV neurons. One of its end is outside the cell (in the extracellular matrix), while the other end is in contact with the cytoplasm (the intracellular tail) (see fig. 1.5). Upon encountering a copy of itself, Dscam1 binds with this

copy (homodimerization) and triggers a repulsive signaling pathway that inhibits growth. However, the repulsive signal is not activated if two different forms of the Dscam1 molecule encounter each other. Hence, when a dendritic tip contacts a dendrite belonging to the same tree, the homophilic binding of Dscam1 inhibits further tip growth. Furthermore, Dscam1 endows the cell with a molecular identity via the alternative splicing of the Dscam1 locus, which can create at least 19,000 isoforms [97]. Thus, the molecular diversity of Dscam1 allows the cell to distinguish between self and non-self neurites, which is essential for the coexistence of dendritic arborization neurons of different types in a given receptive field.

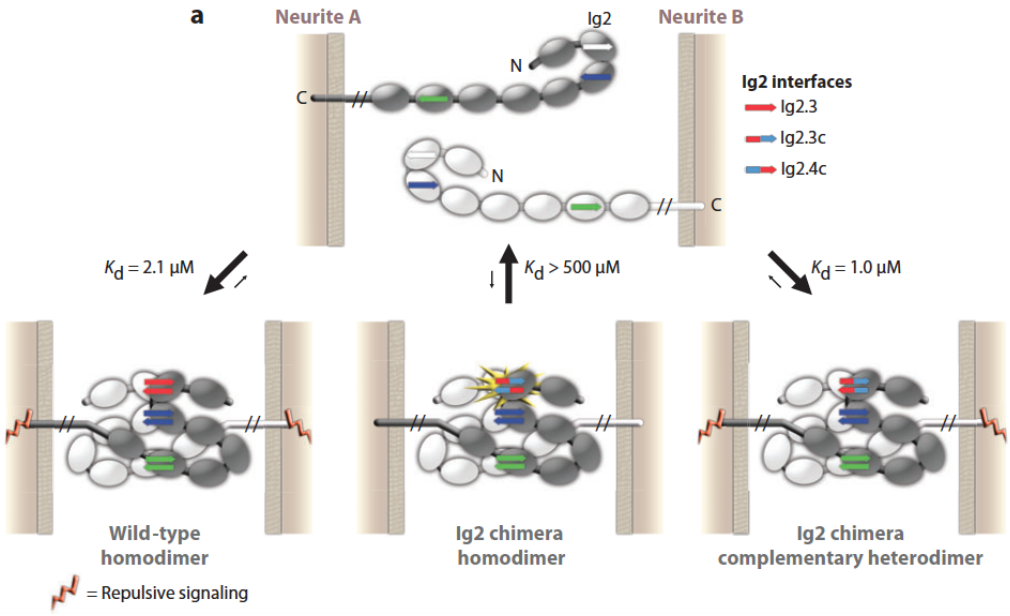

Figure 1.5 – Binding kinetics of the DSCAM molecule
Reproduced from figure 2a of [97]. Two DSCAM molecules bind with one another only when they are homodimers or complementary heterodimers. Upon binding, a repulsive signaling is transmitted through the cytoplasmic tail.

By inhibiting the growth of dendrites that collide with one another, class IV neurons are effectively pruning their dendritic trees in regions of high dendrite density where the tip collision frequency is increased. However, since this pruning mechanism is contact-mediated, a sufficient probability of contact is necessary to ensure that neighboring dendrites avoid each other. This condition is ensured by integrins and cadherins, which maintain the dendrites tightly bound to the basal

membrane of the epidermis [20, 32, 74]. Thus, the dendritic arbor is constrained on a two-dimensional plane making contacts more likely to occur compared to a three-dimensional space geometry. Therefore, the anchoring molecules work in consortion with Dscam1 to prune the dendritic tree via contacts.

In addition, mutation of *Dscam1* in Class III da neurons have shown that it also counters the effect of targeting cues by netrins [50]. This suggests that more complex da neurons like class III and class IV organize the spacing and distribution of their dendritic branches dynamically by the combined effect of autonomous dendrites growth and contact-based repulsion.

Tiling

At 48 hr AEL, the class IV neurons establish almost complete coverage of the larva's epidermis in a tiled fashion as shown in fig. 1.3. In *Drosophila*, this phenotype is known as *tiling* and it occurs by preventing overgrowth of class IV neurons [19]. Tiling has also been observed in other neuronal systems such as the visual nervous system in mammals [2, 4, 87, 88]. However, it is not universal across the *Drosophila* nervous system. For example, in the developing central nervous system, there is partial evidence that the initial positioning of motor neurons is not a consequence of neighboring neuron repulsion, but is instead controlled by early developmental cues [38]. Moreover, the tiling phenotype is not exhibited by all dendritic arborization neurons, but only the class III and IV neurons [18].

Although the type-specific dendrites repulsion controlled by Dscam1 would be an effective strategy to establish the boundaries of the neuron's receptive field, several studies have found that Dscam1 is not required for the tiling of class IV neurons [25, 51, 73]. Instead, experimental evidence shows that the tiling of class IV neurons is controlled by a more complex pathway that includes the 7-pass trans-

membrane cadherin Flamingo [16, 33, 79] and the kinases Hippo and Tricornered [11, 12].

Once tiling is established, the growth of class IV neurons scales with the growth of the organism. One study has shown that this scaled growth is regulated by the microRNA bantam (*ban*) [62]. In this study, they observed that *ban* mutants exhibited overgrown dendritic trees indicating that microRNAs, which are known to be temporal regulators of development, play an active role in dendritic growth. In addition, they found that the inhibitory function of *ban* was not autonomous in class IV neurons, but required signaling with the underlying epithelial cells indicating that the substrate also plays a significant part in the growth of dendrites.

In summary, the tiling of class IV neurons helps the larva to gather sensory information in an efficient and non-redundant manner.

1.2 Models of branching morphogenesis

Class IV neurons are a complex biological system that develop an intricate branching pattern throughout their development. Such designs are not unique to the *Drosophila* nervous system, but are found in many living organisms and arise from a multitude of processes that shape the morphology of the tree in specific ways. Understanding how these processes create the branching patterns that are observed has motivated researchers to propose models of branching morphogenesis based on established principles of growth. In this section, I describe several models of branching morphogenesis that are relevant to our model system and explain how each of them succeeds at reproducing the observed morphology using a given set of branching rules.

1.2.1 Branching morphogenesis as an optimization process

A century ago, Ramón y Cajal [5] proposed architectural principles in neuronal anatomy and Wilfrid Ralls [66] subsequently build upon these ideas to start developing a neuron theory that considers both morphological and electrophysiological properties. Iterating on the ideas of Ramón y Cajal and Ralls, Cuntz *et al.* proposed the idea that the process of branching morphogenesis seeks to minimize the total dendritic material while maximizing the signal transduction to the cell body [9].

More specifically, the morphogenesis optimization principle aims to minimize the following cost function:

$$C = \sum_i \ell_i + bf \sum_j L_j(\vec{x}_j) \tag{1.1}$$

where ℓ_i corresponds to the length of the i^{th} branch in a given tree, $L_j(\vec{x}_j)$ is the length of the shortest path from the root of the tree to the target position $\vec{x}_j$ and bf is a parameter that weights the relative strength of the two costs. The first term in eq. (1.1) corresponds to the material cost of the tree, while the second term corresponds to the cost of transmitting an attenuating signal from a set of positions $\vec{x}_j$. These two opposing costs were initially proposed by Cajal, namely that the cytosol or material must be minimized (first term) while also minimizing the conduction time (second term). To build the tree from a given set of targets, the model uses a greedy algorithm that iterates through each target point and connects them to the tree with a path that minimizes the total cost.

Then, by varying the single parameter of this optimization problem, namely the balancing factor bf, the landscape of morphologies is explored by optimizing the arbor for a given set of target points $\vec{x}_j$ (see fig. 1.6). To test the sufficiency of the optimization, the authors attempt to reproduce the morphology of several cell types include amacrine cells, hippocampal granule cells and cortical pyramidal cells.

For each cell type, the set of target points that is used to generate synthetic trees is determined by sampling the measured density of tree nodes and the number of targets varies in each cell type.

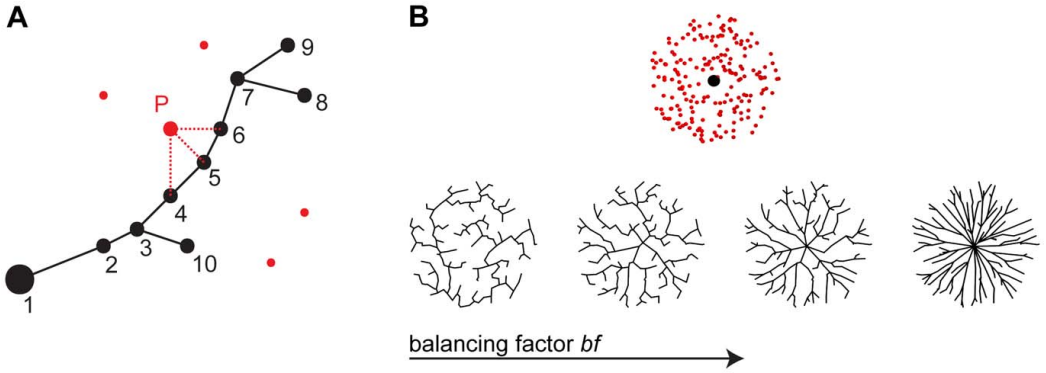

Figure 1.6 – Minimal spanning tree algorithm of the Cuntz *et al.* model
Reproduced from figure 2 of [9] A) Example of the trade-off that is considered during the construction of the tree with the minimal spanning tree algorithm. To construct the tree, the target points (red circles) are connected to the dendritic tree (black circles). In this example, the target point P 5 is closest to point 5 in euclidean distance, but the path that goes through point 5 is longer than the one that goes through point 4. Depending on the value of the balancing factor, one path will incur a smaller total cost than the other. B) Examples optimal morphologies for increasing values of the balancing factor bf. The red circles corresponds to the set of targets from which the conduction is minimized.

The model succeeds at reproducing a wide range of morphologies as assessed by comparing the branch depth distribution, the branch length distribution, the Sholl intersections and the electrotonic map, which determines the sizes and quantities of sub-trees. The model also succeeds at reproducing the tiling of contiguous neurons, as seen in Purkinje cells, by running many optimizations that compete to reach target points.

Insights

The success of the Cuntz *et al.* model hints that optimization of material cost and connectivity may be at work during the development of neurons. Indeed, since neurons must function right from the onset of development, it is plausible that

their activity and the availability of cellular material during development drive their formation. Moreover, the fact that synthetic and real neurons share many morphological similarities for various cell types indicate that such optimization principles may be universal across neurons.

Limitations

Although the Cuntz *et al.* model succeeds at reproducing diverse neuronal morphologies from a simple optimization principle, it has no physical foundation. Indeed, the model provides a formula for constructing an optimal and realistic dendritic tree, but it does not explain how such tree is constructed by physical processes. Moreover, the final shape of the spanning tree is strongly determined by the position of the target points and it is unclear how these target points arise in neuronal systems. To produce the synthetic trees, the authors define the target points from the density of measured trees. Since the target points are highly correlated with the real trees, the extent to which the algorithm is simply sampling the real morphology distribution is unknown.

1.2.2 Turing patterns in class IV neuron morphogenesis

In 1952, Alan Turing proposed the idea that the diverse structural patterns in living organisms were an emergent phenomenon of the underlying chemical reactions of biological constructs, nowadays known as Turing patterns [84]. Following this hypothesis, Sugimura *et al.* proposed a model of branching morphogenesis that consists of a set of three chemical species that diffuse and react with one another to create dendritic shapes [78].

Specifically, the model species consist of 1) core molecules $c(\vec{x},t)$, meant to represent inert dendrites, 2) activators $u(\vec{x},t)$ that promote the growth of dendrites

c and 3) suppressors $v(\vec{x},t)$ that inhibit dendritic growth. The diffusion-reaction dynamics of these species is governed by the following dynamical equations:

$$\frac{\partial u(x,t)}{\partial t} = D_u \nabla^2 u + f(u,v) \tag{1.2}$$

$$\frac{\partial v(x,t)}{\partial t} = D_v \nabla^2 v + g(u,v) \tag{1.3}$$

$$\frac{\partial c(x,t)}{\partial t} = p_h c(a(u)-c)(c-p_k) \tag{1.4}$$

The first term in in the RHS of equations eq. (1.2) and eq. (1.3) models the diffusive motion of activators and suppressors with diffusion constant D_u and D_v, respectively. The authors consider the case where suppressors diffuse faster than activators ($D_v > D_u$). In addition, suppressors and core molecules are free to explore the full 2D space, while activators are constrained to small volume around the core molecules (see fig. 1.8C).

The second terms, f and g, model the specific interactions between activators and suppressors, including self-interactions. More specifically, activators are auto-catalytic ($\frac{\partial f}{\partial u} > 0$), but their growth is inhibted by suppressors ($\frac{\partial f}{\partial v} < 0$), while suppressors are promoted by activators ($\frac{\partial g}{\partial u} > 0$) and their degradation is concentration-dependent ($\frac{\partial g}{\partial v} < 0$).

The last equation eq. (1.4) determines the growth of the dendritic shape, which is entirely determined by the activator-suppressor dynamics. As opposed to u and v, the core molecules do not diffuse and can only grow in the presence of the activators, which is controlled by the function $a(u)$. The RHS of eq. (1.4) indicates that the "state" of the core molecules is *bistable* where $a(u)$ is the switching point between absence ($c = 0$) and presence ($c = 1$) of dendrites.

To better understand how the bistable dynamical system of the core molecules c lead to dendritic growth, the authors graphically explain how $a(u)$ controls the stability of the fixed points of c (see fig. 1.7).

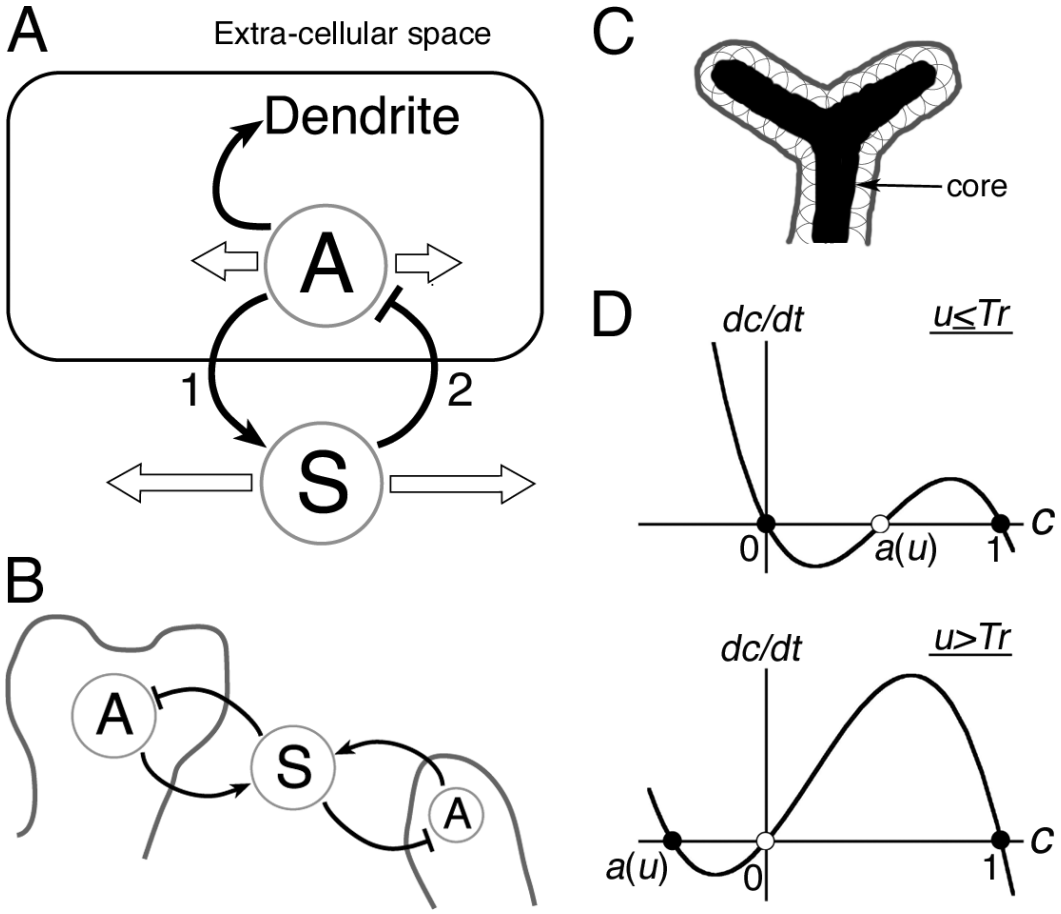

Figure 1.7 – Summary of the cell compartment model introduced by Sugimura *et al.* Reproduced from figure 1 of [78]. A) Summary of the reaction dynamics between the chemical species. Activators **A** promote the growth of dendrites and suppressors **S** (1), while suppressors inhibit the presence of activators (2). In addition, suppressors diffuse faster than activators and the motion of activators is bound by the dendrites volume. B) The extra cellular suppressor molecules inhibit the growth of surrounding dendrites. C) The cell compartment consists of a core (representing the dendrites) surrounded by an envelope where activators can diffuse. The envelope is defined by the union of spheres of radius R centered at each core molecule. D) Summary of the reaction dynamics between the core (c) and activators (u). The growth of dendrites ($\frac{dc}{dt} > 0$) is initiated when the activator concentration reaches a certain threshold Tr. When $u(\vec{x},t)$ is below threshold, $c = 0$ is a stable fixed point. When $u(\vec{x},t)$ is above threshold, $c = 0$ is an unstable fixed point.

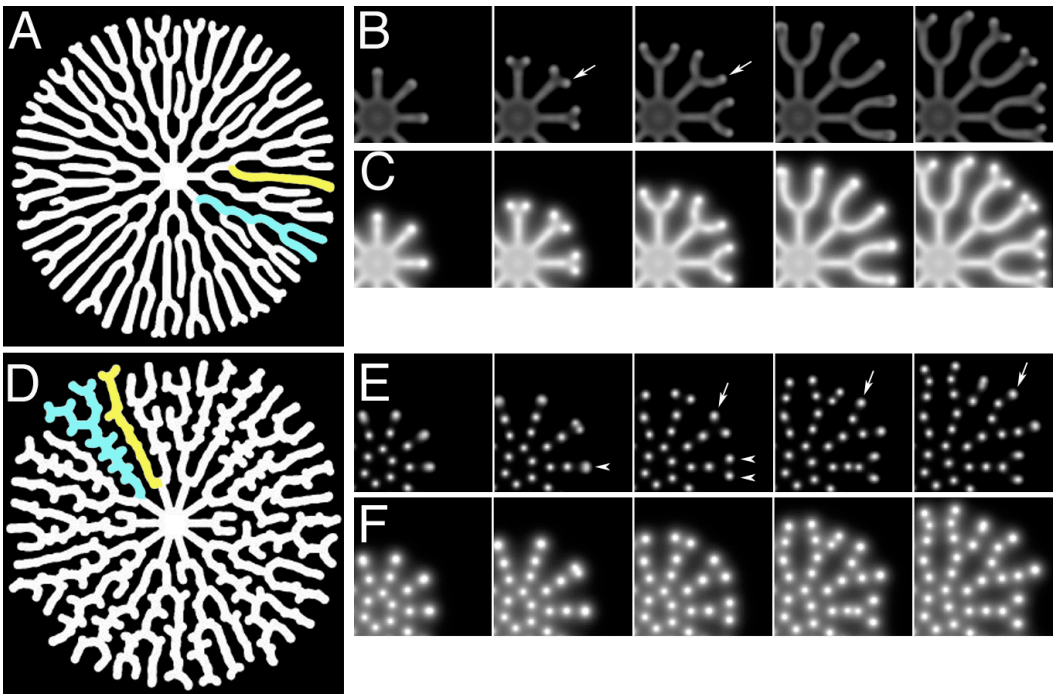

Figure 1.8 – Mean-field dynamics of the Sugimura *et al.* model
Reproduced from figure 2 of [78]. A,D) Examples of simulated dendrites in the cell compartment model of Sugimura model. B,E) Concentration profile of activators. C,F) Concentration profile of suppressors.

Insights

The simplicity of the Sugimura model is its greatest strength. Based on a simple set of reaction-diffusion equations, the model can produce branched networks that are similar in shape to the class IV neuron dendritic tree. Moreover, the fact that the tree is built entirely from the local activator-suppressor dynamics, which is itself constrained by the local dendrites density, indicates that a self-organizing branching process is sufficient to form a dendritic tree.

Limitations

Although the simplicity of this model facilitates intuition, it also limits its representation of real systems. One of the hallmark of biological systems is their ability to adapt

to changes in their environment. This adaptability requires continuous sampling of their environment, which lead to stochastic behaviors. In class IV neurons, the adaptability of the shape to fill space originates from the stochastic growth of branch tips, which constantly go through phases of growth and shrinkage. In this model, such stochasticity is absent in branch tips since the dendritic tree in the bulk quickly reaches an equilibrium given by the steady-state of the activator-suppressor dynamics. In addition, the authors presume the presence of activators and suppressors, but their biological origin is unclear. Consequently, it is difficult to assess the feasibility of the parameter values in physiological conditions.

1.2.3 Mechanistic model of mammary gland morphogenesis

Studying the mouse mammary gland, kidney and the human prostate, Hannezo *et al.* [21] proposed a model of branching morphogenesis that recapitulates the statistical properties of the branched network exemplified in these organs. Taking a non-reductionist approach, the authors aimed to predict the large-scale statistical properties of the branched networks using rules of growth that are loosely dependent on the cellular and molecular scale dynamics. This summary focuses on the two-dimensional ductal network of the mouse mammary gland epithelium studied by the authors.

The Hannezo *et al.* model is based on the theory of branching and annihilating random walks (BARWs) [7] where the growth of branch tips is regulated by three local rules: 1) tip branching, 2) tip elongation and 3) tip termination. The rules are summarized graphically in figure fig. 1.9. Stochastic simulation of these rules show that they can generate branched networks with statistical properties that are similar to the organs' network. The statistical properties were assessed by several metrics such as the average tip termination probability, i.e. the fraction of tips that terminate at a given level, the distribution of subtree sizes and the subtree persistence, i.e. the

fraction of subtrees at the 6^{th} level that are still present at a deeper level. As shown in fig. 1.9, the model predicted networks that were in agreement with the ductal networks.

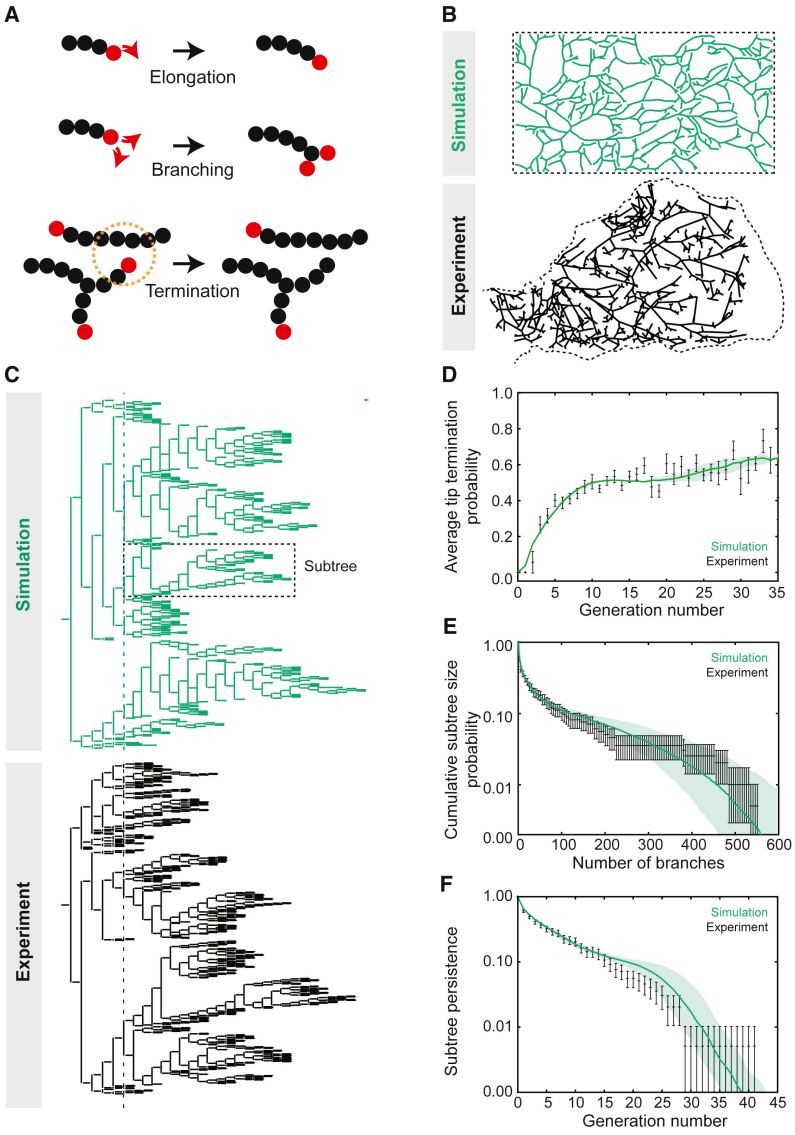

Figure 1.9 – Graphical summary of the Hannezo *et al.* model
Reproduced from figure 2 of [21]. A) Model rules for the growth of ductal networks. B) Comparison of simulated and experimental ductal networks. C) Comparison of the simulated and experimental tree topology. The origin of a subtree starts at generation $n = 6$. D-F) Statistical metrics of simulated and experimental trees. The shaded region corresponds to mean $\pm$ SD.

Supporting the simulations, the hydrodynamic limit of the branching rules was also considered using a 1D mean-field approach that involves two species: active

a (tips) and inactive i (ducts) particles. The dynamical equations that govern the evolution of these two species are the following:

$$\frac{\partial a}{\partial t} = D\nabla^2 a + r_b a\left(1 - \frac{a+i}{n_0}\right) \tag{1.5}$$

$$\frac{\partial i}{\partial t} = r_e a + \frac{r_b}{n_0} a(a+i) \tag{1.6}$$

In the active tip equation, the first term models the motion of the tips through diffusion while the second term results from branching events, which increase the local number of active tips by 1 with probability r_b. Finally, the last term corresponds to the annihilation of active tips upon encountering another active tip or duct particle. This term is normalized by n_0, the steady state density of ducts, such that no more new branches are created when the local density of ducts and tips reaches a steady state.

In the inactive ducts equation, the first term models the process of tip elongation whereby inactive ducts are produced at a rate r_e in the vacant space created by the moving active tips. The second term is the counterpart of the last term of the active tip equation where inactivation of an active tip produces inactive particles.

With this formulation, the mean-field model predicts duct and tip densities that are in agreement with the observations (see fig. 1.10). Moreover, the model predicts that the ductal network of the mammary gland epithelium grows through the propagation of a constant-speed solitary density wave of active branch tips.

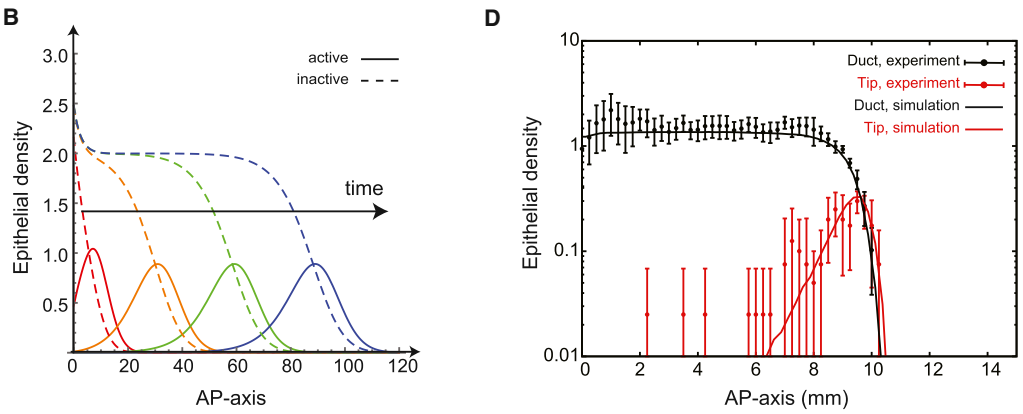

Figure 1.10 – Mean-field predictions of the Hannezo *et al.* model
Reproduced from figure 3 of [21]. B) Temporal evolution of the predicted densities of active and inactive tips. D) Comparison of theoretical and experimental density profiles.

Insights

Hannezo *et al.* proposed a model of branching morphogenesis based on a simple set of local rules (tip elongation, tip bifurcation, tip termination) that can quantitatively predict observed morphologies. Moreover, the model reproduces the small amount of branch crossovers seen in the ductal networks of mammary glands, similar to the dendritic network of class IV neurons. In the model, this is ensured by terminating the growth of active tips that are in proximity of inactive ducts. The success of this mechanism suggests that the branching morphogenesis of ductal networks is a stochastic self-organized process contrary to the idea that it is governed deterministically by a genetic program. Since this self-organizing branching process was observed in several 2D and 3D tissues, they propose that it could be universal in organic tissue development.

Limitations

Although the proposed model is certainly successful at recapitulating key aspects of branching morphogenesis in tissues, it is unlikely that this branching model unifies

all biological branching processes. One branching rule that is most limiting is the tip branching. Indeed, in class IV neurons, although dendritic tips can certainly branch into two branches, most new tips are born out of the inert dendrites (which corresponds to the inactive ducts in this model). In further iterations of the main model, side-branching was considered, but the side-branches were constrained to grow for only a typical length, could not branch further and were only created during tip branching events. Moreover, as the branching process occurs solely at the tips, the majority of new tips are located at the periphery of the network, which is also predicted by the mean-field model. This is undoubtedly different than the branching process of class IV neurons since branch tips are born across the entire network. Finally, the tip termination process also limits the universality of the model. In class IV neuronal growth, dendritic tips do not terminate upon contact, but retract and potentially regrow in other directions depending on their dynamics.

1.2.4 Mechanistic model of class I neuron morphogenesis

Palavalli *et al.* [61] proposed a computational model of branching morphogenesis for *Drosophila* class I neuron at the early developmental stage (15-25 hr AEL), which incorporates both deterministic and stochastic rules of growth. The model is summarized in fig. 1.11.

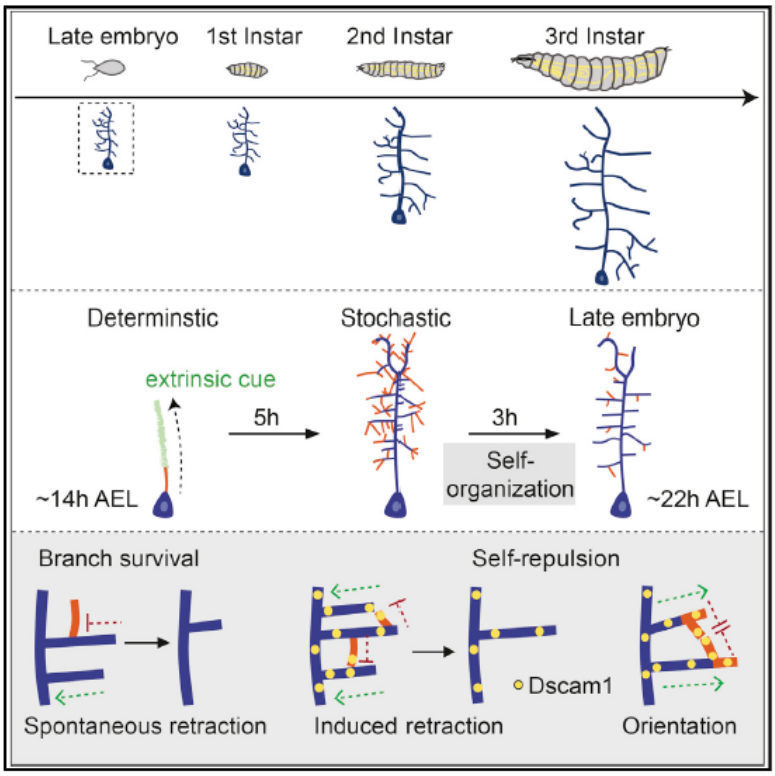

Figure 1.11 – Graphical summary of the Palavalli *et al.* model
Reproduced from graphical abstract of [61].

The model starts from a vertical branch of length $30\mu m$, which corresponds approximately to the geometry of class I neuron at 15 hr AEL. From this initial branch, new branches are born out of existing branches at a rate of λL, where λ corresponds to the branching rate per unit length of dendrites and L represents the length of any potential parent branch. Once branches are spawned, they grow at a velocity v_{on} that is constrained by measurements. The initial growth direction is uniformly distributed and the subsequent orientation is controlled by the persistence length l_p set to $17\mu m$. Then, with a certain rate k_{off}, branches transition to a shrinking state that shortens the branch at a rate v_{off}. The depolymerizing state can also be induced by contacts with other dendrites, which is motivated by the contact-based retraction triggered by the Dscam pathway. Upon contact, branches switch to the depolymerizing state with a probability p_{off}, which is set to 1 for the wild-type cases. Finally, reversion to the polymerizing state is controlled by another rate, k_{on}. In addition, the model

distinguishes between primary, secondary, tertiary and quaternary branches and assigns them different parameters: $\lambda_i, k_{i,on}, k_{i,off}, v_{i,on}, v_{i,off}$ where i indexes the order.

To evaluate their model, they measure the total dendritic length over developmental time and categorize the length distribution by the branch order, which corresponds to the depth of a given branch in the tree hierarchy. They also compare the number of secondary and tertiary branches and measure the growth rate of branches to constrain the switching rates (k_{on}, k_{off}).

Then, they explore the model parameter space by changing the value of $r = \frac{k_{on}}{k_{off}}$. They find that the density of the arbor depends strongly on r, where increasing r leads to denser trees. This is expected since a higher value of r implies a higher value of k_{on}, which means that branches spend more time in the polymerizing state. Moreover, they find that these simple rules of growth cannot recapitulate the number of secondary and tertiary branches measured in class I neurons. Indeed, in their simulations, the number of secondary branches is overestimated almost twofold compared to the measurements, while the number of tertiary branches increases monotonically with time.

To rescue the model, they introduce an aging process where the switching rates and tip velocities decrease by a constant factor every 2 hrs. The switching rates and branching rate are reduced by a factor f_i, while the velocities are reduced by a different factor $f_{v,i}$. In addition, the decay factor changes for each branch order (2 to 4). With this new model, they are able to reproduce the branch number, the mean branch length of secondary and tertiary branches and the branching angle distribution, i.e. the angle between secondary and primary branches. Although their predictions are in agreement with experimental observations, their aging protocol introduces 6 new parameters that are unconstrained by measurements, henceforth reducing the predictive power of the model.

Overall, their model demonstrates that class I dendritic trees are shaped autonomously by the dynamics of their branch tips without external cues. Moreover, the model highlights two important mechanisms that determine the tree morphology. First, the branching of secondary and tertiary branches act as a maturation process that prevents the retraction of primary branches. Second, the contact-based retraction is a negative feedback that shapes the tree's architecture based on the local dendrites density.

Insights

The success of the model at reproducing the number of branches and branch length distribution hints that the development of class I neuron may be an autonomous process that is independent of extrinsic factors. Moreover, the success of the model in recovering the Gaussian distribution of the measured branching angle reinforces the idea that the arbor geometry emerges from the local growth dynamics.

Limitations

Although the model predictions are in agreement with the measurements, the comparison is only performed over 10 hours of growth from 15 to 25 hr AEL, which corresponds to 10% of the larva's lifetime. It is unclear if the model would still hold at later developmental stages. Moreover, the aging process parameters are unconstrained by measurements. It is possible that such an aging process occurs *in vivo*, but the particular functional dependence of the parameters on the aging process is not supported by experimental observations. Finally, the model recapitulates coarse-grained metrics of the tree topology like branch length and branch number, but spatial metrics like the density of dendrites are not compared. Although prediction of the tree topology is a necessary condition for the model's success, it is also necessary that it recapitulates the spatial distribution of the branches, as this is

an important driver of the contact-based retraction. The qualitative comparison of the simulated and real trees presented by the authors indicate that spatial metrics are also in agreement. However, it is difficult to assess the accuracy of the model on these metrics without quantification.

1.3 Question and hypothesis

Defective dendritic arbors are known to be the cause of several neurological disorders such as schizophrenia, autism spectrum disorders and neurodegenerative diseases [35]. The molecular mechanisms of these pathologies are still unknown and the design of new therapies is impeded by our limited understanding of the fundamental developmental processes of dendritic arbors. This lack of knowledge stems from the diversity of dendritic arbors and the complexity of the underlying molecular mechanisms. The need to develop a comprehensive understanding of neuronal development that connects molecular processes to cellular morphology motivates the following question:

How do neuronal dendrites grow?

To answer this question, we hypothesize that dendritic growth is an emergent property of the molecular scale dynamics (see fig. 1.12).

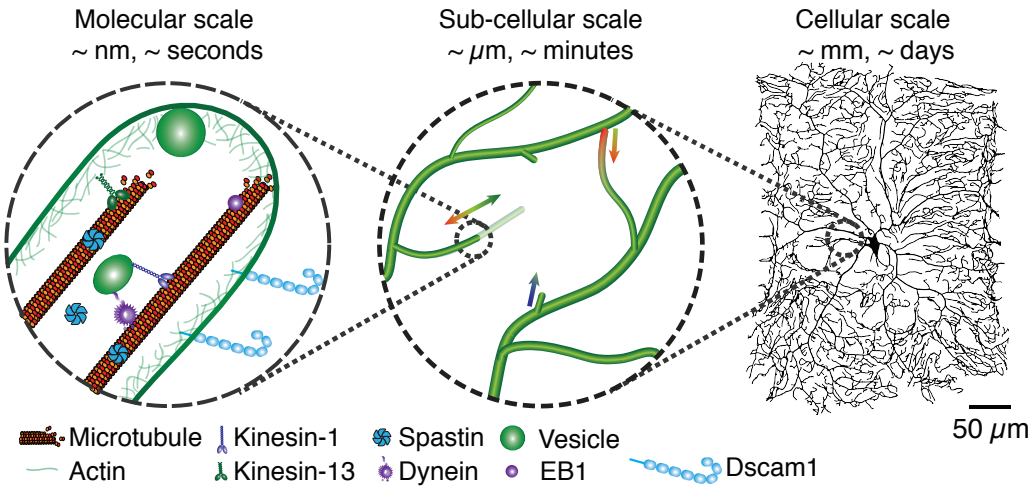

Figure 1.12 – The emergence of dendritic morphogenesis
Molecules, including molecular-motors, cytoskeletal polymers, severing proteins and cell adhesion molecules, interact with one another at the nanometer length scale over the second time scale, which leads to the growth of the dendritic tip at the micrometer length scale and over the minute time scale. Furthermore, the growth dynamics of the dendritic tip is modulated by the tip environment, which consists of the extra-cellular matrix, the epithelium and other dendrites, which ultimately generate the morphology of the dendritic tree at the millimeter length scale over the day time scale. Figure designed in collaboration with Sabyasachi Sutradhar.

This hypothesis prompts the following sub-questions:

- What molecular mechanisms drive dendritic growth?
- How do the spatial and temporal dynamics of the dendrite affect the overall growth of the dendritic tree?
- How do the molecular mechanisms change over development?
- Are there universal principles of dendritic growth that have been evolutionarily promoted by environmental factors?

The verification of this hypothesis requires establishing a direct link between the molecular processes of dendritic growth and the cellular structure of the class IV dendritic tree. Although extensive research in the past decades have shone new light

on the molecular landscape of *Drosophila* dendritic growth [27, 41, 71, 97], there is still much to be learned about their effect on the large-scale dendritic growth. In addition, multi-scale data-driven models are also necessary to reinforce the causal relationships between the molecular processes and cellular structure evidenced by experimental observations.

To take part in this arduous endeavor, I focus on building the connection between the sub-cellular growth processes and the cellular morphology, using the dendritic tip as the elementary unit. To establish this correspondence, I use the class IV neurons of the *Drosophila melanogaster* larva as a model system for several reasons: 1) the neurons are nearly two-dimensional making them easier to observe compared to three-dimensional neurons, 2) the genetic tools are well-developed, which makes mutation experiment easier to design and 3) the short life cycle provides rapid developmental observations compared to mammalian model systems. In this physical study of the class IV neuron dendritic growth, I have made several contributions as detailed in each chapter of this thesis and summarized in the conclusion.

2 Material and Methods

In this chapter, I describe the data acquisition and image analysis techniques that were used to process the static and dynamic observations of the dendritic growth in *Drosophila* class IV neurons.

The sample preparation and image acquisition were performed by Sonal Shree. The dendritic tip tracking was performed by Sabyasachi Sutradhar. The image analysis was performed in collaboration with Sonal Shree and Sabyasachi Sutradhar.

2.1 Sample preparation and microscopy

The fly line used to image class IV dendritic arborization neurons in this study was Bloomington stock 35842, possessing the following genotype: +;ppk-CD4-tdGFP;. The fly stock was maintained at 20°C in a humidity-controlled incubator on standard D-2 glucose medium vials (Archon Scientific) with a 12-hour light/dark cycle. Fly crosses were maintained in fly chamber at 25 °C, 60 % humidity. The plate used to collect the fly embryos was apple juice agar-based containing a mixture of apple agar concentrate, propionic acid, phosphoric acid and water. Also, large drops of yeast paste were deposited in the center of the plate to stimulate egg laying.

Before imaging, the larva was washed with 20% and 5% sucrose solutions, anesthetized using FlyNap (Carolina Biologicals, Burlington, NC, USA), and transferred

to an apple agar plate to recover. After recovery, the larva was gently positioned on a 1% agar bed with their dorsal side, put on a slide, and imaged in a drop of 50% PBS, 50% Halocarbon oil 700 (Sigma Aldrich). The larva was further immobilized by gently pressing a 22×22 mm^2 coverslip lined with Vaseline or vacuum grease.

For imaging, samples were mounted on the microscope stage, illuminated with a Nikon laser (488 nm at 18-21 % laser power) and imaged with a spinning disk confocal microscope. The microscope consisted of 1) a Yokogawa CSU-W1 disk with a pinhole size of 50 μm, which was built on a fully automated Nikon TI inverted microscope with a perfect focus system, 2) an sCMOS camera (Zyla 4.2 plus sCMOS) and 3) Nikon Elements software with either a 40X (1.25 NA, 0.1615 μm pixel size) or 60X (1.3 NA, 0.106 μm pixel size) water immersion objective. The temperature of the sample region was maintained using an objective space heater at 25°C (OKO labs stage heater). Samples were manually focused onto the third or fourth abdominal body segments (A3 or A4) prior to image acquisition. Movies were collected in a frame of 2048×2048 pixels and a complete stack of images with a depth of 6-8 μm was produced every 4, 5 or 6 s. The stacks were then projected along the depth to find the maximal pixel intensity (maximal intensity projection).

2.2 Datasets

To analyze the class IV neuron dendritic growth, three dataset of class IV neurons were assembled.

The first dataset consists of static images of class IV neurons collected at 24, 48, 72, 96 and 120 hr AEL. A 60X objective was used at 24 hr AEL while a 40X objective was used at the later developmental stages. At 72 hr AEL, the class IV dendritic tree reaches a size of $\sim 300 \times 400\,\mu m^2$, which did not fit into one field of

view of the camera at a 40X magnification ($330 \times 330\,\mu m^2$). To image the entire dendritic tree, a set of overlapping images was taken for each neuron and stitched together in post-processing (see section 2.4). This dataset was used to measure the static morphometrics including the branching angle, neuron size, branch length, persistence length, branch orientation, fractal dimension, meshsize, interbranch distance and dendrites, branch points and branch tips densities (see section 3.3 and section 3.2.4).

The second dataset consists of movies of class IV dendritic growth collected at 18, 24, 48, 72 and 96 hr AEL. Similar to the static image dataset, a 60X objective was used at 18, 24 and 48 hr AEL while a 40X objective was used at the later developmental stages. The duration of the movies varied between 20 and 30 minutes depending on imaging conditions. Movies were stabilized after acquisition using the algorithm developed in [43] to reduce the effect of muscle twitches and drifts. This dynamic dataset was used to track the dendritic tips (see section 2.3), analyze their growth process (see section 3.1) at 24, 48 and 96 hr AEL. Moreover, the embryo stage movies at 18 hr AEL were used to measure the dynamics of the tip post-collision (see section 3.1.4). Finally, the branch birth and death rate was measured at 24, 48, 72 and 96 hr AEL using the dynamic dataset (see section 3.2).

Finally, the last dataset consists of static images collected at $24, 48, 72$ and 96 hr AEL using a magnification of 20X. This dataset was used to measure the body segment size (see section 3.3.1).

A summary of the datasets's statistics is given in table 2.1.

	18 hr AEL	24 hr AEL	48 hr AEL	72 hr AEL	96 hr AEL	120 hr AEL
Static dataset						
# of cells	0	13	6	8	7	5
# of animals	0	8	5	7	6	5
Dynamic dataset						
# of cells	102	9	6	6	6	0
# of animals	18	3	4	6	6	0
Segment size dataset						
# of cells	0	12	12	12	12	0
# of animals	0	3	3	3	3	0

Table 2.1 – Summary of datasets

2.3 Branch tip tracking

Using the dataset of dendritic growth movies, the growth process of the dendritic tip was tracked. First, dendritic tips were selected by visual inspection based on the criterion that they did not touch other dendrites during the recording. This was necessary since the planarity of the maximally projected images prevented the identification of tips when they overlapped with other dendrites. Moreover, the tip selection was also necessary to avoid the effect of muscle twitches and the drifting motion of the larva outside of the focal plane, which prevented accurate tracking. During a muscle twitch, regions of the dendritic tree would move drastically for one or two frames making tracking impossible. Dendritic tips were selected to be outside of these regions.

Once a sufficient amount of tips was gathered, movies were cropped around each tip to segment a sufficiently-large neighborhood of the tip that captured the dynamics over the entire recording. This segmentation process created a small-size movie for each selected tip. Using this movie, the tip position was located by fitting a

2D gaussian function convolved with an error function (see fig. 2.1b). The functional form of the fit is given by:

$$I(\vec{x}) = I_0 \exp\left[\frac{(\hat{\theta}(\theta)\cdot(\vec{x}-\vec{x}_0))^2}{2\sigma_\theta^2}\right] \operatorname{erfc}\left[\frac{\hat{r}(\theta)\cdot(\vec{x}-\vec{x}_0)}{\sigma_r}\right] + I_b \tag{2.1}$$

$$\hat{r}(\theta) = (\cos(\theta), \sin(\theta)) \tag{2.2}$$

$$\hat{\theta}(\theta) = (-\sin(\theta), \cos(\theta)) \tag{2.3}$$

where erfc is the complementary error function, $\vec{x}_0$ corresponds to the position of the tip and θ denotes its orientation. Once the tip was located, the center of the branch was determined by fitting a 1D gaussian along the perpendicular direction (see fig. 2.1c):

$$I(y) = \tilde{I}_0 \exp\left[\frac{(y-y_0)^2}{2\sigma^2}\right] + \tilde{I}_b \tag{2.4}$$

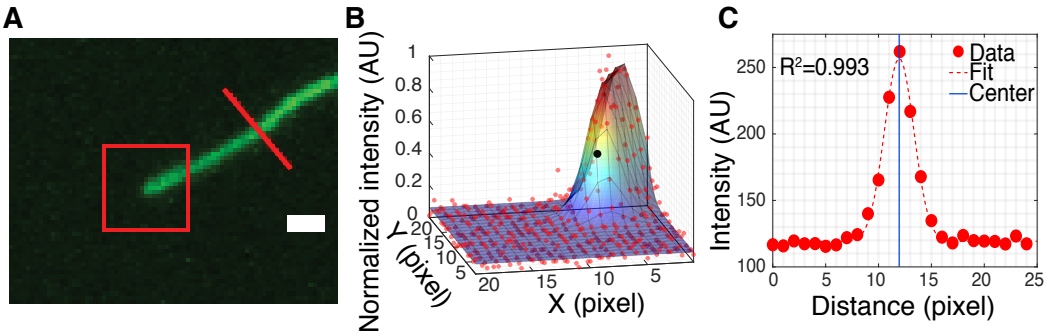

Figure 2.1 – Tracking of the class IV dendritic tips
A. Neighborhood of a tip. Scale bar represents 1 μm. **B.** Two-dimensional tip intensity profile fit. **C.** Perpendicular intensity fit. Figure provided by Sabyasachi Sutradhar.

Finally, the accuracy of the tracking method was tested with static simulated images of filaments of various size and shapes (see fig. 2.2). For most size and shapes, the tracking algorithm was accurate within a half-pixel size. However, when the shape of the filament was oscillatory, the error was considerably high as shown in fig. 2.2. However, since dendritic branches do not exhibit such kind of rapid

oscillations, the tracking algorithm was deemed accurate for the purpose of fitting class IV dendrites.

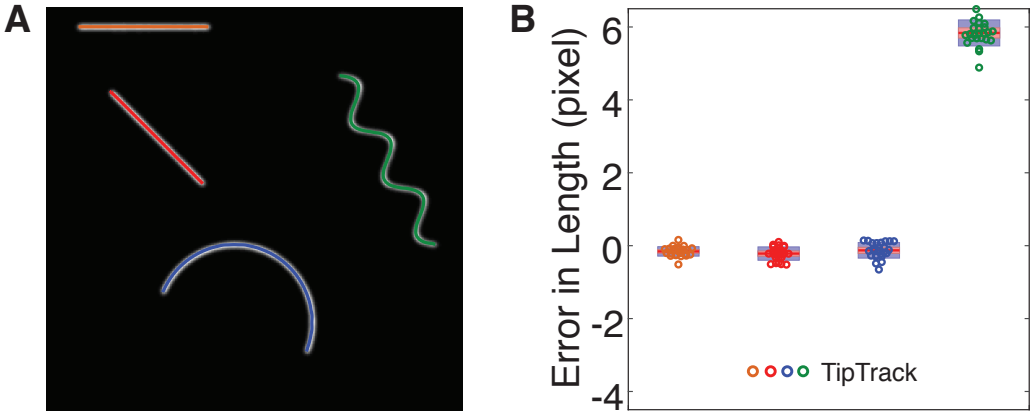

Figure 2.2 – Accuracy tests of the dendritic tip tracking method
A. Examples of simulated filaments tracked with the tracking method. **B**. Tracking error of the type of filaments shown in **A**. Figure provided by Sabyasachi Sutradhar.

2.4 Image stitching

As explained above, tiled images of class IV neurons were collected at 72, 96 and 120 hr AEL. Hence, reconstruction of the full dendritic tree required stitching the images together. In still images, image stitching can be easily accomplished by phase correlation [65] since a translation is sufficient to align two contiguous patches. However, in recording living organisms such as the *Drosophila* larva, the subtle motion of the larva or muscles twitches between the recording of one patch and another makes stitching more difficult. An example of stitching two patches of class IV neuron at 72 hr AEL using a translation derived from phase correlation is depicted in fig. 2.3a. As shown by the color channels, the branches of the dendritic network in the overlapping region do not align perfectly creating a spurious motion blur. For the analysis of coarse-grained metrics, a translation-based stitching may be sufficient, but for the purpose of our analysis, dendritic branches need to be perfectly aligned

in the overlapping region and continuous at the boundaries in order to ensure proper skeletonization (as explained in section 2.5).

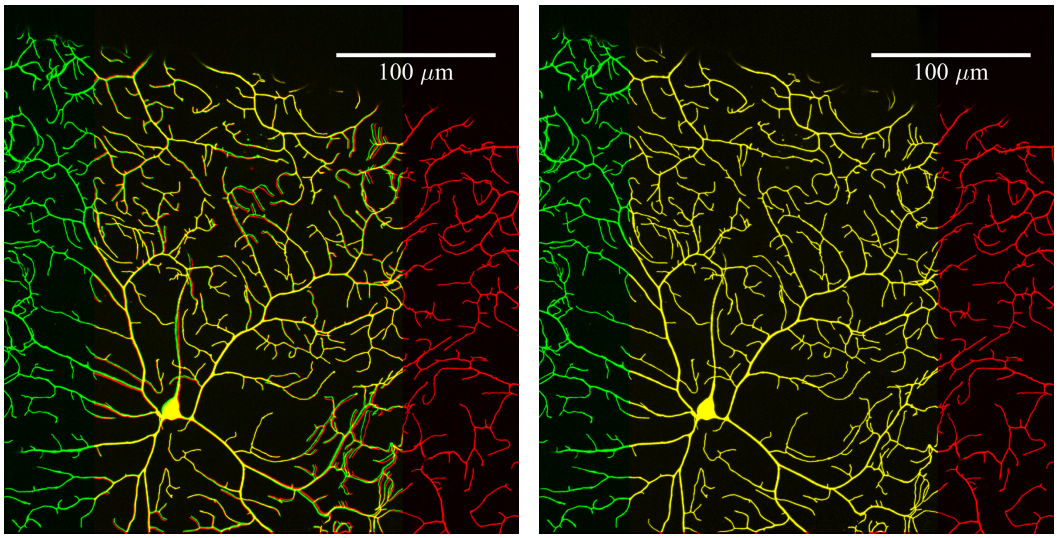

(a) Phase correlation method **(b)** Maxwell demons method

Figure 2.3 – Comparison of two stitching methods using a class IV neuron at 72 hr AEL
The novel stitching method based on the demons registration technique is better suited to align dendritic branches in regions where two patches overlap (yellow channel).

To resolve this issue, I designed a stitching algorithm in Matlab using non-rigid transformations. The main routine of the algorithm uses the built-in Matlab function *imregdemons*, which registers one image onto a reference image using a continuous displacement field derived from diffeomorphic demons [83, 86]. Since the displacement field can change continuously throughout the overlapping region,it provides more freedom to register two images with one another. However, one limitation of diffeomorphic demons is the fact that the displacement field is not-invertible. In other words, if $\vec{D}(\vec{x})$ registers image 1 onto image 2, the same field cannot be used to register image 2 onto image 1. Therefore, a reference image must be identified first before stitching. For the stitching of class IV dendritic trees, the selection of a reference image is ambiguous as there is no patch that is more trustworthy than another. To resolve this ambiguity, two displacement fields $\vec{D}_1(\vec{x}), \vec{D}_2(\vec{x})$ are calculated where $\vec{D}_i(\vec{x})$ uses image i as a reference to align the

other image. Then, these two fields are spatially interpolated to define the final displacement field that moves image 2 onto image 1:

$$\vec{D}_f(\vec{x}) = I(\vec{x})\vec{D}_1(\vec{x}) + (1 - I(\vec{x}))\vec{D}_2(\vec{x}) \tag{2.5}$$

where $0 \leq I(\vec{x}) \leq 1$ and $\vec{x}$ corresponds to the pixel coordinate in the overlapping region. $I(\vec{x})$ approaches 1 as $\vec{x}$ approaches the boundaries of image 1, while it approaches zero as $\vec{x}$ approaches the boundaries of image 2. The interpolation of the fields ensures that the final stitched image is continuous at the boundary of the overlapping region. Indeed, as $\vec{x}$ approaches image 1, using image 1 as a reference is increasingly more valid, hence the weight of $\vec{D}_1(\vec{x})$ increases accordingly.

Finally, the interpolator $I(\vec{x})$ is defined by the solution of the heat equation in the two-dimensional overlapping region using Dirichlet boundary conditions:

$$\frac{dI}{dt} = \alpha \nabla^2 I \tag{2.6}$$

$$I(\vec{x}) = \begin{cases} 1 & \vec{x} \in \Omega_1 \setminus \Omega_2 \\ 0 & \vec{x} \in \Omega_2 \setminus \Omega_1 \\ 0.5 & \vec{x} \in \Omega_1 \cap \Omega_2 \end{cases} \tag{2.7}$$

where the second equation defines the boundary conditions and Ω_i corresponds to the set of boundary pixels that are adjacent to image i. The thermal conductivity α controls the smoothness of the interpolation between the two images. For simplicity, $\alpha = 1$ is used. A stitched image example produced by this method is given in fig. 2.3b. As shown, the two sets of dendritic branches in the overlapping region are now sufficiently aligned to preserve the continuity of the dendritic network.

2.5 Skeletonization

To characterize the topology and geometry of the class IV neuron, microscopy images of class IV neurons are segmented to extract the skeleton of the dendritic tree. To trace the skeleton, I designed an automatic skeletonization algorithm that builds upon a voxel scooping method previously proposed in [70].

The voxel scooping method traces the skeleton of a binary image by iteratively scooping bright pixels in a local neighborhood. The voxel (or pixel) scooping is performed by scoopers, which are point-like agents that move through the binary image by attraction to bright pixels, analogous to a bacterium that moves through an environment to ensure a continuous supply of food (bright pixels). The algorithm starts from a seed position where the scooper is initialized. Then, the scooper moves towards the center of mass of the unscooped bright pixels that are connected to its occupied region. When the neighboring unscooped pixels form a disconnected set, which happens when the scooper reaches a branch point in the tree, new scoopers are initiated for each disconnected subset of the neighboring pixels. The scooping process is summarized graphically in fig. 2.4.

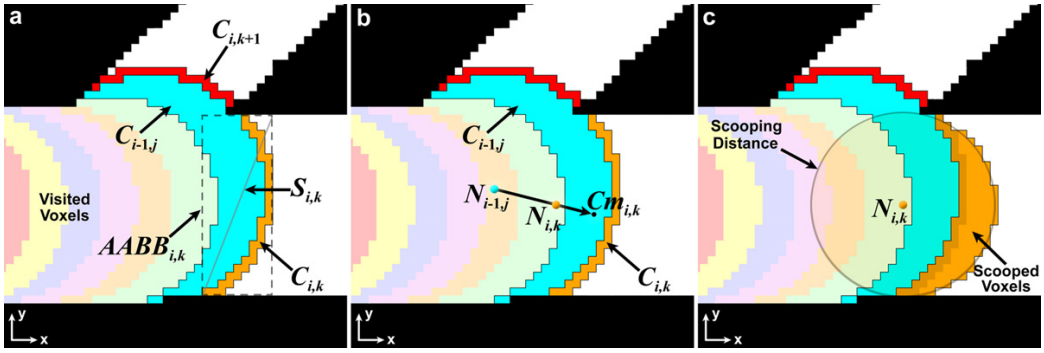

Figure 2.4 – Summary of voxel scooping tracing method
Reproduced from figure 2 of [70].

More specifically, the scooping process is initialized from an input seed position, which defines the root of the tree $\vec{N}_{0,1}$. Moreover, let $C_{i-1,j}$ correspond to the cluster

of pixels scooped at iteration $i-1$ by the j^{th} scooper (see fig. 2.4a) and let $\vec{N}_{i-1,j}$ correspond to the respective cluster position, which ultimately defines the position of a node on the skeleton. At the next iteration i, the image is scanned around $C_{i-1,j}$ to find unscooped bright pixels, which yields a set of disconnected subsets of unscooped pixels $\{C_{i,k}, C_{i,k+1}, \ldots\}$ where k corresponds to the number of clusters found so far in this iteration. Then, the center-of-mass $\vec{Cm}_{i,k}$ of each disconnected subset $C_{i,k}$ is calculated. Using the center-of-mass, the position of the new clusters $\vec{N}_{i,k}$ is defined by linearly interpolating between $\vec{Cm}_{i,k}$ and $\vec{N}_{i-1,j}$ (see fig. 2.4b). The distance where $\vec{N}_{i,k}$ is located along the interpolated line is defined in terms of the size of the cluster. Namely,

$$\vec{N}_{i,k} = \vec{N}_{i-1,j} + 0.5^{s_{i,k}}(\vec{Cm}_{i,k} - \vec{N}_{i-1,j}) \tag{2.8}$$

$$s_{i,k} = \min\left(\frac{S_{i,k}}{S_{i-1,j}}, \frac{S_{i-1,j}}{S_{i,k}}\right) \tag{2.9}$$

where $S_{i,k}$ corresponds to the diagonal of the bounding box that encloses $C_{i,k}$ (see fig. 2.4a). Once $\vec{N}_{i,k}$ are defined, the scooping process is performed by adding all unscooped pixels that are within a certain radius $r_{i,k}$ of $\vec{N}_{i,k}$ to the cluster $C_{i,k}$ (see fig. 2.4b). The scooping radius is defined as the maximal distance between the cluster position and the cluster pixels:

$$r_{i,k} = \max_m |\vec{N}_{i,k} - \vec{x}_{i,k,m}| \quad \vec{x}_{i,k,m} \in C_{i,k} \tag{2.10}$$

As the scooping iterations proceed, the newly added clusters $C_{i,k}, C_{i,k+1}, \ldots$ are defined as children of the parent cluster $C_{i-1,j}$. Once all pixels have been scooped, this hierarchical ordering and the clusters position $\vec{N}_{i,k}$ defines the nodes of the skeleton.

Before skeletonization, the images are cured manually by removing pixels that belong to the axon in order to retain the dendritic tree only. Moreover, images are cropped to remove pixels that belong to adjacent neurons. Then, the recorded

gray-scale images are binarized by finding an approximate contour of the dendritic tree and filling its interior. The contour of the tree is found using a Canny edge detector [6] and the interior of the shape is traced with two-dimensional random walkers that drift along the image intensity gradient starting from the contour pixels. In general, the image intensity is brighter inside a branch compared to its periphery, hence the random walkers are attracted towards the interior of the tree.

To define the root of the tree, which corresponds to the position of the soma or cell body, the distance transform of the binary mask is used to find the shortest distance to the background. Since the soma is generally more bulky than any branches, the soma region contains pixels that are furthest from the background compared to other pixels in the dendritic network. Therefore, the soma position is defined as the furthest pixel from the background.

Once the skeleton is built from the binary mask, branches are pruned. Depending on the smoothness of the binary shape boundary, the scooping may sometimes create small branches that are smaller than the thickness of the branches. To avoid this spurious effect, branches whose length is smaller than the average diameter of the parent branch are removed. Furthermore, the nodes of the branches are resampled at an equal distance of $0.1\,\mu m$ along the path of the branch.

Finally, the accuracy of the skeletonization algorithm is assessed by comparison with methods that were previously developed. Several automatic skeletonization methods have been proposed in the past such as [31, 44, 45, 55, 64, 95]. For simplicity, the novel skeletonization algorithm is compared with the App2 algorithm [92], which is a 3D automatic tracing method used in the Vaa3D software [63], and the Matlab [49] built-in function *bwmorph* [39], which uses the medial axis transform. As shown in fig. 2.5, the scooping method is comparable to the App2 algorithm and is more accurate than *bwmorph*. Furthermore, based on the nature of the scooping iteration, the scooped skeletons do not have any closed loops,

which is preferable since the class IV dendritic tree does not generally form close loops. However, loops are more frequent at 120 hr AEL as shown in fig. 2.6, and consequently, the scooping algorithm over-estimates the amount of branches at this stage.

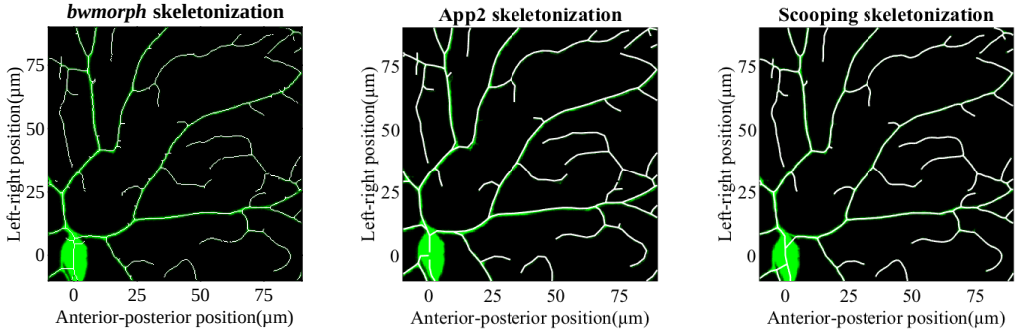

Figure 2.5 – Comparison of automatic skeletonization methods
The image corresponds to a region of a class IV neuron at 72 hr AEL.

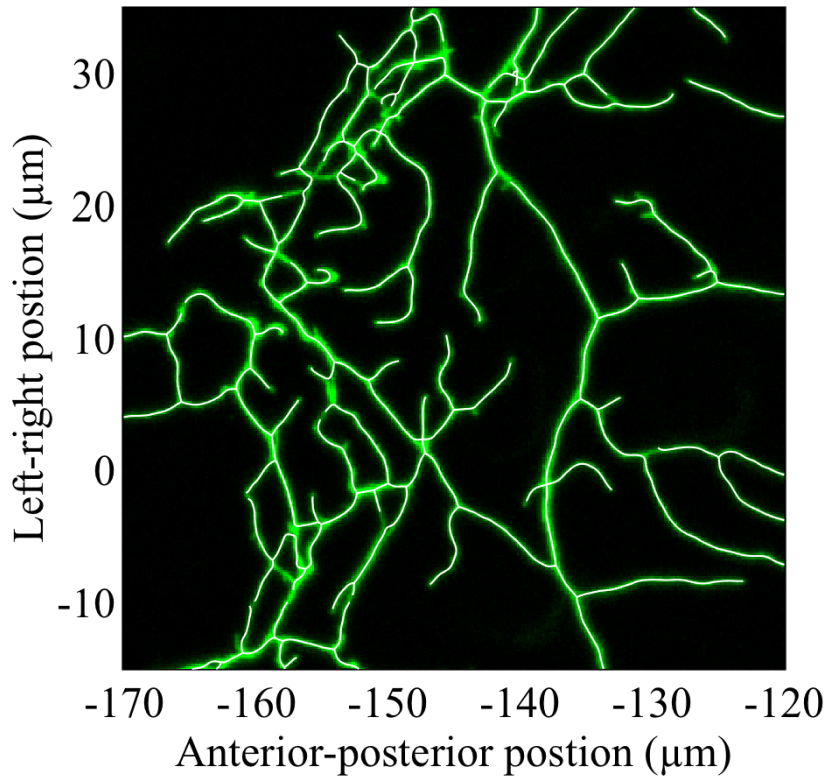

Figure 2.6 – Example of over-skeletonization effects occurring at 120 hr AEL
The z-projection of the image stacks creates apparent dendrite loops on the 2D image. Such loops are broken by the skeletonization algorithm, overestimates the number of tree branches.

3 Dynamic and Static Properties of Class IV Neuron Morphogenesis

In this chapter, the stochastic growth of class IV neurons is characterized. Specifically, the branch tip growth and the branching process are analyzed to build the foundations of our proposed models. In addition, the morphology of class IV dendritic tree is assessed with various metrics.

The branch tip growth analysis was performed in collaboration with Sabyasachi Sutradhar using the raw tracking data produced by his tracking algorithm. The analysis of the branching process was performed in collaboration with Sonal Shree using movies of class IV neurons development that she acquired. The morphological analysis was performed on skeletons of class IV neurons extracted from static microscopic images provided by Sonal Shree.

3.1 Tip state dynamics

3.1.1 Fitting process of the tip growth tracks

The dendritic tip tracking produces a set of time series that specify the changes in length of dendritic branches over the course of 20-30 min. Tracking of the dendritic

tips is repeated at 24, 48 and 96 hr AEL and the resulting tracks are used to quantify the dendritic growth process. An example of a dendritic tip track at 24 hr AEL is shown in fig. 3.1. As shown, the growth of the tip is stochastic in nature and exhibits three distinguishable processes whereby the branch grows, stays idle or retracts. These observations motivated us to use a 3-state dynamical system to fit the dendritic growth process.

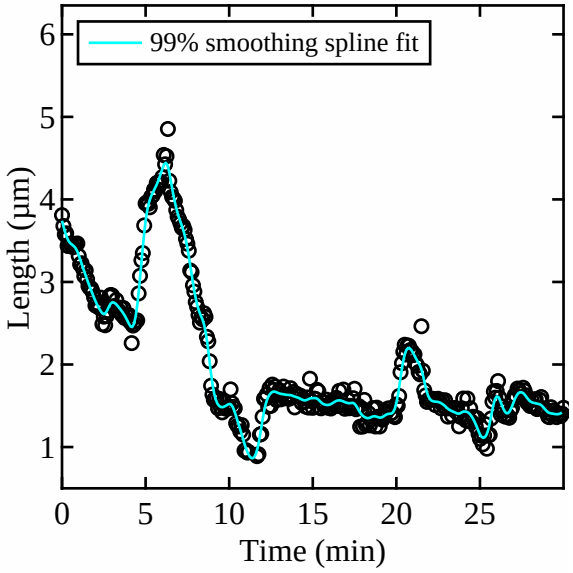

Figure 3.1 – Example of a 24 hr AEL dendritic tip track fitted with a smoothing spline

First, the phase velocity is defined as the average velocity of the tip in a given phase of growth. To determine the distribution of phase velocities at which a tip grows, the tip tracks are fitted with a piecewise-linear continuous function. The main difficulty in performing a piecewise-linear fit is to identify the number of segments in the function and the position of the joints that connect the linear segments together, i.e. the points at which the derivative is discontinuous. To solve this problem, the fitting process is separated into two stages. In the first stage, the tip tracks are over-fitted to find the maximal number of segments and the joints that connect them. In the second stage, the fits are regularized by removing redundant segments.

In the first stage, the tracks are over-fitted using a smoothing spline. A smoothing spline fit uses a spline function f_{ss} to approximate a set of data points $\{(x_i, y_i)\}$ and is regularized by the smoothness of the spline. More specifically, the following objective function is minimized by the fit:

$$\mathcal{O}(\{(x_i, y_i)\}, f_{ss}) = p\sum_i (f_{ss}(x_i) - y_i)^2 + (1-p)\int \left|\frac{d^2 f_{ss}}{dx^2}\right|^2 dx \tag{3.1}$$

where $0 \leq p \leq 1$ is a hyper-parameter that controls the weight given to the minimization of the total squared error (first term) and the smoothness of the spline (second term). $p = 1$ corresponds to a complete over-fit where the spline function goes through all data points while $p = 0$ corresponds to the case where the spline is constant over the domain of the data. In our case, $p = 0.99$ is used for the initial over-fit of the tip tracks in order to average out some noise and reduce the effect of outliers. A spline fit is performed on each track time series (t_i, ℓ_i^j) where ℓ_i^j denotes the length of track j at time t_i. An example of a $p = 0.99$ smoothing spline fit is shown in fig. 3.1.

Using the smoothing spline, the derivative of the fit at the sampled time points t_i is evaluated to calculate the instantaneous velocity of the tip v_i^j where j indexes the track. The empirical distribution of the instantaneous velocities is constructed by combining all tracks at a given stage and is fitted with a mixture model composed of two log-normal and one normal distributions:

$$p(v) = p_S \frac{\Theta(-v)}{|v|\sqrt{2\pi\sigma_S^2}} \text{Exp}[\frac{(\log(|v|) - \mu_S)^2}{2\sigma_S^2}] \tag{3.2}$$

$$+ (1 - p_S - p_G)\frac{1}{\sqrt{2\pi\sigma_P^2}} \text{Exp}[\frac{(v - \mu_P)^2}{2\sigma_P^2}] \tag{3.3}$$

$$+ p_G \frac{\Theta(v)}{|v|\sqrt{2\pi\sigma_G^2}} \text{Exp}[\frac{(\log(|v|) - \mu_G)^2}{2\sigma_G^2}] \tag{3.4}$$

where $\Theta(v)$ is the Heavyside step function, which allows us to fit the log-normal component to the positive (resp. negative) domain of the distribution when fitting the growing (shrinking) state velocity distribution. Each component of the mixture model fits the velocity of the track in one of its three states: the first log-normal distribution fits the shrinking state velocities, the normal distribution fits the paused state velocities and the second log-normal distribution fits the growing state velocities. In total, this model has 8 free parameters, where 2 of them, p_S, p_G, control the weight of each component on the total distribution while $\mu_S, \sigma_S, \mu_P, \sigma_P, \mu_G, \sigma_G$ control their shape. To reduce the dimensionality of the fit, the average velocity of the paused state is fixed to 0, $\mu_P = 0$. In addition, an upper bound on the width of the paused-state velocity is imposed to prevent the central Gaussian from invading the entire domain of the distribution. Specifically, $\sigma_P < 0.1\,\mu m\,\text{min}^{-1}$. An example fit of the instantaneous velocities at 24 hr AEL is shown in fig. 3.2 with the best-fit parameters of the mixture model and the average velocity of the tip in each state.

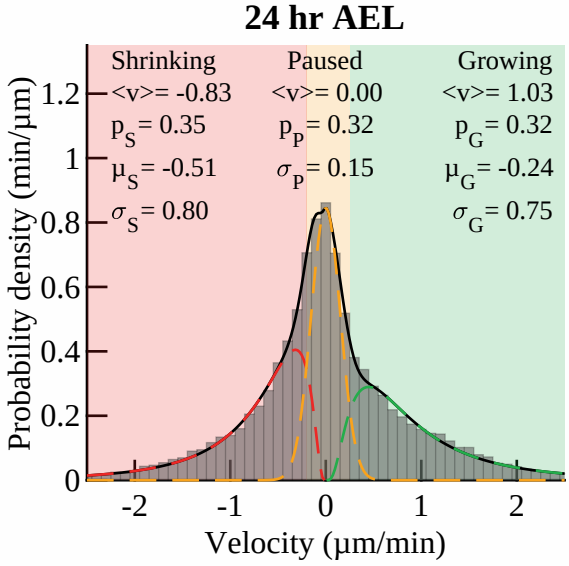

Figure 3.2 – Instantaneous velocity distribution at 24 hr AEL

Once the initial fit to the velocity distribution is established, the dynamical state of the tracks is identified using the velocity fit. More precisely, the tip state is defined

by binning its velocity into three contiguous regions. The position of the boundary that separates these three regions is controlled by the width of the paused state velocity component. Let $s_i^j(v_i^j)$ correspond to the instantaneous state of the j^{th} track at time t_i where the dependence on the velocity v_i^j is emphasized. Then, $s_i^j(v_i^j)$ is defined as follows:

$$s_i^j(v_i^j) = \begin{cases} S \text{ or Shrinking} & \text{if} \quad -\infty < v_i^j < -w_0 \\ P \text{ or Paused} & \text{if} \quad -w_0 < v_i^j < w_0 \\ G \text{ or Growing} & \text{if} \quad w_0 < v_i^j < \infty \end{cases} \tag{3.5}$$

$$w_0 = \sqrt{2\log(2)}\sigma_P \tag{3.6}$$

where w_0 is the half-width at half-max of the paused state Gaussian distribution.

With this definition, the instantaneous state of the tip is defined in all tracks. However, the times at which the state of the tip changes is still unknown. One of the main advantage of using a smoothing spline fit is the C^2 continuity of the function, i.e. its first derivative is continuous. This property is paramount since the continuity of the instantaneous velocity produces well-defined state transitions, which correspond to the time points at which the velocity crosses the velocity state boundaries. More precisely, let $T^j_{\text{begin},k}$ and $T^j_{\text{end},k}$ correspond to the beginning and end times of the k^{th} phase of track j. The phase endpoints are defined by the sequence of states s_i^j and the sampled times t_i:

$$T^j_{\text{end},k} = \min_i \left\{ t_i \,\middle|\, t_i > T^j_{\text{begin},k}, s_i^j \neq S^j_{i+1} \right\} \tag{3.7}$$

$$T^j_{\text{begin},k+1} = T^j_{\text{end},k} \tag{3.8}$$

$$T^j_{\text{begin},0} = t_0 \tag{3.9}$$

Given the endpoints of each phase in each track, the phase velocity V_k^j is determined by the length change using the smoothing spline:

$$V_k^j = \frac{f_{ss}(T^j_{\text{end},k}) - f_{ss}(T^j_{\text{begin},k})}{T^j_{\text{end},k} - T^j_{\text{begin},k}} \tag{3.10}$$

At this point, a collection of dynamical phases with a well-defined state, duration and velocity is obtained for each track. The properties of these phases derive from the piecewise-linear fits of the tracks and the fit to the instantaneous track velocity distribution. However, a fit of the phase velocity distribution is the sought-after quantity since it is a better indicator of the average velocity of the tip in each state and since it is less prone to fluctuations caused by the over-fitted spline. Initially, the phase velocities were undefined since the phase velocity distribution depends on the state definition and the definition of the states depends on the fit to the phase velocity distribution.

This causal problem is resolved in the second stage of the fitting process. Since the piecewise-linear fits and the phase velocity distributions are inter-dependent, the fitting process is iterated several times to ensure that their definitions are consistent with one another. However, two steps are modified in the iteration of the fit: 1) the phase velocity distribution is fitted instead of the instantaneous velocity distribution and 2) the state of the phase is defined by binning its phase velocity instead of using the instantaneous velocity. As the iterations proceed, the velocity fit changes as a function of the new phase velocities. The update of σ_0 then redefines the velocity state boundaries, which changes the state of the track phases accordingly. As a result of the states redefinition, contiguous phases in a given track may be given the same state. When such event occurs, the two phases are combined into one phase whose duration is given by the sum of the duration of the two phases, and its velocity is defined by the length change between the beginning of the first combined phase and the end of the second combined phase. This merging process reduces the number of

phases in a given track, which further regularizes the piecewise-linear fit. Finally, the iterations continue until the phases of all fits of a given developmental stage do not change for three consecutive iterations, which is the criterion of convergence. In practice, the fitting stops after $5-10$ iterations. In addition, before the iterative fitting starts, all phases whose duration is smaller than 0.5 min are removed. After the removal of a short phase, the endpoints of the adjacent phases are joined together at the midpoint of the short phase. This additional pruning ensures that the phases are long-enough to contain enough sampled time points and prevents over-fitting with very short and highly oscillatory phases. In the datasets, the sampling period varies between $4,5,6$ seconds, which implies that a phase of 0.5 min has $\sim 4-5$ points.

When the fitting iteration terminates, a set of growth phases of various duration and velocity and a fit of the phase velocity distribution at each developmental stage is obtained. Examples of tracks with their growth phases and the associate phase velocity distributions are shown in fig. 3.3 and fitted using a bin width of $0.1\,\mu m\text{min}^{-1}$. As depicted, the piecewise-linear fits succeed at capturing the various growth phases of the tracks while being resistant to noise. Furthermore, while the phase velocity distribution is well separated into three peaks at 24 hr AEL, this separation is less pronounced at the later stages. This indicates that the dynamicity of the tip growth slows down as the neuron ages. This is also evidenced by the decrease of the average shrinking or growing speed towards zero.

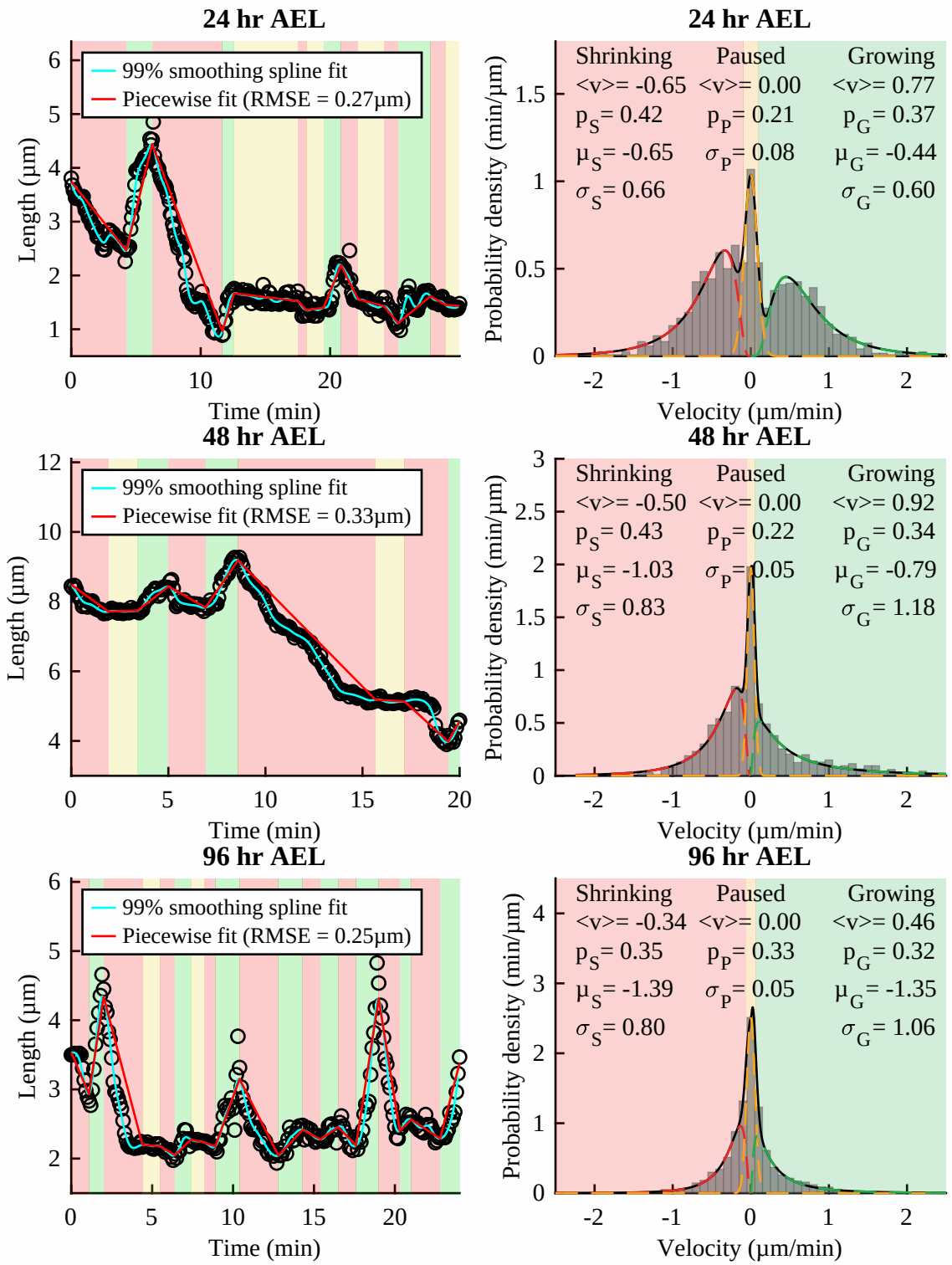

Figure 3.3 – Examples of dendritic track fits with their associate velocity distributions The colors of the shaded areas in the tracks indicate the state of the phase as given by the velocity distribution. The raw tracks data is provided by Sabyasachi Sutradhar.

In summary, the two-stage fitting process is described by the following pseudocodes:

Algorithm 1: Tip fitting process - first stage

Result: $S_i^j, T^j_{\text{begin},k}, T^j_{\text{end},k}, V_k^j$

Initialization: $t_i, \ell_i^j, \quad i = 1, \ldots, n, \quad j = 1, \ldots, m$;

for $1 \leq j \leq m$ **do**

  Fit track j with a smoothing spline $f_{ss}^j(t)$ using data t_i, ℓ_i^j;

  Define the instantaneous track velocity: $v_i^j = \left.\frac{df_{ss}^j(t)}{dt}\right|_{t=t_i}$;

end

Calculate $p_S, p_G, \mu_S, \sigma_S, \mu_P, \sigma_P, \mu_G, \sigma_G$ by fitting the distribution of instantaneous track velocities $\{v_i^j\}$ using the mixture model $p(v)$;

Calculate the half-width of the paused-state Gaussian: $w_0 = \sqrt{2\log(2)}\sigma_P$;

Calculate the state velocity boundaries: $B_v =]-\infty, -w_0, w_0, \infty[$;

for $1 \leq j \leq m$ **do**

  Define the instantaneous states of track j, s_i^j, by binning v_i^j with B_v;

  Define the begining and end of each phase, $T^j_{\text{begin},k}, T^j_{\text{end},k}$, and the number of phases N_j, using s_i^j and t_i;

  Calculate the phase velocity, V_k^j , using $T^j_{\text{begin},k}, T^j_{\text{end},k}$ and $f_{ss}^j(t)$;

end

Algorithm 2: Tip fitting process - second stage

Result: $S_i^j, T_{\text{begin},k}^j, T_{\text{end},k}^j, V_k^j$

Initialization: $t_i, f_{ss}^j, N^j, S_i^j, T_{\text{begin},k}^j, T_{\text{end},k}^j, V_k^j, \quad i = 1,\ldots,n, \quad j = 1,\ldots,m$;

for $1 \leq j \leq m$ **do**

  for $1 \leq k \leq N^j$ **do**

    Remove phase k if $T_{\text{end},k}^j - T_{\text{begin},k}^j < 0.5\,\text{min}$;

  end

end

while *Tracks have changed in the last 3 iterations* **do**

  Calculate $p_S, p_G, \mu_S, \sigma_S, \mu_P, \sigma_P, \mu_G, \sigma_G$ by fitting the distribution of phase velocities $\{V_i^k\}$ using the mixture model $p(v)$;

  Calculate the half-width of the paused-state Gaussian: $w_0 = \sqrt{2\log(2)}\sigma_P$;

  Calculate the state velocity boundaries: $B_v =]-\infty, -w_0, w_0, \infty[$;

  for $1 \leq j \leq m$ **do**

    for $1 \leq k \leq N^j$ **do**

      Define the state of phase k, S_k^j, by binning V_k^j with B_v;

      if $S_k^j == S_{k-1}^j$ **then**

        Combine phase $k-1$ with phase k;

        Update $T_{\text{begin},k}^j, T_{\text{end},k}^j, V_k^j$ using f_{ss}^j;

      end

    end

    Update N_j;

  end

end

3.1.2 Tip growth is a 3-state dynamical process

Using the set of fitted growth tracks at each developmental stage, the transition process of the tip state is further characterized. More precisely, the transition between each dynamical state is modeled as a 3-state Markov chain.

A Markov process is a stochastic process that describes a sequence of events whose probability are independent of past events. The property by which the probability of new events is independent of past events is called memorylessness or more commonly called the Markov property. In other words, memorylessness is the defining property of Markov processes. Moreover, the sequence of events described by a Markov process imply a temporal dimension and can be categorized into states, which belong to a finite or measurable space. As such, Markov processes are classified into four categories that specify whether the state space is countable or continuous and whether time is discrete or continuous. To model the class IV neuron tip growth dynamics, continuous-time Markov chains are used since they have a finite state space and a continuous temporal dimension.

To quantify the continuous-time Markov chain that models the tip growth process, the finite state space is defined as $\mathcal{S} = \{S, P, G\}$, which characterizes the average velocity of the tip, and the rate of transition from state i to state j is denoted by $\{k_{ij} | i, j \in \mathcal{S}\}$. Moreover, the state probability vector $\vec{P}(t) = (P_S(t), P_P(t), P_G(t))$ represents the probability to find the tip in each of the three states at time t, given that the tip was initialized in some initial state $\vec{P}_0$ at time $t = 0$. The master equation of this 3-state Markov chain is given by the following differential equations:

$$\frac{dP_S(t)}{dt} = -(k_{SP} + k_{SG})P_S(t) + k_{PS}P_P(t) + k_{GS}P_G(t) \tag{3.11}$$

$$\frac{dP_P(t)}{dt} = -(k_{PS} + k_{PG})P_P(t) + k_{SP}P_S(t) + k_{GP}P_G(t) \tag{3.12}$$

$$\frac{dP_G(t)}{dt} = -(k_{GS} + k_{GP})P_G(t) + k_{SG}P_S(t) + k_{PG}P_P(t) \tag{3.13}$$

Using the following state label map:

$$S \to 1, \quad P \to 2, \quad G \to 3 \tag{3.14}$$

the master equation can be expressed succinctly in matrix form:

$$\frac{d\vec{P}(t)}{dt} = K\vec{P}(t) \tag{3.15}$$

$$K = \begin{pmatrix} -k_{SP} - k_{SG} & k_{PS} & k_{GS} \\ k_{SP} & -k_{PS} - k_{PG} & k_{GP} \\ k_{SG} & k_{PG} & -k_{GS} - k_{GP} \end{pmatrix} \tag{3.16}$$

$$(K)_{ij} = \begin{cases} -\sum_k k_{jk}, & i = j \\ k_{ji}, & i \neq j \end{cases} \tag{3.17}$$

where $(K)_{ij}$ corresponds to the $(i,j)^{\text{th}}$ element of the matrix K. A general solution of the system above can be expressed in terms of the eigenvalues (λ_i) and eigenvectors ($\vec{w}_i$) of the transition matrix K:

$$\vec{P}(t) = \sum_i a_i \vec{w}_i e^{\lambda_i t} \tag{3.18}$$

where a_i are coefficients that are defined by the initial condition $\vec{P}(0) = \vec{P}_0$. More precisely, expressions for a_i are found by inverting the matrix of eigenvectors:

$$\vec{a} = \begin{pmatrix} a_1 \\ a_2 \\ a_3 \end{pmatrix} = U^{-1}\vec{P}_0, \qquad U = [\vec{w}_1, \vec{w}_2, \vec{w}_3] \tag{3.19}$$

where $[\ldots]$ corresponds to concatenation of column vectors. When the tip is initialized in a particular state i, the state vector is given by the Kronecker delta:

$$P_i(0) = 1 \Rightarrow \left(\vec{P}_0^{(j)}\right)_i = \delta_{ij} \tag{3.20}$$

where the superscript (j) denotes the initial state. Solving for the eigenvalues of K involves finding the roots of its characteristic equation:

$$\det(K - \lambda I) = -\lambda^3 - k_1\lambda^2 - k_2^2\lambda = 0 \tag{3.21}$$

$$k_1 = k_{GP} + k_{GS} + k_{PG} + k_{PS} + k_{SG} + k_{SP} \tag{3.22}$$

$$\begin{aligned} k_2^2 = {} & k_{PG}k_{SG} + k_{PS}k_{SG} + k_{PG}k_{SP} \\ & + k_{GS}\left(k_{PG} + k_{PS} + k_{SP}\right) + k_{GP}\left(k_{PS} + k_{SG} + k_{SP}\right) \end{aligned} \tag{3.23}$$

The characteristic polynomial of this 3-state system has no constant term, which guarantees the existence of a zero eigenvalue, whose eigenvector is the steady state solution P_{ss}. Moreover, since $k_1 > 0$ and $k_2^2 > 0$, the other two eigenvalues are guaranteed to have a negative real part, which corresponds to decaying modes. Expression for the eigenvalues are given by:

$$\lambda_1 = 0 \tag{3.24}$$

$$\lambda_2 = \frac{-k_1 - \sqrt{k_1^2 - 4k_2^2}}{2} \tag{3.25}$$

$$\lambda_3 = \frac{-k_1 + \sqrt{k_1^2 - 4k_2^2}}{2} \tag{3.26}$$

with the associate eigenvectors:

$$\vec{P}_{ss} = \vec{w}_1 = \begin{pmatrix} \dfrac{k_{GP}k_{PS} + k_{GS}(k_{PG} + k_{PS})}{(k_{PG} + k_{PS})(k_{GS} + k_{SG}) + (k_{GS} + k_{PG})k_{SP} + k_{GP}(k_{PS} + k_{SG} + k_{SP})} \\ \dfrac{k_{GS}k_{SP} + k_{GP}(k_{SG} + k_{SP})}{(k_{PG} + k_{PS})(k_{GS} + k_{SG}) + (k_{GS} + k_{PG})k_{SP} + k_{GP}(k_{PS} + k_{SG} + k_{SP})} \\ \dfrac{k_{PS}k_{SG} + k_{PG}(k_{SG} + k_{SP})}{(k_{PG} + k_{PS})(k_{GS} + k_{SG}) + (k_{GS} + k_{PG})k_{SP} + k_{GP}(k_{PS} + k_{SG} + k_{SP})} \end{pmatrix} \tag{3.27}$$

$$\vec{w}_2 = \begin{pmatrix} \dfrac{\sqrt{k_1^2 - 4k_2^2} - k_{GP} - k_{GS} - k_{PG} + k_{PS} + k_{SG} + k_{SP}}{2(k_{PG} - k_{SG})} \\ \dfrac{-\sqrt{k_1^2 - 4k_2^2} + k_{GP} + k_{GS} - k_{PG} - k_{PS} + k_{SG} - k_{SP}}{2(k_{PG} - k_{SG})} \\ 1 \end{pmatrix} \tag{3.28}$$

$$\vec{w}_3 = \begin{pmatrix} \dfrac{-\sqrt{-4k_2^2 + k_1^2} - k_{GP} - k_{GS} - k_{PG} + k_{PS} + k_{SG} + k_{SP}}{2(k_{PG} - k_{SG})} \\ \dfrac{\sqrt{-4k_2^2 + k_1^2} + k_{GP} + k_{GS} - k_{PG} - k_{PS} + k_{SG} - k_{SP}}{2(k_{PG} - k_{SG})} \\ 1 \end{pmatrix} \tag{3.29}$$

Note that $\vec{w}_1$ is normalized with respect to the L_1 norm, namely $\vec{1} \cdot \vec{w}_1 = \sum_i \vec{w}_{1,i} = 1$ where $\vec{1} \equiv (1,1,1)$. With this normalization, the first eigenvector corresponds to the steady-state probabilities, $\vec{w}_1 = \vec{P}_{ss}$.

To estimate the transition rates k_{ij} from the tracks, two methods are considered: 1) Maximum-likelihood estimation (MLE) of k_{ij} and 2) fit of the phase duration distribution. First, the maximum-likelihood estimate of the transition rates is calculated by counting the total amount of each transition type and the total exposure

time in each state. Specifically, let N_{ij} correspond to the total amount of observed transitions from state i to state j and let T_i correspond to the total time spent in state i across all tracks. The MLE for k_{ij} is given by:

$$k_{ij} = \frac{N_{ij}}{T_i} \tag{3.30}$$

$$T_i = \sum_j \sum_{k=1}^{N_j} \Delta T_k^j \delta_{S_k^j, i} \tag{3.31}$$

$$\Delta T_k^j = (T_{\text{end},k}^j - T_{\text{begin},k}^j) \tag{3.32}$$

where $\delta_{i,j}$ is the Kronecker delta and $T_{\text{begin},k}^j, T_{\text{end},k}^j, S_k^j$ correspond to the beginning time, end time and state of phase k of track j as defined in the previous section. The MLE of the transition rate matrix K is given in fig. 3.4 for each developmental stage.

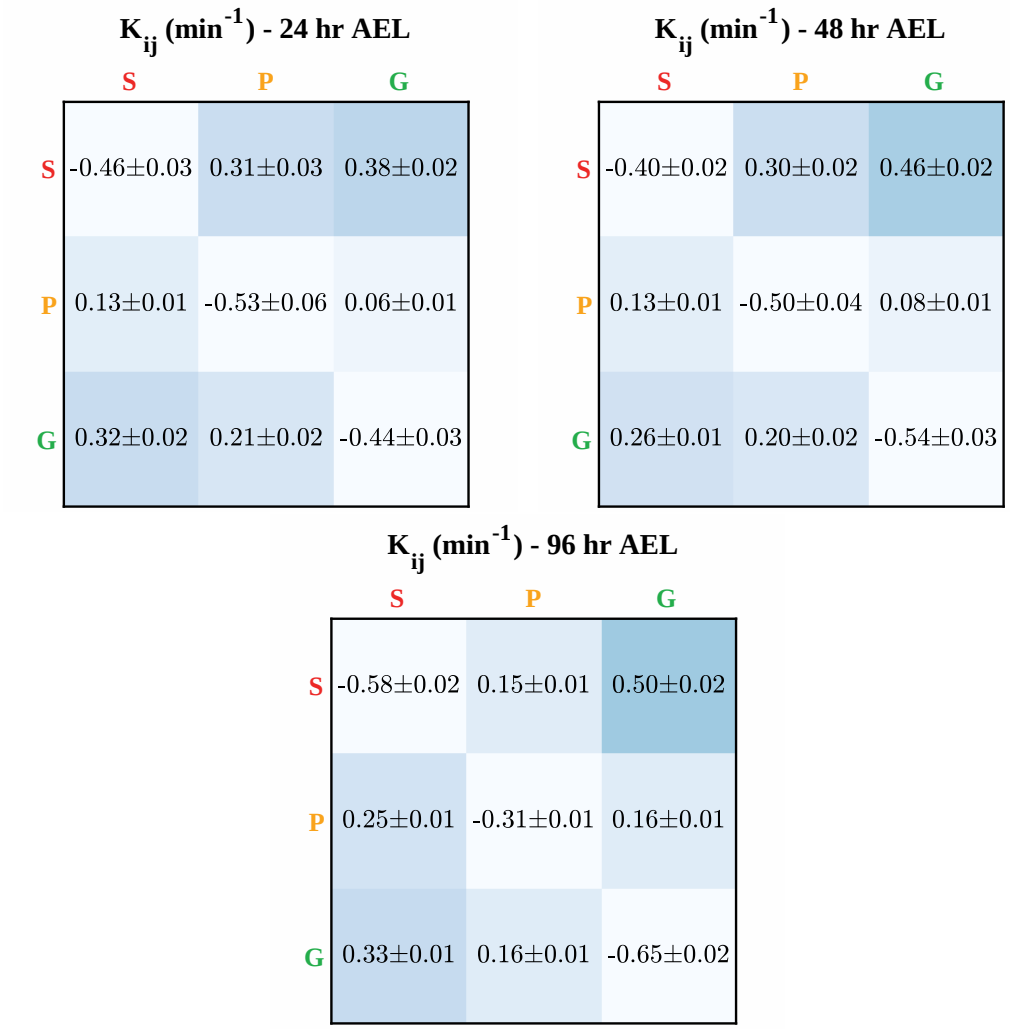

Figure 3.4 – Maximum likelihood estimates of the transition matrix K over development

Using the same measurements, the conditional transition probabilities p_{ij} is defined as the probability that the tip transitions to state j given that it was in state i before the transition, and the rate at which the tip exits the i^{th} state k_i:

$$p_{ij} = \frac{N_{ij}}{\sum_j N_{ij}} \tag{3.33}$$

$$k_i = \sum_j k_{ij} = \frac{\sum_j N_{ij}}{T_i} \tag{3.34}$$

$$\Rightarrow k_{ij} = \frac{N_{ij}}{T_i} = \frac{N_{ij}}{\sum_j N_{ij}} \frac{\sum_j N_{ij}}{T_i} = p_{ij} k_i \tag{3.35}$$

Note that eq. (3.35) can be used as an alternative estimate of the transition rates, provided p_{ij} and k_i are given. This is the essence of the second method, where p_{ij} is evaluated by counting the state transitions N_{ij} and k_i is estimated by fitting the distribution of the state duration. Indeed, for a Markov process, the time spent in each state is exponentially distributed with an average of $\frac{1}{k_i}$ where k_i is the exit rate as defined above. This can be derived directly from the master equation.

Consider a time interval Δt that is separated into n sub-intervals of length $dt = \frac{\Delta t}{n}$. Furthermore, assume that the initial state of the tip is m, i.e. $\vec{P}_i(0) = \delta_{im}$. Recall that $\vec{P}_i(t)$ provides the probability that the tip is in state i after time t given that the initial state is $\vec{P}(0)$. Then, assuming that n is large enough, the following expression for $\vec{P}_i(t)$ is obtained:

$$\vec{P}(dt) \overset{n \gg 1}{\approx} \vec{P}(0) + \left.\frac{d\vec{P}(t)}{dt}\right|_{t=0} dt \tag{3.36}$$

$$= \vec{P}(0) + K\vec{P}(0)dt \tag{3.37}$$

$$= (\mathbf{1} + Kdt)\vec{P}(0) \tag{3.38}$$

$$\Rightarrow \vec{P}_i(dt) = \delta_{im}\left(1 - \sum_j k_{mj} dt\right) = \delta_{im}\left(1 - k_m dt\right) \tag{3.39}$$

where $\mathbf{1}$ is the identity matrix. Finally, let $p(t > \Delta t)$ be the probability that the tip transitions in a time greater than Δt and let $s(t)$ correspond to the state of the tip at time t. This quantity is given by the product of the probability that it remains in its initial state in all the sub-intervals dt. Taking the infinitesimal limit $n \to \infty$, the exact expression for $p(t > \Delta t)$ becomes:

$$
\begin{aligned}
p(t > \Delta t) &= \lim_{n\to\infty} p(s(t_i) = m, \forall i, 1 \leq i \leq n) && (3.40)\\
&= \lim_{n\to\infty} \prod_{i=1}^{n} p(s(t_i) = m | s(t_i - dt) = m) && (3.41)\\
&= \lim_{n\to\infty} \prod_{i=1}^{n} p(s(dt) = m | s(0) = m) (\text{Markov property}) && (3.42)\\
&= \lim_{n\to\infty} \prod_{i=1}^{n} \vec{P}_m(dt) && (3.43)\\
&= \lim_{n\to\infty} \prod_{i=1}^{n} (1 - k_m dt) && (3.44)\\
&= \lim_{n\to\infty} \left(1 - \frac{k_m \Delta t}{n}\right)^n && (3.45)\\
&= e^{-k_m \Delta t} && (3.46)
\end{aligned}
$$

Note that the ability to simplify the product of probabilities is a consequence of the Markov property. The cumulative and probability density function of the state duration t can then be derived directly from eq. (3.46):

$$
\begin{aligned}
p(t \leq \Delta t) &= 1 - p(t > \Delta t) && (3.47)\\
\Rightarrow p(t = t') &= \left.\frac{dp(t \leq \Delta t)}{dt'}\right|_{\Delta t = t'} && (3.48)\\
&= k_m e^{-k_m t} && (3.49)
\end{aligned}
$$

which is recognized as the exponential distribution with an average of $\langle t \rangle = \frac{1}{k_m}$. Using this fact, the state duration distributions is fitted to obtain an estimate of k_i, which is used in eq. (3.35) to evaluate the transition rates. The corresponding transition rate matrix K is given in fig. 3.5 and the state duration fits are shown

in fig. 3.6 for each developmental stage. The fit of the duration is performed over the restricted range $1\,\text{min} \leq t \leq 3 < t >$ to avoid the censorship effect caused by the fitting process, which removes phases whose duration are shorter than $0.5\,\text{min}$. As depicted, the exponential distribution is a good fit to the state duration distribution for all states at each developmental stage. Moreover, the average duration of each state averages to $\sim 1\,\text{min}$, except for the paused state at 96 hr AEL, which lasts $2\,\text{min}$ on average. This indicates that the tip is less dynamic at 96 hr AEL as it spends a higher proportion of its time in an idle state, compared to the earlier stages. In subsequent analyses, the transition rate matrices derived from the state duration fit are used since they are more resilient to the censorship of short phases.

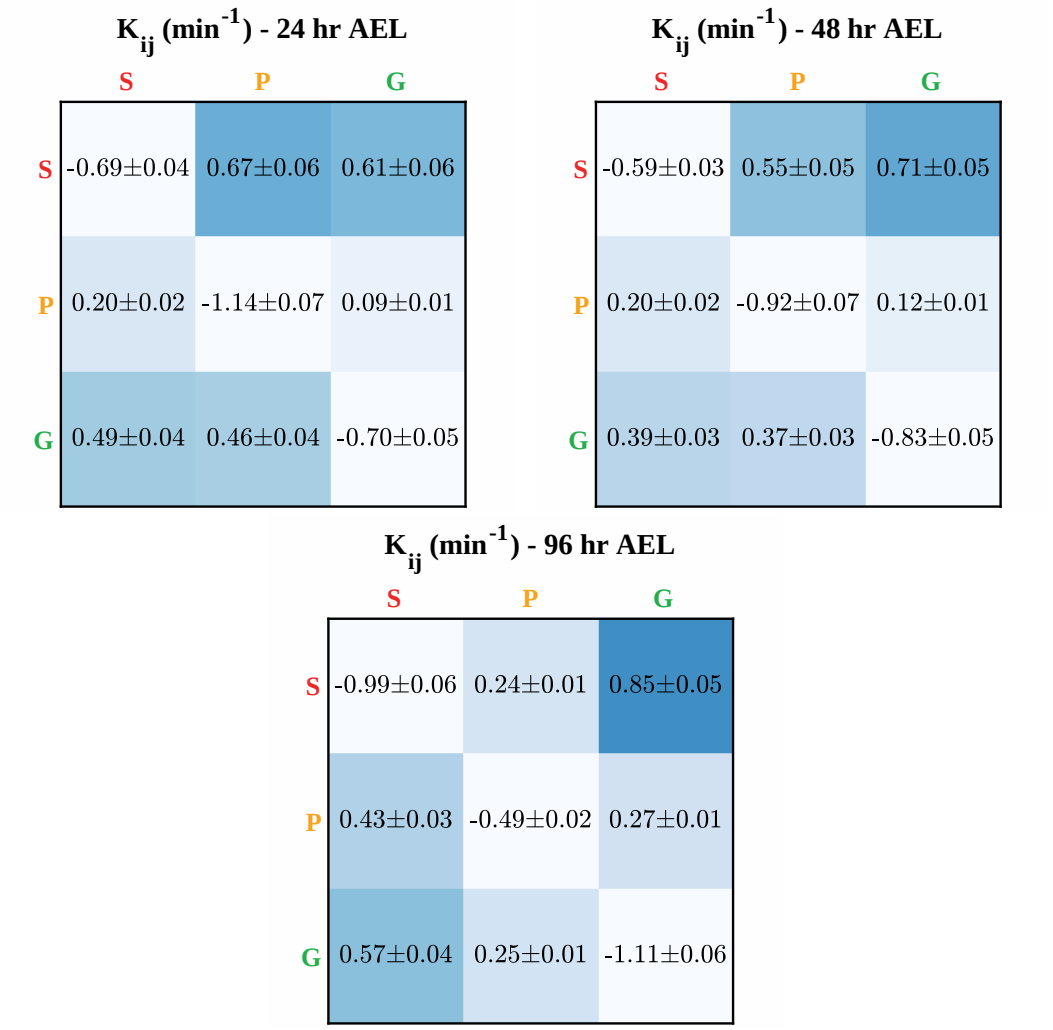

Figure 3.5 – Transition matrix estimates derived from the fitted exit rates over development

3.1.3 The tip transition process is approximately Markov

The main assumption of the 3-state model of dendritic tip growth is the fact that the transition dynamics is independent of the past. The exponential distribution of the state duration at all stages is certainly a signature of the Markov property of the transitions. To verify this further, the transition matrix eigenvalues are estimated at increasing lag times and compared to the expected eigenvalues from a Markov

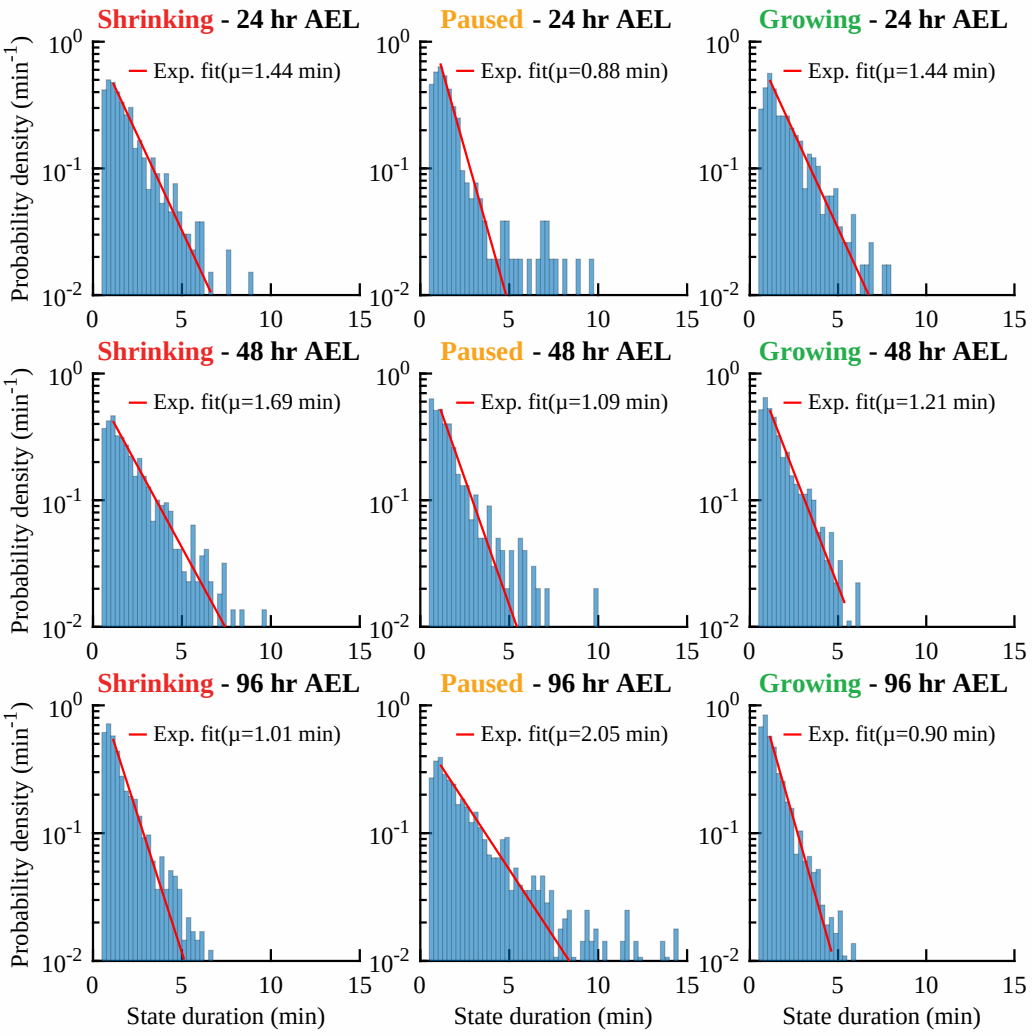

Figure 3.6 – State duration distributions over development
The distributions are fitted with an exponential distribution in the range $1 \leq t \leq 3\langle t \rangle$ using a non-linear least squares fit. The bin width is $0.25\,\text{min}$.

process. Let $T_{ij}(t+dt|t)$ correspond to the probability that the tip is found in state j at time $t+dt$ when initiated in state i at time t. Then, if the tip is in some state vector $\vec{P}(t)$ at time t, its state vector at time $t+dt$ is given by multiplying by the transition matrix $T(t+dt|t)$:

$$\vec{P}(t+dt) = T(t+dt|t)\vec{P}(t) \tag{3.50}$$

If the transitions are Markov, the transition matrix $T(t+dt|t)$ is independent of the previous history, which implies that $T(t+dt|t) = T(dt|t=0) = T(dt)$. In other words, the transition probabilities do not change with time. Note that $T(dt)$ is different than the transition rate matrix K mentioned above. However, since K is the generator of transitions, one can relate $T(dt)$ to K by exponentiation:

$$T(dt) = e^{Kdt} \overset{dt \ll 1}{\approx} 1 + Kdt \tag{3.51}$$

Therefore, if the tip state transition is a pure Markov process, the state vectors can be determined at all future times using T and the initial state vector $\vec{P}(0)$, namely:

$$\vec{P}(t+ndt) = T(dt)\vec{P}((n-1)dt) = (T(dt))^2 \vec{P}((n-2)dt) = \ldots = (T(dt))^n \vec{P}(0) \tag{3.52}$$

This property can be used to test the Markovianess of the transition process in the following way. First, consider all pairs of time points separated by a time ndt and calculate an estimate of $T(ndt)$ by measuring the proportion of each transition type from a given state:

$$\hat{T}_{ij}(ndt) = \frac{n_{ij}}{\sum_j n_{ij}} \tag{3.53}$$

where n_{ij} is the number of point pairs whose first point is in state i and whose second point is in state j. Then, according to eq. (3.52), one expects that $\hat{T}_{ij}(ndt) \approx$

$\left(\hat{T}_{ij}(dt)\right)^n$ if the transition process is Markov. An effective way to compare these matrices is to compare their eigenvalues:

$$\lambda_i(ndt) = (\lambda_i(dt))^n = e^{n\ln(\lambda_i(dt))} = e^{-ndt\left(-\frac{\ln(\lambda_i(dt))}{dt}\right)} \tag{3.54}$$

In other words, the eigenvalues of $\hat{T}_{ij}(ndt)$ decay exponentially with a rate of $-\frac{\ln(\lambda_i(dt))}{dt}$ where $\lambda_i(dt) \leq 1$ for a Markov process. Using these expressions, the eigenvalues of $\hat{T}_{ij}(ndt)$ are estimated at each sampled values of n and compared against the eigenvalues expected from a Markov process. The comparison is shown in fig. 3.7. The eigenvalue associated with the stationary state has a value of 1 and is not expected to decay since its decay rate vanishes. For the non-unit eigenvalues, their value decays as the lag time increases, which is consistent with a Markov process. However, the decay rate is only similar to the Markov decay rate at times $t \leq 0.5\,\text{min}$. At later times, the decay rate is slower, which indicates that transitions have a long-time dependence on the past. Moreover, the non-unit eigenvalues exhibit two exponential decays where the initial decay is fast and short and the second decay is slow and long. In other words, although the eigenvalues are decaying in time, the decay rates are slower than expected from a Markov process indicating that the tip transition may not be purely Markov.

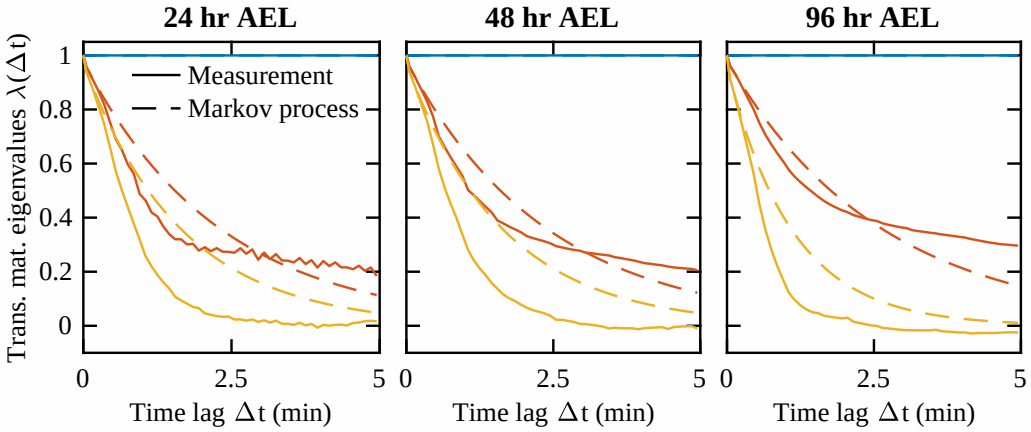

Figure 3.7 – Markov property test of the state transition process
Each color represents a different eigenvalue. The Markov process lines correspond to $\exp\left[-\Delta t\left(-\frac{\ln(\lambda_i(dt))}{dt}\right)\right]$ where $\lambda_i(dt)$ is the eigenvalue estimated from pairs of points separated by one time step Δt

3.1.4 The tips retract upon contact with other dendrites

As a result of the branch growth process, dendritic branches elongate and occupy a larger portion of their local neighborhood. Consequently, branch tips ultimately collide with other dendrites in the tree and stop growing. Furthermore, as a result of the DSCAM mechanism (as explained in section 1.1.2), branches start shrinking after contacting other dendrites. To quantify this process, the duration of the tip contacts is measured throughout development as shown in fig. 3.8. The average duration is estimated within the range $1 \leq t \leq 5\,\mathrm{min}$ for the 24 and 48 hr stage, while the range $1 \leq t \leq 10\,\mathrm{min}$ is used for the 96 hr stage. To fit the distribution, the maximum likelihood estimate of an exponential distribution with the calculated mean is overlayed on top of the measured distribution. As depicted, the exponential distribution is a good fit of the experimental distribution. Moreover, this analysis shows that contacts are not instantaneous, but lasts an average of $\sim 2.7\,\mathrm{min}$ over the course of the development.

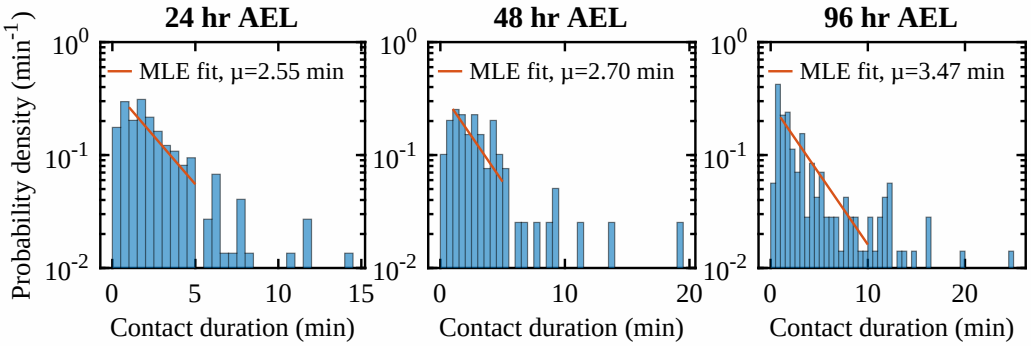

Figure 3.8 – Distribution of the branch tips contact duration
The distributions are fitted with an exponential distribution using maximum-likelihood. The maximum-likelihood estimate of the mean is given by the empirical mean of the data over the fitted range. Measurements were performed in collaboration with Qiwei Yu.

In addition, the post-collision transition dynamics is measured in a manner similar to the previous analysis. To do so, branch tips were tracked only after they started retracting from their collision point. However, due to the difficulty of

identifying clear collision events followed by retractions, the post-collision dynamics was only measured at 18 hr AEL where the dataset was the richest. The estimate of the transition matrix derived from the state duration fits and the phase velocity distribution are shown in fig. 3.9. As indicated by the exit rates, the post-collision tip dynamics is biased towards the shrinking state. This bias can also be seen in the values of k_{PS} and k_{GS}, which are high compared to the other rates. Moreover, the velocity distribution shows three distinct peaks that identify the three states with average velocities that are similar to what was found previously at 24 hr AEL (see 3.3).

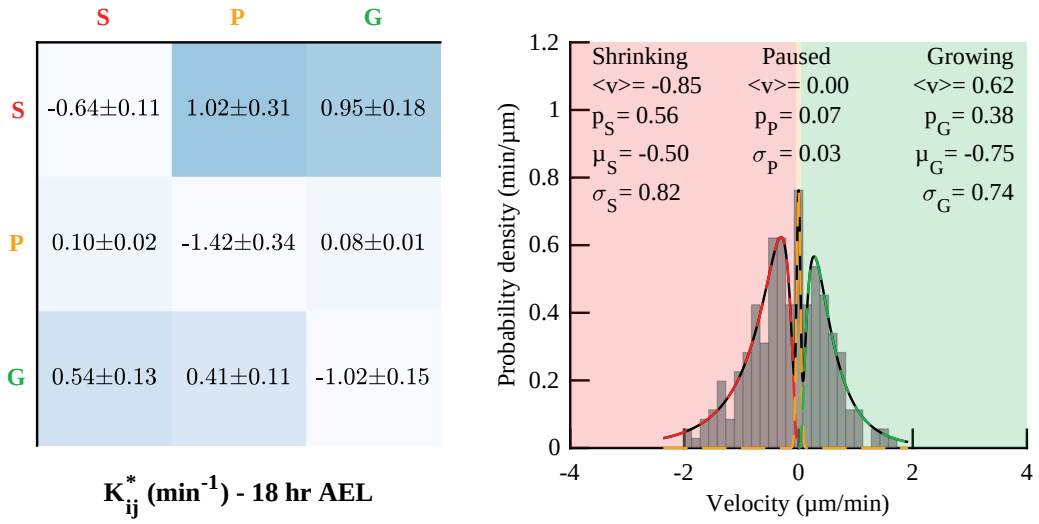

Figure 3.9 – Post-collision transition matrix K^* and velocity distribution at 18 hr AEL

3.2 Branching process

In this section, the spatial and temporal characterization of the branching process is summarized. This analysis was performed in collaboration with Sonal Shree using dynamical movies of class IV neurons that she provided.

3.2.1 The complexity of the dendritic tree increases over development

As seen in fig. 1.3, the number of branches in the tree increases over development as a result of the branching process. To quantify this morphological change, a dataset of static neuron images is used to calculate the number of branches, branch points and branch tips over development as shown in fig. 3.10. The complexity of the tree increases considerably over the course of its development. The number of branches increases ~ 10 fold from ~ 250 at 24 hr AEL to ~ 2000 at 96 hr AEL, and similar increases are observed for the number of branch points and branch tips. To quantify this increase, the number of each species is fitted with a cubic polynomial fit as shown in fig. 3.10. Note that since four developmental stages are fitted, there are no degrees of freedom remaining in the fit.

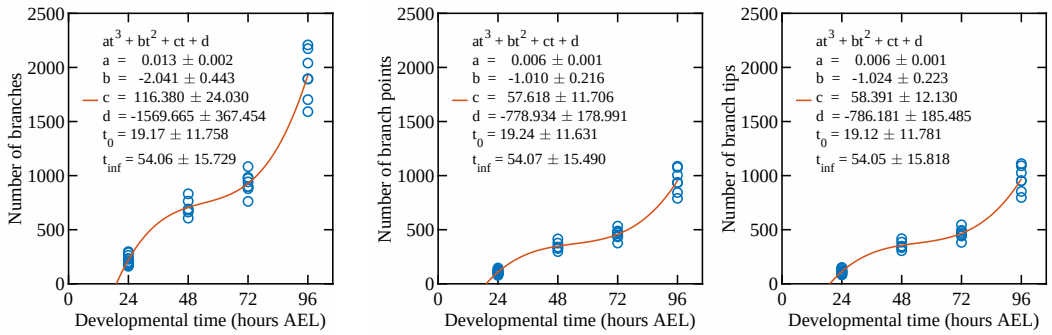

Figure 3.10 – Evolution of the dendritic tree complexity over development
The real root of the cubic fits is given by t_0 and the inflection point is given by t_{inf}.

There are a few interesting features to note about the fits. First, the single real root of the fit t_0 is calculated using the standard formula of the roots of a cubic polynomial. For all three species, the root is located at ~ 19 hr AEL, which is close to the beginning of morphogenesis that starts at ~ 14 hr AEL [3]. Moreover, for a cubic polynomial of the form: $N(t) = at^3 + bt^2 + ct + d$, the inflection point is located at $t_{\text{inf}} = -\frac{b}{3a}$, which corresponds to the point where the second derivative

vanishes, $N(t)'' = 0$. The three different fits indicate that $t_{\text{inf}} \approx 54$ hr AEL. This corresponds approximately to the time when the neuron size reaches the size of the segment, which happens at ~ 48 hr AEL. This indicates that contact with the segment boundary initiates a change in the branching mechanism at the whole-tree level.

Moreover, the fact that the inflection point and root of all three fits coincide is a consequence of the definitions of branches, branch points and branch tips. Indeed, according to these definitions and assuming that class IV neurons are binary trees, the following equivalence exists between the number branches N_{Branches}, branch points $N_{\text{Branch points}}$ and branch tips $N_{\text{Branch tips}}$:

$$N_{\text{Branches}} = N_{\text{Branch points}} + N_{\text{Branch tips}} \tag{3.55}$$

In addition, since the birth of a new branch tip is always accompanied by a new branch point, $N_{\text{Branch tips}}$ and $N_{\text{Branch points}}$ only differ by the initial amount of branch tips. Therefore, at later times, since the initial amount of branch tips is of order ~ 1, one finds that $N_{\text{Branch points}} \approx N_{\text{Branch tips}}$, which also implies that the number of branches is approximately twice the number of branch tips or branch points, i.e. $N_{\text{Branches}} \approx 2N_{\text{Branch tips}} \approx 2N_{\text{Branch points}}$. In other words, all three species are proportional to one another, which explains why the cubic fits have similar shapes.

3.2.2 The branching rate is an extensive property of the tree

Next, time-lapse images of class IV neurons over a period of 15 to 30 minutes are used to measure the branching process at each developmental stage. After segmenting each neuron individually, the total number of branching events is counted manually in each neuron. All recorded branching events at each developmental stage are shown in fig. 3.11.

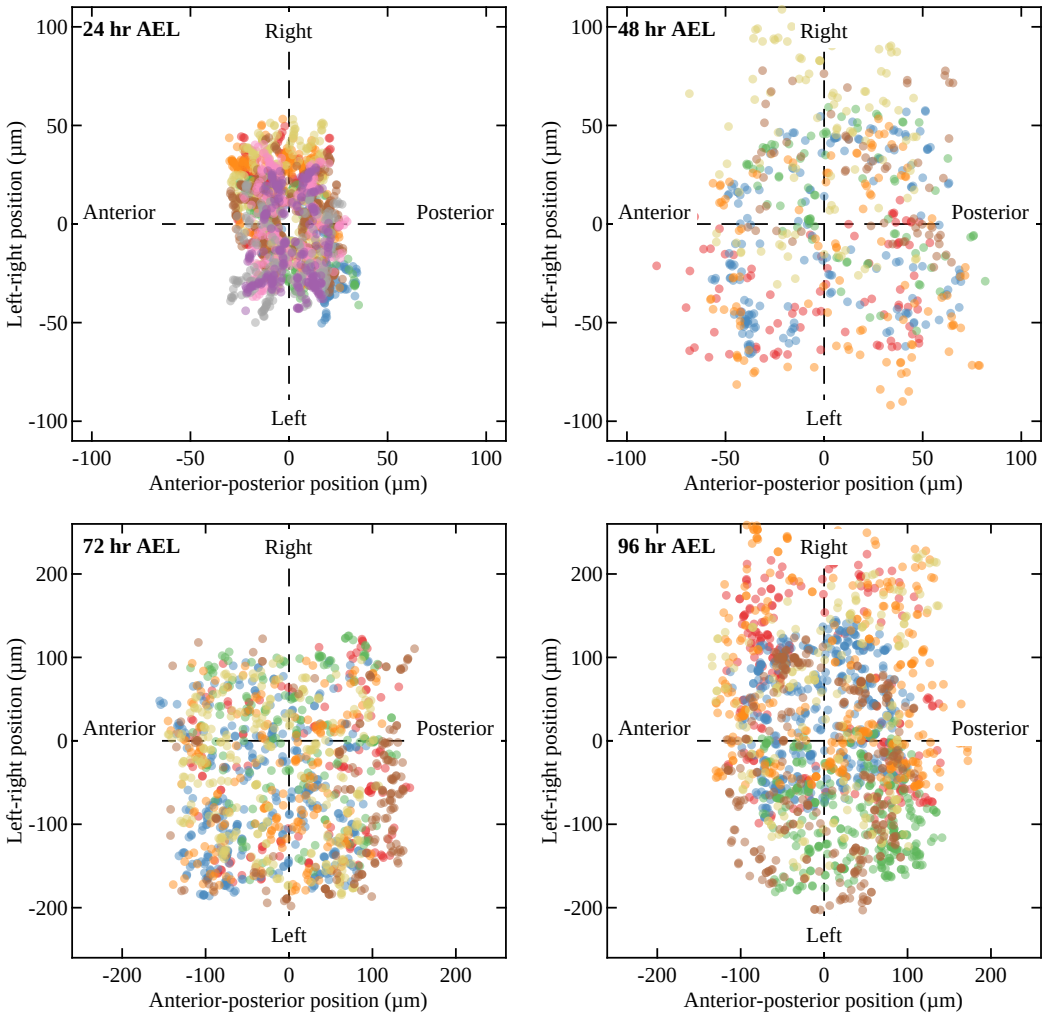

Figure 3.11 – Measurement of branching events over development
Each color represents measurements from an individual neuron. The branching events are centered with respect to the soma position and rotated to align the left-right body axis along the vertical direction.

Using the total number of branching events observed $N_{\text{Branching events}}$ and the duration of the observation ΔT, an estimate of the absolute branching rate ω_b is calculated for each neuron as follows:

$$\omega_b = \frac{N_{\text{Events}}}{\Delta T} \tag{3.56}$$

The resulting estimates for ω_b are shown in fig. 3.12a. From a first impression, the absolute branching rate of each neuron appears approximately constant over

development. However, this is unlikely since the branching rate at 72 and 96 hr AEL is under-estimated due to the fact that the neuron's dendritic tree does not fit completely into the field of the view of the microscope. Indeed, the field of view of the microscope is $330\,\mu m$ at a magnification of 40X, while the body segment where the dendritic tree grows reaches dimensions of $400 \times 300\,\mu m^2$ at 96 hours (see section 3.3.1 for more details on size measurements).

The partial coverage of the dendritic tree field prompted us to normalize the branching rate by the amount of total dendritic length observed during the observation. First, the total branch length L_{tot} is calculated from the dendritic tree skeleton of the first frame, which is constructed using a custom-made skeletonization algorithm (see section 2.5). As shown later in fig. 3.27a, the total branch length increases by $0.2\,mm\,\text{hr}^{-1} \sim 3.3\,\mu m\,\text{min}^{-1}$, which implies that it does not change considerably over the course of the 30 min movie. Therefore, the total branch length L_{tot} is assumed to be constant during the observation and its value is estimated using the initial time point. Using L_{tot} and ω_b, a length-normalized branching rate k_b is calculated as follows:

$$k_b = \frac{\omega_b}{L_{\text{tot}}} \tag{3.57}$$

Estimates of the normalized branching rate using eq. (3.57) are shown in fig. 3.12b. As depicted, the branching rate decreases by almost 10 fold from 24 to 48 hr AEL and remains approximately constant afterwards. Moreover, the branching rate is also fitted with a decaying exponential function and a constant value, i.e. $k_b(t) \sim ae^{-bt} + c$. The c parameter indicates that the branching rate reaches a constant value of $0.0012\,\mu m^{-1}\text{min}^{-1}$ at later stages. However, the fit parameters that model the initial exponential decay, a and b are not well-constrained with relative errors of $\sim 200\%$ and $\sim 100\%$, respectively. This is due to the sharp decrease of the branching rate and the variability of the data at 24 hr AEL.

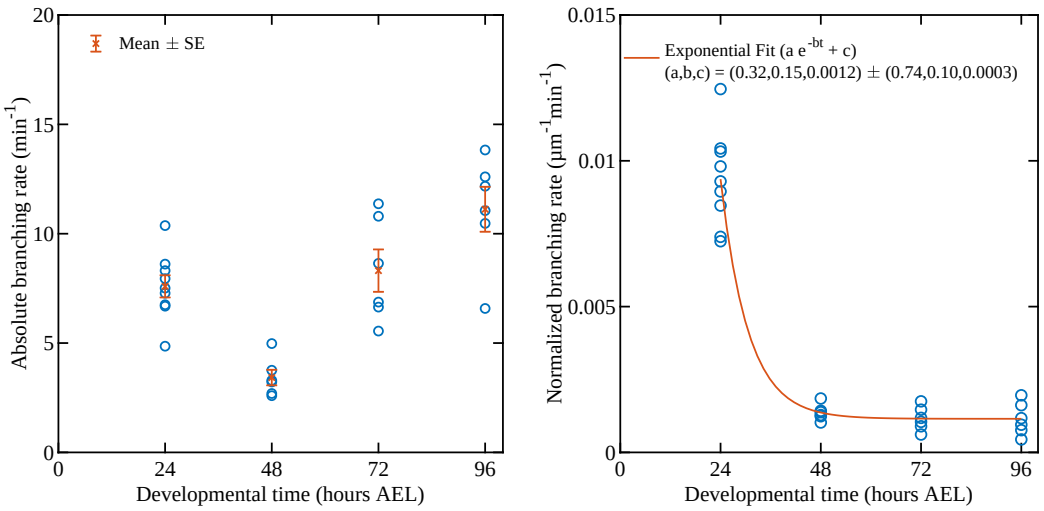

(a) Absolute branching rate

(b) Normalized branching rate

Figure 3.12 – Branching rate over development
Note that the 72 and 96 hr AEL movies only partially cover the entire dendritic tree. Therefore, the absolute branching rate is under-estimated at these stages. The error of the fit parameters are calculated from the standard formula of non-linear least squares fitting.

Aside from the initial transient phase, which is poorly constrained, the data and the fit demonstrate that the branching rate is approximately constant from 48 to 96 hr AEL. This implies that the branching process is an extensive property of the tree, meaning that the absolute branching rate of the tree scales with the overall size or mass of the neuron. This indicates that the intra-cellular material needed for forming new branch tips are produced distributively, and not centrally. In other words, as the tree grows, its production capability for building the intracellular components needed for growth also increases. This hypothesis is consistent with experimental observations that showed that translation regulators are transported in the class IV dendritic arbor providing evidence that protein translation occurs not only at the cell body, but also within the dendritic arbor [93].

3.2.3 The branching process is uniform in space

To further quantify the branching process, the spatial distribution of the branching events is analyzed. First, the area of the neuron is divided into $10 \times 10\,\mu m^2$ bins. This particular bin size was chosen to sample the branching process with sufficient precision as the average branch length varies between $5 - 10\,\mu m$. Then, the number of branching events in each bin is divided by the total observation time and area of the bin to define an absolute branching rate density $\Omega_b(\vec{x})$:

$$\Omega_b(\vec{x}_i) = \frac{N_{\text{Branching events},i}}{A\Delta T} \tag{3.58}$$

where $\vec{x}_i, N_{\text{Branching events},i}$ corresponds to the center and number of recorded branching events in the i^{th} bin, respectively, and A is the area of the bin. The estimate for Ω_b in each bin is then averaged over all cells that have coverage over the given bin at that particular developmental stage. The resulting average values for Ω_b are shown in fig. 3.13 and the number of cells in each bin is shown in fig. 3.14. This measurement is inherently noisy due to the small number of branching events in each bin. To reduce this noise, bins that are covered by at least two cells for each developmental stage are taken into account at the cost of reducing sampling of the periphery. Nonetheless, estimates of the branching rate density demonstrate that the branching rate is uniform over the area of the neuron.

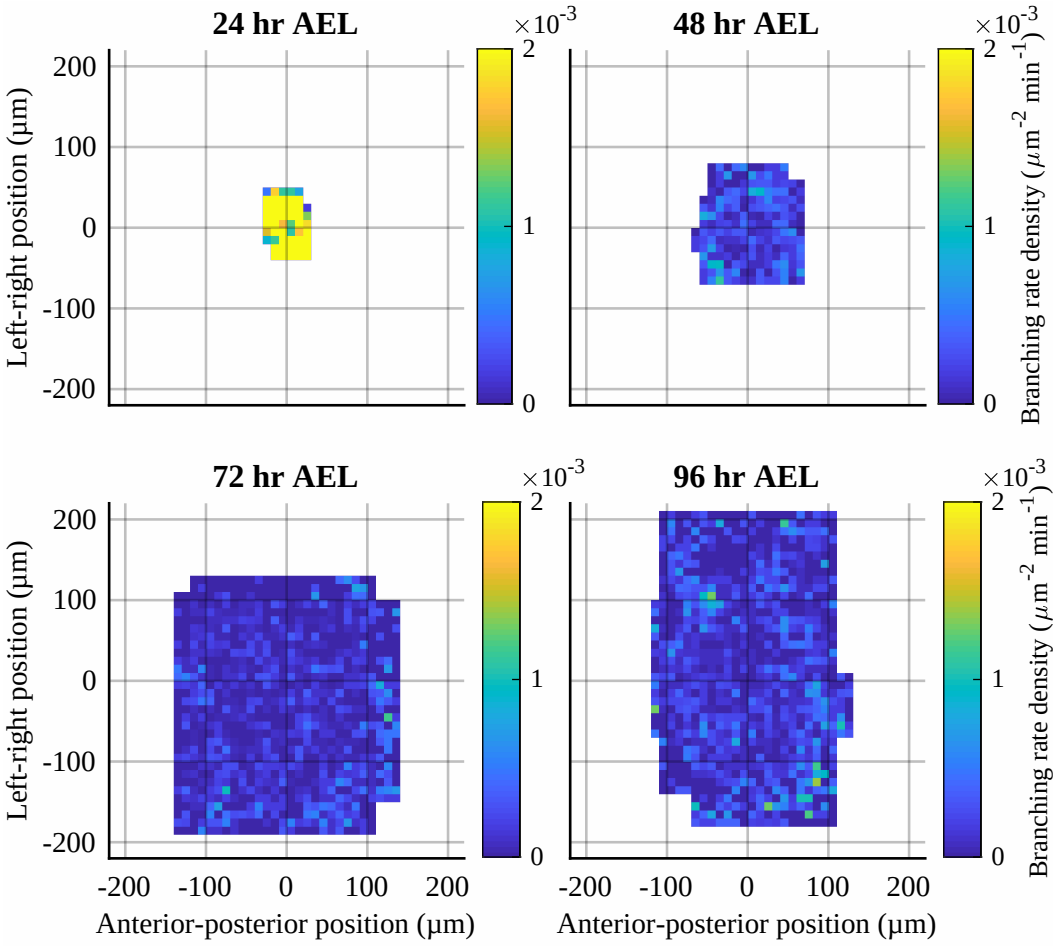

Figure 3.13 – Branching rate density over development

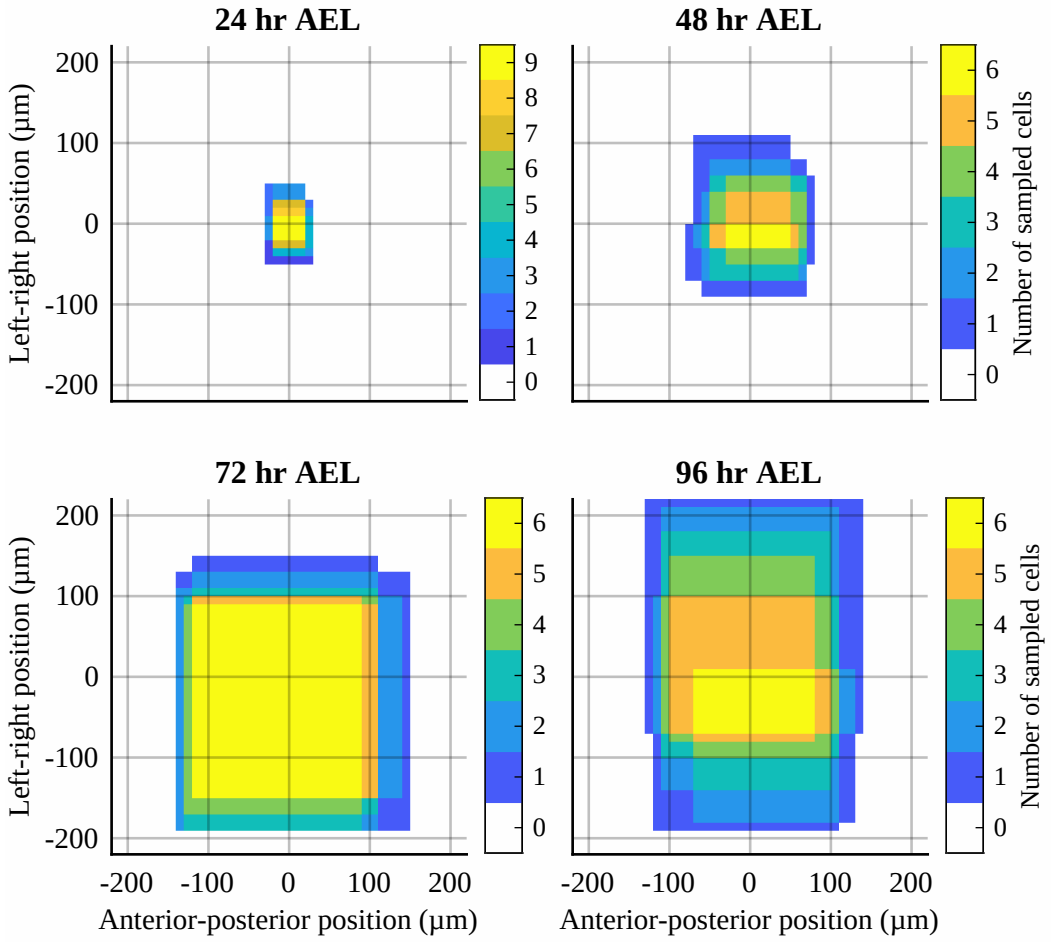

Figure 3.14 – Number of sampled cells in the branching analysis

In addition, similar to the calculation of the normalized branching rate k_b as explained in the previous section, a branching rate $K_b(\vec{x})$ normalized by the total dendritic length in each given bin is calculated:

$$K_b(\vec{x}_i) = \frac{N_{\text{Branching events},i}}{\Delta T A \rho_L(\vec{x}_i)} \tag{3.59}$$

where ρ_L is the dendritic length density calculated with a Gaussian kernel estimator with a bandwidth of $5\mu m$. Since ρ_L is a divider in the calculation of K_b, the smoothness of ρ_L provided by the kernel estimator helps to reduce the noise in K_b. The measured values of K_b are shown in fig. 3.15. Again, the branching process is

uniform in space throughout development. One may observe a slight over-density at the periphery of the neuron at 72 and 96 hr AEL. However, the periphery of the neuron is not as richly sampled as the bulk, as shown in fig. 3.14. Therefore, more data would be required to conclude that the branching rate is higher near the boundary.

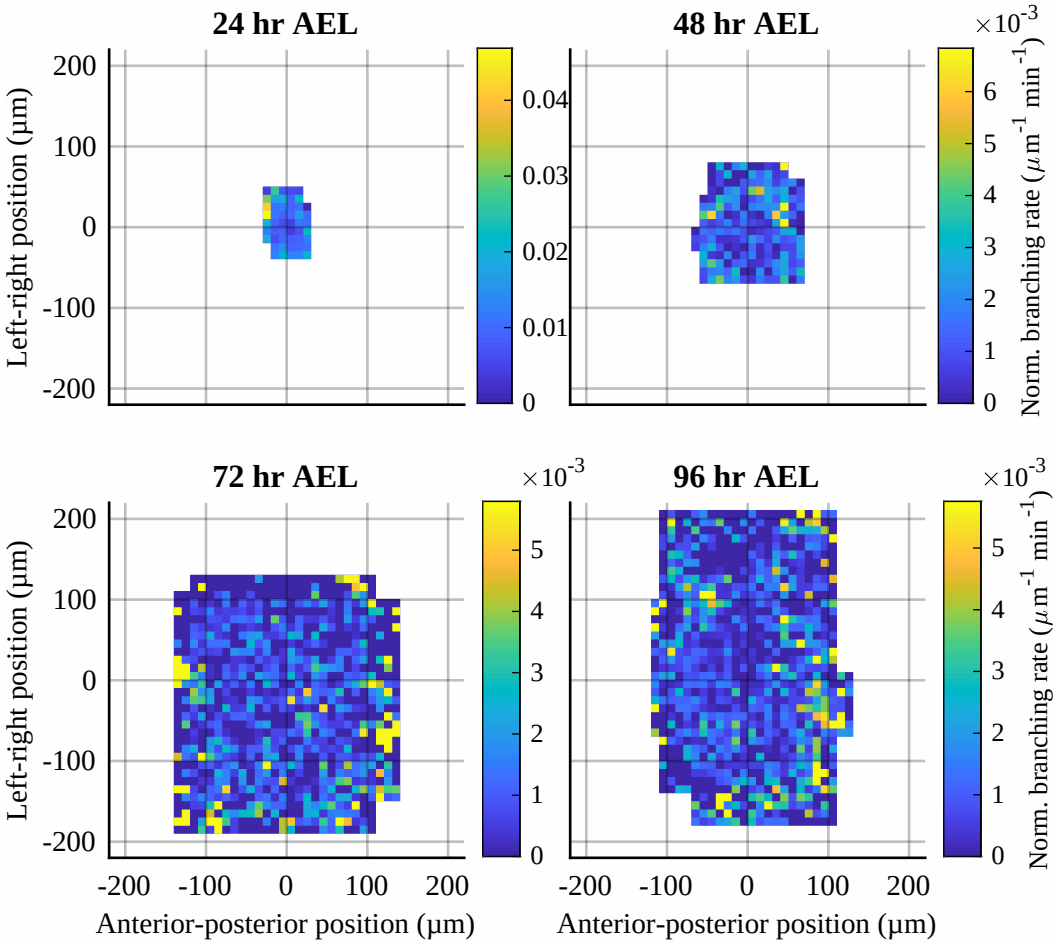

Figure 3.15 – Spatial dependence of normalized branching rate over development

3.2.4 Branching angles are normally distributed

With a better grasp of the temporal and spatial dependence of the branching process, the branching angles are now examined. The branching angle is defined as the

angle between the two branch vectors that define the orientation of a pair of sibling branches that share a common branch point. The orientation of a branch is given by the vector tangent to the branch and oriented towards the deeper end of the tree. Incidentally, since one of the children branches is normally aligned with its parent, the branching angle can also be defined as the angular difference between the orientation vectors of a branch and its parent branch, measured at their common branch point.

The distribution of branching angles is measured using skeletons of static images of class IV neurons taken at each developmental stage. Using these skeletons, the branching angle is calculated as the difference between the orientation of two branches that are sibling to one another. All branching angles from all cells of a given developmental stage are assembled together to construct the branching angle distributions shown in fig. 3.16. The branching angles peak at $\sim 100^\circ$ and have a standard deviation of $\sim 30^\circ$ across all developmental stages. Moreover, the maximum-likelihood estimate of a normal distribution provides a good fit to the empirical distribution. Finally, pooling all measurements together, the branching angle has an average of $99.03 \pm 0.25^\circ$ and a standard deviation of $30.36 \pm 0.18^\circ$.

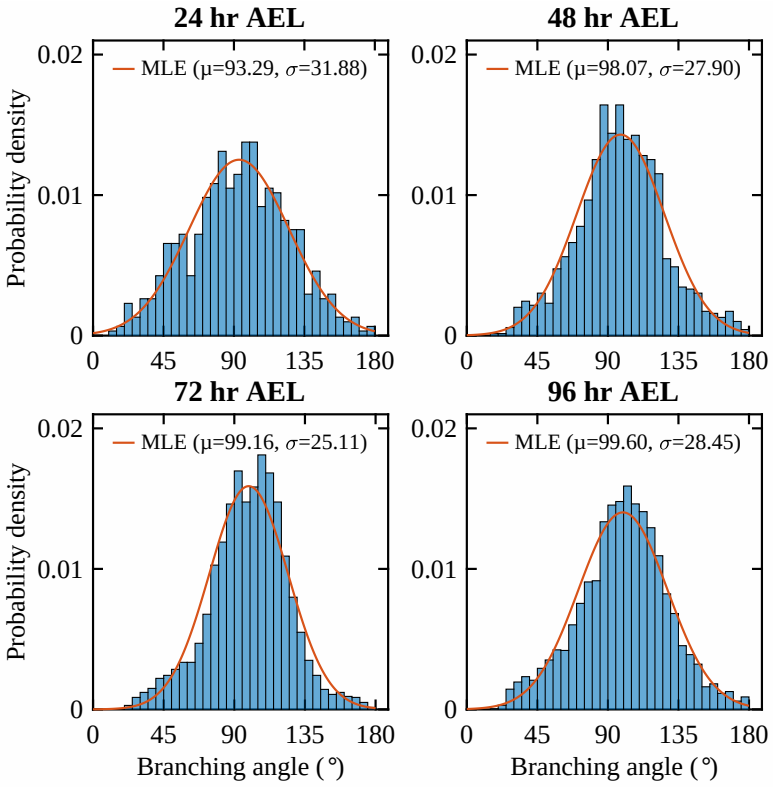

Figure 3.16 – Branching angles over development

3.2.5 Branch tips annihilate after complete retraction

In the previous section, the birth rate of new branches was quantified. As with anything that pertains to the living, birth is ultimately (and unfortunately) followed by death. This holds true for the class IV neuron as most branch tips retract back to their branch point and die as a result of contacts with other branches or due to fluctuations in their growth. The branch tip death process is quantified in two ways.

First, the death rate is measured manually in a manner similar to the measurement of the branching rate. More specifically, the total number of branch death

events $N_{\text{Death events}}$, which correspond to the complete disappearance of a branch tip, is divided by the duration of each movie ΔT to define the absolute death rate:

$$\kappa_d = \frac{N_{\text{Death events}}}{\Delta T} \tag{3.60}$$

The average death rate of any given tip is defined by dividing the absolute death rate by the total number of branch tips N_T observed in each movie:

$$k_d = \frac{\kappa_d}{N_T} \tag{3.61}$$

The resulting measurements are shown in fig. 3.17. Similar to the measurement of the absolute branching rate, the absolute death rate is also under-estimated at 72 and 96 hr AEL, due to the fact that the field of view is smaller than the size of the neuron. However, the death rate per unit tip is trustworthy as it is normalized by the number of observed branch tips. As shown, the death rate per tip decreases ~ 10 fold from 24 to 48 hr AEL similar to what was observed with the branching rate. However, at 72 hr AEL, the death rate increases and later decreases ~ 2 fold.

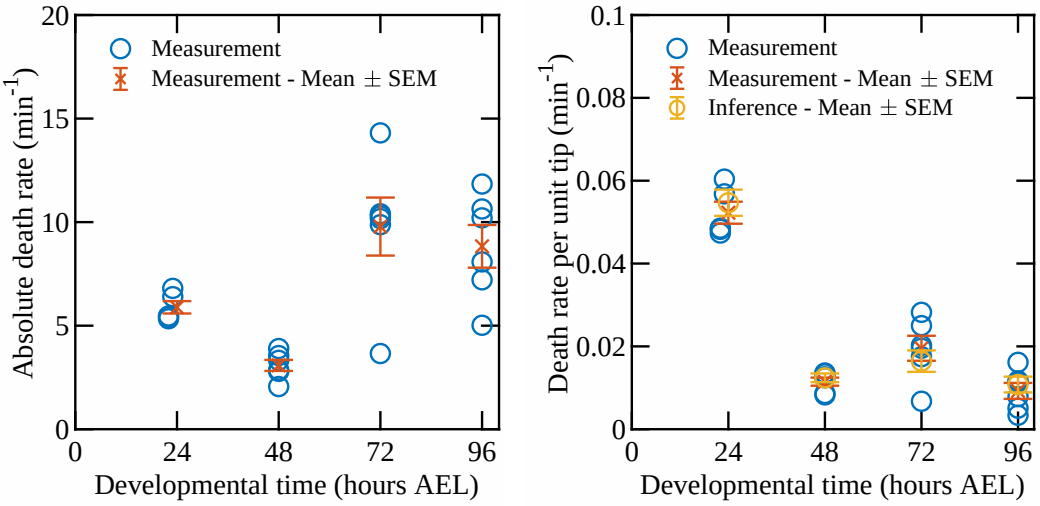

Figure 3.17 – Death rate over development
Note that measurements at the first developmental stage were performed between 22 and 24 hrs. The mean death rate at this stage agglomerates all of these measurements together. The inferred death rate is calculated using the estimated net branching rate and the measured birth rate.

Second, another estimate of the death rate is inferred from the net growth rate of the number of branch tips. Let ω_{net} correspond to the net branching rate, which results from the combined effect of the birth and death process of branch tips, and let k_d correspond to the average death rate of any given tip as defined above. Then, the following relationship holds:

$$\omega_{\text{net}}(t) = \omega_b(t) - k_d(t)N_T(t) \tag{3.62}$$

where dependence on the developmental time t is added for generality. By inverting this relationship, another expression of the death rate is obtained:

$$k_d(t) = \frac{\omega_b(t) - \omega_{\text{net}}(t)}{N_T(t)} \tag{3.63}$$

The net branching rate ω_{net} is estimated by the derivative of the cubic fit of the number of branch tips vs the developmental time (see fig. 3.10). The resulting values for $\omega_{\text{net}}(t)$ are shown in fig. 3.18.

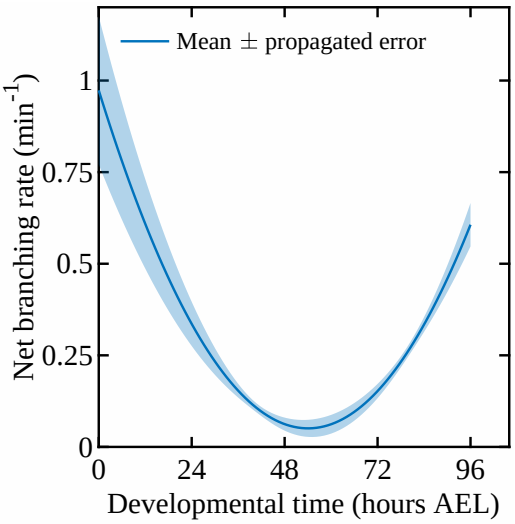

Figure 3.18 – Net branching rate over development
The error is calculated by propagating the error of the parameters that fits the number of branch tips (see fig. 3.10)

Using $\omega_{\text{net}}(t)$ and the measurement of the absolute branching rate ω_b, the death rate k_d is inferred at the various developmental stages using eq. (3.63). The inferred values are shown in fig. 3.17 in comparison with the measurements. As shown, the inferred values agree with the measurements indicating that the branching rate and death rate measurements are consistent with one another.

3.3 Morphometrics of class IV neurons

3.3.1 Neuron and segment size

Throughout development, the size of the class IV neurons increases along with the body of the larvae. Since the class IV dendritic tree is an open shape, the definition of size is ambiguous. To tackle this ambiguity, two methods are considered to calculate the size of the neuron. In addition, the neuron size is compared against the body segment size as measured by Sonal Shree.

Neuron size

The neuron size is calculated using the set of class IV neuron skeletons produced by the custom-made skeletonization algorithm (see section 2.5). An example of a 96 hr AEL skeleton is shown in fig. 3.19 where the origin $(0,0)$ corresponds to the location of the soma found by the skeletonization algorithm.

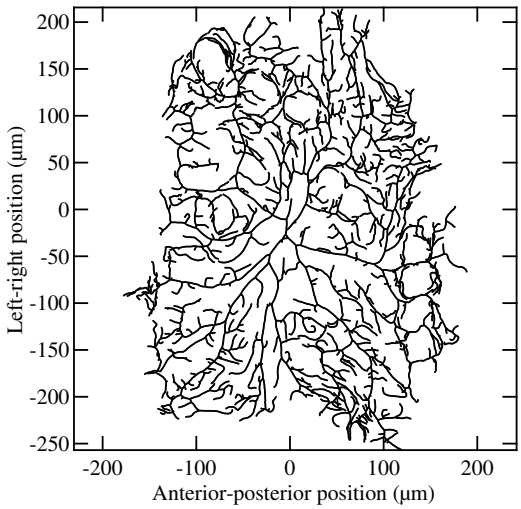

Figure 3.19 – Example of a class IV neuron skeleton at 96 hr AEL

The branches of the skeletons are one-dimensional objects that are formed by a collection of ordered nodes where each branch is sampled at a rate of 1 node every $0.1\mu m$ ($10\frac{\text{nodes}}{\mu m}$). Since each node is associated with a unit amount of dendrite, the mass distribution of the class IV neurons is described by the set of nodes position $\vec{n}_i = (n_{x,i}, n_{y,i})$ where i is the node index. Note that this assumes that the branch thickness is constant across all branches. This is not the case in real neurons, but it is sufficient for analyzing the spatial extension of the dendritic tree.

The first method used to calculate the neuron size assumes that the spatial distribution of the branch nodes is uniform. With this assumption, estimates of the neuron size are proportional to the standard deviation of the mass distribution. Recall that a one-dimensional uniform distribution in the domain (a, b) has a variance of $\frac{(b-a)^2}{12}$. Since $b-a$ corresponds to the range of the distribution, the uniform neuron size is defined as follows:

$$\vec{D}_{\text{uni}} = \sqrt{12\, var(\vec{n}_i)} \tag{3.64}$$

where $var(\cdot)$ and $\sqrt{\cdot}$ are independently applied to each dimension. Therefore, $\vec{D}_{\text{uni}}$ defines both the anterior-posterior (AP) and left-right (LR) sizes. Note that $\vec{D}_{\text{uni}}$ is related to the moment of area I_A in the following way:

$$(D^2_{\text{uni,AP}}, D^2_{\text{uni,LR}}) = \frac{1}{12A}(I_{A,AP}, I_{A,LR}) \tag{3.65}$$

$$I_{A,AP} = \iint_A x^2 dxdy \tag{3.66}$$

$$I_{A,LR} = \iint_A y^2 dxdy \tag{3.67}$$

where A corresponds to the total area of the shape, the x, y axis corresponds to the AP, LR axis respectively, and the axes are centered on the center-of-mass of the shape.

An example of the neuron boundary calculated using the uniform size is shown in fig. 3.20a and the uniform neuron size of all neurons in the static dataset is shown in fig. 3.20b. The neuron grows faster along the LR axis compared to the AP axis. Also, the neuron has a rectangular shape as evidenced by the fact that the AP size is significantly smaller than the LR size.

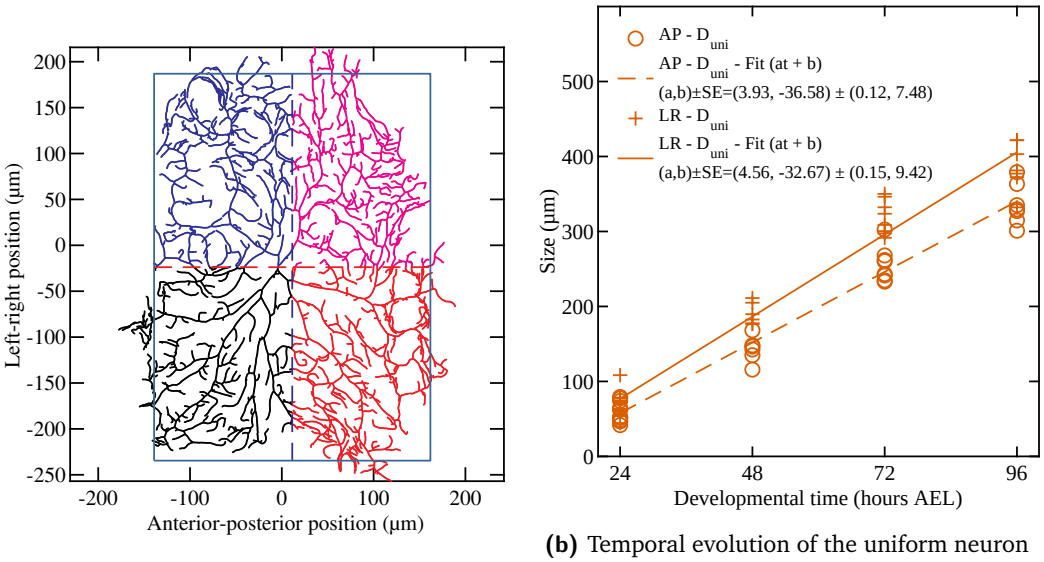

(a) Example of the uniform size boundary

(b) Temporal evolution of the uniform neuron size

Figure 3.20 – Example of the boundary calculation assuming a uniform dendrite distribution
The dashed lines in fig. 3.20a corresponds to the AP and LR axes centered on the center-of-mass of the nodes distribution. The color of the nodes encode whether they are above or below the AP or LR axis.

The second method of the neuron size estimation relaxes the assumption of uniformly distributed branch nodes. In this method, the neuron size is given by the percentiles of the mass distribution in each dimension. Focusing on a single dimension x, let α correspond to a given percentile such that $0 \leq \alpha \leq 1$. Using the inverse cumulative distribution $\mathrm{cdf}_x(z)$ of the nodes distribution, the percentile size $D_{\alpha,x}$ is defined as:

$$D_{\alpha,x} = U_\alpha - L_\alpha \tag{3.68}$$

$$L_\alpha = \mathrm{cdf}_x^{-1}(\beta), \quad U_\alpha = \mathrm{cdf}_x^{-1}(1-\beta) \tag{3.69}$$

$$\mathrm{cdf}_x(z) = \frac{1}{N}\sum_{i=1}^{N}\Theta(z - n_{x,i}), \quad \beta = \frac{1-\alpha}{2} \tag{3.70}$$

$$\Theta(x) = \begin{cases} 0 & x < 0 \\ 0.5 & x = 0 \\ 1 & x > 0 \end{cases} \tag{3.71}$$

where N corresponds to the number of nodes in the tree, $\Theta(x)$ is the Heavyside theta function and L_α, U_α correspond to the lower and upper bounds of the mass distribution that contains a percentage α of the mass. Examples of the percentile size boundary are shown in **??** for various values of α.

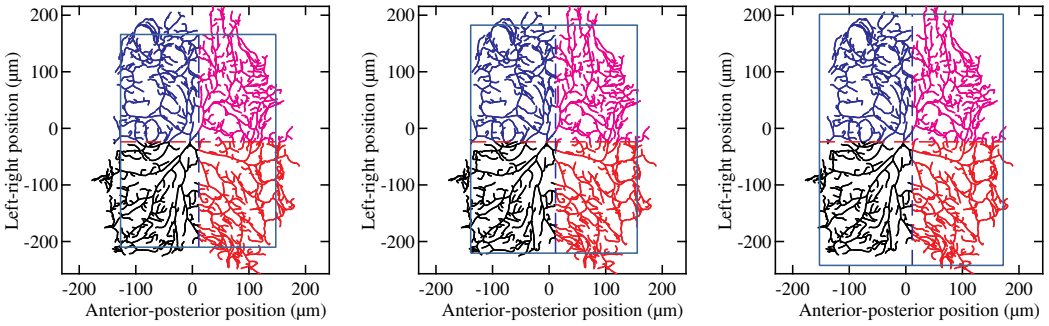

(a) $D_{90\%}$ **(b)** $D_{95\%}$ **(c)** $D_{99\%}$

Figure 3.21 – Examples of the percentile size boundary

As expected, the range of the boundary increases as the fraction α of the contained mass increases. Moreover, the 90% size ($D_{90\%}$) and 95% size ($D_{95\%}$) are slightly too restrictive while the 99% size ($D_{99\%}$) encloses the dendrite mass almost entirely.

Performing this calculation on the full dataset of neurons at different developmental times, a time series of the percentile sizes is obtained as shown in fig. 3.22. As expected, the growth rate of the percentile size shows a trend similar to the uniform size D_{uni} when comparing the AP and LR sizes. Moreover, the growth rates of the $D_{99\%}$ size are comparable to the growth rates of D_{uni} indicating that D_{uni} also measures the full extension of the dendritic tree. This also indicates that the assumption of uniform mass distribution is justified.

In summary, there are several methods that one can use to measure the neuron size. One of the caveat of the percentile size method is that it is a parametric method, as one needs to chose the value of the parameter α. Therefore, since D_{uni}

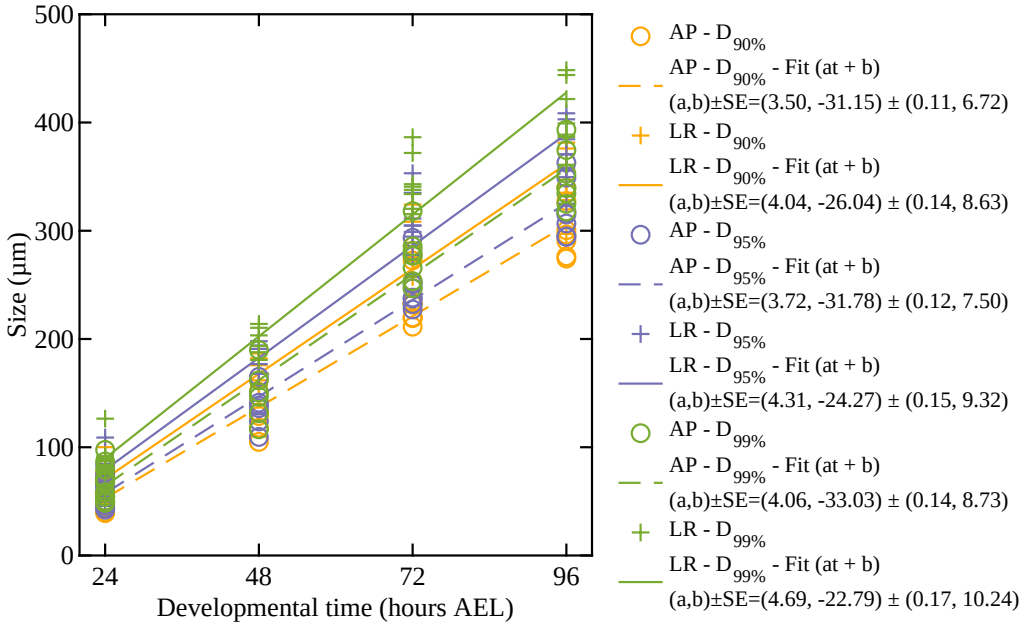

Figure 3.22 – Temporal evolution of the percentile neuron size

is non-parametric and compares to $D_{99\%}$, D_{uni} is chosen as a measure of the neuron size for future analyses.

Segment size

Concurrent to the growth of the neuron during development, the larval body segment in which the neuron is contained also increases in size. The body segment has a rectangular shape that aligns with the left-right and anterior-posterior body axes of the larva. To measure the segment size, a set of low-magnification images is used to measure the distance between two adjacent Class IV neuron somas (see fig. 3.23a). When the two somas belong to different segments, the distance that separates them correspond to the anterior-posterior size (blue dashed line in fig. 3.23a). When the two somas belong to the same segment, the distance that separates them corresponds to the left-right size (orange full line in fig. 3.23a). Performing these measurements on different class IV neurons at $24, 48, 72$ and 96 hr AEL, the temporal evolution of the larval segment sizes is obtained over developmental time (see fig. 3.23b). As

shown, both the AP and LR sizes grow linearly over development and the AP size grows at a slightly slower rate than the LR size. This behavior was also observed with the neuron size as shown in fig. 3.20b.

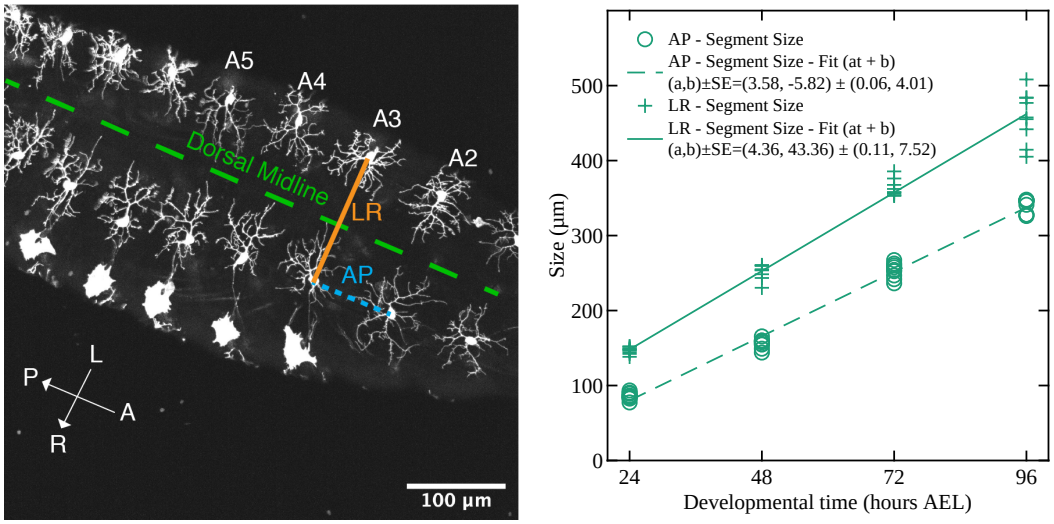

(a) Measurement of the AP and LR segment size

(b) Temporal evolution of the segment size

Figure 3.23 – Measurement of the body segment size over development
The green line identifies the dorsal midline, which separates the left-hand side from the right-hand side of the larvae. The length of the orange and blue lines in fig. 3.23a corresponds to the anterior-posterior (AP) and left-right (LR) segment size, respectively. The arrowheads of the AP-LR compass indicate the positive direction of each axis. Figure a) provided by Sonal Shree.

A subtlety arises from using the distance between somas as a proxy of the segment size. As shown in fig. 3.23a, the soma of class IV neurons are slightly receding away from the dorsal midline. Due to this recession, using the soma-to-soma distance overestimates the segment size.

To correct for this overestimation, the offset between the segment center and the soma is estimated by assuming that the center of the segment coincides with the center-of-mass. Then, the center-of-mass $\vec{R}_{\text{COM}}$ of each neuron is centered at the soma using a coordinate system that aligns the AP and LR body axes. Therefore, the components of $\vec{R}_{\text{COM}}$ correspond to the distance between the segment center and the soma in each dimension.

Once the soma offset of two adjacent neurons is known, the segment size $\vec{L}_S$ is calculated from the soma-to-soma distance $\vec{L}_{S-S}$ as follows:

$$\vec{L}_S = \vec{L}_{S-S} - \Delta\vec{L}_S \tag{3.72}$$

$$\Delta\vec{L}_S = \left({}_L\vec{R}_{\text{COM}} - {}_R\vec{R}_{\text{COM}}\right) \tag{3.73}$$

where ${}_L\vec{R}_{\text{COM}}$ (${}_R\vec{R}_{\text{COM}}$) corresponds to the center-of-mass of the neuron that is on the left-hand side (right-hand side) of the dorsal midline. When the neuron is located on the left-hand side of the dorsal midline, ${}_L R_{\text{COM,LR}} > 0$ if the soma is receding from the midline. Similarly, if the neuron is located on the right-hand side of the dorsal midline, ${}_R R_{\text{COM,LR}} < 0$ if the soma is receding from the midline. The sign of $R_{\text{COM,LR}}$ flips when moving to the other side of the dorsal midline because $\vec{R}_{\text{COM}}$ is defined with respect to the neuron's soma position, and not with respect to a fixed origin. This sign flip is indeed observed when calculating the center-of-mass of the class IV neurons with respect to their soma position (compare circles and crosses in fig. 3.24a).

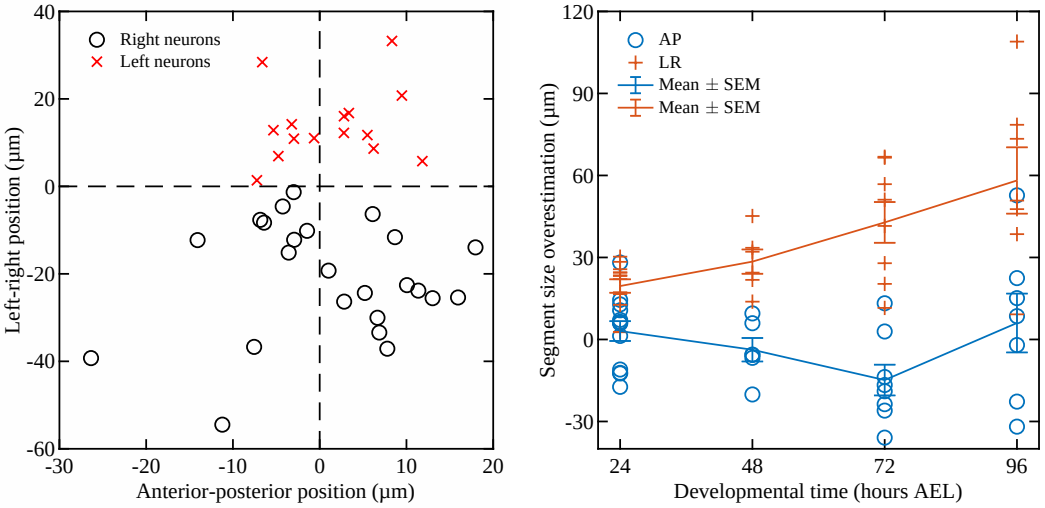

(a) Center-of-mass with respect to the soma

(b) Segment size overestimation estimate

Figure 3.24 – Estimation of the segment size measurement overestimation

In practice, the position of the center-of-mass is calculated using the static class IV neurons dataset as opposed to using the neurons that were used in the measurement of the soma-to-soma distance. The reasons for using this dataset is twofold: First, measuring the center-of-mass of the neurons used in the soma-to-soma measurement would require the segmentation and skeletonization of an additional set of curated neurons. Second, a low magnification was used in the soma-to-soma distance measurement, which leads to less precise measurements of the center-of-mass compared to the more resolved neurons in the static class IV neurons dataset.

One inconvenience of the static image dataset is that neurons are not paired, but are imaged independently, and may not belong to the same larvae. Since the pairing information is missing, each neuron is paired with its mirror image reflected across the AP (resp. LR) axis when calculating the LR (AP) overestimation. This amounts to estimating the overestimation as $\Delta\vec{L}_S = 2\vec{R}_{\text{COM}}$ for each neuron. Performing this calculation at each developmental stage, an average of the overestimation is obtained for each dimension (see fig. 3.24b). The size overestimation increases throughout development on the LR dimension, while it remains close to 0 on the AP dimension. Moreover, comparing the soma-to-soma distance vs the corrected distance, the correction has a significant effect on the growth rate of the LR segment size, while the AP segment size is almost unchanged (see fig. 3.25).

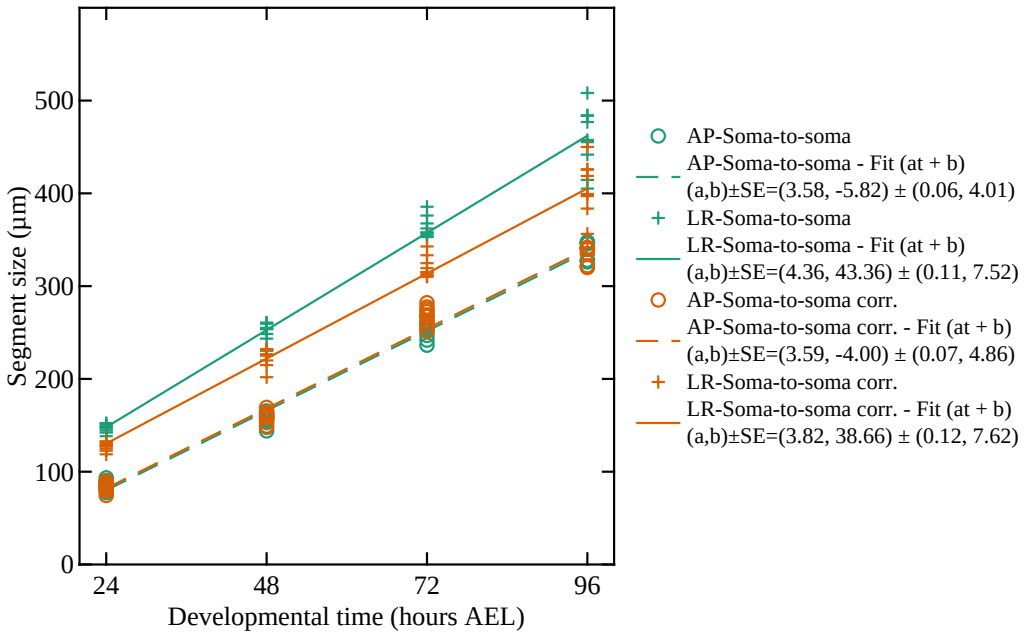

Figure 3.25 – Comparison of the measured and corrected segment size

Neuron size vs segment size

Finally, the neuron size is compared against the segment size as shown in fig. 3.26. On the AP axis, the neuron size is within $\sim 30\,\mu m$ of the segment size at 24 hrs after egg-lay, but the gap slowly decreases over development. On the LR axis, the difference between the neuron size and the segment size is more pronounced. At 24 hours after egg-lay, the neuron and segment size differ by $\sim 80\,\mu m$ and this difference is gradually reduced to $\sim 0\,\mu m$ at 96 hours after egg-lay.

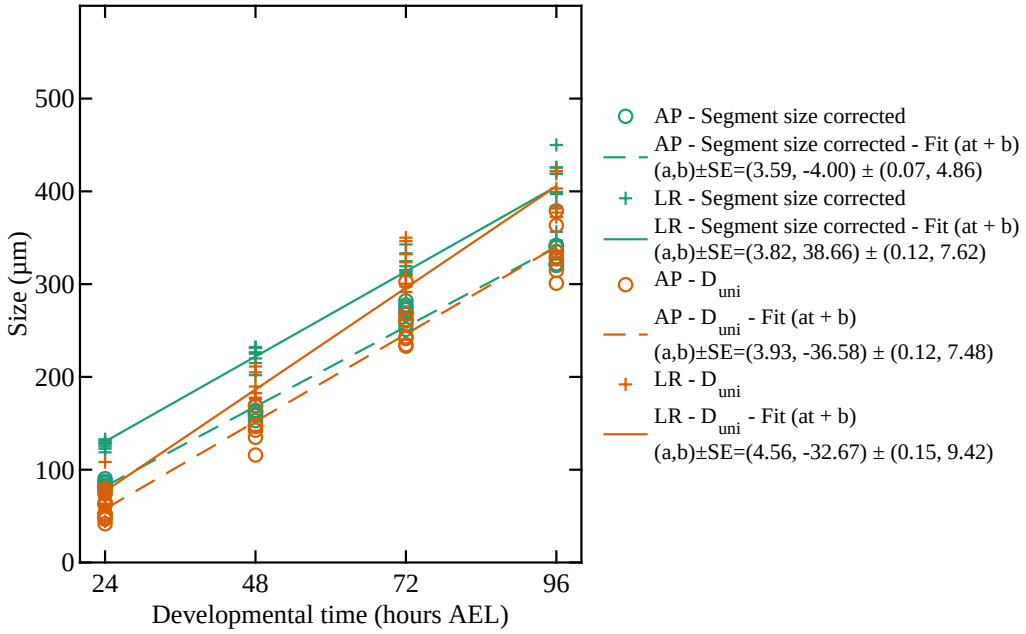

Figure 3.26 – Comparison of the neuron size and segment size growth

Moreover, the growth rate of the neuron sizes is either higher than or similar to the growth rate of their respective segment size. On the LR axis, the growth rate of the neuron size is significantly higher than the growth rate of the segment size. This indicates that the expansion of the neuron on the LR axis overcomes the expansion of the segment such that the neuron ultimately reaches the size of the segment. A similar effect is also observed on the AP axis, although the difference in the growth rate of the neuron and segment size is smaller. This is explained by the fact that the neuron has a smaller amount of empty space to fill along the AP axis compared to the LR axis. Therefore, the growth rate of the neuron along the AP axis matches the growth of the segment faster than the LR axis.

However, relative to the growth of the segment size, the growth rates of the AP and LR neuron size are not significantly different (within ~ 1 standard error):

$$\frac{\frac{dD_{\text{uni,AP}}}{dt}}{\frac{dD_{\text{Seg,AP}}}{dt}} = \frac{3.93 \pm 0.12 \frac{\mu m}{hour}}{3.59 \pm 0.07 \frac{\mu m}{hour}} = 1.10 \pm 0.04 \tag{3.74}$$

$$\frac{\frac{dD_{\text{uni,LR}}}{dt}}{\frac{dD_{\text{Seg,LR}}}{dt}} = \frac{4.56 \pm 0.15 \frac{\mu m}{hour}}{3.82 \pm 0.12 \frac{\mu m}{hour}} = 1.20 \pm 0.05 \tag{3.75}$$

This implies that the expansion of the neuron is tuned to the growth of the segment.

In summary, we find that the class IV neuron is initially smaller than the size of the body segment, but due to its rapid growth, it quickly reaches the size of the segment and completely covers its area at ~ 72 hr AEL. At this stage, class IV neurons efficiently tile the surface of the larvae and the growth of the segment constrains the expansion of the neuron.

3.3.2 Branch length

During development, the total dendritic mass of the class IV neuron increases as a result of cellular growth. To quantify this growth, the total dendritic branch length is calculated using skeletons of class IV neurons at various developmental stages. As shown in fig. 3.27a, the total branch length increases linearly throughout development at a rate of $0.19\, mm \text{hr}^{-1}$. Using estimates of the total branch length L_{tot}, the mean branch length $\langle L \rangle$ is calculated as follows:

$$\langle L \rangle = \frac{L_{tot}}{N_{\text{Branches}}} \tag{3.76}$$

where N_{Branches} corresponds to the total count of branches in the neuron. As shown in fig. 3.27b, the mean length initially increases from 24 to 72 hr AEL, but it decreases from 72 to 120 hr AEL. The initial increase in the mean length could be explained

by a global stretching of the dendritic tree, which would elongate the branches of the tree uniformly. However, by measuring the growth rate of non-terminal branches in proportion to their initial length from 24 to 48 hours and from 48 to 96 hr AEL, no evidence of stretching was found in comparison to the growth of the segment size (see fig. 3.28). Another process that could explain this increase are pruning mechanisms that remove branches in the tree. Indeed, when a branch is annihilated, its sibling and parent branch are joined together into a longer branch thereby increasing the average branch length. Alternatively, the decrease in the mean branch length from 72 to 120 hr AEL could be explained by an increase in the branching rate. However, this not warranted by observations (see fig. 3.12b).

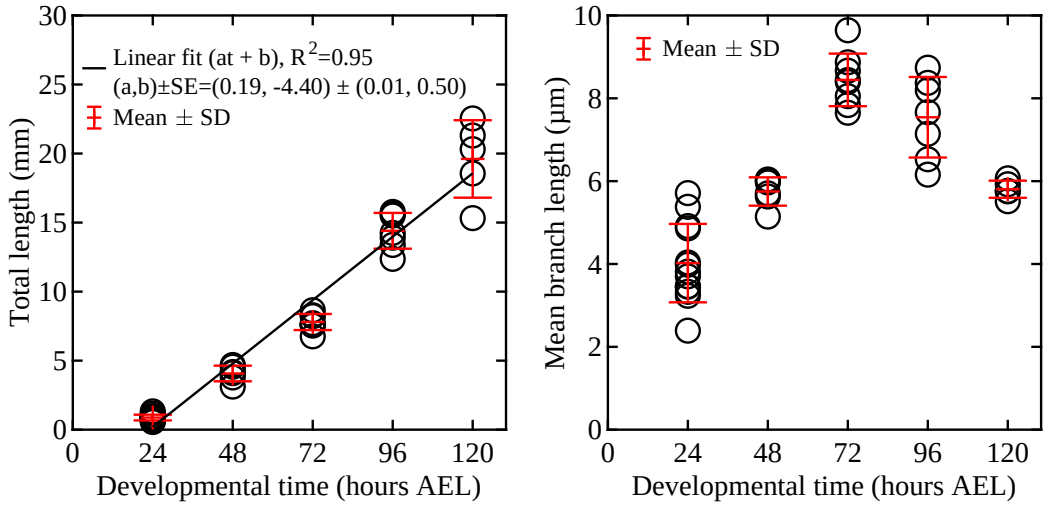

(a) Total branch length **(b)** Mean branch length

Figure 3.27 – Total and mean branch length of class IV neurons over development

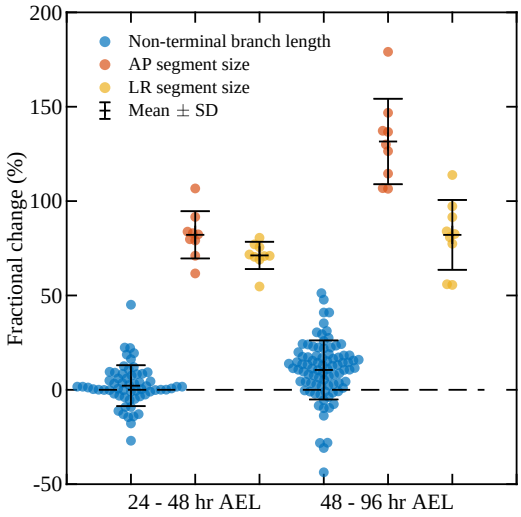

Figure 3.28 – Expansion of non-terminal branches
The fractional change is calculated as $\frac{L_{\text{initial}} - L_{\text{final}}}{L_{\text{initial}}}$. Reproduced from original measurements performed by Sonal Shree.

Finally, the distribution of branch length over the dendritic arbor is analyzed at each developmental stage. As shown in fig. 3.29, the branch lengths are exponentially distributed over the entire duration of the development. An exponential distribution further supports the hypothesis that branching is a Poisson process, since the interval length between Poisson events are exponentially distributed.

Furthermore, the correlation of the branch length $C_l(\Delta d)$ is calculated as a function of the depth of the branches within the tree topology:

$$C_l(\Delta d) = \frac{\langle L(d)L(d+\Delta d)\rangle_d - \langle L(d)\rangle_d^2}{\langle L^2(d)\rangle_d - \langle L(d)\rangle_d^2} \tag{3.77}$$

where $L(d)$ is the length of a given branch at depth d, $L(d+\Delta d)$ is the length of a descendant located Δd levels deeper and $\langle \ldots \rangle_d$ averages over all branch pairs in the tree. As shown in fig. 3.30, the branch length has no correlation further strengthening the hypothesis that the branching process is uniform throughout the arbor.

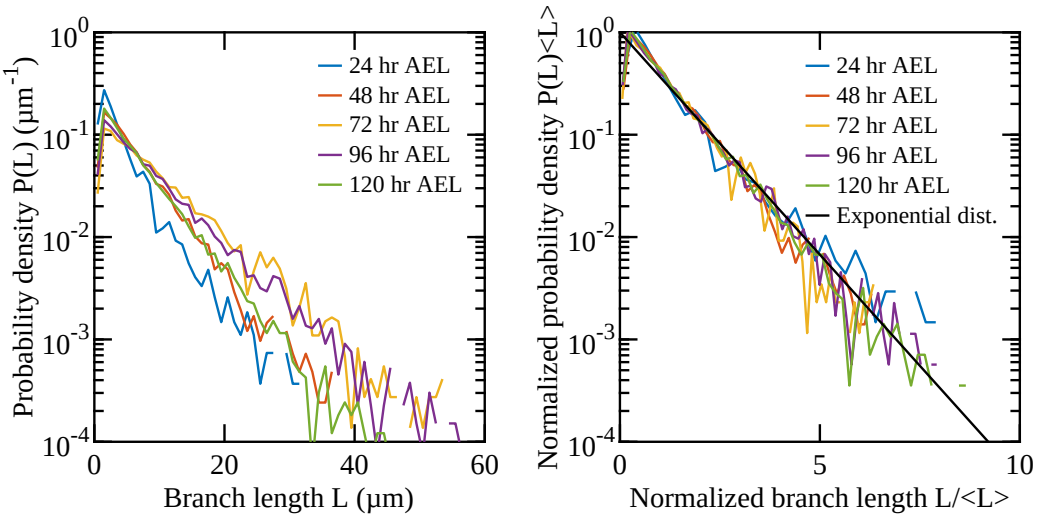

Figure 3.29 – Branch length distribution over development
When comparing the normalized probability densities, the density expected from an exponential distribution is added as a guide.

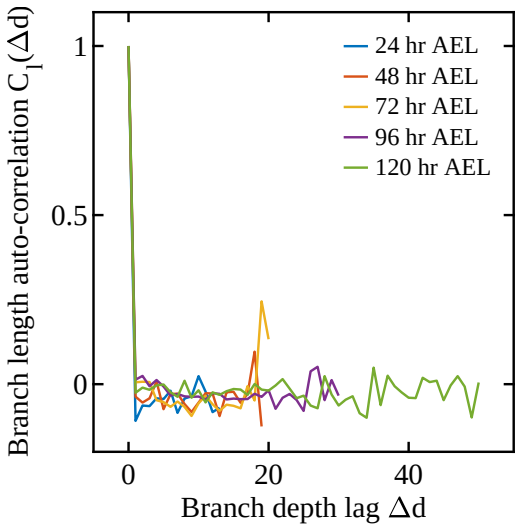

Figure 3.30 – Branch length correlation over development

3.3.3 Persistence length

The shape of the dendritic branches is quantified by their persistence length L_p. In general, the persistence length of a curve quantifies its straightness and increases

as the curve becomes straighter. Mathematically, the persistence length is defined through the correlation of the tangent vectors $\hat{t}(s)$ along the curve:

$$\langle \hat{t}(s) \cdot \hat{t}(s+\Delta s) \rangle = \langle \cos(\Delta\theta(\Delta s)) \rangle = e^{-\frac{\Delta s}{L_p}} \tag{3.78}$$

where $\Delta\theta(\Delta s)$ corresponds to the difference of the angle between two tangent vectors on the curve that are separated by a path length Δs and $\langle\cdot\rangle$ averages over all pairs of points on the curve. In other words, the persistence length corresponds to the decay length of the cosine of the tangential angle as one moves along the path of the curve. To calculate the persistence length of a given dendritic tree, the tangential angles θ of all branches is used to calculate the average $\cos(\Delta\theta(\Delta s))$ over all path length separation Δs and all positions on the tree. Following eq. (3.78), $\langle \cos(\Delta\theta(\Delta s)) \rangle$ is fitted with a non-linear least-squares to obtain an estimate of the persistence length. In addition, $\langle \cos(\Delta\theta(\Delta s)) \rangle$ is fitted over the range $0 \leq \Delta s \leq \langle L \rangle$ to avoid the abrupt change of the tangential angle that occurs at the branch points. An example of the $\langle \cos(\Delta\theta(\Delta s)) \rangle$ fit is shown in fig. 3.31a.

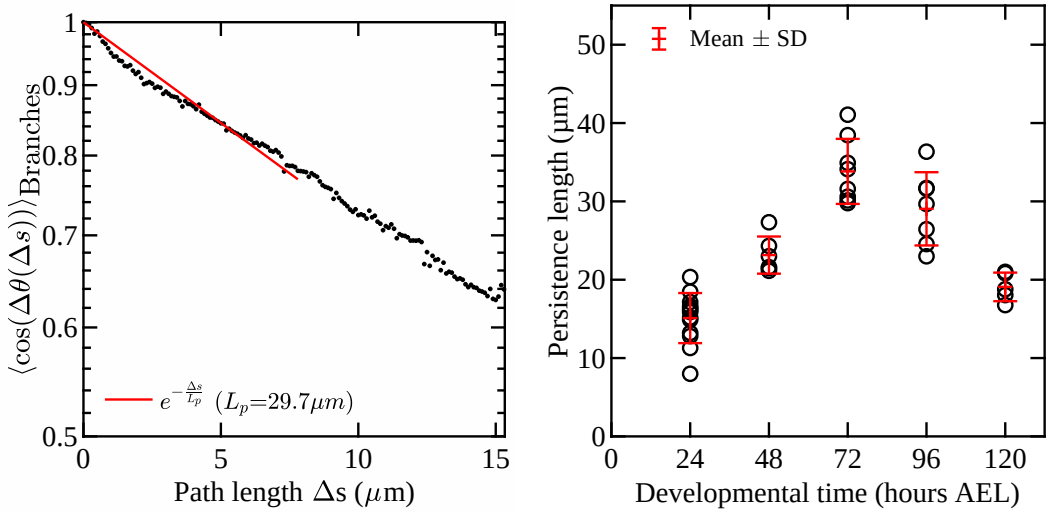

(a) Persistence length estimation at 96 hr AEL

(b) Persistence length over development

Figure 3.31 – Persistence length of class IV neurons

As depicted, the persistence length gradually increases from 24 to 72 hr AEL, and decreases from 72 to 120 hr AEL. The straightening of the branches from 24 to 72 hr AEL may be explained by the maturation of the dendritic tree. In the early stage of morphogenesis, the tree is still being formed with many short flexible branches that grow in various directions to fill space. At the tree develops, short branches are pruned near the soma leading to a higher amount of long straight branches. This can be seen as well in the images where later trees have long straight branches near the soma compared to the earlier trees (see fig. 1.3). From 72 to 120 hr AEL, branches become less straight and reach levels of undulation that are comparable to the early stage. This increase in the amount of flexible branches at later stages may be a consequence of the increasing absolute branching rate, which increases the amount of young and malleable branches.

3.3.4 Branch orientation

The persistence length is useful in understanding the average shape of the branches in the tree. However, as a single measure, it does not capture the fine structure of the branching morphology. To better understand the shape of the branches, the spatial distribution of the branch orientation is measured throughout the tree.

First, the tangential angles of the branches are measured from the tangent vectors that define the two-dimensional path of the branches. In the class IV neuron skeletons, the tangent vectors are sampled every $0.1\,\mu m$ along each branch. The angle of the tangent vectors is determined by sliding a window of $1\,\mu m$ along the path of the branch and performing a principle component analysis (PCA) on the set of 10 branch nodes to find the vector that best fits the nodes. This running average along the branch path helps to reduce the noise that originates from the branch nodes' position. The distribution of the tangential angles as a function of the radial position of the tangent vector is shown in fig. 3.32 at each developmental stage. The

distributions agglomerate all angles from all branches in all trees of the given stage. The estimated distributions demonstrate that the tangential angles are uniformly distributed at all stages indicating that branches are oriented in all directions across the tree, irrespective of the radial position of the branch. This indicates that branches grow freely in space and are not biased towards any specific direction. Moreover, the bulk of the tangential angles is centered at a given radius, which increases throughout development indicating that the tree expands. In addition to the radial translation of the distribution, the spread also increases indicating that the tree is filling its occupied area as it is expanding. The uniformity of the distribution is also evident after summing over the radial direction as shown in fig. 3.33).

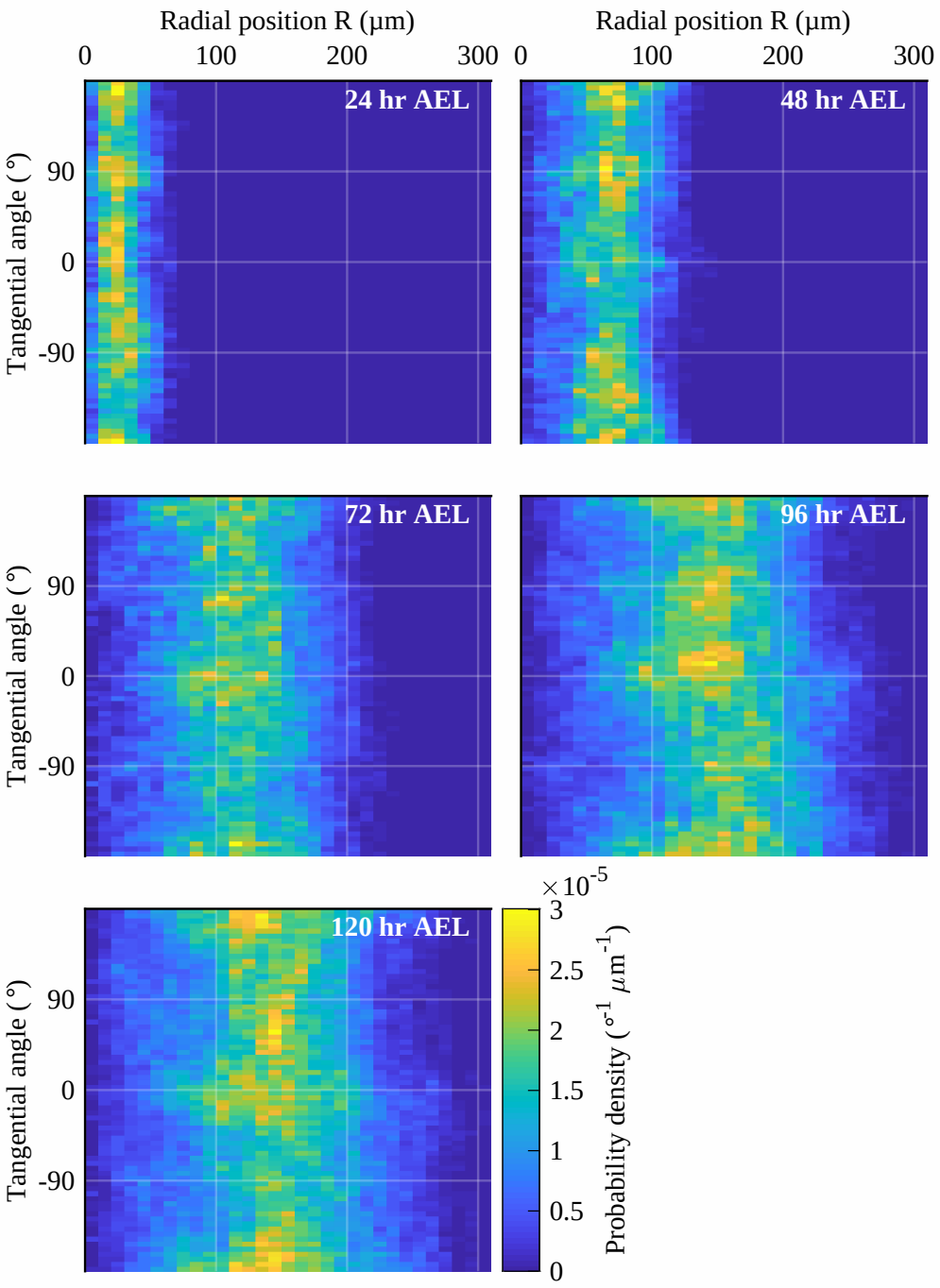

Figure 3.32 – Radial dependence of the tangential angle distribution over development

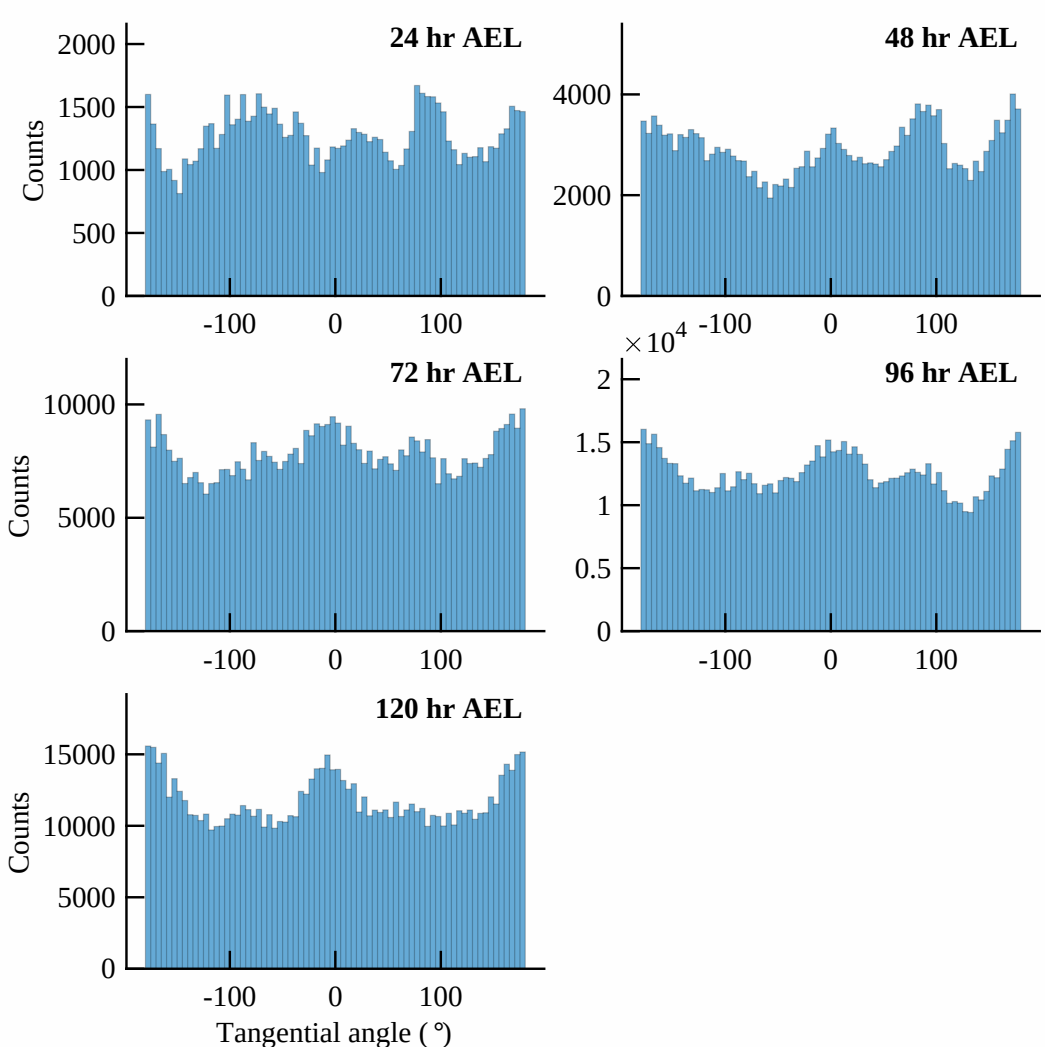

Figure 3.33 – Tangential angle distribution over developmental time

Similar to the tangential angle, the *polar tangential angle* is also measured. The polar tangential angle is the difference between the tangential angle and the two-dimensional polar angle at the given position. More specifically, if ϕ_i^j corresponds to the tangential angle at the j^{th} node of the i^{th} branch, the polar tangential angle is given by:

$$\psi_i^j = \phi_i^j - \theta_i^j \tag{3.79}$$

$$\vec{x}_i^j = |r_i^j|(\cos(\theta_i^j), \sin(\theta_i^j)) \tag{3.80}$$

where $\vec{x}_i^j$ denotes the 2D position of the j^{th} node of the i^{th} branch and the origin is located at the soma. In other words, $\psi = 0°$ ($\psi = 180°$) corresponds to the positive (negative) radial direction while $\psi = 90°$ ($\psi = -90°$) corresponds to the anti-clockwise (clockwise) angular direction. In a similar fashion to the tangential angle analysis, the polar tangential angle distribution is calculated by assembling all measurements of a given developmental stage (see fig. 3.34). As shown, the polar tangential angle is centered at the origin across all developmental stages. This indicates that the branches' orientation is biased towards the outward radial direction. As an aside, this is a general property of two-dimensional trees, which was qualitatively observed by Leonardo da Vinci as inscribed in one of his notebooks [42, p. 395]. Since the branches of a tree ultimately converge to a common root, their orientation is biased towards the radial direction. Indeed, in the extreme case where branches are purely angular, they do not converge to their common root, and consequently a tree cannot be formed. The bulk of the polar angle distribution is mostly contained within $[-45°, 45°]$ indicating that the bias is about halfway between purely radial and purely angular. Again, summing over the radial direction, the one-dimensional polar tangential angle distribution is shown in fig. 3.35. This alternative analysis more evidently shows that branches are biased towards the radial direction with a dispersion of $\sim 45°$.

Several mechanisms could be the cause of this radial bias in the branch orientation in addition to the structure constraint imposed by the tree geometry. The branches' orientation may be biased towards the positive radial direction because growth is mostly unhindered in this direction. Indeed, since branch growth is inhibited by contact with other branches, branches are more likely to grow in a direction where there are no other branches. When branches grow at the edges of the tree, the positive radial direction is void of branches and therefore has the least amount of growth obstacles. However, although this is likely the case for the early stages when class IV neurons have not tiled the larva's surface, this is not true at the later stages

when the neurons are in contact with their neighbors. Therefore, this rationale can only partially explain the radial bias.

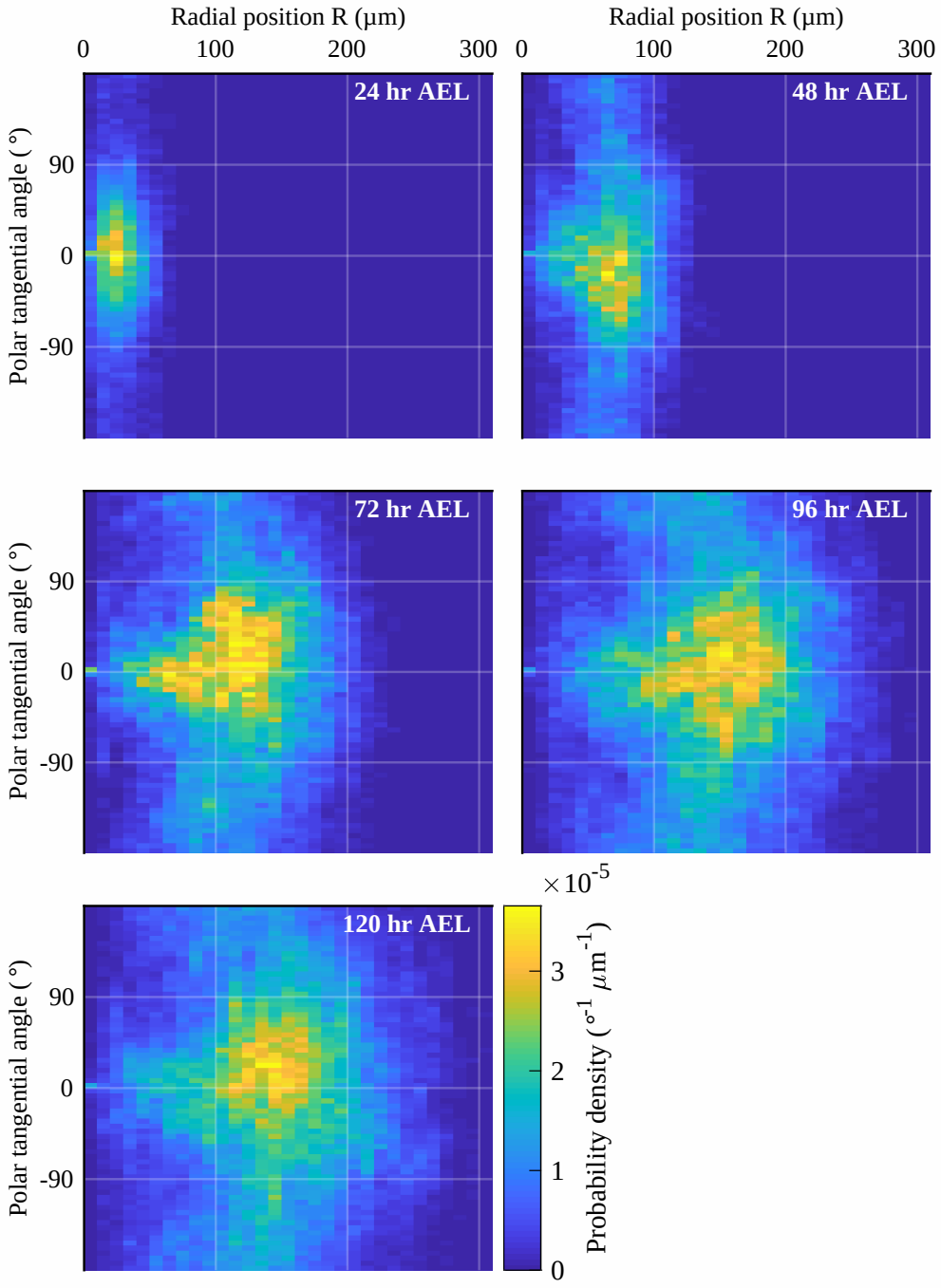

Figure 3.34 – Radial dependence of the polar tangential angle distribution over development

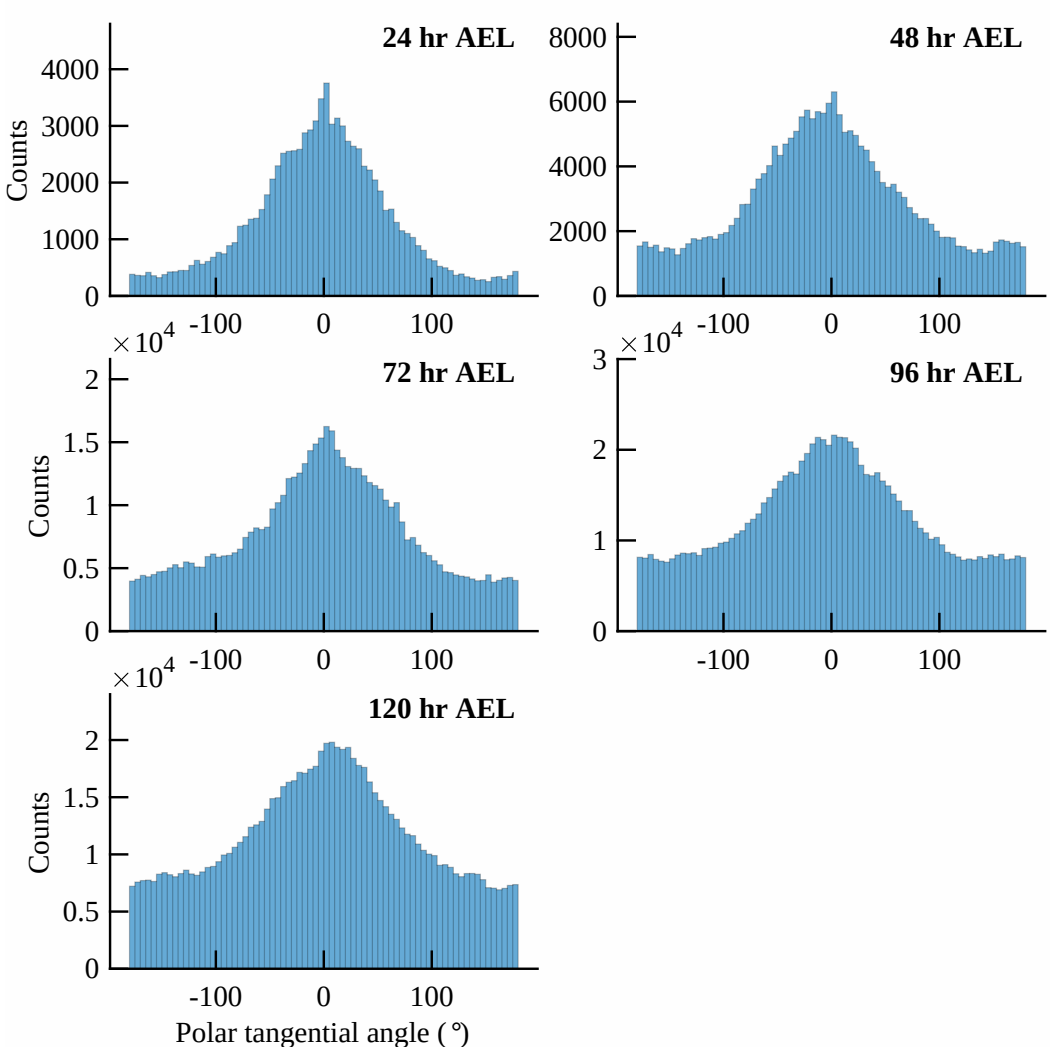

Figure 3.35 – Polar tangential angle distribution over development

In anticipation of the proposed models of morphogenesis, the average cosine and sine of the polar tangential angle is shown in fig. 3.36. As expected, the cosine components are significantly above 0, while the sine component fluctuates around 0. Note that $\langle \cos(\psi) \rangle$ decays slightly over development due to the spread of the polar tangential angle at later stages.

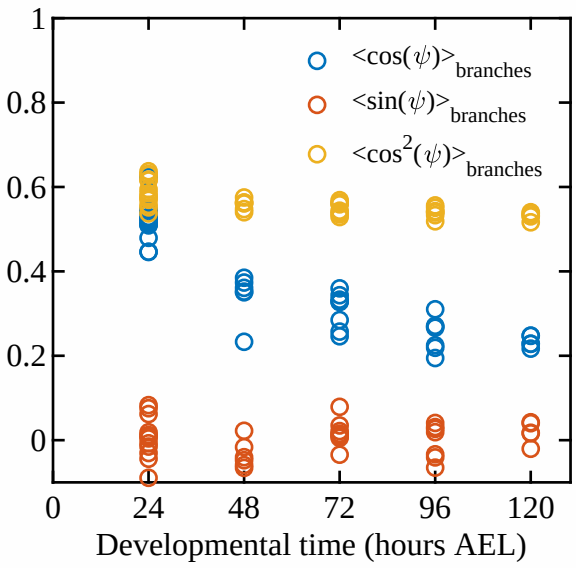

Figure 3.36 – Average cosine and sine of the polar tangential angle over development

3.3.5 Fractal dimension

Motivated by the branched dendritic network of class IV neurons, the fractal dimension d_f is utilized as one measure of density. In 2D, the fractal dimension varies between 1 and 2 and indicates how a shape is closer to a line ($d_f = 1$) or a surface ($d_f = 2$) in a continuous manner. In other words, the fractal dimension quantifies the ability of a shape to fill space. There are many ways to define the fractal dimension such as the box counting dimension or the Hausdorff dimension [13]. For simplicity, this analysis considers only the correlation and box-counting dimensions. First, the correlation dimension is defined in terms of the correlation integral of the shape [17]. More precisely, let us assume that a shape is discretized by a set of N points

with position $\vec{x}_i$. Given this set of points, the correlation dimension d_c is defined in terms of the correlation integral $C(r)$:

$$C(r) = \frac{2}{N(N-1)} \sum_{\substack{i,j=1 \\ i<j}} \Theta(r - |\vec{x}_i - \vec{x}_j|) \tag{3.81}$$

$$C(r) \sim r^{d_c} \tag{3.82}$$

where $\Theta(x)$ is the Heavyside step function. In other words, $C(r)$ is equal to the fraction of pairs of points that are separated by a distance of at most r. For a fractal, $C(r)$ is expected to be a power law whose power corresponds to the fractal dimension.

On the other hand, the box counting dimension d_b is defined in terms of a set of boxes that covers the shape. Given a box size r, let $N(r)$ correspond to the number of boxes needed to cover the entire shape. As the size of the boxes increases, $N(r)$ decreases since a smaller amount of bigger boxes are needed to cover the given shape. Again, the functional behavior of $N(r)$ is a power law whose power corresponds to the box-counting dimension:

$$N(r) \sim r^{-d_b} \tag{3.83}$$

In this morphometric analysis, these power laws are exploited to estimate the fractal dimension. Since the neurons have a finite shape, the fractal nature is only expected to hold over a certain range of radii. At small distances, the power laws are lost due to the finite sampling rate of the branches while at large distances, $C(r)$ and $N(r)$ saturate due to the finite size of the neuron. Therefore, to estimate the approximate fractal nature of the neuron, the power laws are fitted over the range $\frac{\langle L \rangle}{2} \leq r \leq R_g$ where $\langle L \rangle$ is the mean branch length of the tree and R_g is the radius of gyration.

To estimate the correlation dimension, $C(r)$ is calculated using the neurons' skeletons where each branch is sampled at a rate of $\frac{1\,\text{point}}{0.1\mu m}$. Then, a linear least-squares fit is performed on the logged $(r, C(r))$ data to find the correlation dimension. An example of the correlation integral for a class IV neuron at 96 hr AEL is shown in fig. 3.37a.

To estimate the box dimension, a set of boxes of size r is laid out on a square lattice and the number of non-empty boxes is counted. This process is repeated for all given radii to establish the behavior of $N(r)$. The logged $(r, N(r))$ data is then fitted with a linear least-squares to find the box-counting dimension. An example of the functional form of $N(r)$ for the same class IV neuron example is shown in fig. 3.37b. As depicted, the fractal dimension varies by approximately 5% between the two methods.

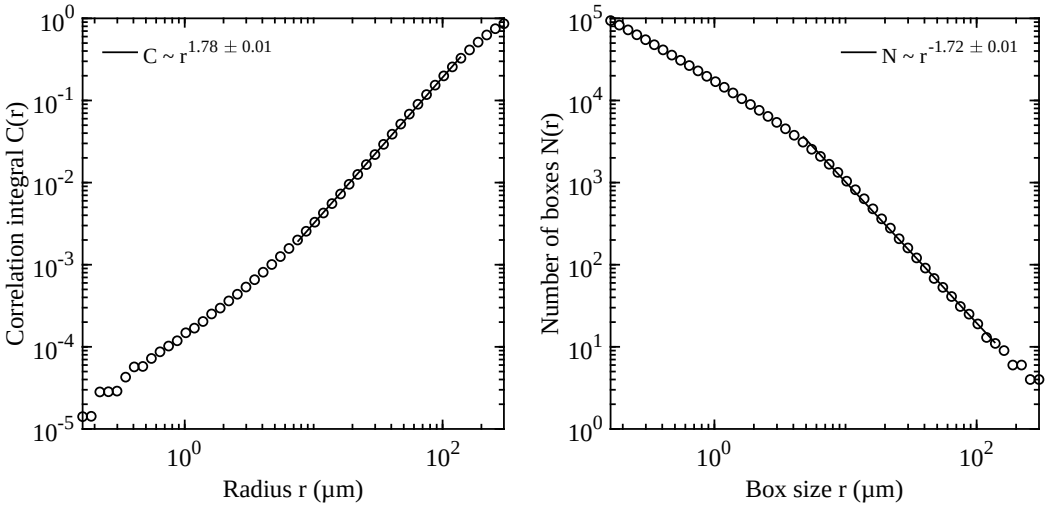

(a) Correlation dimension d_c **(b)** Box-counting dimension d_b

Figure 3.37 – Fractal dimensions of a class IV neuron at 96 hr AEL

Although fitting the power laws over a restricted range helps to alleviate the finite size effects, it is insufficient. When measuring $C(r)$ to estimate the correlation dimension, points that are within a distance r of the boundary are underestimating $C(r)$ since part of their neighborhood is empty due to the boundary. To alleviate

this effect, periodic boundaries are used. This amounts to calculating a modified correlation integral $C'(r)$:

$$C'(r) = \frac{2}{N(N-1)} \sum_{\substack{i,j=1 \\ i<j}} \Theta(r - |\vec{d}_{ij}|) \tag{3.84}$$

$$\vec{d}_{ij}^{(k)} = \min(|\vec{x}_i^{(k)} - \vec{x}_j^{(k)}|, |L^{(k)} - (\vec{x}_i^{(k)} - \vec{x}_j^{(k)})|) \tag{3.85}$$

where $\vec{d}_{ij}^{(k)}$ corresponds to the shortest distance between $\vec{x}_i$ and $\vec{x}_j$ along the k^{th} dimension and $L^{(k)}$ is the size of the neuron in the k^{th} dimension. In practice, before $C(r)$ is calculated, the points in the shape are centered at the center-of-mass and the periodic boundaries are located at half the uniform size $\vec{D}_{\text{uni}}/2$ on each side of the tree (see section 3.3.1). Moreover, points that fall outside the boundary are removed to avoid overestimating the correlation integral.

To test the effect of the periodic boundaries, a set of points on a square lattice is generated with a lattice spacing of $d = 0.01$ (see fig. 3.38a). This shape is expected to have a correlation dimension of 2 since it fills the entire space. As shown in fig. 3.38b, this value is recovered only when periodic boundaries are used indicating that periodic boundaries are effective in removing the underestimation of $C(r)$ due to the boundary effects.

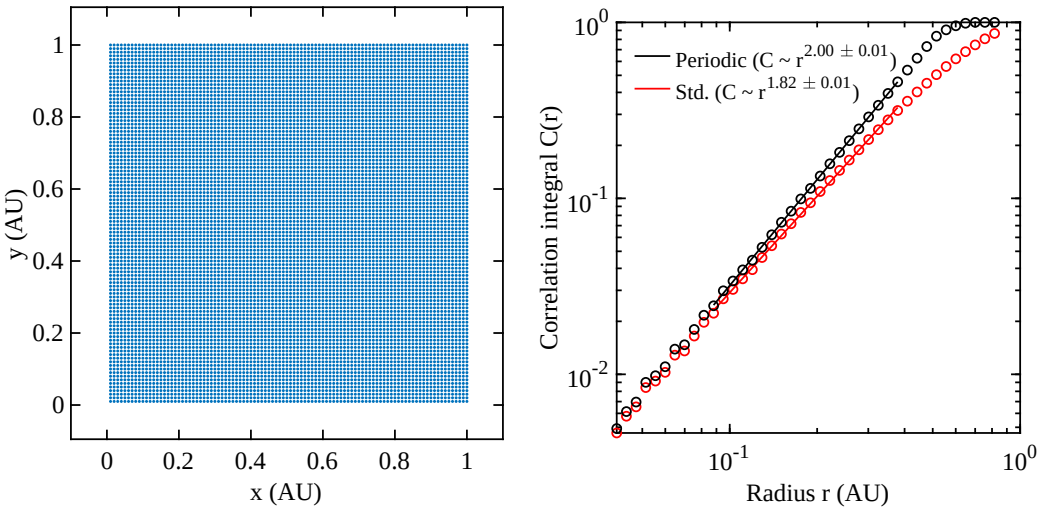

(a) Square lattice with a spacing of $d = 0.01$

(b) Correlation dimension fit

Figure 3.38 – Effect of periodic boundaries on the correlation dimension

In summary, there are many ways that one can calculate the fractal dimension. Since this analysis of the fractal nature of class IV neurons does not aim to be exhaustive, the correlation dimension d_c calculated with periodic boundaries will be used for subsequent comparisons of the fractal dimension.

Finally, the fractal dimension of class IV neurons is analyzed over their development. As shown in fig. 3.39, it remains relatively constant at a value of ~ 1.8 during the larval development. However, at 24 hr AEL, the fractal dimension is slightly smaller at a value of ~ 1.7 and also shows more variability. This indicates that the shape of the neuron in the early developmental stage has not reached maturation and is still under construction. Moreover, the fact that the fractal dimension reaches a constant early in its development indicates that the class IV dendritic tree is quick to fill its receptive field. This is also consistent with the hypothesis that the shape of the tree is optimized to fill its area aiming to detect the mechanical stimuli that it receives.

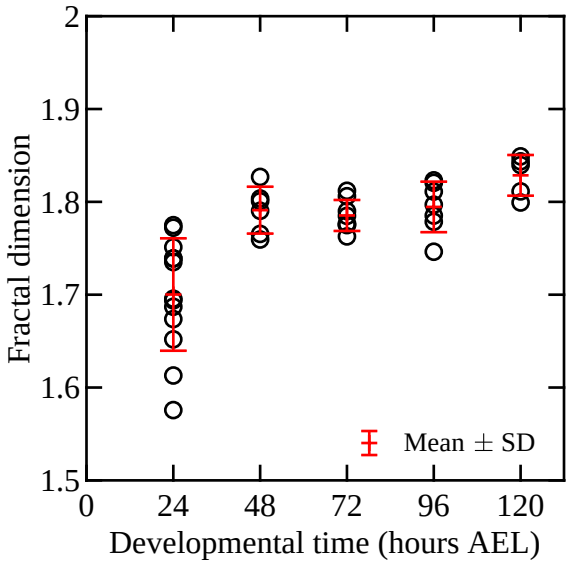

Figure 3.39 – Fractal dimension of class IV neurons over development

3.3.6 Meshsize

Complementary to the fractal dimension, the size of the empty space between the dendrites is also quantified. Since the tree is an open shape, the size of the empty space is not mathematically well-defined. However, one can use approximate measures that capture this intuition. The lacunarity of a given shape is one example that assesses the size of empty space or holes in a given shape [47]. For this analysis, we propose a novel metric that is inspired by the function of the class IV neuron: the hitting probability.

Recall that Class IV neurons are nociceptors that detect mechanical stimuli. These mechanical stimuli come in the form of a puncture of a given size that jabs the class IV dendritic tree and stimulates its sensorial receptors. Depending on their ability to fill space, class IV neurons are able to detect punctures of various sizes. Motivated by this sensory function, we define the hitting probability $h(r)$ of a shape as the probability that a box of size r randomly collides with the given shape. As r

increases, the hitting probability increases and captures the distribution of the holes' size within the shape.

To calculate the hitting probability, a square lattice of box centers $\vec{c}_i, i = 1, \ldots, M$ is laid out on a fine grid. The lattice points correspond to the random positions of the box center. As an alternative, one could also define the box centers from a set of uniformly random variables that extend over the range of the tree in each dimension. Once the box centers are defined, the fraction of boxes of a given size r that collides with any points $\vec{x}_j$ on the discretized shape $\mathcal{X}$ is calculated. One way to perform this calculation is to count the fraction of boxes of size r that hits the shape:

$$h(r) = \frac{1}{N} \sum_i \mathbf{1}_{\mathcal{X}}(r, \vec{c}_i) \tag{3.86}$$

$$\mathbf{1}_{\mathcal{X}}(r, \vec{c}_i) = \left[\frac{1}{M} \sum_{j=1}^{M} \Theta\left(\frac{r}{2} - |\vec{x}_j - \vec{c}_i| \right) \right] \tag{3.87}$$

where $\Theta(x)$ is the Heavyside step function and $\mathbf{1}_{\mathcal{X}}(r, \vec{c}_i)$ is an indicator function that equals one when the i^{th} box centered at $\vec{c}_i$ is within a distance r of at least one point on the shape $\mathcal{X}$. In other words, $h(r)$ counts the fraction of boxes that are within a distance r of the shape. In practice, this method works for calculating the hitting probability. However, due to the fact that collision tests must be performed for each box at each radius, one can only evaluate $h(r)$ for a small set of radii for computational efficiency. To circumvent this limitation, we approach the problem with a different angle. Instead of asking what fraction of boxes of a given size r hit the shape, we seek the smallest box size d_i that hits the shape at every given center $\vec{c}_i$. This can be computed using the Chebyshev distance $D_c(\vec{x}, \vec{y})$ between $\vec{c}_i$ and the points on the shape $\vec{x}_j$:

$$d_i = 2 \min_j D_c(\vec{c}_i, \vec{x}_j) \tag{3.88}$$

$$D_c(\vec{x}, \vec{y}) = \max_k |\vec{x}^{(k)} - \vec{y}^{(k)}| \tag{3.89}$$

The appearance of the Chebyshev distance arises from the fact that boxes are used in the hitting test. If one used circles instead of boxes, one would need to use the normal euclidean distance in the above formula. Once the smallest hitting sizes d_i are computed, one instantly knows that all boxes of size $r \geq d_i$ centered at $\vec{c}_i$ will hit the shape. In other words, the fraction of boxes of size r that hit the shape corresponds to the fraction of d_i that are less than or equal to r. This fraction is no less than the empirical cumulative distribution of d_i. This leads to the following definition of $h(r)$:

$$h(r) = \frac{1}{M} \sum_i \Theta(r - d_i) \tag{3.90}$$

This definition of $h(r)$ captures the same information as in the previous method, but the use of the empirical cumulative distribution allows us to evaluate $h(r)$ at many more points for the same computational cost. In practice, a square lattice of 500×500 box centers is laid out to span the range $[-R_g, R_g]$ in each dimension where R_g in the radius of gyration. R_g is used as the limits of the square lattice to avoid segmentation effects at the boundary. Once d_i is calculated at each box center, the value of the hitting probability is estimated at $500^2 = 250\,000$ points, which is practically continuous over the dynamical range of $h(r)$. An example of the hitting probability calculated with this technique is shown in fig. 3.40b for a class IV neuron at 96 hr AEL.

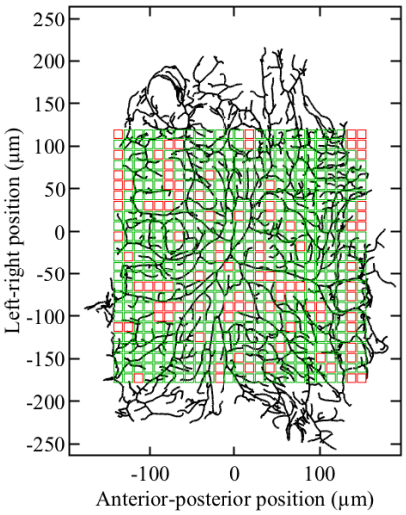

(a) 20 × 20 square lattice of boxes with size $10\,\mu m$

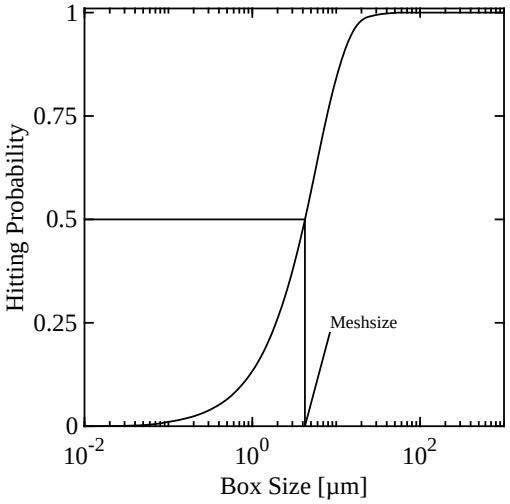

(b) Hitting probability

Figure 3.40 – Hitting probability of a class IV neuron at 96 hr AEL

Using the hitting probability curve $h(r)$, the meshsize r_h is defined as the box size that attains a hitting probability of 50%. The threshold of 50% is chosen as it corresponds to the inflection point of the hitting probability by definition. Therefore, the meshsize captures the critical point at which the hits change from mostly missing to mostly hitting. As such, the meshsize provides a definition of the size of the holes in the shape.

Again, the temporal evolution of the meshsize is quantified over development using the set of class IV neuron skeletons (see fig. 3.41a). The meshsize increases almost 2-fold from 24 to 72 hr AEL indicating that the class IV dendritic tree becomes sparser over the first instar of the development. From 72 to 120 hr AEL, the meshsize decreases in a manner similar to the evolution of the mean branch length. Indeed, when the meshsize is normalized by the mean branch length, $\frac{r_h}{\langle L \rangle}$, this quantity is conserved over the development of the dendritic tree as shown in fig. 3.41b. This conservation indicates that the ability of the tree to fill space is contingent on the size and quantity of its branches. As the mean branch length decreases, the size of

the holes in the tree also decreases. This is a consequence of the fact that smaller branches more easily fill space compared to longer branches due to the persistence length of the branches. Indeed, for a fixed amount of dendritic length, a large number of small branches have more degrees of freedom than a low number of longer branches.

Given the initial increase of the meshsize and the scaling behavior between the meshsize and the mean branch length, these observations indicate that there is a mechanism that increases the length of the branches in the early stages. This could be the result of a branch pruning process whereby branches disappear, which increases the size of the holes in the dendritic tree shape. Alternatively, there could also be a stretching of the tree branches, which would increase the mean branch length. However, this is in contradiction with our measurement of the branch extension, which shows that inner branches do not significantly stretch in comparison with the body segment (see fig. 3.28).

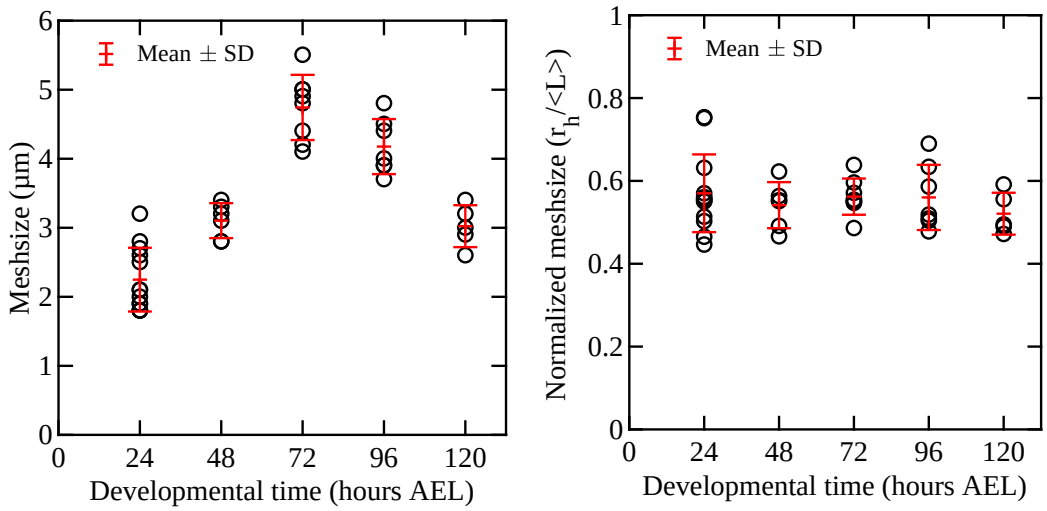

(a) Meshsize r_h

(b) Normalized meshsize $\frac{r_h}{\langle L \rangle}$

Figure 3.41 – Meshsize of class IV neurons over development

3.3.7 Interbranch distance

Recall that the class IV dendritic tree aims to fill its receptive field with dendrites to perform its sensory function. As explained in the previous section, the meshsize is a morphometric that quantifies the average size of the holes in the shape formed by the tree. In this section, the distribution of distances between branches is analyzed as an attempt to define a finer metric that quantifies the size of holes and the distribution of empty space.

Let us define the interbranch distance $\ell_I(\beta)$ as the distance between two branches along a branching angle β. More specifically, consider a position $\vec{x}$ on a branch where the tangential angle at this position is given by ϕ. From this position, a line is traced at an angle $\phi+\beta$ until it collides with another branch. The length of this line corresponds to the collision distance at position $\vec{x}$ and angle β, denoted as $\ell_I(\beta,\vec{x})$. Repeating this process over all positions, the interbranch distance is then given by the positional average of the collision distances:

$$\ell_I(\beta) = \langle \ell_I(\beta,\vec{x}) \rangle_{\vec{x}} \tag{3.91}$$

The angle β is understood as the angle at which a nascent branch tip may grow relative to the orientation of the branch ϕ. After averaging over all positions $\vec{x}$ and branching angles β, $\langle \ell_I(\beta) \rangle_\beta$ captures a notion similar to a mean free path for one-dimensional objects. Using this intuition, one could say that $\ell_I(\beta)$ corresponds to the average distance at which a branch tip will contact another branch when branching at an angle β relative to its parent branch orientation.

Given this definition, skeletons of class IV neurons are used to calculate the interbranch distance by scanning for collisions across the full range of branching angles. The resulting interbranch distance $\ell_I(\beta)$ is shown in fig. 3.42. In practice, since the shape is not closed, there will be cases in which no collisions are detected.

For example, this can happen at the boundary when the branching angle is outwardly directed. In these cases, $\ell_I(\beta, \vec{x})$ is undefined since no collisions happen. These cases are therefore omitted in the averages shown in fig. 3.42.

First, one notices that the interbranch distance is symmetric around $\beta = 0$. This indicates that branches are approximately parallel with their neighbors. Indeed, if the collision distance at some position $\vec{x}$ and branching angle β is given by $\ell_I(\beta, \vec{x})$ due to a collision with a neighboring branch node positioned at $\vec{y}$, the same collision distance is expected when scanning from position $\vec{y}$ at the reflected angle $-\beta$, i.e. $\ell_I(\beta, \vec{x}) = \ell_I(-\beta, \vec{y})$. Then, when all positions are averaged, the same distance is counted for both β and $-\beta$. Second, one also notices that the interbranch distance increases from 24 to 72 hr AEL, and decreases from 72 to 120 hrs. This trend is also observed when averaging over all branching angles as shown in fig. 3.43a. This feature is also captured by the meshsize, which shows an increase at the early stage and a slight decrease at the later stages. Third, one also notices that the interbranch distance decays to 0 as $|\beta| \to 180°$, but remains non-zero as $\beta \to 0$. This is an effect caused by the branch tips, which have non-zero collision distances along the orientation of the branch ($\beta = 0$). Finally, note that the interbranch distance peaks at a given branching angle, whose average varies between $60°$ and $80°$ over development as shown in fig. 3.43b. The fact that the interbranch distance is longest in a certain direction relative to the branch indicates that there are favorable directions at which a branch can grow. However, one could argue that the branching angle range $|\beta| \in [50, 130]$ has similar interbranch distances, which indicates that branching perpendicularly offers sufficient freedom for growth.

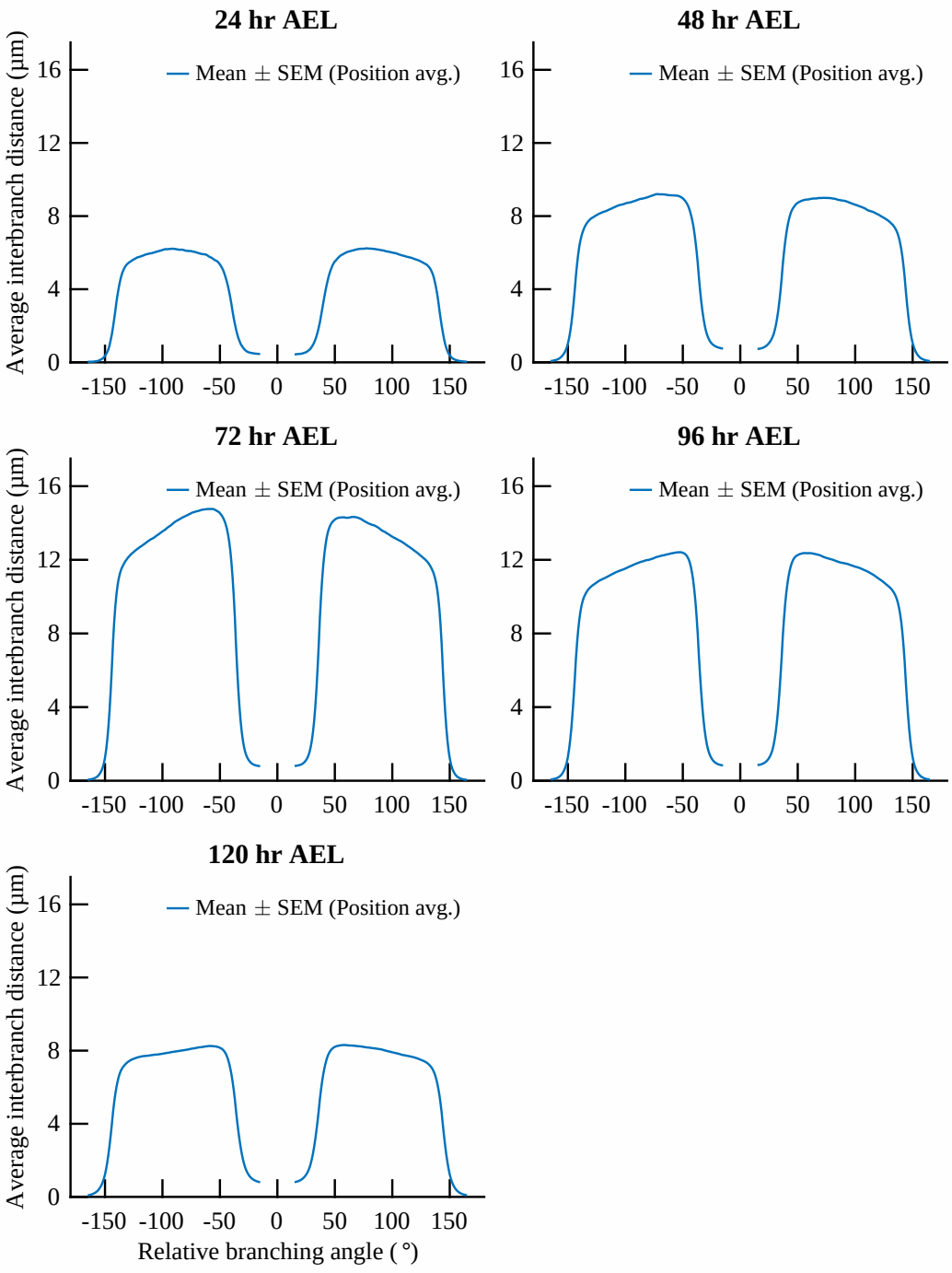

Figure 3.42 – Interbranch distances over development

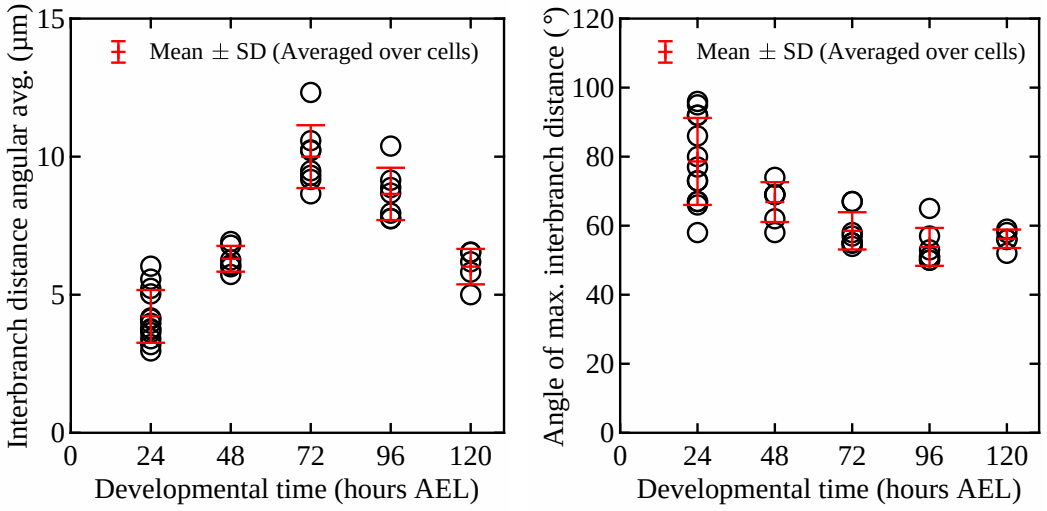

(a) Average interbranch distance **(b)** Angle of maximal interbranch distance

Figure 3.43 – Average interbranch distance over development

In summary, the interbranch distance indicates that the tree becomes sparser from 24 to 72 hr AEL, but grows denser from 72 to 120 hr AEL, similar to the behavior of the the meshsize. In addition, the angular dependence of $\ell_I(\beta)$ indicates that branching perpendicularly from an existing branch provides the least amount of obstruction for growth.

3.3.8 Dendrite, branch point and branch tip densities

Finally, to analyze the spatial properties of the dendritic tree, we analyze the densities of 3 types of species: dendrites, branch points and branch tips. Since the dendrites are one-dimensional objects that are embedded in two-dimensional space, the dendrites density is a line density with units of μm^{-1}. On the other hand, the branch point and branch tip density are point densities with units of μm^{-2}. First, the two-dimensional species densities is averaged over all cells of the same developmental stage as shown in fig. 3.44. As depicted, the dendrites density is uniform across the area covered by the neurons from 24 to 72 hr AEL. However,

at 96 hr AEL, there is a slight over-density near the periphery of the neuron in a band of $\sim 50\mu m$. The branch points and branch tips density show a similar behavior where the over-density is even apparent at 72 hr AEL. In addition, the number of branch points and branch tips are approximately equal as found in fig. 3.10.

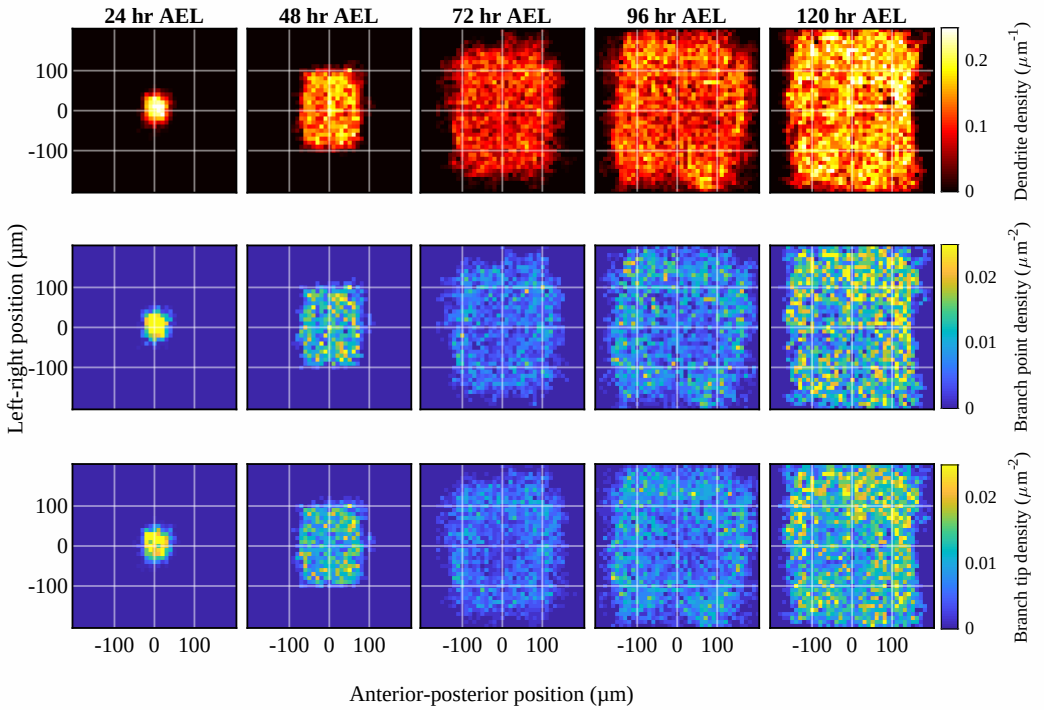

Figure 3.44 – Two-dimensional species density over development
The species density is evaluated in $10 \times 10\,\mu m^2$ bins and averaged over all cells of the same developmental stage. The dendrites mass is measured as a line density while the branch points and branch tips are point densities.

In addition, the species density is quantified as a function of the radial distance from the soma (see fig. 3.45). To calculate the radial density at a given radius R, the amount of species contained in an annulus with dimension $r \in [R - W/2, R + W/2], \theta \in [0, 2\pi]$ ($W = 10\,\mu m$ is the radial bin width) is divided by the area of the annulus. The temporal evolution of all species density indicates that the dendritic tree expands at a steady rate as evidenced by the propagation of the density front over periods of 24 hrs. Moreover, the steady-state densities in the bulk of the tree

decays from 24 to 72 hr AEL, stabilizes from 72 to 96 hr AEL, and increases again at 120 hr AEL.

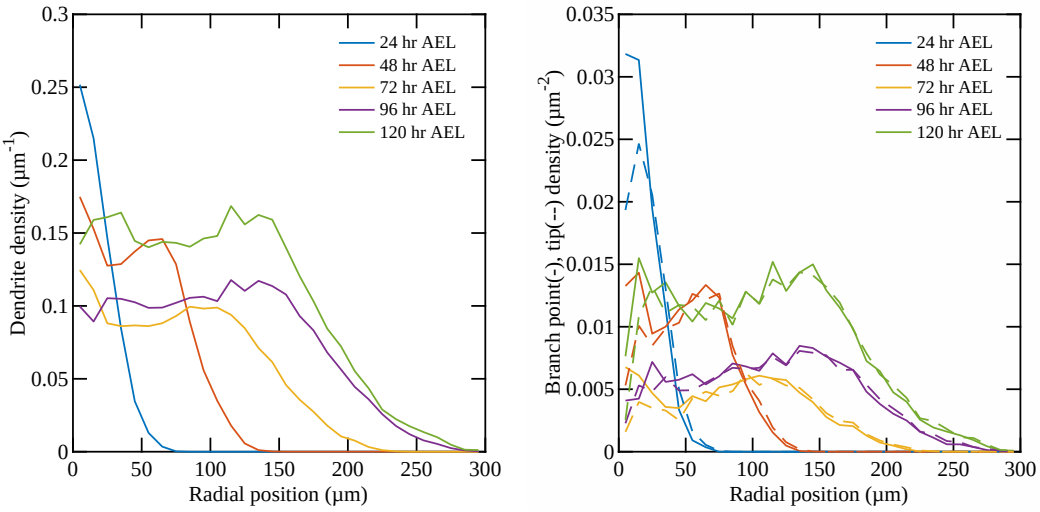

Figure 3.45 – Radial species density over development
The species density is calculated in radial bins of $10\,\mu m$. Each color represents the average over all cells within the same developmental stage.

Since the real neurons are not spherically symmetric, but possess a non-unit aspect-ratio, the projected density is calculated along each axis of its rectangular geometry. More precisely, the two-dimensional species density is mean-projected along the left-right (anterior-posterior) axis to calculate the density along the anterior-posterior (left-right) axis. When performing the projection along a given dimension, only non-empty bins are considered to avoid under-estimating the projected density. The resulting projected densities are shown in fig. 3.46 after averaging over all cells. Similar to what is shown by the radial densities, the projected species density along the AP and LR axis both demonstrate that the species density is approximately constant near the origin and decays to zero near the boundary of the cell. Moreover, the temporal behavior of the projected density is similar to the behavior of the radial density.

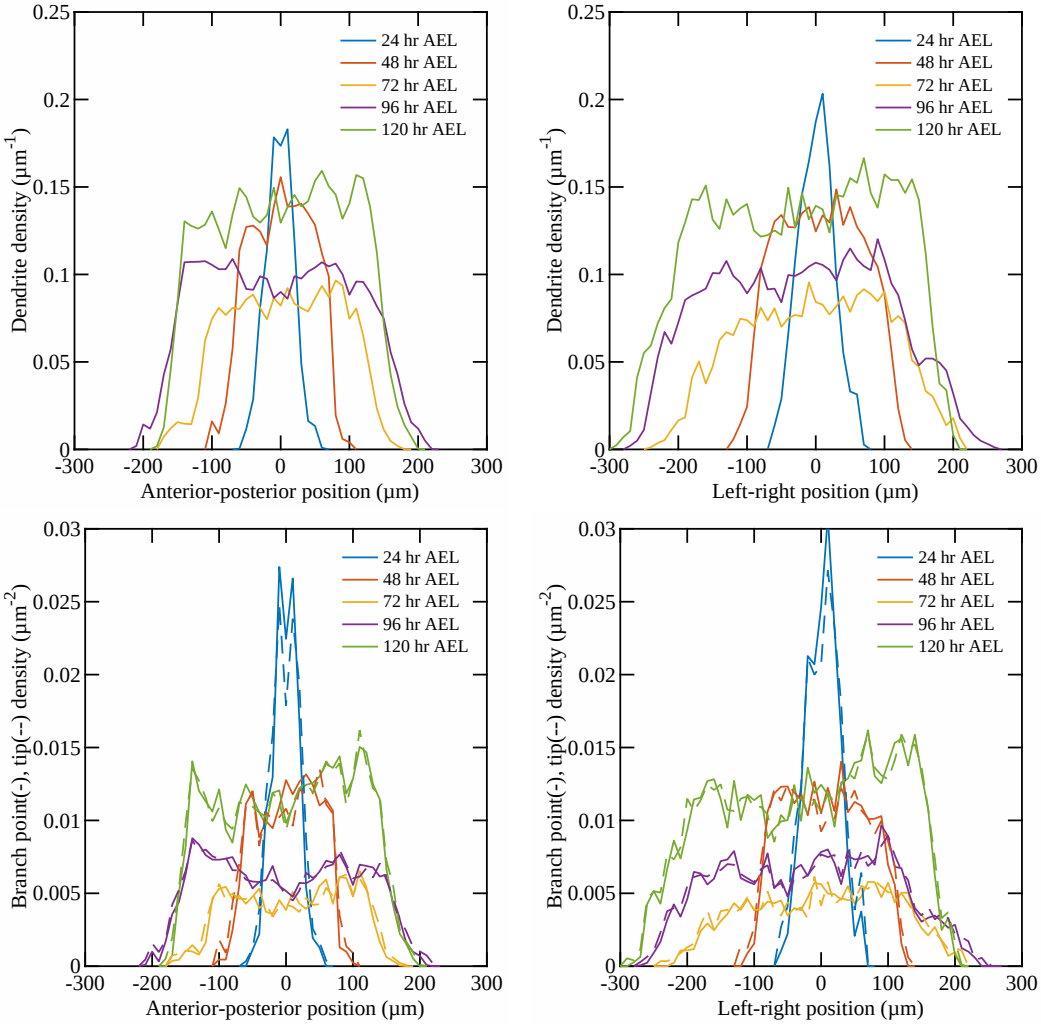

Figure 3.46 – Axial species density along the AP and LR axis over development
The species density is evaluated in $10 \times 10 \mu m^2$ square bins and averaged over the LR (AP) axis when calculating the AP (LR) axis density. Each color represents the average over all cells of the same developmental stage.

First, the decay length of the dendrites density profiles is quantified. Since the neuron has a rectangular geometry, the non-spherical geometry smears the radial density at the boundary of the shape in comparison with the axial densities. Instead, the decay length is evaluated by fitting the dendrites axial density on each side of the cell along each dimension. However, since the density decays on the scale of $\sim 10 \mu m$, the binned density do not provide enough sampled points to fit. To resolve this issue, the dendrites density is upsampled using a Gaussian kernel with

a bandwidth of $2.5\,\mu m$. This particular bandwidth is selected in order to smooth the profile at the boundaries while keeping the specific features of the decay. Using the kernel density, the bulk density ρ_{bulk} is calculated as the average density of the sampled points in the inner 50% of the profile. Then, each side of the kernel density profile is fitted independently with an exponential function from $\frac{\rho_{\text{bulk}}}{2}$ to 0 (see fig. 3.47a). The resulting decay lengths of the exponential fit are shown in fig. 3.47b over development. As shown, the density decays rapidly at the boundary at 24 and 48 hr AEL. At 72 hr AEL, the decay is more smooth over a length that is almost twice as large as the early-stage decay length. However, from 72 to 120 hr AEL, the density decay sharpens and the decay length decreases to a value that is similar to the early-stage value.

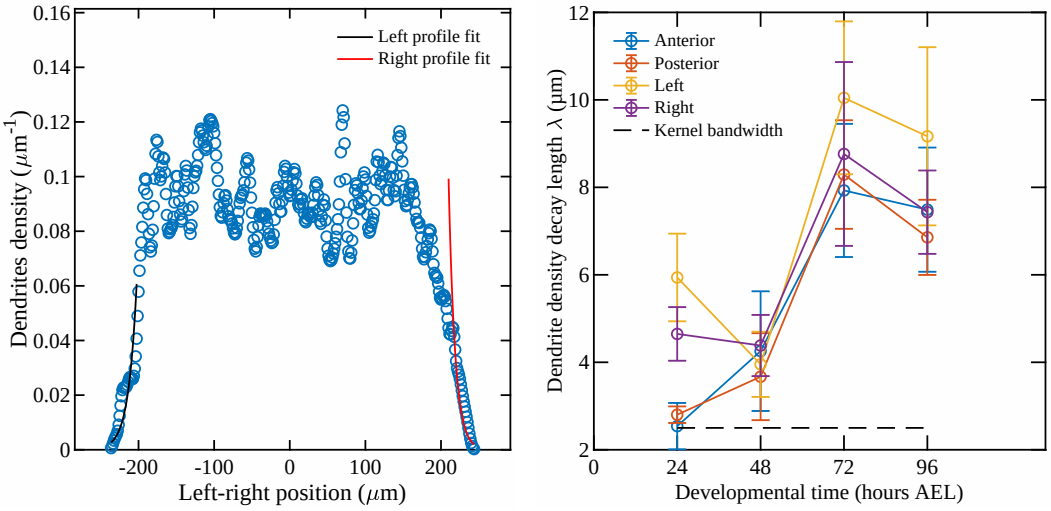

(a) Example of dendrite LR density at 96 hr AEL **(b)** Decay length of dendrite density profile

Figure 3.47 – Decay length of dendrite axial density over development

Finally, the species density is averaged over the area of the neuron defined by the uniform size (see section 3.3.1). As shown in fig. 3.48, the density initially decreases until 72 hr AEL, but increases subsequently until 120 hr AEL.

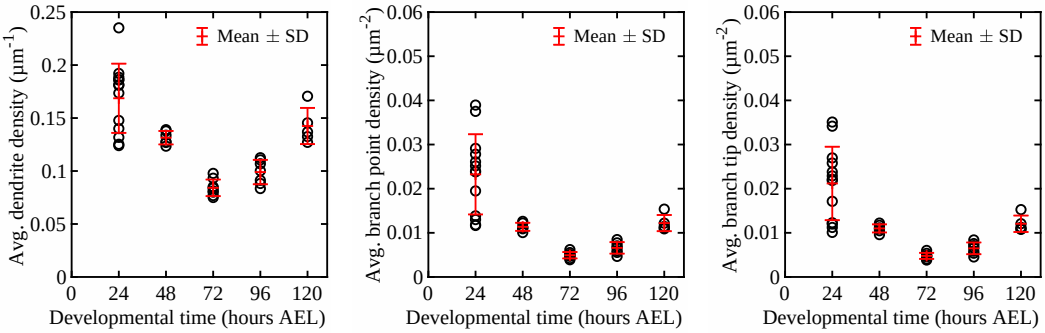

Figure 3.48 – Average species density inside the uniform boundary over development The average dendrites density is evaluated as the total branch length divided by the area of the uniform boundary. The branch points and branch tips density are calculated by counting the total number of the respective species and dividing by the area of the uniform boundary.

In summary, the density of dendrites, branch points and branch tips decreases as the dendritic tree expands from 24 to 72 hr AEL, but increases from 72 to 120 hr AEL.

3.4 Conclusions

- We characterize the tip growth dynamics using movies of the class IV neuron development and find that it is well-approximated by a 3-state Markov process.
- We quantify the rate of branching and find that it is an extensive and spatially uniform property of the dendritic tree.
- We assess the change in the morphology of the tree using established and novel metrics and find that the tree expands throughout development. Furthermore, the dendrites density decreases at the early stage, reaches a steady-state during the second instar of development and increases again at the later stages.

4 Mean-Field Models of Dendritic Morphogenesis

The dendrites of Class IV neurons in *Drosophila* grow through various dynamical processes. In this chapter, we present several mean-field approaches to model the dendritic tree growth as a drift-diffusion-reaction dynamical system comprising 5 types of species: dendrites, branch points, shrinking, paused and growing branch tips. We derive expressions for the tree expansion velocity as a function of the microscopic parameters and make predictions on their value using our measurements of the morphometrics.

The proposal and design of the mean-field models were done by Yuhai Tu. Predictions and mathematical derivations were performed in collaboration with Yuhai Tu and Qiwei Yu.

4.1 5-species model

The 5-species mean-field model consists of a set of dynamical equations that governs the temporal evolution of 5 species: dendrites (U'), branch points (B), paused (P), growing (G) and shrinking tips (S). Each species is described by a probability density of point particles that depends on both space and time. Moreover, the species are categorized into two groups: immobile and mobile:

- $U'(\vec{x},t)$: Immobile dendrites that are not dynamic
- $B(\vec{x},t)$: Immobile branch points that are located at intersection of branches
- $P(\vec{x},t)$: Immobile branch tips that are neither growing nor shrinking
- $G(\vec{x},t)$: Mobile growing branch tips
- $S(\vec{x},t)$: Mobile retracting branch tips
- $T(\vec{x},t) = U' + B + S + P + G$: Total density of all species
- $R(\vec{x},t) = S + P + G$: Total density of branch tips

In this model, the various morphogenesis events are modeled as reactions among the species. In addition to the reaction terms, the motion of the mobile species is modeled with drift and diffusion terms. In the next sections, we describe the precise form of the dynamical terms that model the morphogenetic processes.

4.1.1 Reaction terms

Dendrite growth

During morphogenesis, dendritic tips elongate leading to an increase in the total mass of dendrites. In the mean-field approach, this phenomenon is modeled as the growth of immobile dendrite particles U' promoted by the presence of mobile growing branch tips G:

$$G \xrightarrow{k_G} G + U'$$
$$\Rightarrow \frac{\partial U'}{\partial t} = \ldots + k_G G(1 - \lambda_{GT}^2 T) \tag{4.1}$$

where λ_{GT} is an interaction length scale that controls the effective distance at which growing tips collide with other species and the factor of $1-\lambda_{GT}^2 T$ represents the probability that a growing tip encounters empty space. This multiplicative factor models the condition that sufficient space is necessary for the growth of dendrites. $1-\lambda_{GT}^2 T$ is in fact an approximation of the exact term: $1-\int_{S(\vec{x})} T(\vec{y})d^2\vec{y}$ where $S(\vec{x})$ is a small surface, centered at the tip position $\vec{x}$. For simplicity, we define $S(\vec{x})$ as a square of size λ_{GT} and assume that λ_{GT} is sufficiently small such that $T(\vec{y})$ is approximately constant over the surface:

$$1-\int_{S(\vec{x})} T(\vec{y})d^2\vec{y} \approx 1-\lambda_{GT}^2 T(\vec{x}) \quad (\lambda_{GT} \ll 1) \tag{4.2}$$

Therefore, in regions where the probability density of finding any species is high (close to ~ 1), $1-\lambda_{GT}^2 T$ approaches 0 and inhibits the growth of new dendrites. Finally, k_G is the rate constant at which growing tips produce dendrites. This parameter is determined by the average speed of growing tips v_G and the particle size a: $k_G = \frac{v_G}{a}$.

Dendrite shrinkage

In addition to elongation, dendritic branches also shrink whereby their dendritic tip retracts towards their original branch point leading to a reduction in the total mass of dendrites. Similar to growth, this phenomenon is modeled as the removal of immobile dendrite particles U' promoted by the presence of mobile retracting branch tips S:

$$\begin{aligned} & S + U' \xrightarrow{k_S} S \\ \Rightarrow & \frac{\partial U'}{\partial t} = \ldots - k_S S \end{aligned} \tag{4.3}$$

In other words, shrinking tips S act as sinks of dendrite particles. The rate at which dendrites are depleted from the presence of shrinking tips is determined by the rate constant k_S, which is a function of the average speed of shrinking tips v_S and the particle size a: $k_S = \frac{v_S}{a}$.

Tip dynamics

During morphogenesis, branch tips exhibit a dynamical behavior: they grow, shrink or remain immobile for a certain amount of time. Given our previous observations of the tip dynamics, we model the branch tip dynamics as a Markov chain with 3 dynamical states: shrinking, paused, growing. The transitions between each of these states are determined by a total of 6 rate constants:

$$S \underset{k_{PS}}{\overset{k_{SP}}{\rightleftarrows}} P, \quad P \underset{k_{GP}}{\overset{k_{PG}}{\rightleftarrows}} G, \quad G \underset{k_{SG}}{\overset{k_{GS}}{\rightleftarrows}} S$$

$$\Rightarrow \frac{\partial S}{\partial t} = \ldots - (k_{SP} + k_{SG})S + k_{PS}P + k_{GS}G \tag{4.4}$$

$$\Rightarrow \frac{\partial P}{\partial t} = \ldots - (k_{PS} + k_{PG})P + k_{SP}S + k_{GP}G \tag{4.5}$$

$$\Rightarrow \frac{\partial G}{\partial t} = \ldots - (k_{GS} + k_{GP})G + k_{SG}S + k_{PG}P \tag{4.6}$$

where $k_{ij}, i, j \in \{S, P, G\}$ correspond to the transition rate constants.

Branching

Concurrent to tip dynamics, new dendritic tips are born out of existing branches. We call this process *branching*. Guided by our investigation of the branching process (see section 3.2), we assume that the probability of branching is proportional to the amount of dendrites, which implies that regions with a high density of dendrites are more likely to spawn new branches. Therefore, the branching process is modeled as

the creation of a branch point B and a growing tip G promoted by the presence of immobile dendrite particles U':

$$
\begin{aligned}
& U' \xrightarrow{k'_b} B + G \\
\Rightarrow & \frac{\partial U'}{\partial t} = \ldots - k'_b U' (1 - \lambda^2_{BU'} B) && (4.7) \\
\Rightarrow & \frac{\partial B}{\partial t} = \ldots + k'_b U' (1 - \lambda^2_{BU'} B) && (4.8) \\
\Rightarrow & \frac{\partial G}{\partial t} = \ldots + k'_b U' (1 - \lambda^2_{BU'} B) && (4.9)
\end{aligned}
$$

where k'_b is the branching rate. Here, k'_b is a rate constant with units of inverse time ($[k'_b] = \frac{1}{\text{Time}}$) whereas the measured branching rate has units of inverse time and length ($[k_b] = \frac{1}{\text{Time} \cdot \text{Length}}$). One can relate these two quantities using the particle size a: $k'_b = k_b a$. The multiplicative factor $(1 - \lambda^2_{BU'} B)$ models branching inhibition mechanisms similar to the $1 - \lambda^2_{GT} T$ factor of the growth term (see above) where the presence of branch points inhibits the local branching rate. $\lambda_{BU'}$ is a length scale that controls the distance at which B particles effectively interact with dendrites. In the simplest scenario, one can set $\lambda_{BU'} = a$ indicating that branch points are point-like and cannot stack with one another. Alternatively, one could set $\lambda_{BU'}$ to an experimentally determined length scale that models the inhibition of new branch tips near existing branch points.

Contact inhibition

As a pruning mechanism, the Down-Syndrome Cell Adhesion Molecule (DSCAM) in class IV neurons mediates contact inhibition whereby a growing branch tip starts retracting upon contact with another branch. In the mean-field approach, this

process is modeled as the conversion of growing tips G to shrinking tips S upon collision with all species:

$$
\begin{aligned}
&G+T \rightarrow S+T \\
&\quad \Rightarrow \frac{\partial G}{\partial t} = \ldots - k_G \lambda_{GT}^2 GT && (4.10) \\
&\quad \Rightarrow \frac{\partial S}{\partial t} = \ldots + k_G \lambda_{GT}^2 GT && (4.11)
\end{aligned}
$$

where λ_{GT} is the same interaction length scale that was introduced in the growth term. Also, k_G is the same constant that appears in the dendrite growth term since this phenomenon is mediated by the contact of growing tips G.

Branch annihilation

Finally, when branch tips retract back to their original branch point, the branch tip and branch point disappear. In the mean-field model, this event is modeled as a collision between a shrinking tip S and a branch point B that annihilate them and create an immobile dendrite:

$$
\begin{aligned}
&S+B \rightarrow U' \\
&\quad \Rightarrow \frac{\partial U'}{\partial t} = \ldots + k_S \lambda_B^2 SB && (4.12) \\
&\quad \Rightarrow \frac{\partial B}{\partial t} = \ldots - k_S \lambda_B^2 SB && (4.13) \\
&\quad \Rightarrow \frac{\partial S}{\partial t} = \ldots - k_S \lambda_B^2 SB && (4.14)
\end{aligned}
$$

where λ_B is the interaction length scale between branch points and branch tips. Note that k_S is the same constant that is used for the dendrite shrinkage term since this phenomenon is mediated by the contact of shrinking tips S.

4.1.2 Transport terms

To model the motion of the mobile tips, drift-diffusion terms are used for the growing and shrinking tips. We consider two cases where the dynamics occur in one or two spatial dimensions. In 1D, these terms are given by:

$$\mathcal{L}_{+,\mathrm{1D}}(G(x)) = \left(-v_+ \frac{\partial}{\partial x} + D_+ \frac{\partial^2}{\partial x^2}\right) G(x) \tag{4.15}$$

$$\mathcal{L}_{-,\mathrm{1D}}(S(x)) = \left(v_- \frac{\partial}{\partial x} + D_- \frac{\partial^2}{\partial x^2}\right) S(x) \tag{4.16}$$

where v_+, v_- are the drift velocities of the growing and shrinking tips and D_+, D_- are the associated diffusion constants.

In 2D, the transport terms are:

$$\mathcal{L}_{+,\mathrm{2D}}(G(r,\theta)) = \left(-v_{+,r} \frac{\partial}{\partial r} + D_{+,r} \frac{\partial^2}{\partial r^2} + \frac{D_{+,\theta}}{r^2} \frac{\partial^2}{\partial \theta^2}\right) G(r,\theta) \tag{4.17}$$

$$\mathcal{L}_{-,\mathrm{2D}}(S(r,\theta)) = \left(v_{-,r} \frac{\partial}{\partial r} + D_{-,r} \frac{\partial^2}{\partial r^2} + \frac{D_{-,\theta}}{r^2} \frac{\partial^2}{\partial \theta^2}\right) S(r,\theta) \tag{4.18}$$

where $D_{+,r}, D_{-,r}$ and $D_{+,\theta}, D_{-,\theta}$ correspond to the radial and angular diffusion constants of the growing and shrinking tips, respectively. In addition, $v_{+,r}$ and $v_{-,r}$ correspond to the radial drift velocity of the growing and shrinking tips, respectively. Note that $v_{+,r}, v_{-,r}$ are different than the tip speeds v_G, v_S as $v_{+,r}, v_{-,r}$ accounts for the two-dimensional motion of the tips while v_G, v_S describes the one-dimensional growth dynamics of the branches. Also, notice that the $r^{-1}\partial_r$ term of the diffusion operator is absent in the transport terms as will be explained later in section 4.4.

4.1.3 Summary

In summary, the reaction processes of morphogenesis are modeled as a 5-dimensional dynamical system:

$$\left.\frac{\partial U'}{\partial t}\right|_{\text{Reaction}} = k_G G(1-\lambda_{GT}^2 T) - k_S S - k_b' U'(1-\lambda_{BU'}^2 B) + k_S \lambda_B^2 SB \tag{4.19}$$

$$\left.\frac{\partial B}{\partial t}\right|_{\text{Reaction}} = k_b' U'(1-\lambda_{BU'}^2 B) - k_S \lambda_B^2 SB \tag{4.20}$$

$$\left.\frac{\partial P}{\partial t}\right|_{\text{Reaction}} = -(k_{PS}+k_{PG})P + k_{SP} S + k_{GP} G \tag{4.21}$$

$$\left.\frac{\partial G}{\partial t}\right|_{\text{Reaction}} = -(k_{GS}+k_{GP})G + k_{SG} S + k_{PG} P - k_G \lambda_{CI}^2 GT + k_b' U'(1-\lambda_{BU'}^2 B) \tag{4.22}$$

$$\left.\frac{\partial S}{\partial t}\right|_{\text{Reaction}} = -(k_{SP}+k_{SG})S + k_{PS} P + k_{GS} G + k_G \lambda_{CI}^2 GT - k_S \lambda_B^2 SB \tag{4.23}$$

which is also summarized diagrammatically in fig. 4.1.

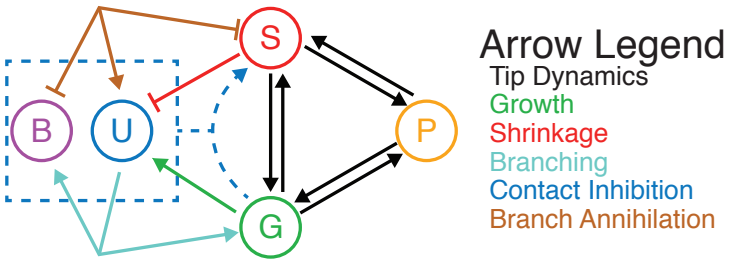

Figure 4.1 – Reaction dynamics of the 5-species mean-field model
Arrowheads indicate positive contributions to the respective species density while flat ends indicate negative contributions.

The reaction equations possess a conservation law that arises from the fact that branching events create an equal amount of branch points (B) and branch tips (G, S, P). This can be readily seen by summing eqs. (4.20) to (4.23):

$$\left.\frac{\partial}{\partial t}(G+S+P-B)\right|_{\text{Reaction}} = 0 \tag{4.24}$$

In other words, $G+S+P-B$ is a conserved quantity that is determined by the initial conditions:

$$G+S+P-B=K(\vec{x}) \tag{4.25}$$

where $K(\vec{x})$ the initial difference between the density of branch tips and branch points. As the initial density of species is highly-localized, we assume that $K(\vec{x})\approx 0$ over the spatial range of the tree.

Finally, with the addition of the growing and shrinking tip transport terms, the complete dynamical system of the 5-species model is given by:

$$\frac{\partial U'}{\partial t}=k_G G(1-\lambda_{GT}^2 T)-k_S S-k_b' U'(1-\lambda_{BU'}^2 B)+k_S\lambda_B^2 SB \tag{4.26}$$

$$\frac{\partial B}{\partial t}=k_b' U'(1-\lambda_{BU'}^2 B)-k_S\lambda_B^2 SB \tag{4.27}$$

$$\frac{\partial P}{\partial t}=-(k_{PS}+k_{PG})P+k_{SP}S+k_{GP}G \tag{4.28}$$

$$\frac{\partial G}{\partial t}=\mathcal{L}_+(G)-(k_{GS}+k_{GP})G+k_{SG}S+k_{PG}P-k_G\lambda_{CI}^2 GT+k_b' U'(1-\lambda_{BU'}^2 B) \tag{4.29}$$

$$\frac{\partial S}{\partial t}=\mathcal{L}_-(S)-(k_{SP}+k_{SG})S+k_{PS}P+k_{GS}G+k_G\lambda_{CI}^2 GT-k_S\lambda_B^2 SB \tag{4.30}$$

4.2 3-species model

Although the 5-species model is heuristically well grounded, it is hard to intuit due to the complexity of the equations. In addition, the treatment of the branch tip states as three independent quantities is a fundamental problem. Since S,P,G represent the internal dynamical state of the tip and not physical quantities, their probability densities are not independent from one another, but are bound by the density of branch tips. This property is not captured in the 5-species model since the growing and shrinking tips move independently with their own transport terms. In

reality, the density of dendritic tips $R = S + P + G$ is the true physical quantity that is independent from the branch points B and dendrites U'.

As we found previously in our analysis of the tip dynamics (see section 3.1.2), the tip growth process is on the minute time scale, while the growth of the tree occurs over the course of several days. Since the model aims to predict the long-time growth behavior of the tree, we use the separation of these two time scales to argue that the tip dynamics is at equilibrium over the time scale of the development. Therefore, the dynamics between S, P and G is treated as changing the effective motion of the dendritic tips. Since the tip dynamics is modeled as a Markov process, the steady state, or stationary state, of the Markov chain is easily found by solving the following set of linear differential equations:

$$0 = -(k_{SP} + k_{SG})P_S(t) + k_{PS}P_P(t) + k_{GS}P_G(t) \tag{4.31}$$

$$0 = -(k_{PS} + k_{PG})P_P(t) + k_{SP}P_S(t) + k_{GP}P_G(t) \tag{4.32}$$

$$0 = -(k_{GS} + k_{GP})P_G(t) + k_{SG}P_S(t) + k_{PG}P_P(t) \tag{4.33}$$

where $P_S(t), P_P(t), P_G(t)$ represent the probabilities of finding a tip in the respective S, P or G state at any given time t. Exact expressions of the steady state was given in our analysis of the tip dynamics (see section 3.1.2). For simplicity, let us denote the steady state probabilities as $(P_{S,ss}, P_{P,ss}, P_{G,ss}) = (f_S, f_P, f_G)$ where f_i depend on the rate constants k_{ij}. Assuming that the tip dynamics is at steady state, we approximate the densities of the internal state variables S, P, G as proportions of the tips density R:

$$S \to f_S R, \quad P \to f_P R, \quad G \to f_G R \tag{4.34}$$

With these substitutions, we reduce the 5-species mean-field model to a 3-dimensional system:

$$\frac{\partial U'}{\partial t} = k_G f_G R(1-\lambda_{GT}^2 T) - k_S f_S R - k_b' U'(1-\lambda_{BU'}^2 B) + k_S \lambda_B^2 f_S RB \tag{4.35}$$

$$\frac{\partial B}{\partial t} = k_b' U'(1-\lambda_{BU'}^2 B) - k_S \lambda_B^2 f_S RB \tag{4.36}$$

$$\frac{\partial R}{\partial t} = \mathcal{L}_R(R) + k_b' U'(1-\lambda_{BU'}^2 B) - k_S \lambda_B^2 f_S RB \tag{4.37}$$

where $\mathcal{L}_R(R)$ contains the transport terms of the tips. In 2D, these terms are given by:

$$\mathcal{L}_R(R(r,\theta)) = \left(v_{R,r} \frac{\partial}{\partial r} + D_{R,r} \frac{\partial^2}{\partial r^2} + \frac{D_{R,\theta}}{r^2} \frac{\partial^2}{\partial \theta^2} \right) R(r,\theta) \tag{4.38}$$

where $v_{R,r}$ is the radial drift velocity and $D_{R,r}, D_{R,\theta}$ are the radial and angular diffusion constants of the tips.

4.3 2 species model

Although the 3-species model is more appealing than the 5-species model, there are still modifications that one can make to further simplify the mean-field equations. First, we make the following simplifications:

1. $T \approx U'$

   Most of the dendritic tree is formed by immobile dendrites. Therefore, the density of branch points B and branch tips R are negligible in comparison to U', which warrants the approximation $T = U' + R + B \approx U'$.

2. $(1-\lambda_{BU'}^2 B) \approx 1$

   Recall that this factor arises in the branching term, which enforces the condition that branch points cannot spawn on top of one another. However, if we consider

the branch points as point-like particles with a negligible size, branch points are very unlikely to spawn next to one another. This effectively implies that $\lambda_{BU'} \approx 0$. Another way to explain this simplification is to recall that $(1-\lambda_{BU'}^2 B)$ is an approximation of the more exact term $\frac{U'}{U'+B'}$, which corresponds to the fraction of dendrites that are free of branch points. In real class IV neurons, we expect this fraction to be $\approx \frac{\langle L \rangle}{\langle L \rangle + a}$ where $\langle L \rangle \sim 10\,\mu m$ is the average length of dendritic branches. Again, since we expect that the particle size is much smaller than the average branch length, i.e. $a \ll \langle L \rangle$, we have $\frac{U'}{U'+B'} \approx \frac{\langle L \rangle}{\langle L \rangle + a} \approx 1$

With these simplifications, the new mean-field equations become:

$$\frac{\partial U'}{\partial t} = k_G f_G R(1-\lambda_{GT}^2 U') - k_S f_S R - k_b' U' + k_S \lambda_B^2 f_S R B \tag{4.39}$$

$$\frac{\partial B}{\partial t} = k_b' U' - k_S \lambda_B^2 f_S R B \tag{4.40}$$

$$\frac{\partial R}{\partial t} = \mathcal{L}_R(R) + k_b' U' - k_S \lambda_B^2 f_S R B \tag{4.41}$$

One of the caveats of the 5-species and 3-species models is the definition of the particle size a, which is somewhat arbitrary. Furthermore, the definition of the dendrites density U' also creates a problem since the dendritic tree is composed of a set of connected one-dimensional tree branches that occupy a two-dimensional space. Therefore, dendrites more closely resemble linear structures than point-like particles and should therefore be treated as such.

In order to construct a model in terms of the branch density, we recast the mean-field equations using the dendrites line density $U = aU'$ and take the limit where the particle size a goes to zero, while keeping U constant. Recall that the particle size enters in the following definitions:

$$k_S = \frac{v_S}{a}, \quad k_G = \frac{v_G}{a}, \quad k_b' = a k_b, \quad U' = \frac{U}{a} \tag{4.42}$$

where the units of U and k_b are now: $[U] = \frac{1}{\text{Length}}, [k_b] = \frac{1}{\text{Length}\cdot\text{Time}}$. Substituting these expressions into the simplified equations, we obtain:

$$\frac{1}{a}\frac{\partial U}{\partial t} = \frac{v_G}{a} f_G R\left(1 - \lambda_{GT}^2 \frac{U}{a}\right) - \frac{v_S}{a} f_S R - k_b U + \frac{v_S}{a}\lambda_B^2 f_S RB \tag{4.43}$$

$$\frac{\partial B}{\partial t} = k_b U - \frac{v_S}{a}\lambda_B^2 f_S RB \tag{4.44}$$

$$\frac{\partial R}{\partial t} = \mathcal{L}_R(R) + k_b U - \frac{v_S}{a}\lambda_B^2 f_S RB \tag{4.45}$$

In the limit $a \to 0$, the dependence of the interactions length scale λ_B and λ_{GT} on the particle size is unknown. This implies that they cannot be safely removed, which leads to the following redefinition of the interaction length scales:

$$\lambda_{RB} = \frac{\lambda_B^2}{a} \tag{4.46}$$

$$\lambda_{RU} = \frac{\lambda_{GT}^2}{a} \tag{4.47}$$

yielding the following equations:

$$\frac{\partial U}{\partial t} = v_G f_G R(1 - \lambda_{RU} U) - v_S f_S R - a k_b U + a v_S \lambda_{RB} f_S RB \tag{4.48}$$

$$\frac{\partial B}{\partial t} = k_b U - v_S \lambda_{RB} f_S RB \tag{4.49}$$

$$\frac{\partial R}{\partial t} = \mathcal{L}_R(R) + k_b U - v_S \lambda_{RB} f_S RB \tag{4.50}$$

Taking the $a \to 0$ limit, the system simplifies to:

$$\frac{\partial U}{\partial t} = (v_G f_G - v_S f_S) R - v_G f_G \lambda_{RU} RU \tag{4.51}$$

$$\frac{\partial B}{\partial t} = k_b U - v_S \lambda_{RB} f_S RB \tag{4.52}$$

$$\frac{\partial R}{\partial t} = \mathcal{L}_R(R) + k_b U - v_S \lambda_{RB} f_S RB \tag{4.53}$$

The disappearance of the $a v_S \lambda_{RB} f_S RB$ term in the $\frac{\partial U}{\partial t}$ equation due to the $a \to 0$ limit can be understood heuristically. Recall that this term arises from the branch annihilation process whereby a branch tip that retracts back to its branch point

disappears along with the branch point resulting in the creation of a dendrite particle. However, under the small particle size assumption, the creation of this dendrite particle is minuscule compared to the local dendrites density, and can therefore be neglected. The same argument holds for the disappearance of the ak_bU term. As a result of the branching process, a dendrite particle is converted into a branch tip and a branch point. However, this loss of dendrite particles is again negligible compared to the local line density of dendrites.

Finally, a problem still remains with the treatment of the branch annihilation process. During morphogenesis, branches disappear when their branch tip retracts back to their birth place, the branch point of the branch. The retraction of the branch tip can be triggered in two ways: 1) by the stochastic behavior of the growth or 2) by the contact of the tip with surrounding dendrites, which is regulated by the DSCAM pathway. The key aspect of this process is that the branch annihilation occurs only when the branch tip "collides" with its own branch point. In the current model, this condition is not satisfied since there are no variables that track each pair of branch point and branch tip. A branch tip can annihilate with any other branch points and not solely with the branch point from which it originated.

To resolve this issue, we instead treat the branch annihilation process as a death process that depends on the dynamics of the tip and the local density of dendrites. Consequently, this removes the need to use a destructive interaction term between branch points and branch tips to model the tip annihilation process. Moreover, since the branching process conserves the quantity $R - B$, as explained earlier in section 4.1.3, the density of branch points can be recovered from the density of

branch tips and is therefore redundant. We can then simplify the model using only two species:

$$\frac{\partial U}{\partial t} = v_R R - c_{RU} RU \tag{4.54}$$

$$\frac{\partial R}{\partial t} = \mathcal{L}_R(R) + k_b U - k_d(U) R \tag{4.55}$$

where $v_R = (v_G f_G - v_S f_S)$, $c_{RU} = v_G f_G \lambda_{RU}$ and $k_d(U)$ is the death rate of the dendritic tips. Note that $k_d(U)$ is a non-linear function of the dendrites line density U that increases as the local dendrites density increases. The zeroth-order term models the spontaneous annihilation of the tip that results from the tip dynamics while the non-linear component accounts for the conjoint effect of stochastic growth and contact inhibition.

For the rest of this chapter, we will be focusing on the 2-species model, detailing the microscopic origin of the model parameters and making coarse-grained predictions on the morphogenesis.

4.4 Dendritic tip growth as a 1D biased random walk

In this section, we explain how growth of dendritic tips is modeled as a random walk with drift and diffusion and provide theoretical estimates on how the transport parameters are related to the microscopic parameters of the Markovian tip dynamics.

4.4.1 2D motion of dendritic tips

In two dimensions, the dendritic tip effectively behaves as a random walker. This walk results from two processes: 1) the one-dimensional random walk that models its growth process and 2) the persistent orientation of the growth that is distributed with a given mean and variance with respect to the branch orientation. Recall that the 2-dimensional motion of dendritic tips is modeled using the following transport terms:

$$\mathcal{L}_R(R(r,\theta)) = \left(v_{R,r}\frac{\partial}{\partial r} + D_{R,r}\frac{\partial^2}{\partial r^2} + \frac{D_{R,\theta}}{r^2}\frac{\partial^2}{\partial \theta^2} \right) R(r,\theta) \tag{4.56}$$

where $v_{R,r}$ is the radial drift velocity and $D_{R,r}, D_{R,\theta}$ are the radial and angular diffusion constants of the tips. Moreover, let $p(x,t|x_0,t_0)$ denote the probability density that the tip has a length x at time t, given that it had a length x_0 at time t_0. The 1D biased random walk that models the tip growth process can be understood with the following drift-diffusion equation:

$$\frac{\partial p(x,t|x_0,t_0)}{\partial t} = -v_R\frac{\partial p}{\partial x} + D_R\frac{\partial^2 p}{\partial x^2} \tag{4.57}$$

where v_R and D_R are the drift velocity and diffusion constant of the 1D tip growth. Furthermore, let $\hat{d}$ represent the orientation of the dendrite growth in the two-dimensional neuron. Denoting ψ as the angular difference between the angle of the vector tangent to the dendrite branch and the radial direction $\hat{r}$, also called the polar tangential angle, the explicit form of $\hat{d}$ is:

$$\hat{d} = \cos(\theta+\psi)\hat{x} + \sin(\theta+\psi)\hat{y} = \cos(\psi)\hat{r} + \sin(\psi)\hat{\theta} \tag{4.58}$$

Assuming that the growth direction ψ is a random variable with a distribution $p(\psi)$, our goal is to relate $v_{R,r}, D_{R,r}, D_{R,\theta}$ to $v_R, D_R, p(\psi)$. Using the growth vector $\hat{d}$, the flux of the tip density R is:

$$\vec{J}_R = \hat{d}(v_R R - D_R \hat{d}\cdot\nabla R) = \hat{d}\left(v_R R - D_R\left(\cos(\psi)\frac{\partial R}{\partial r} + \sin(\psi)\frac{1}{r}\frac{\partial R}{\partial \theta}\right)\right) \tag{4.59}$$

The transport terms are derived by taking the divergence of this flux. However, for any given dendritic tip, the growth of the tip is constrained along the direction $\hat{d}$. Therefore, there will be no contribution arising from the divergence of $\hat{d}$, i.e. $\nabla\cdot\hat{d} = 0$. This leads to the following transport terms:

$$\mathcal{L}_d(R) = -\nabla\cdot\vec{J}_R \tag{4.60}$$

$$= -v_R\hat{d}\cdot\nabla R + D_R\hat{d}\cdot\nabla\left(\cos(\psi)\frac{\partial R}{\partial r} + \sin(\psi)\frac{1}{r}\frac{\partial R}{\partial \theta}\right) \tag{4.61}$$

$$= -v_R\left(\cos(\psi)\frac{\partial R}{\partial r} + \sin(\psi)\frac{1}{r}\frac{\partial R}{\partial \theta}\right) \tag{4.62}$$

$$+ D_R\cos(\psi)\left(\cos(\psi)\frac{\partial^2 R}{\partial r^2} + \sin(\psi)\left(-\frac{1}{r^2}\frac{\partial R}{\partial \theta} + \frac{1}{r}\frac{\partial^2 R}{\partial r\partial\theta}\right)\right) \tag{4.63}$$

$$+ D_R\frac{\sin(\psi)}{r}\left(\cos(\psi)\frac{\partial^2 R}{\partial r\partial\theta} + \sin(\psi)\frac{1}{r}\frac{\partial^2 R}{\partial\theta^2}\right) \tag{4.64}$$

$$= -v_R\left(\cos(\psi)\frac{\partial R}{\partial r} + \sin(\psi)\frac{1}{r}\frac{\partial R}{\partial \theta}\right) \tag{4.65}$$

$$+ D_R\left(\cos^2(\psi)\frac{\partial^2 R}{\partial r^2} + \frac{2\cos(\psi)\sin(\psi)}{r}\frac{\partial^2 R}{\partial r\partial\theta} - \frac{\cos(\psi)\sin(\psi)}{r^2}\frac{\partial R}{\partial\theta} + \sin^2(\psi)\frac{1}{r^2}\frac{\partial^2 R}{\partial\theta^2}\right) \tag{4.66}$$

Taking the average over ψ and assuming that its distribution is symmetric with respect to $\psi = 0$, we have:

$$\mathcal{L}(R) = \langle\mathcal{L}_d(R)\rangle_d = -v_R c_1\frac{\partial R}{\partial r} + D_R\left(c_2\frac{\partial^2 R}{\partial r^2} + (1-c_2)\frac{1}{r^2}\frac{\partial^2 R}{\partial\theta^2}\right) \tag{4.67}$$

where $c_1 = \langle \cos(\psi) \rangle$ and $c_2 = \langle \cos^2(\psi) \rangle$. The radial and angular transport parameters are then given by:

$$v_{R,r} = c_1 v_R \tag{4.68}$$

$$D_{R,r} = c_2 D_R \tag{4.69}$$

$$D_{R,\theta} = (1 - c_2) D_R \tag{4.70}$$

The c_1, c_2 constants are evaluated using the experimental measurements of $p(\psi)$ (see fig. 3.36). Finally, given the approximate azimuthal symmetry observed in the dendritic trees, we assume that dendritic growth has no angular dependence, i.e. $R(r, \theta) \approx R(r)$. This assumption simplifies the transport terms to:

$$\mathcal{L}_R(R(r)) = -v_{R,r} \frac{\partial R}{\partial r} + D_{R,r} \frac{\partial^2 R}{\partial r^2} \tag{4.71}$$

4.4.2 Microscopic origin of the tip growth drift velocity v_R

Under the assumption that the tip dynamical system has reached steady state, the tip growth drifts at a constant velocity v_R, which is given by the steady-state-weighted average of the state velocities:

$$v_R = \langle v_G \rangle P_{G,ss} + \langle v_P \rangle P_{P,ss} - \langle v_S \rangle P_{S,ss} \tag{4.72}$$

$$= \langle v_G \rangle P_{G,ss} - \langle v_S \rangle P_{S,ss} \tag{4.73}$$

where $\langle v_S \rangle, \langle v_P \rangle, \langle v_G \rangle$ correspond to the average speed of the tip in each state. Moreover, we assume that the paused state velocity is centered at 0, $\langle v_P \rangle = 0$. eq. (4.73) provides an expression for the drift velocities in terms of the microscopic parameters of the tip dynamics, i.e. the transition rate parameters k_{ij} and the state velocities v_i. Although this expression could be used in practice to estimate v_R, its precision is highly dependent on the absolute error of $\langle v_G \rangle P_{G,ss}$ and $\langle v_S \rangle P_{S,ss}$,

since v_R is constructed from the difference of these two quantities. More precisely, assuming for simplicity that $P_{G,ss}, P_{S,ss}$ have no error, the relative error of v_R is given by:

$$\left(\frac{\Delta v_R}{v_R}\right)^2 = \frac{P_{G,ss}}{v_R^2}\Delta\langle v_G\rangle^2 + \frac{P_{S,ss}}{v_R^2}\Delta\langle v_S\rangle^2 \tag{4.74}$$

$$= \frac{P_{G,ss}\langle v_G\rangle^2}{v_R^2}\left(\frac{\Delta\langle v_G\rangle}{\langle v_G\rangle}\right)^2 + \frac{P_{S,ss}\langle v_S\rangle^2}{v_R^2}\left(\frac{\Delta\langle v_S\rangle}{\langle v_S\rangle}\right)^2 \tag{4.75}$$

Thus, if v_R is small, but $\langle v_S\rangle \approx \langle v_G\rangle \gg v_R$, the relative error $\frac{\Delta v_R}{v_R}$ can be very large as it increases with the magnitude of $\langle v_G\rangle, \langle v_S\rangle$, even if the relative errors of $\langle v_S\rangle$ and $\langle v_S\rangle$ are small.

Alternatively, one can measure the tip growth drift velocity v_R directly from the average displacement of the tip growth tracks. This method provides a better precision and is detailed in section 4.4.4.

4.4.3 Microscopic origin of the tip growth diffusion constant D_R

To relate the effective diffusion coefficient of the branch tips to the microscopic growth parameters, we use the Green-Kubo relation for material transport:

$$D_R = \int_0^\infty \langle \left[v(t+t') - \langle v(t+t')\rangle_{t'}\right]\left[v(t') - \langle v(t')\rangle_{t'}\right]\rangle_{t'} dt \tag{4.76}$$

where $v(t)$ corresponds to the velocity of the tip at time t. In other words, the diffusion constant is defined as the integral of the auto-correlation function of the tip velocity. To start, we first calculate the velocity auto-correlation:

$$\mathcal{C}_v(t,t') = \langle v(t+t')v(t')\rangle = \int_{-\infty}^{\infty}\int_{-\infty}^{\infty} vw\, p(v,t+t',w,t')dvdw \tag{4.77}$$

where $p(v,t+t',w,t')$ is the joint probability density that the tip velocity equals v at time t and that it equals w at time $t+t'$. Given the 3-state model of the tip dynamics, the velocity distribution is easier to derive by conditioning on the discrete dynamical states of the tip. Let us define $P(S(t)=i)$ as the probability that the tip is in state i at time t and $P(S(t+t')=j|S(t)=i)$ as the conditional probability that the tip is in state j at time $t+t'$ given that it was in state i at time t. We then have the following formula:

$$p(v,t+t',w,t') = \sum_i p(v,t+t',w,t'|S(t')=i)P(S(t')=i) \tag{4.78}$$

$$= \sum_i \left(P(S(t+t')=i|S(t')=i)\delta(v-w) + \sum_{j\neq i} P(S(t+t')=j|S(t)=i)p_j(v) \right) p_i(w)P(S(t')=i) \tag{4.79}$$

$$= \sum_i \left(P(S(t)=i|S(0)=i)\delta(v-w) + \sum_{j\neq i} P(S(t)=j|S(0)=i)p_j(v) \right) p_i(w)P(S(t')=i) \tag{4.80}$$

where $p_i(w)$ represents the velocity probability density in state i, $\delta(x)$ is the Dirac delta function and summations are performed over the indices $i \in \{1,2,3\} = \{S,P,G\}$. To derive the expression above, we assumed that the velocity correlation is a delta function ($\delta(v-w)$) if the state does not change. In other words, we assume that the tip velocity is constant over the duration of the state and only changes during state transitions. Moreover, we also used the fact that the transition probability of the tip state is invariant under time translation. In other words, $\forall t', P(S(t+t')=i|S(t')=j) = P(S(t)=i|S(0)=j)$.

Moreover, using the fact that:

$$\langle P(S(t)=i)\rangle_t = \lim_{T\to\infty} \frac{1}{T}\int_0^T P(S(t)=i)dt = P_{i,ss} \tag{4.81}$$

where $P_{i,ss}$ denotes the steady-state probability to find the tip in state i, and taking the average over all time t', we have:

$$\langle p(v,t+t',w,t')\rangle_{t'} = \sum_i \Bigg(P(S(t)=i|S(0)=i)\delta(v-w) + \sum_{j\neq i} P(S(t)=j|S(0)=i)p_j(v) \Bigg) p_i(w)P_{i,ss} \tag{4.82}$$

This leads us to define the stationary velocity correlation function, which only depends on the lag t:

$$\mathcal{C}_{s,v}(t) = \langle \mathcal{C}_v(t,t')\rangle_{t'} \tag{4.83}$$

$$= \int_{-\infty}^{\infty}\int_{-\infty}^{\infty} \Bigg(\sum_i P(S(t)=i|S(0)=i)\delta(v-w)p_i(w)P_{i,ss} \tag{4.84}$$

$$+ \sum_i \sum_{j\neq i} P(S(t)=j|S(0)=i)p_j(v)p_i(w)P_{i,ss} \Bigg) vw\,dv\,dw \tag{4.85}$$

$$= \sum_i \Bigg(P(S(t)=i|S(0)=i)\langle v_i^2\rangle + \sum_{j\neq i} P(S(t)=j|S(0)=i)\langle v_i v_j\rangle \Bigg) P_{i,ss} \tag{4.86}$$

$$= \sum_i \Bigg(\sum_j P(S(t)=j|S(0)=i)\langle v_i v_j\rangle \Bigg) P_{i,ss} \tag{4.87}$$

where v_i is a random variable that corresponds to the tip velocity in the i state. This implies that the average $\langle\cdot\rangle$ is applied over all random variables inside the bracket. Moreover, we assumed that the velocity distribution across different state is uncorrelated $\langle v_i v_j\rangle = \langle v_i\rangle\langle v_j\rangle$. Using the following identity:

$$v_i = \sum_k v_k \delta_{ki} = \sum_k v_k P(S(0)=k|S(0)=i) \tag{4.88}$$

where δ_{ij} is the Kronecker delta, and defining $V^{(i)}(t)$ as the time-dependent random variable that represents the expected tip velocity at time t given that it was initiated in state i:

$$V^{(i)}(t) = \sum_j P(S(t) = j | S(0) = i) v_j \tag{4.89}$$

we can express $\mathcal{C}_{s,v}(t)$ in a more familiar form:

$$\mathcal{C}_{s,v}(t) = \sum_i \left(\sum_j \sum_k P(S(0) = k | S(0) = i) P(S(t) = j | S(0) = i) \langle v_k v_j \rangle \right) P_{i,ss} \tag{4.90}$$

$$= \sum_i \left(\langle \left(\sum_j P(S(t) = j | S(0) = i) v_j \right) \left(\sum_k P(S(0) = k | S(0) = i) v_k \right) \rangle \right) P_{i,ss} \tag{4.91}$$

$$= \sum_i \langle V^{(i)}(t) V^{(i)}(0) \rangle P_{i,ss} \tag{4.92}$$

In other words, $\mathcal{C}_{s,v}(t)$ corresponds to the velocity auto-correlation of $V^i(t)$ averaged over all initial state i weighted by the steady-state probability of each state.

Before moving forward, we rewrite $\langle v(t+t')\rangle_{t'}$ in terms of the variable $V_i(t)$:

$$\langle v(t+t')\rangle_{t'} = \lim_{T\to\infty}\frac{1}{T}\int_0^T\int_{-\infty}^{\infty} p(v,t+t')vdvdt' \tag{4.93}$$

$$= \lim_{T\to\infty}\frac{1}{T}\int_0^T\int_{-\infty}^{\infty}\sum_{ij} p_i(v)P(S(t+t')=i|S(t')=j)P(S(t')=j)vdvdt' \tag{4.94}$$

$$= \lim_{T\to\infty}\frac{1}{T}\int_0^T\int_{-\infty}^{\infty}\sum_{ij} p_i(v)P(S(t)=i|S(0)=j)P(S(t')=j)vdvdt' \tag{4.95}$$

$$= \sum_{ij} P(S(t)=i|S(0)=j)\left(\int_{-\infty}^{\infty} p_i(v)vdv\right)\left(\lim_{T\to\infty}\frac{1}{T}\int_0^T P(S(t')=j)dt'\right) \tag{4.96}$$

$$= \sum_{ij} P(S(t)=i|S(0)=j)\langle v_i\rangle P_{j,ss} \tag{4.97}$$

$$= \sum_{j}\langle V^{(j)}(t)\rangle P_{j,ss} \tag{4.98}$$

In addition, let us introduce the following definitions:

$$\vec{v} = (-v_S, 0, v_G)^T \tag{4.99}$$

$$V_{ss} = \langle\vec{v}\rangle\cdot\vec{P}_{ss} = \sum_j\langle v_j\rangle P_{j,ss} = \sum_j\langle V^{(j)}(0)\rangle P_{j,ss} \tag{4.100}$$

$$\Delta V^{(i)}(t) = V^{(i)}(t) - \sum_j\langle V^{(j)}(0)\rangle P_{j,ss} \tag{4.101}$$

$$= V^{(i)}(t) - V_{ss} \tag{4.102}$$

where v_G, v_S are random variables that represent the speed of the tip in the growing or shrinking state, V_{ss} is the tip velocity at steady state and $\Delta V^{(i)}(t)$ is the deviation

of the velocity from the steady-state velocity V_{ss}. Using these definitions, the expression of the diffusion coefficient is simplified in the following way:

$$D_R = \int_0^\infty \left(\mathcal{C}_{s,v}(t) - \langle v(t+t')\rangle_{t'}\langle v(t')\rangle_{t'}\right) dt \tag{4.103}$$

$$= \sum_i P_{i,ss} \int_0^\infty \left(\langle V^{(i)}(t)V^{(i)}(0)\rangle - \sum_j \langle V^{(i)}(t)\rangle \langle V^{(j)}(0)\rangle P_{j,ss} \right) dt \tag{4.104}$$

$$= \sum_i P_{i,ss} \int_0^\infty \left(\langle V^{(i)}(t) \left(V^{(i)}(0) - \sum_j \langle V^{(j)}(0)\rangle P_{j,ss} \right) \rangle \right) dt \tag{4.105}$$

$$= \sum_i P_{i,ss} \int_0^\infty \left(\langle V^{(i)}(t)\Delta V^{(i)}(0)\rangle - V_{ss}\langle \Delta V^{(i)}(0)\rangle \right) dt \tag{4.106}$$

$$= \sum_i P_{i,ss} \int_0^\infty \langle \Delta V^{(i)}(t)\Delta V^{(i)}(0)\rangle dt \tag{4.107}$$

To derive the last expression, we have added 0 using the fact that $\sum_i P_{i,ss}\langle \Delta V^{(i)}(0)\rangle = 0$. Expanding the expression for $\Delta V^{(i)}(t)$, we have:

$$\Delta V^{(i)}(t) = v_G P_G^{(i)}(t) - v_S P_S^{(i)}(t) - (\langle v_G\rangle P_{G,ss} - \langle v_S\rangle P_{S,ss}) \tag{4.108}$$

where $P_G^{(i)}(t), P_S^{(i)}(t)$ are short forms for $P(S(t) = S|S(0) = i), P(S(t) = G|S(0) = j)$, respectively. Recall that these quantities can be expressed in terms of the right eigenvectors $\vec{w}_j$ and eigenvalues λ_j of the state transition generator K (see sec. section 3.1):

$$\vec{P}^{(i)}(t) = \sum_j a_j^{(i)} \vec{w}_j e^{\lambda_j t} \tag{4.109}$$

where the (i) index emphasizes the dependence on the initial conditions, $\left(\vec{P}^{(i)}(0)\right)_j = \delta_{ij}$. To derive an expression for $\Delta V^{(i)}(t)$, recall that $\vec{1} = (1,1,1)$ is a left eigenvector of K with eigenvalue 0:

$$\vec{1}K = 0 \tag{4.110}$$

This implies that $\vec{1}$ is orthogonal to $\vec{w}_2, \vec{w}_3$:

$$\vec{1}K\vec{w}_j = \lambda_j \vec{1}\cdot\vec{w}_j \qquad (j \neq 1) \tag{4.111}$$

$$\Rightarrow 0 = \lambda_j \vec{1}\cdot\vec{w}_j \tag{4.112}$$

$$\Rightarrow 0 = \vec{1}\cdot\vec{w}_j \qquad (\lambda_j \neq 0, \forall j \neq 1) \tag{4.113}$$

Therefore, if we assume that the initial state of the Markov chain $\vec{P}_0$ is also normalized with the L_1 norm, $\vec{1}\cdot\vec{P}_0 = 1$, we have:

$$\vec{P}_0 = \sum_j a_j \vec{w}_j = a_1\vec{P}_{ss} + a_2\vec{w}_2 + a_3\vec{w}_3 \tag{4.114}$$

$$\Rightarrow \vec{1}\cdot\vec{P}_0 = 1 = a_1\vec{1}\cdot\vec{P}_{ss} + a_2\vec{1}\cdot\vec{w}_2 + a_3\vec{1}\cdot\vec{w}_3 \tag{4.115}$$

$$1 = a_1 + 0 + 0 \tag{4.116}$$

therefore a_1 always equals 1 due to our choice of eigenvectors $\vec{w}_j$ and normalization of $\vec{P}^{(i)}(t)$. This implies the following form for $\vec{P}^{(i)}(t)$:

$$\vec{P}^{(i)}(t) = \sum_j a_j^{(i)}\vec{w}_j e^{\lambda_j t} = \vec{P}_{ss} + \sum_{i=2}^{3} a_j^{(i)}\vec{w}_j e^{\lambda_j t} \tag{4.117}$$

Using this general expression and the definition of the state velocity vector $\vec{v} = (-v_S, 0, v_G)^T$, we can express $\Delta V^{(i)}(t)$ in a succinct form:

$$\Delta V^{(i)}(t) = v_G P_G^{(i)}(t) - v_S P_S^{(i)}(t) - (\langle v_G\rangle P_{G,ss} - \langle v_S\rangle P_{S,ss}) \tag{4.118}$$

$$= \vec{v}\cdot\vec{P}^{(i)}(t) - \langle\vec{v}\rangle\cdot\vec{P}_{ss} \tag{4.119}$$

$$= \vec{v}\cdot\left(a_2^{(i)}\vec{w}_2 e^{\lambda_2 t} + a_3^{(i)}\vec{w}_3 e^{\lambda_3 t}\right) + (\vec{v} - \langle\vec{v}\rangle)\cdot\vec{P}_{ss} \tag{4.120}$$

$$= b_2^{(i)} e^{\lambda_2 t} + b_3^{(i)} e^{\lambda_3 t} + (\vec{v} - \langle\vec{v}\rangle)\cdot\vec{P}_{ss} \tag{4.121}$$

$$b_j^{(i)} = a_j^{(i)}\vec{v}\cdot\vec{w}_j \tag{4.122}$$

As explained at the beginning of this derivation, we assume that the velocity of each state is uncorrelated with any other state. Moreover, we assume that the velocity

does not change unless the dynamical state changes. Consequently, we have the following identities:

$$\langle v_i^2 \rangle - \langle v_i \rangle^2 = 0 \tag{4.123}$$

$$\langle b_j^{(i)} b_l^{(k)} \rangle = \langle b_j^{(i)} \rangle \langle b_l^{(k)} \rangle \tag{4.124}$$

In addition, using the definition of $\vec{P}^{(i)}(0)$, we also find:

$$\vec{v} \cdot \vec{P}^{(i)}(0) = v_i = \sum_j a_j^{(i)} \vec{v} \cdot \vec{w}_j = \vec{v} \cdot \vec{P}_{ss} + b_2^{(i)} + b_3^{(i)} \tag{4.125}$$

$$\Rightarrow b_2^{(i)} + b_3^{(i)} = v_i - \vec{v} \cdot \vec{P}_{ss} \tag{4.126}$$

Using the above expression and the non-correlation assumptions, we obtain the following form for the velocity auto-correlation $\langle \Delta V^{(i)}(t) \Delta V^{(i)}(0) \rangle$:

$$\langle \Delta V^{(i)}(t) \Delta V^{(i)}(0) \rangle = \langle \left(b_2^{(i)} e^{\lambda_2 t} + b_3^{(i)} e^{\lambda_3 t} + (\vec{v} - \langle \vec{v} \rangle) \cdot \vec{P}_{ss} \right) \left(b_2^{(i)} + b_3^{(i)} + (\vec{v} - \langle \vec{v} \rangle) \cdot \vec{P}_{ss} \right) \rangle \tag{4.127}$$

$$= \langle \left(b_2^{(i)} e^{\lambda_2 t} + b_3^{(i)} e^{\lambda_3 t} \right) \left(b_2^{(i)} + b_3^{(i)} \right) \rangle \tag{4.128}$$

$$= \left(\langle b_2^{(i)} \rangle e^{\lambda_2 t} + \langle b_3^{(i)} \rangle e^{\lambda_3 t} \right) \left(\langle v_i \rangle - \langle V_{ss} \rangle \right) \tag{4.129}$$

Finally using the fact that the real part of λ_2, λ_3 is negative, we find the following expression for the diffusion coefficient:

$$\int_0^\infty \langle \Delta V^{(i)}(t) V^{(i)}(0) \rangle dt = \left(\langle v_i \rangle - \langle V_{ss} \rangle \right) \int_0^\infty \left(\langle b_2^{(i)} \rangle e^{\lambda_2 t} + \langle b_3^{(i)} \rangle e^{\lambda_3 t} \right) dt \tag{4.130}$$

$$= - \left(\langle v_i \rangle - \langle V_{ss} \rangle \right) \left(\frac{\langle b_2^{(i)} \rangle}{\lambda_2} + \frac{\langle b_3^{(i)} \rangle}{\lambda_3} \right) \tag{4.131}$$

$$D_R = \sum_i P_{i,ss} \int_0^\infty \langle \Delta V^{(i)}(t) V^{(i)}(0) \rangle dt \tag{4.132}$$

$$= - \sum_{i=1}^{3} \sum_{j=2}^{3} P_{i,ss} \left(\langle v_i \rangle - \langle V_{ss} \rangle \right) \frac{\langle b_j^{(i)} \rangle}{\lambda_j} \tag{4.133}$$

4.4.4 Measurements of the tip growth drift velocity v_R and diffusion constant D_R

To determine the drift velocity v_R and diffusion coefficient D_R, we analyze the average displacements of the tip tracks vs time at each developmental stage. At each developmental stage, we are given a set of timeseries indicating the branch length $L_i^{(j)}$ associated to a given tip j at a certain time t_i over the course of the recording. Using this data, we calculate the spatial and temporal displacements as follows:

$$\Delta L_{i,k}^{(j)} = L_i^{(j)} - L_{i-k}^{(j)} \tag{4.134}$$

$$\Delta t_{i,k} = t_i - t_{i-k} \tag{4.135}$$

where the index k denotes the number of time steps separating the two points in the difference measurements. For a one-dimensional biased random walk, the drift velocity V and diffusion constant D are determined by the mean and variance of the displacements ΔL:

$$\langle \Delta L \rangle = V \Delta t \tag{4.136}$$

$$\langle \Delta L^2 \rangle - \langle \Delta L \rangle^2 = 2D\Delta t + \sigma^2 \tag{4.137}$$

where σ^2 arises from the assumption of a Gaussian measurement noise. Therefore, to estimate the drift and diffusion constant, we fit the mean and variance of the displacements to linear functions of the temporal difference Δt. For simplicity, let us assume that the measurements are sampled at a constant period ΔT, such that

$t_i = i\Delta T$. Then, we calculate the mean and the variance of the displacements as follows:

$$\mu_{\Delta L_k} = \langle \Delta L_k \rangle = \frac{1}{N_k} \sum_j \sum_{i=k+1}^{n_j} \left(L_i^{(j)} - L_{i-k}^{(j)} \right) \tag{4.138}$$

$$\sigma^2_{\Delta L_k} = \langle \Delta L_k^2 \rangle - \langle \Delta L_k \rangle^2 = \frac{1}{N_k - 1} \sum_j \sum_{i=k+1}^{n_j} \left(L_i^{(j)} - L_{i-k}^{(j)} - \langle \Delta L_k \rangle \right)^2 \tag{4.139}$$

where n_j is the number of time points in the j^{th} track and the sums run over all tracks (j) and all pairs of points (i) separated by a time $k\Delta T$ such that N_k is the total number of such pairs across the whole dataset. The expected error of these estimates are calculated using the formula for the standard error of the mean and variance (see [67], sec. 6h):

$$\mathrm{SE}(\mu_{\Delta L_k}) = \frac{\sigma_{\Delta L_k}}{\sqrt{\tilde{N}_k}} \tag{4.140}$$

$$\mathrm{SE}(\sigma^2_{\Delta L_k}) = \sqrt{\frac{1}{\tilde{N}_k} \left(\mu_{4,\Delta L_k} - \left(\frac{\tilde{N}_k - 3}{\tilde{N}_k - 1} \right) \sigma^4_{\Delta L_k} \right)} \tag{4.141}$$

$$\tilde{N}_k = \sum_j \left\lfloor \frac{t_{n_j} - t_1}{k\Delta T} \right\rfloor \tag{4.142}$$

where $\mu_{4,\Delta L_k} = \langle (\Delta L_k - \mu_{\Delta L_k})^4 \rangle$ is the fourth central moment, $\lfloor \cdot \rfloor$ is the floor operator and $\tilde{N}_k$ is the effective number of independent pairs of points separated by a time $k\Delta T$.

Using the formulas for the mean and variance of the displacements ΔL_k, we fit these quantities with a weighted linear least squares fit where the weights w of the mean and variance are given by the squared inverse of the standard error:

$$w_{\mu_{\Delta L_k}} = \frac{1}{\mathrm{SE}^2(\mu_{\Delta L_k})} = \frac{\tilde{N}_k}{\sigma^2_{\Delta L_k}} \tag{4.143}$$

$$w_{\sigma^2_{\Delta L_k}} = \frac{1}{\mathrm{SE}^2(\sigma^2_{\Delta L_k})} = \frac{\tilde{N}_k}{\left(\mu_{4,\Delta L_k} - \left(\frac{\tilde{N}_k - 3}{\tilde{N}_k - 1} \right) \sigma^4_{\Delta L_k} \right)} \tag{4.144}$$

Furthermore, to mitigate the effect of the correlations induced by taking all possible pairs of points in the calculation of the displacements, only powers of 2 of the sampling period are fitted. In other words, the time delays of the fitted means and variances are:

$$\Delta t_{\text{fitted}} = 2^m \Delta T, \quad m \in \{0, 1, \ldots\} \tag{4.145}$$

To test the accuracy and precision of the fitting method, we simulated tip growth with a given drift velocity and diffusion constant and recovered the transport parameters by fitting the mean and variance of the track displacements. $N = 100$ growth tracks were simulated with a sampling interval period of 6 s, a drift velocity of $V = 0.1\,\mu m\,\text{min}^{-1}$ and a diffusion constant of $D = 0.15\,\mu m^2\,\text{min}^{-1}$. The initial track length was uniformly distributed between 0 and 5 μm and the track lasted $30\,\text{min}$ unless it hit the boundaries at $L = 0\,\mu m$ or $L = 10\,\mu m$. In addition, we added a measurement white noise on the track length with a variance of $0.15^2\,\mu m^2$, which is a precision of ~ 1 pixel in our experimental setup. As we can see in fig. 4.2, the fitting method accurately recovers the input drift velocity and diffusion constant.

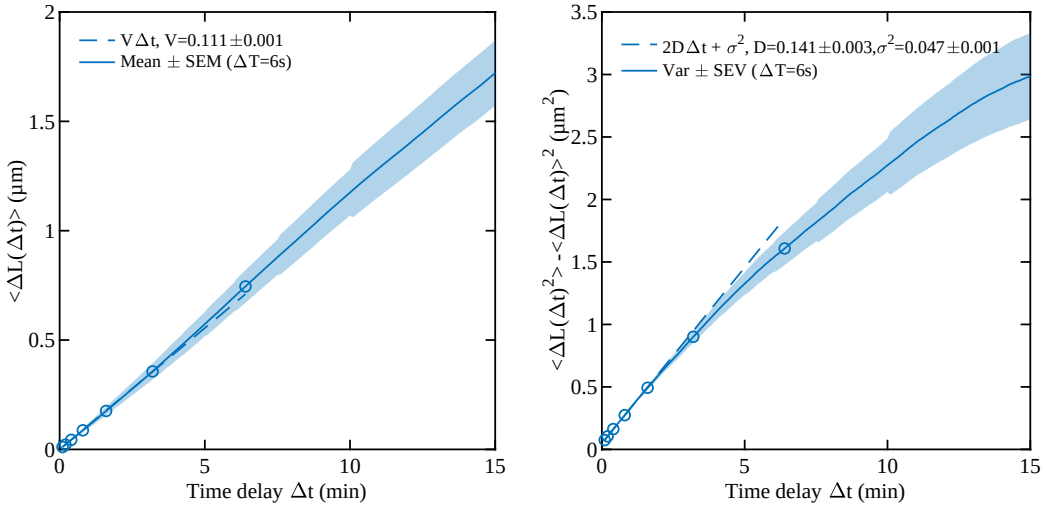

Figure 4.2 – Test of the drift and diffusion constants measurements
Mean and variance of the displacements of 100 simulated growth tracks, sampled every $\Delta T = 6s$ with a drift velocity of $V = 0.1\,\mu m\,\mathrm{min}^{-1}$ and a diffusion constant of $D = 0.15\,\mu m^2\,\mathrm{min}^{-1}$. The initial track length is uniformly distributed between 0 and $5\,\mu m$ and the track lasts 30min unless it hits any of the boundaries at $L = 0\,\mu m$ or $L = 10\,\mu m$. A length measurement white noise with $\sigma_L = 0.15\,\mu m$ is also added. The open circles identify the fitted points and the shaded area corresponds to the given statistic $\pm$ 1 standard error. The error of the fitted parameters are derived from the standard formula for a weighted linear least squares fit.

Using our fitting method, we estimate the drift velocity and diffusion constant of the tip growth tracks in class IV neurons. The fits are displayed in figs. 4.3 and 4.4. We also re-plot the diffusion constant fits on logarithmic scales in fig. 4.5 to better display the small time behavior. In the dataset, multiple movies were combined together with different sampling periods. A fit is performed for each sampling period found at the given developmental stage and the values of each fit parameters is averaged with a weight proportional to the squared inverse of the fit parameter error. Points are fitted in the interval $0\,\mathrm{min} \leq \Delta t \leq 10\,\mathrm{min}$ for the drift velocity fits, while points are fitted in the interval $0.25\,\mathrm{min} \leq \Delta t \leq 10\,\mathrm{min}$ for the diffusion constant fits. The upper threshold of $10\,\mathrm{min}$ is used to select only the displacements with the highest precision. The lower threshold of $0.25\,\mathrm{min}$ is used for the diffusion constant fit in order to ensure that the linear behavior of the variance was fitted. This is especially important for the 48 hr AEL fit, where the noise of the variance

is significant for $\Delta t \leq 0.25$ min. Note that the diffusion constant fits are displayed on a logarithmic scale, but the least-squares linear fit is performed on linear scale, which assumes normally-distributed errors. Also, the intercept of the diffusion fits is sometimes negative, which we interpret as a consequence of the fact that the small time behavior $\Delta t \leq 0.25$ is omitted in the fits.

In general, the fits accurately reproduce the behavior of the mean and variance of the displacements. The drift velocities are similar in magnitude at 24 and 48 hr AEL but decreases by a factor of 10 at 96 hr AEL. This is likely an effect of the maturation of the neuron, which has a lifespan of $\sim$144 hours. A similar behavior is observed in the diffusion constants, although the magnitude of the decrease is not as significant as the decrease of the drift velocity.

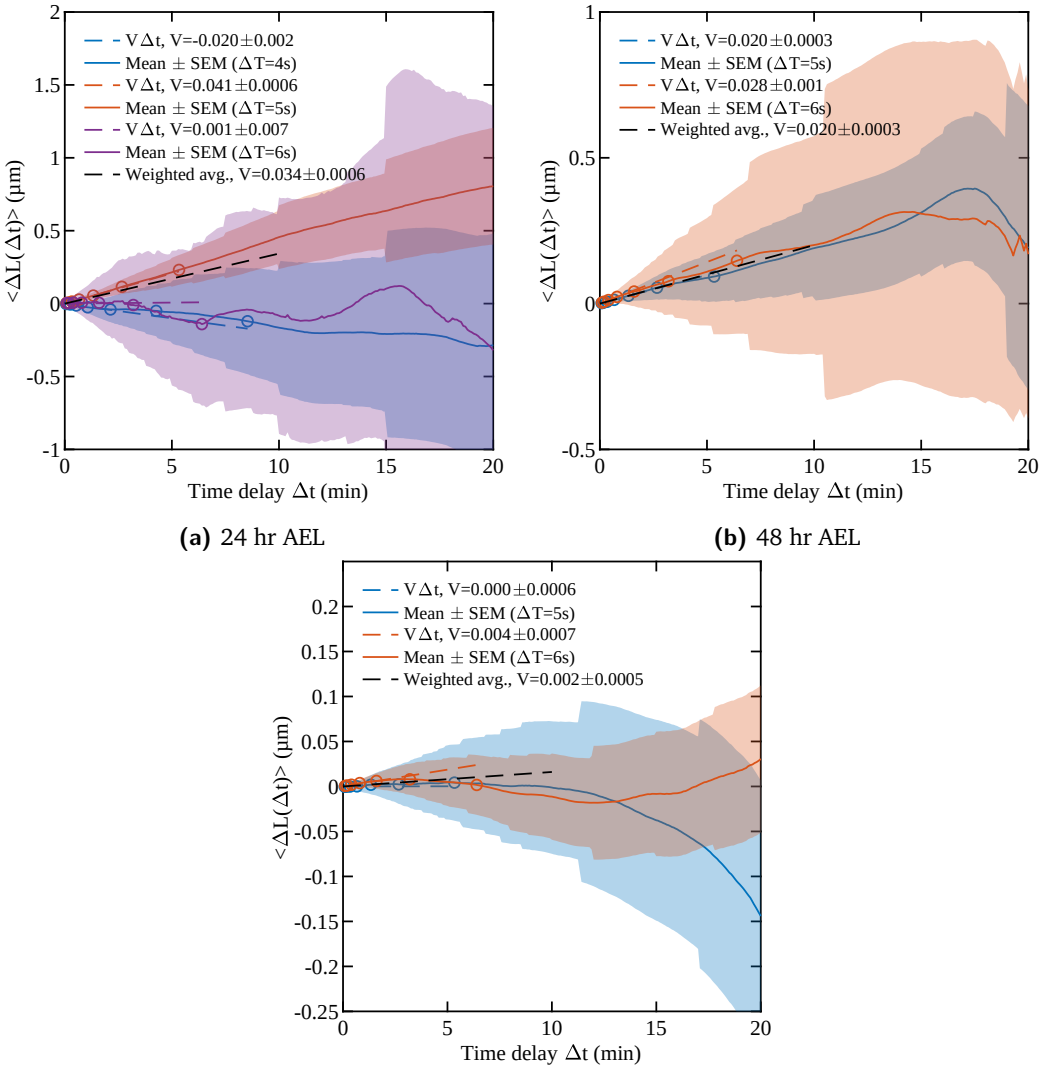

(a) 24 hr AEL

(b) 48 hr AEL

(c) 96 hr AEL

Figure 4.3 – Drift velocities of dendritic tip growth over development
The colors identify the sampling periods found in the dataset. The open circles correspond to the fitted points.

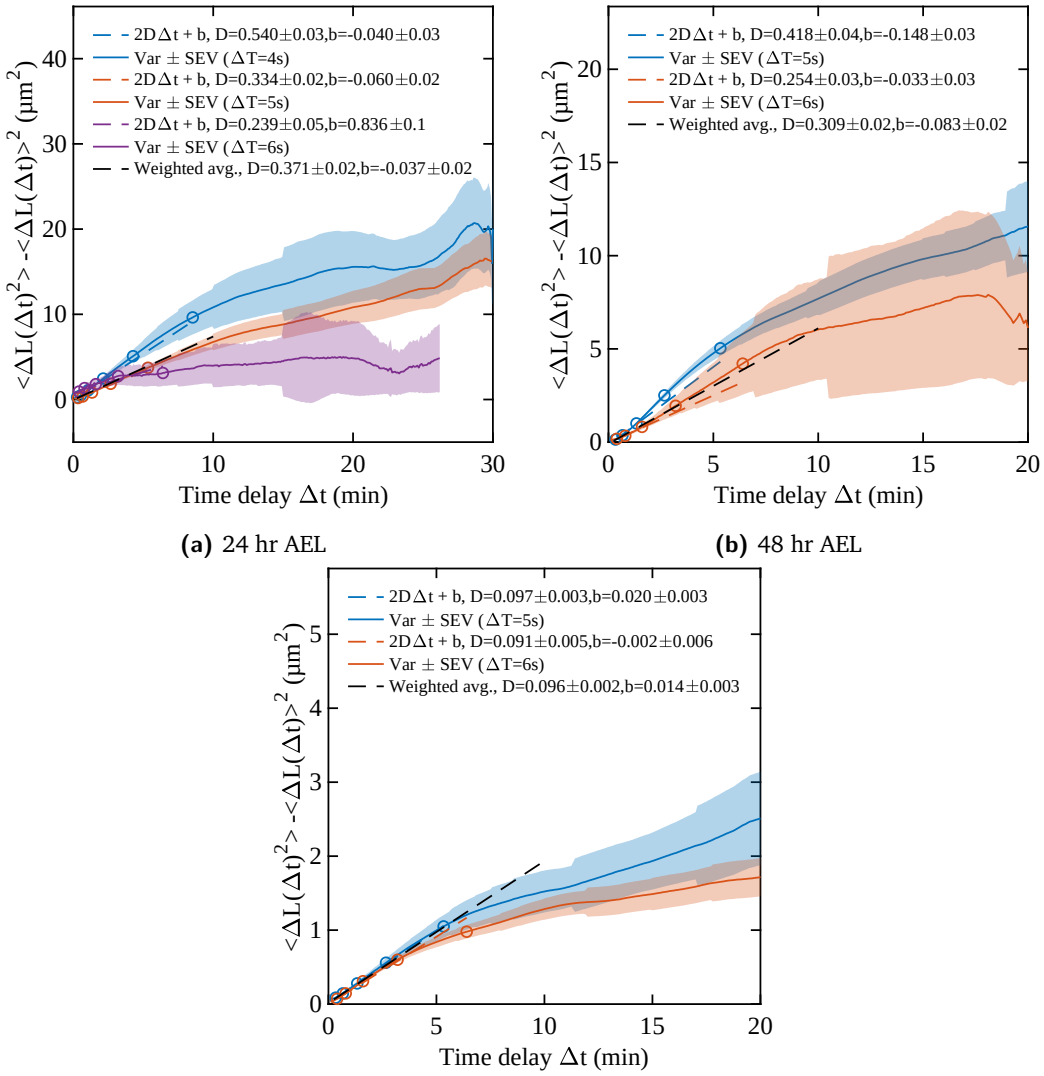

(a) 24 hr AEL **(b)** 48 hr AEL

(c) 96 hr AEL

Figure 4.4 – Diffusion constants of dendritic tip growth over development
The colors identify the sampling periods found in the dataset. The open circles correspond to the fitted points.

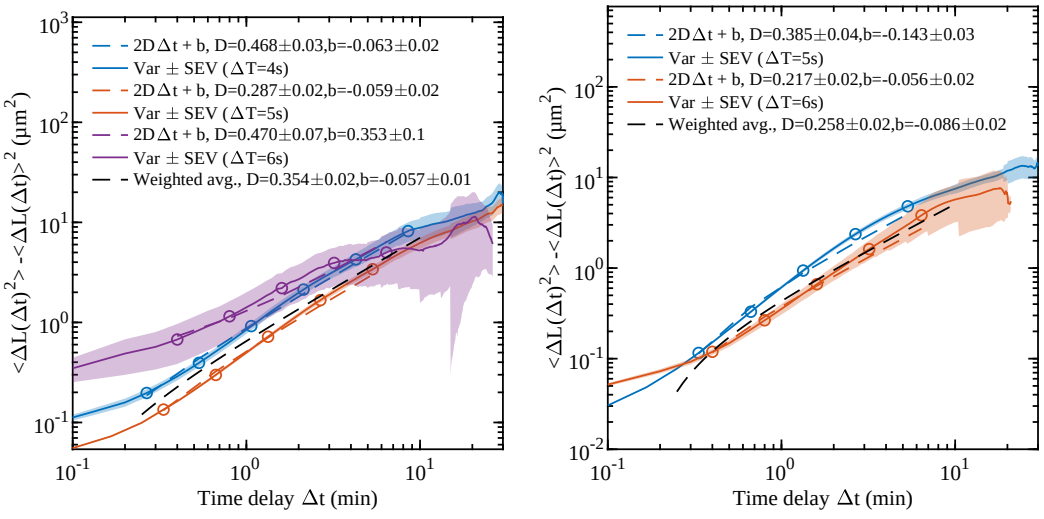

(a) 24 hr AEL **(b)** 48 hr AEL

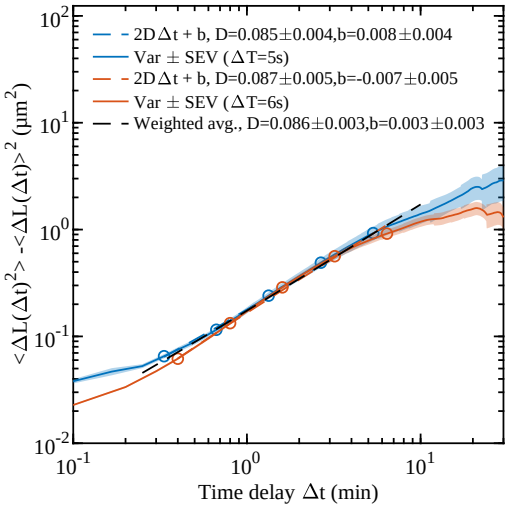

(c) 96 hr AEL

Figure 4.5 – Diffusion constants of dendritic tip growth over development on logarithmic scales
The colors identify the sampling periods found in the dataset. The open circles correspond to the fitted points.

In summary, we find the following estimates of the drift velocity and diffusion constants throughout neuronal development:

Parameters\Stage	24 hr AEL	48 hr AEL	96 hr AEL
V ($\mu m\,\mathrm{min}^{-1}$)	0.0343 ± 0.000592	0.0200 ± 0.000304	0.00161 ± 0.000451
D ($\mu m^2\,\mathrm{min}^{-1}$)	0.354 ± 0.0156	0.258 ± 0.0187	0.0858 ± 0.00293

Finally, we compare the measurements of the drift velocity and diffusion constant with our microscopic estimates that stem from the assumption that the growth tip transition dynamics is at steady state:

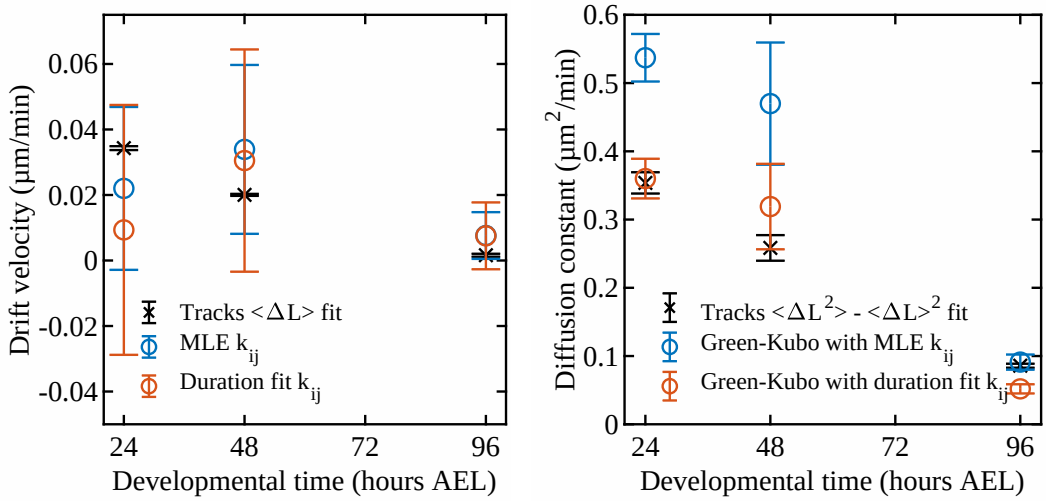

Figure 4.6 – Comparison of estimates of the drift velocity v_R and diffusion constant D_R

As explained before, we see that the drift velocity estimates from the tip dynamics parameters have a low precision, while the track displacement fit estimates are better constrained. Moreover, at 24 and 48 hr AEL, the two Green-Kubo estimates of the diffusion constant differ significantly. This is potentially related to the noise in the growth tracks that was also observed in the diffusion constant fit at $\Delta t \leq 0.25\,\text{min}$.

4.5 Contact inhibition

Upon contact with another branch, a growing tip stops and switches to a shrinking state. As a result, the collision of the tip modifies the master equation of the tip dynamics in the following way:

$$\frac{dP_S(t)}{dt} = -(k_{SP} + k_{SG})P_S(t) + k_{PS}P_P(t) + k_{GS}P_G(t) + k_{CI}P_G(t) \tag{4.146}$$

$$\frac{dP_P(t)}{dt} = -(k_{PS} + k_{PG})P_P(t) + k_{SP}P_S(t) + k_{GP}P_G(t) \tag{4.147}$$

$$\frac{dP_G(t)}{dt} = -(k_{GS} + k_{GP})P_G(t) + k_{SG}P_S(t) + k_{PG}P_P(t) - k_{CI}P_G(t) \tag{4.148}$$

where k_{CI} is the rate at which growing tips contact other dendrites. The collision rate of a growing tip with a dendrite is proportional to the line density of dendrites U and the average growth velocity v_G:

$$k_{CI} = \alpha v_G U \tag{4.149}$$

where α is a geometrical factor that arises from averaging over all contact angles. More specifically, if a growing tip is oriented parallel to its neighboring dendrite, collision will not happen, while the collision rate is maximal perpendicular to the neighbor dendrite. In other words, the rate of collision is proportional to $|\sin(\varphi)|$ where φ is the difference between the growing tip orientation and the average orientation of the neighboring dendrites. Assuming that φ is uniformly distributed and averaging over all contact angles, we get:

$$\alpha = \frac{1}{2\pi}\int_{-\pi}^{\pi} |\sin(\varphi)| d\varphi = \frac{2}{\pi} \tag{4.150}$$

Analyzing the modified master equation in eqs. (4.146) to (4.148), contact inhibition effectively increases the k_{GS} rate to:

$$k'_{GS} = k_{GS} + k_{CI} \tag{4.151}$$

As a result of this modification of k_{GS}, the steady-state of the tip will shift towards the shrinking state. Under the assumption that k_{CI} is small, we can approximate the change in the steady-state probabilities $\vec{P}_{ss}$ by expanding to first order in k_{CI}:

$$\vec{P}'_{ss} = \vec{P}'_{ss}(k'_{ij}) = \vec{P}_{ss}(k_{ij} + \delta_{iG}\delta_{jS}k_{CI}) = \vec{P}_{ss} + \frac{d\vec{P}_{ss}}{dk_{GS}}k_{CI} \tag{4.152}$$

where $\vec{P}'_{ss}$ are the new steady-state probabilities and $\vec{P}_{ss}$ are the steady-state probabilities of the bare master equation, without contact inhibition. Using the expressions of $\vec{P}_{ss}$ derived previously in eq. (3.27), the derivative of the steady state is given by:

$$\frac{d\vec{P}_{ss}}{dk_{GS}} = \frac{k_{PG}\left(k_{SG}+k_{SP}\right)+k_{PS}k_{SG}}{k_2^4}\begin{pmatrix} k_{PG}+k_{PS}+k_{GP} \\ k_{SP}-k_{GP} \\ -k_{SP}-k_{PG}-k_{PS} \end{pmatrix} \tag{4.153}$$

where k_2 is defined in eq. (3.23). As expected, the derivative of the steady state with respect to k_{GS} is positive for the shrinking state ($P_{S,ss} = \vec{P}_{ss,1}$) and negative for the growing state steady state ($P_{G,ss} = \vec{P}_{ss,3}$). The new steady-state can then be written as a function of the bare steady-state probabilities:

$$P'_{S,ss} = P_{S,ss} + \Delta f_S \alpha v_G U, \qquad P'_{G,ss} = P_{G,ss} - \Delta f_G \alpha v_G U \tag{4.154}$$

$$\Delta f_S = \frac{\left(k_{PG}\left(k_{SG}+k_{SP}\right)+k_{PS}k_{SG}\right)\left(k_{PG}+k_{PS}+k_{GP}\right)}{k_2^4} \tag{4.155}$$

$$\Delta f_G = \frac{\left(k_{PG}\left(k_{SG}+k_{SP}\right)+k_{PS}k_{SG}\right)\left(k_{SP}+k_{PG}+k_{PS}\right)}{k_2^4} \tag{4.156}$$

Recall that the tip transition steady-state probabilities $P_{S,ss}, P_{G,ss}$ enter in the mean-field equations through the tip growth speed: $v_R = v_G P_{G,ss} - v_S P_{S,ss}$. Substituting the new steady-state constants $P'_{S,ss}, P'_{G,ss}$ into v_R and rewriting the U equation in terms of the bare transition steady-state probabilities $P_{S,ss}, P_{G,ss}$, we obtain:

$$\begin{aligned}\frac{\partial U}{\partial t} &= (P'_{G,ss} v_G - P'_{S,ss} v_S) R \\ &= (P_{G,ss} v_G - P_{S,ss} v_S) R - (\Delta f_G v_G + \Delta f_S v_S) \alpha v_G R U \\ &= v_R R - c_{RU} R U \end{aligned} \tag{4.157}$$

with:

$$c_{RU} = \frac{2}{\pi} v_G (\Delta f_G v_G + \Delta f_S v_S) \tag{4.158}$$

Therefore, accounting for contact inhibition adds an additional RU term in the U equation, whose coefficient corresponds to the c_{RU} coefficient that was introduced previously.

In addition, we also consider modeling the effect of contact inhibition as "sticky" contacts. In this case, upon contact, a tip does not start shrinking right away, but instead pauses for some time, which is regarded as promoting the $G \to P$ transition in the master equation:

$$\frac{dP_S(t)}{dt} = -(k_{SP} + k_{SG}) P_S(t) + k_{PS} P_P(t) + k_{GS} P_G(t) \tag{4.159}$$

$$\frac{dP_P(t)}{dt} = -(k_{PS} + k_{PG}) P_P(t) + k_{SP} P_S(t) + k_{GP} P_G(t) + k_{CI} P_G(t) \tag{4.160}$$

$$\frac{dP_G(t)}{dt} = -(k_{GS} + k_{GP}) P_G(t) + k_{SG} P_S(t) + k_{PG} P_P(t) - k_{CI} P_G(t) \tag{4.161}$$

Therefore, in the sticky contact assumption, the effective k_{GP} rate is modified. Proceeding through the same process as before, we find the following expressions for the contact inhibition coefficient $\tilde{c}_{RU}$:

$$\frac{d\vec{P}_{ss}}{dk_{GP}} = \frac{k_{PG}(k_{SG}+k_{SP})+k_{PS}k_{SG}}{k_2^4}\begin{pmatrix} k_{PS}-k_{GS} \\ k_{SP}+k_{SG}+k_{GS} \\ -k_{SP}-k_{SG}-k_{PS} \end{pmatrix} \tag{4.162}$$

$$\Delta\tilde{f}_S = \frac{(k_{PG}(k_{SG}+k_{SP})+k_{PS}k_{SG})(k_{PS}-k_{GS})}{k_2^4} \tag{4.163}$$

$$\Delta\tilde{f}_G = \frac{(k_{PG}(k_{SG}+k_{SP})+k_{PS}k_{SG})(k_{SP}+k_{SG}+k_{PS})}{k_2^4} \tag{4.164}$$

$$\tilde{c}_{RU} = \frac{2}{\pi}v_G(\Delta\tilde{f}_G v_G + \Delta\tilde{f}_S v_S) \tag{4.165}$$

4.6 Death rate estimate of dendritic tips from a first-passage problem with drift and diffusion

The last parameter that remains to be explained in the 2-species model is the tip death rate $k_d(U)$. To derive an expression for the death rate in terms of the microscopic parameters, we treat the dynamical processes of tip growth, collision and death as a 1D biased random walk in a finite domain with a reflecting boundary and an absorbing boundary. More precisely, we imagine that a branch of length x grows with a net drift velocity v_R and diffusion coefficient D_R. The position $x = 0$ corresponds to the branch point position and is treated as an absorbing boundary since the branch disappears when reaching back to the branch point. The position $x = L$ is imagined to be the average length that a branch reaches when colliding with other dendrites, and is treated as a reflecting boundary since the branch tip retracts upon contact with other dendrites. We assume that the branch is initialized

with a length x_0 and we aim to answer the following question: what is the average death rate of the branch?

4.6.1 The first-passage time probability density

To derive an expression for the average death rate, let us first introduce some definitions to frame the first-passage problem. Let $p(x,t|x_0)$ be the probability density that a branch has a length x at time t given that it had an initial length of x_0. Given the drift and diffusion parameters of the branch growth, the differential equation that governs the growth of the branch is the well-know drift-diffusion equation:

$$\frac{\partial p}{\partial t} = -v_R \frac{\partial p}{\partial x} + D_R \frac{\partial^2 p}{\partial x^2} = -\frac{\partial J}{\partial x} \tag{4.166}$$

$$J(x,t) = v_R p - D_R \frac{\partial p}{\partial x} \tag{4.167}$$

where $J(x,t)$ is the probability density flux. As explained above, the initial and boundary conditions are:

$$p(x,0|x_0) = \delta(x - x_0) \tag{4.168}$$

$$p(0,t|x_0) = 0 \tag{4.169}$$

$$J(L,t) = v_R p(L,t|x_0) - D_R \frac{\partial p(x,t|x_0)}{\partial x}\bigg|_{x=L} = 0 \tag{4.170}$$

where $\delta(x)$ is the Dirac delta function.

Let us define $f(\tau)$ as the first-passage time probability density, where $f(\tau)d\tau$ represents the probability that a tip of initial length x_0 reaches the origin $x = 0$ at time τ. The definition of $f(\tau)$ is closely related to the survival probability $S(t)$ that the branch tip hasn't reached the origin $x = 0$ at time t. The survival probability

is simply given by the integral of the probability density $p(x,t|x_0)$ over the spatial domain:

$$S(t) = \int_0^L p(x,t|x_0)dx \tag{4.171}$$

Given $S(t)$, the probability that the tip reaches the origin between time τ and $\tau + d\tau$ is given by the difference of the survival probability between these two times. In other words:

$$f(\tau)d\tau = S(\tau) - S(\tau + d\tau) \tag{4.172}$$

In the infinitesimal limit $d\tau \to 0$, we obtain the following definition for $f(\tau)$:

$$f(\tau) = -\frac{\partial S(\tau)}{\partial \tau} \tag{4.173}$$

This also implies the following relation between $S(t)$ and $f(\tau)$ assuming that $S(0) = 1$:

$$S(t) = 1 - \int_0^t f(\tau)d\tau \tag{4.174}$$

With the first-passage time probability density $f(\tau)$, the mean first-passage time is simply defined as the first moment of this distribution:

$$\langle \tau \rangle = \int_0^\infty f(\tau)\tau d\tau \tag{4.175}$$

Moreover, we define the average death rate as:

$$k_d = \langle \frac{1}{\tau} \rangle = \int_0^\infty \frac{1}{\tau} f(\tau)d\tau \tag{4.176}$$

One can also define another death rate k_d' from the inverse of the mean first-passage time:

$$k_d' = \frac{1}{\langle \tau \rangle} \tag{4.177}$$

In our analysis, we will use k_d as the definition of the death rate since k_d' underestimates the effect of short-lived branches.

It is also useful to derive equivalent formulas in the Laplace temporal space $t \to s$. Using well-known Laplace transform identities, we have the following expressions:

$$\tilde{S}(s) = \int_0^\infty S(t) e^{-st} dt, \qquad F(s) = \int_0^\infty f(t) e^{-st} dt \tag{4.178}$$

$$\lim_{t\to\infty} S(t) = 1 - F(0) \tag{4.179}$$

$$\langle \tau \rangle = \lim_{s\to 0} \frac{-dF(s)}{ds} \tag{4.180}$$

$$\langle \frac{1}{\tau} \rangle = \int_0^\infty F(s) ds \tag{4.181}$$

$$\tilde{S}(s) = \frac{1 - F(s)}{s} \tag{4.182}$$

4.6.2 Mean first-passage time vs lifetime

A subtlety arises in the mean first-passage time formula. In the case where no particles survive at long times, $f(\tau)$ is properly normalized as a probability distribution and the mean first-passage time represents the average lifetime of the particles:

$$\lim_{t\to\infty} S(t) = 0 \Rightarrow \int_0^\infty f(\tau) d\tau = 1 \tag{4.183}$$

However, in the case where some particles survive at long times, which can happen for example in infinite spatial domains, the mean first-passage time and the average lifetime of the particles differ. In this case, $f(\tau)$ accounts only for the

particles that do not survive as seen in eq. (4.174). To account for the surviving particles, we propose the following formula for the average lifetime of a particle:

$$\langle \tau_\ell \rangle = \lim_{T\to\infty} \left(\int_0^T f(\tau)\tau d\tau + TS(T) \right) \tag{4.184}$$

The intuition behind this formula is simple: the average lifetime at time T is a weighted sum of the particles that did not survive from $t = 0$ to $t = T$ and the particles that survived until time $t = T$. Moreover, by applying the definitions above, one finds that $\langle \tau_\ell \rangle$ is simply given by the integral of the survival probability $S(t)$:

$$\begin{aligned}
\langle \tau_\ell \rangle &= \lim_{T\to\infty} \left(\int_0^T f(\tau)\tau d\tau + TS(T) \right) \\
&= \lim_{T\to\infty} \left(-\int_0^T \frac{\partial S(\tau)}{\partial \tau}\tau d\tau + TS(T) \right) \\
&= \lim_{T\to\infty} \left(-S(\tau)\tau\Big|_0^T + \int_0^\infty S(\tau)d\tau + TS(T) \right) \\
&= \int_0^\infty S(\tau)d\tau
\end{aligned} \tag{4.185}$$

As we can see, the average lifetime of the particles is finite only when the survival probability decays sufficiently fast with time t. Otherwise, when $\lim_{t\to\infty} tS(t) \neq 0$, the average lifetime diverges, capturing the intuition that some particles survive indefinitely. Therefore, when particles survive at long times, the system can still have a finite mean first-passage time $\langle \tau \rangle$ while having an infinite mean lifetime. This is simply stating that, if a particle reaches back to the origin, it will do so in a finite time, which on average is given by $\langle \tau \rangle$. We can also build the same intuition using the Laplace transforms introduced previously. First, note that:

$$\langle \tau_\ell \rangle = \lim_{s\to 0} \tilde{S}(s) \tag{4.186}$$

Analyzing the cases of surviving or no-surviving particles separately, we have:

1. Surviving particles ($\lim_{t\to\infty} S(t) \neq 0$)

$$\lim_{t\to\infty} S(t) = 1 - F(0) \neq 0 \tag{4.187}$$

$$\langle \tau_\ell \rangle = \lim_{s\to 0} \tilde{S}(s) = \lim_{s\to 0} \frac{1-F(s)}{s} = \infty \tag{4.188}$$

As we see, the average lifetime diverges due to the $\frac{1}{s}$ singularity.

2. No surviving particles ($\lim_{t\to\infty} S(t) = 0$)

$$\lim_{t\to\infty} S(t) = 1 - F(0) = 0 \tag{4.189}$$

$$\langle \tau_\ell \rangle = \lim_{s\to 0} \tilde{S}(s) = \lim_{s\to 0} \frac{1-F(s)}{s} \overset{\text{L'Hôpital}}{=} \lim_{s\to 0} \frac{-F'(s)}{1} = \langle \tau \rangle \tag{4.190}$$

In this case, the $\frac{1}{s}$ singularity of $\tilde{S}(s)$ is an essential singularity that is cured by the fact that $1 - F(s)$ also converges to 0 as $s \to 0$ since no particles survive at long times.

4.6.3 First-passage problem in a semi-infinite spatial domain

Before deriving the complete solution of the first-passage problem that models the branch growth, we study the case where the branch grows unhindered in a semi-infinite domain. In the infinite domain $x \in (-\infty, \infty)$, the solution of the drift-diffusion equation is the well-known expanding Gaussian (see [68]):

$$\frac{\partial p}{\partial t} = -v_R \frac{\partial p}{\partial x} + D_R \frac{\partial^2 p}{\partial x^2} \tag{4.191}$$

$$p(x, 0|x_0) = \delta(x - x_0) \tag{4.192}$$

$$p(x, t|x_0) = \frac{1}{\sqrt{4\pi D_R t}} e^{\frac{-(x-x_0-v_R t)^2}{4D_R t}} \tag{4.193}$$

To solve the same equation in the semi-infinite domain $x \in [0, \infty)$, we use the method of images and the solution of the infinite domain. Since the particle is initialized

at $x = x_0$, the image particle must be located at $x = -x_0$ in order to satisfy the absorbing boundary condition at $x = 0$. Therefore, the semi-infinite domain solution is given by:

$$p(x,t|x_0) = \frac{1}{\sqrt{4\pi D_R t}} \left(e^{\frac{-(x-x_0-v_R t)^2}{4D_R t}} - e^{-\frac{v_R x_0}{D_R}} e^{\frac{-(x+x_0-v_R t)^2}{4D_R t}} \right) \tag{4.194}$$

where the weight of the image particle $e^{-\frac{v_R x_0}{D_r}}$ is tuned to satisfy the condition $p(0,t|x_0) = 0$ at all times. With this solution, we calculate the survival probability by integrating over the semi-infinite domain:

$$\begin{aligned} S(t) &= \int_0^\infty p(x,t,|x_0) dx \\ &= \frac{1}{2} \left(1 - e^{-\frac{x_0 v_R}{D_R}} \left(1 + \operatorname{erf}\left(\frac{-x_0 + t v_R}{2\sqrt{t D_R}} \right) \right) + \operatorname{erf}\left(\frac{x_0 + t v_R}{2\sqrt{t D_R}} \right) \right) \end{aligned} \tag{4.195}$$

$$\operatorname{erf}(z) = \frac{2}{\sqrt{\pi}} \int_0^z e^{-t^2} dt \tag{4.196}$$

where $\operatorname{erf}(z)$ is the error function. Taking the derivative of $S(t)$, we get the first-passage time density function $f(\tau)$:

$$f(\tau) = \frac{x_0}{2\sqrt{\pi D_R} \tau^{3/2}} e^{-\frac{(x_0 + \tau v_R)^2}{4D\tau}} \tag{4.197}$$

The mean first-passage time is then:

$$\langle \tau \rangle = \int_0^\infty \tau f(\tau) d\tau = \frac{x_0}{v_R} e^{-\frac{v_R x_0}{D_R}} \tag{4.198}$$

At first glance, this is somewhat unintuitive since the mean first-passage time decreases as the initial length x_0 increases. Indeed, one might expect the mean first-passage time to increase as x_0 increases. This intuition holds for the lifetime of the particles or the survival probability of the particles at a given time t, but not for the first-passage time. Recall that the first-passage time is the time that a

particle returns to the origin, *given that it returns*. Particles that do not return are not accounted for in the first-passage time density function. The reason why the mean first-passage time decreases with increasing x_0 is due to the interplay between the drift and diffusion. If a particle must return, it must do so through a diffusive motion since the drift is moving the particle away from the origin. Therefore, if the particle returns to the origin, it must do so in a short time period since the drift motion overthrows the diffusive motion at long times. As x_0 increases, it becomes even more difficult for diffusion to overthrow drift and bring the particle back to the origin. Therefore, the return to the origin must take a shorter time as x_0 increases such that the drift doesn't have sufficient time to counter the diffusive motion.

Finally, we find the following expression for the mean death rate in the semi-infinite domain:

$$k_d = \langle \frac{1}{\tau} \rangle = \int_0^\infty \frac{1}{\tau} f(\tau) d\tau = \frac{e^{-\frac{x_0 v_R}{D_R}} (2D_R + x_0 v_R)}{x_0^2} \tag{4.199}$$

Note that this is a monotonic function of x_0, i.e. $\forall x_0 > 0, \frac{dk_d}{dx_0} < 0$.

4.6.4 First-passage problem in a finite spatial domain

Although solving first-passage problems in infinite spatial domains provide intuition on the death process, the growth of the tip occurs in a finite spatial domain where the upper boundary $x = L$ is reflecting and models the growth inhibition by contacts. To derive an expression of the average death rate in this context, we first solve for the Laplace transform of the first-passage time probability density $F(s)$.

Recall that $p(x,t|x_0)$ is the probability density that a branch has a length x at time t given that it had an initial length of x_0. The differential equation that determines the evolution of this probability is the same as introduced before:

$$\frac{\partial p}{\partial t} = -v_R \frac{\partial p}{\partial x} + D_R \frac{\partial^2 p}{\partial x^2} = -\frac{\partial J}{\partial x} \tag{4.200}$$

$$J(x,t) = v_R p - D_R \frac{\partial p}{\partial x} \tag{4.201}$$

where $\delta(x)$ is the Dirac delta function and $J(x,t)$ is the probability density flux. In the finite spatial domain relevant to tip growth, the initial and boundary conditions become:

$$p(x,0|x_0) = \delta(x - x_0) \tag{4.202}$$

$$p(0,t|x_0) = 0 \tag{4.203}$$

$$J(L,t) = v_R p(L,t|x_0) - D_R \left.\frac{\partial p(x,t|x_0)}{\partial x}\right|_{x=L} = 0 \tag{4.204}$$

Next, we apply the Laplace transform of the probability density $p(x,t|x_0)$ over the temporal coordinate t:

$$P(x,s) = \int_0^\infty e^{-st} p(x,t) dt \tag{4.205}$$

The differential and boundary conditions for $P(x,s)$ become:

$$sP - p(x,0) = -v_R \frac{\partial P}{\partial x} + D_R \frac{\partial^2 P}{\partial x^2} \tag{4.206}$$

$$\Rightarrow sP + v_R \frac{\partial P}{\partial x} - D_R \frac{\partial^2 P}{\partial x^2} = \delta(x - x_0) \tag{4.207}$$

$$P(0,s) = 0 \tag{4.208}$$

$$J(L,s) = v_R P(L,s) - D_R \left.\frac{\partial P(x,s)}{\partial x}\right|_{x=L} = 0 \tag{4.209}$$

As we can see, solving for $P(s,x)$ amounts to solving for the Green's function of the operator on the left of eq. (4.207). The general solution to the homogeneous equation is:

$$P(x,s) = A_+ e^{k_+(s)x} + A_- e^{k_-(s)x} \tag{4.210}$$

$$k_\pm(s) = \frac{v_R \pm \sqrt{v_R^2 + 4D_R s}}{2D_R} = \frac{v_R}{2D_R} \pm \lambda(s) \tag{4.211}$$

$$\lambda(s) = \frac{\sqrt{v_R^2 + 4D_R s}}{2D_R} \tag{4.212}$$

For $x < x_0$, the left Green's function must satisfy the absorbing boundary condition $P(0,s) = 0$, which implies the following solution:

$$P_L(x,s) = A_L e^{\frac{v_R}{2D_R}x} \sinh(\lambda(s)x) \tag{4.213}$$

For $x > x_0$, the right Green's function must satisfy the reflecting boundary condition, which implies the following solution:

$$0 = v_R\left(A_+ e^{k_+ L} + A_- e^{k_- L}\right) - D_R\left(A_+ k_+ e^{k_+ L} + A_- k_- e^{k_- L}\right) \tag{4.214}$$

$$\Rightarrow A_+ = (v_R - D_R k_-) e^{-k_+ L} A_R, \quad A_- = -(v_R - D_R k_+) e^{-k_- L} A_R \tag{4.215}$$

$$\begin{aligned}
\Rightarrow P_R(x,s) &= A_R\left(e^{k_+(-L+x)}(v_R - k_- D_R) - e^{k_-(-L+x)}(v_R - k_+ D_R)\right) \\
&= A_R e^{\frac{v_R}{2D_R}(-L+x)}\left(e^{\lambda(-L+x)}(v_R - k_- D_R) - e^{-\lambda(-L+x)}(v_R - k_+ D_R)\right) \\
&= A_R e^{\frac{(-L+x)v_R}{2D_R}}\left(2\lambda D_R \cosh(\lambda(L-x)) - v_R \sinh(\lambda(L-x))\right)
\end{aligned} \tag{4.216}$$

Next, we impose continuity of the Green's function at $x = x_0$:

$$P_L(x_0, s) = P_R(x_0, s) \tag{4.217}$$

$$A_L e^{\frac{v_R x_0}{2D_R}} \sinh(\lambda x_0) = A_R e^{\frac{v_R(-L+x_0)}{2D_R}} \left(2\lambda D_R \cosh(\lambda(L-x_0)) - v_R \sinh(\lambda(L-x_0))\right) \tag{4.218}$$

$$A_L = \frac{A e^{-\frac{v_R x_0}{2D_R}}}{\sinh(\lambda x_0)} \tag{4.219}$$

$$A_R = \frac{A e^{-\frac{v_R(-L+x_0)}{2D_R}}}{2\lambda D_R \cosh(\lambda(L-x_0)) - v_R \sinh(\lambda(L-x_0))} \tag{4.220}$$

The left and right Green's function become:

$$P_L(x, s) = A e^{\frac{v_R(x-x_0)}{2D_R}} \left(\frac{\sinh(\lambda x)}{\sinh(\lambda x_0)}\right) \tag{4.221}$$

$$P_R(x, s) = A e^{\frac{v_R(x-x_0)}{2D_R}} \left(\frac{2\lambda D_R \cosh(\lambda(L-x)) - v_R \sinh(\lambda(L-x))}{2\lambda D_R \cosh(\lambda(L-x_0)) - v_R \sinh(\lambda(L-x_0))}\right) \tag{4.222}$$

Finally, the last arbitrary constant A is fixed by the discontinuity of the first derivative:

$$\lim_{\epsilon \to 0} \int_{x_0-\epsilon}^{x_0+\epsilon} \left(sP + v_R \frac{\partial P}{\partial x} - D_R \frac{\partial^2 P}{\partial x^2}\right) dx = 1 \tag{4.223}$$

$$v_R \left(P_R(x_0, s) - P_L(x_0, s)\right) - D_R \left(P_R'(x_0, s) - P_L'(x_0, s)\right) = 1 \tag{4.224}$$

$$P_R'(x_0, s) - P_L'(x_0, s) = \frac{-1}{D_R} \tag{4.225}$$

where $'$ denotes derivatives with respect to x. In the simplification of the last line, we used the continuity of $P(x, s)$ at $x = x_0$. Imposing the discontinuity condition, we obtain the following expression for A:

$$-\frac{1}{D_R} = -A\lambda \left(\frac{\cosh(\lambda x_0)}{\sinh(\lambda x_0)}\right) + A \frac{\left(-2\lambda^2 D_R \sinh(\lambda(L-x_0)) + \lambda v_R \cosh(\lambda(L-x_0))\right)}{2\lambda D_R \cosh(\lambda(L-x_0)) - v_R \sinh(\lambda(L-x_0))} \tag{4.226}$$

$$A = \frac{\sinh(\lambda x_0)\left(2\lambda D_R \cosh(\lambda(L-x_0)) - v_R \sinh(\lambda(L-x_0))\right)}{\lambda D_R \left(2\lambda D_R \cosh(\lambda L) - v_R \sinh(\lambda L)\right)} \tag{4.227}$$

The final expression for the Green's function is then:

$$P(x,s) = \begin{cases} e^{\frac{v_R(x-x_0)}{2D_R}} \frac{\sinh(\lambda x)(2\lambda D_R \cosh(\lambda(L-x_0)) - v_R \sinh(\lambda(L-x_0)))}{\lambda D_R(2\lambda D_R \cosh(\lambda L) - v_R \sinh(\lambda L))} & x \leq x_0 \\ e^{\frac{v_R(x-x_0)}{2D_R}} \frac{\sinh(\lambda x_0)(2\lambda D_R \cosh(\lambda(L-x)) - v_R \sinh(\lambda(L-x)))}{\lambda D_R(2\lambda D_R \cosh(\lambda L) - v_R \sinh(\lambda L))} & x > x_0 \end{cases} \tag{4.228}$$

$$= e^{\frac{v_R(x-x_0)}{2D_R}} \frac{\sinh(\lambda x_<)\left(2\lambda D_R \cosh\left(\lambda\left(L-x_>\right)\right) - v_R \sinh\left(\lambda\left(L-x_>\right)\right)\right)}{\lambda D_R\left(2\lambda D_R \cosh(\lambda L) - v_R \sinh(\lambda L)\right)} \tag{4.229}$$

$$x_< = \min(x, x_0) \tag{4.230}$$

$$x_> = \max(x, x_0) \tag{4.231}$$

Using this solution, we now find an expression for the Laplace transform of the first-passage time probability density $F(s)$ by evaluating the Laplace-transformed flux $J(x,s)$ at $x = 0$:

$$f(\tau) = -\frac{dS(\tau)}{d\tau} = -\int_0^L \frac{\partial p(x,\tau|x_0)}{\partial \tau} dx = \int_0^L \frac{\partial J(x,\tau)}{\partial x} dx = -J(0,\tau) \tag{4.232}$$

$$\begin{aligned} \Rightarrow F(s) &= -J(0,s) \\ &= -\left(v_R P(0,s) - D_R \left.\frac{\partial P(x,s)}{\partial x}\right|_{x=0}\right) \\ &= -\left(v_R P_L(0,s) - D_R \left.\frac{\partial P_L(x,s)}{\partial x}\right|_{x=0}\right) \\ &= \frac{e^{-\frac{v_R x_0}{2D_R}}\left(2\lambda D_R \cosh\left(\lambda\left(L-x_0\right)\right) - v_R \sinh\left(\lambda\left(L-x_0\right)\right)\right)}{2\lambda D_R \cosh(\lambda L) - v_R \sinh(\lambda L)} \end{aligned} \tag{4.233}$$

where $\lambda = \lambda(s)$ is a function of s. For finite L, the mean first-passage time is:

$$\begin{aligned}
\langle \tau \rangle &= \lim_{s\to 0} \frac{-dF(s)}{ds} \\
&= \lim_{s\to 0} -e^{-\frac{v_R x_0}{2D_R}} \lambda'(s) \\
&\left(\frac{(2\lambda D_R \cosh(\lambda(L-x_0)) - v_R \sinh(\lambda(L-x_0)))\left((2D_R - Lv_R)\cosh(L\lambda) + 2L\sinh(L\lambda)D_R\lambda\right)}{\left(2D_R\lambda\cosh(L\lambda) - v_R\sinh(L\lambda)\right)^2} \right. \\
&\left. - \frac{(2\lambda D_R (L-x_0)\sinh(\lambda(L-x_0)) + (2D_R - v_R(L-x_0))\cosh(\lambda(L-x_0)))}{2D_R\lambda\cosh(L\lambda) - v_R\sinh(L\lambda)} \right) \\
&= \frac{e^{-\frac{v_R x_0}{2D_R}} \left(2D_R \sinh\left(\frac{v_R x_0}{2D_R}\right) + v_R x_0 \left(\cosh\left(\frac{v_R(2L-x_0)}{2D_R}\right) - \sinh\left(\frac{v_R(2L-x_0)}{2D_R}\right)\right)\right)}{\left(\cosh\left(\frac{Lv_R}{2D_R}\right) - \sinh\left(\frac{Lv_R}{2D_R}\right)\right)^2 v_R^2} \\
&= \frac{D_R e^{\frac{Lv_R}{D_R}}}{v_R^2}\left(1 - e^{\frac{-v_R x_0}{D_R}}\right) - \frac{x_0}{v_R}
\end{aligned} \tag{4.234}$$

which coincides with our previous expression of the mean first-passage time in the semi-infinite domain (see eq. (4.198)).

To verify our expression, we analyze the limit $L \to \infty$ and compare our expression with our previous results. First, we go back to the expression for $F(s)$ before taking the $s \to 0$:

$$F(s) \overset{L\to\infty}{\approx} e^{-\frac{v_R x_0}{2D_R}} e^{-\lambda x_0} = e^{-\left(\frac{v_R + \sqrt{v_R^2 + 4D_R s}}{2D_R}\right) x_0} \tag{4.235}$$

The corresponding mean first-passage time is then:

$$\begin{aligned}
\langle \tau_\infty \rangle &= \lim_{s\to 0} \lim_{L\to\infty} \frac{-dF(s)}{ds} \\
&= \lim_{s\to 0} \frac{e^{-\left(\frac{v_R + \sqrt{v_R^2 + 4D_R s}}{2D_R}\right) x_0} x_0}{\sqrt{4sD_R + v_R^2}} \\
&= \frac{x_0}{v_R} e^{-\frac{v_R x_0}{D_R}}
\end{aligned} \tag{4.236}$$

which agrees with out previous expression (eq. (4.198)). Furthermore, we also recover the full distribution $f(\tau)$ by taking the inverse Laplace transform of $F(s)$, which amounts to taking the inverse Fourier transform since $F(s)$ has no singularities:

$$\begin{aligned} f(\tau) &= \lim_{T\to\infty} \frac{1}{2\pi i} \int_{-iT}^{iT} e^{s\tau} F(s) ds \\ &= \frac{1}{2\pi} \int_{-\infty}^{\infty} e^{i\omega\tau} F(i\omega) d\omega \qquad s = i\omega \\ &= \frac{1}{2\pi} \int_{-\infty}^{\infty} e^{i\omega\tau} e^{-\left(\frac{v_R + \sqrt{v_R^2 + 4D_R i\omega}}{2D_R}\right) x_0} d\omega \\ &= \frac{x_0}{2\sqrt{\pi D_R}\tau^{3/2}} e^{-\frac{(\tau v_R + x_0)^2}{4\tau D_R}} \end{aligned} \tag{4.237}$$

which is the same expression that was found previously in the semi-infinite domain case (eq. (4.197)).

4.6.5 Mean death rate in the $L \to \infty$ limit

Finally, we derive an expression for the tip's death rate $k_d(U)$ as a non-linear function of the dendrites density U. As an approximation, we only consider the first two leading order terms of $k_d(U)$ in the limit where $U \ll 1$. Since $U \sim \frac{1}{L}$, this limit corresponds to the $L \to \infty$ limit in the first-passage problem considered above:

$$k_d(U) = \langle \frac{1}{\tau} \rangle \approx k_{d,0} + k_{d,1}(U) \tag{4.238}$$

Recall that $k_{d,0}$ was already found in eq. (4.199) when studying the case of a semi-infinite boundary. We now focus on the next order term $k_{d,1}(U)$. To do so,

we use the Laplace transform $F(s)$ of the first-passage time density $f(\tau)$ in finite domain case:

$$k_d = \langle \frac{1}{\tau} \rangle = \int_0^\infty \frac{1}{\tau} f(\tau) d\tau = \int_{0^+}^\infty F(s) ds \tag{4.239}$$

where $F(s)$ was derived in eq. (4.233):

$$F(s) = \frac{e^{-\frac{v_R x_0}{2D_R}} \left(2\lambda D_R \cosh\left(\lambda\left(L - x_0\right)\right) - v_R \sinh\left(\lambda\left(L - x_0\right)\right)\right)}{2\lambda D_R \cosh(\lambda L) - v_R \sinh(\lambda L)} \tag{4.240}$$

$$\lambda(s) = \frac{\sqrt{v_R^2 + 4D_R s}}{2D_R} \tag{4.241}$$

To simplify the expressions, we use the following dimensionless variables:

$$t = \sqrt{1 + \frac{4D_R}{v_R^2} s} \tag{4.242}$$

$$P_e = \frac{v_R L}{2D_R} \tag{4.243}$$

$$y_0 = \frac{v_R x_0}{2D_R} \tag{4.244}$$

In terms of these variables, the $L \to \infty$ limit translates to $P_e \to \infty$. Using these expressions yields the following expression for k_d:

$$k_d = \frac{v_R^2 e^{-y_0}}{2D_R} \int_1^\infty F(t) dt \tag{4.245}$$

$$F(t) = \frac{t\left(t\cosh\left(\left(P_e - y_0\right)t\right) - \sinh\left(\left(P_e - y_0\right)t\right)\right)}{t\cosh\left(P_e t\right) - \sinh\left(P_e t\right)} \tag{4.246}$$

$$= t e^{-y_0 t} \left(\frac{t - 1 + (t+1) e^{-2t(Pe - y_0)}}{t - 1 + (t+1) e^{-2tPe}} \right) \tag{4.247}$$

In the limit $P_e \to \infty$, the zeroth-order term in $F(t)$ is given by:

$$F^{(0)}(t) = t e^{-y_0 t} \tag{4.248}$$

Integrating over t gives the zeroth-order term of the death rate:

$$\begin{aligned} k_{d,0} &= \frac{v_R^2 e^{-y_0}}{2D_R} \int_1^\infty F^{(0)}(t)dt \\ &= \frac{v_R^2 e^{-y_0}}{2D_R} \left(e^{-y_0} \left(\frac{1+y_0}{y_0^2} \right) \right) \\ &= \frac{e^{-\frac{v_R x_0}{D_R}} (2D_R + v_R x_0)}{x_0^2} \end{aligned} \tag{4.249}$$

which corresponds to the same quantity that we found before in eq. (4.199). To derive the next order, we subtract the zeroth-order term from the full expression of $F(t)$ and retain only the leading order terms:

$$\begin{aligned} F^{(1)}(t) &= F(t) - F^{(0)}(t) \\ &= te^{-ty_0} \left(\frac{t-1+(t+1)e^{-2t(P_e-y_0)}}{t-1+(t+1)e^{-2tP_e}} - 1 \right) \\ &= te^{-ty_0} e^{-2tP_e} (t+1) \left(\frac{e^{2ty_0}-1}{t-1+(t+1)e^{-2tP_e}} \right) \end{aligned} \tag{4.250}$$

To expand the denominator in this expression, one must be careful since both $f_1(t) = t-1$ and $f_2(t) = (t+1)e^{-2tP_e}$ can be small over the integration range and in the $P_e \to \infty$ limit. Note that $f_1(t)$ is monotonically increasing for $t \in (1, \infty)$, while $f_2(t)$ is monotonically decreasing (given P_e is large enough). Therefore, we expect a cross-over point t_* where $f_1(t_*) = f_2(t_*)$. To find this point, we need to solve the following transcendental equation:

$$t_* - 1 = (t_* + 1)e^{-2t_* P_e} \tag{4.251}$$

$$\Rightarrow t_* = 1 + (t_* + 1)e^{-2t_* P_e} \tag{4.252}$$

To solve for t_*, we iterate the approximation for t_* using the transcendental equation. To zeroth-order, we have:

$$t_*^{(0)} = 1 \tag{4.253}$$

Substituting this expression back into the transcendental equation yields the first-order estimate:

$$\begin{aligned} t_*^{(1)} &\approx 1 + (t_*^{(0)} + 1) e^{-2t^{*(0)} P_e} \\ &= 1 + 2e^{-2P_e} \\ &= 1 + r_* \end{aligned} \tag{4.254}$$

$$r_* = 2e^{-2P_e} \tag{4.255}$$

Using $t_* = t_*^{(1)}$ as the cross-over point and the monotonicity of $f_1(t)$ and $f_2(t)$, we can ensure that there is non-vanishing expansion center by splitting the integral range into two parts:

$$t \in (1, 1 + r_*) \Rightarrow f_1(t) \leq f_2(t) \tag{4.256}$$

$$t \in (1 + r_*, \infty) \Rightarrow f_1(t) \geq f_2(t) \tag{4.257}$$

$$\int_1^\infty F^{(1)}(t) dt = I_L + I_R \tag{4.258}$$

$$I_L = \int_1^{1+r_*} F^{(1)}(t) dt \tag{4.259}$$

$$I_R = \int_{1+r_*}^\infty F^{(1)}(t) dt \tag{4.260}$$

Below the cross-over point t_*, $F^{(1)}(t)$ is exponentially close to $t = 1$ in the large P_e limit. This warrants a Taylor expansion of the integrand around $t = 1$. We then obtain the following expression for I_L:

$$F_L^{(1)}(t) = 2\sinh(y_0) + \left(-e^{2P_e}\sinh(y_0) + 2(y_0\cosh(y_0) + \sinh(y_0))\right)(t-1) + O\left((t-1)^2\right) \tag{4.261}$$

$$\begin{aligned} \Rightarrow I_L &= \int_1^{1+r_*} F_L^{(1)}(t) dt \\ &\approx 2\sinh(y_0) r_* + \left(-e^{2P_e}\sinh(y_0) + 2(y_0\cosh(y_0) + \sinh(y_0))\right) \frac{r_*^2}{2} \\ &\approx 2\sinh(y_0) e^{-2P_e} + 4\left(y_0\cosh(y_0) + \sinh(y_0)\right) e^{-4P_e} \end{aligned} \tag{4.262}$$

For the part above the cross-over point, we expand the denominator around $f_1(t)$ since it is greater than $f_2(t)$. We then obtain the following approximation for $F_R^{(1)}(t)$:

$$\begin{aligned} F_R^{(1)}(t) &= te^{-ty_0}e^{-2tP_e}\,(t+1)\left(\frac{e^{2ty_0}-1}{t-1+(t+1)e^{-2tP_e}}\right) \\ &= te^{-ty_0}e^{-2tP_e}\left(\frac{t+1}{t-1}\right)\left(\frac{e^{2ty_0}-1}{1+\frac{t+1}{t-1}e^{-2tP_e}}\right) \\ &\approx te^{-ty_0}e^{-2tP_e}\left(\frac{t+1}{t-1}\right)\left(e^{2ty_0}-1\right)\left(1-\frac{t+1}{t-1}e^{-2tP_e}\right) \end{aligned} \tag{4.263}$$

To simplify the notation further, we recast the above expression using the variable $r = t-1$:

$$F_R^{(1)}(r) = (r+1)e^{-(r+1)(2P_e+y_0)}\left(\frac{r+2}{r}\right)\left(e^{2(r+1)y_0}-1\right)\left(1-\frac{r+2}{r}e^{-2(r+1)P_e}\right) \tag{4.264}$$

$$= e^{-(r+1)(2P_e+y_0)}\left(e^{2(r+1)y_0}-1\right)\left(r+3+\frac{2}{r}-\left(r+5+\frac{8}{r}+\frac{4}{r^2}\right)e^{-2(r+1)P_e}\right) \tag{4.265}$$

When integrating $F_R^{(1)}(r)$ over the range (r_*,∞), integrands will have the form $r^n e^{-a(r+1)}$, where $n \in \{-2,-1,0,1\}$. Therefore, we evaluate the following generic integrals in the limit where r_* is small:

$$h(a,r_*,n) = \int_{r_*}^{\infty} r^n e^{-a(r+1)}dr \tag{4.266}$$

The relevant solutions for $h(a, r_*, n)$ are given by:

$$h(a, r_*, 1) = \frac{(1 + ar_*)}{a^2} e^{-a(1+r_*)} \tag{4.267}$$

$$h(a, r_*, 0) = \frac{1}{a} e^{-a(1+r_*)} \tag{4.268}$$

$$h(a, r_*, -1) = e^{-a} \Gamma(0, ar_*) \tag{4.269}$$

$$h(a, r_*, -2) = e^{-a} \left(\frac{e^{-ar_*}}{r_*} - a\Gamma(0, ar_*) \right) \tag{4.270}$$

$$\Gamma(a, b) = \int_b^\infty t^{a-1} e^{-t} dt \tag{4.271}$$

where $\Gamma(a, b)$ is the incomplete Gamma function. Since r_* is exponentially small, we seek an expression for $\Gamma(0, x)$ in the limit where x is small:

$$\Gamma(0, x) = -\gamma - \log(x) + x + O(x^2) \tag{4.272}$$

where $\gamma \approx 0.577216$ is the Euler-Mascheroni constant. Expanding all terms in eq. (4.265), we obtain the following expression for I_R:

$$\begin{aligned}
I_R = {} & h(2P_e - y_0, r_*, 1) - h(2P_e + y_0, r_*, 1) \\
& - h(4P_e - y_0, r_*, 1) + h(4P_e + y_0, r_*, 1) \\
& + 3h(2P_e - y_0, r_*, 0) - 3h(2P_e + y_0, r_*, 0) \\
& - 5h(4P_e - y_0, r_*, 0) + 5h(4P_e + y_0, r_*, 0) \\
& + 2h(2P_e - y_0, r_*, -1) - 2h(2P_e + y_0, r_*, -1) \\
& - 8h(4P_e - y_0, r_*, -1) + 8h(4P_e + y_0, r_*, -1) \\
& - 4h(4P_e - y_0, r_*, -2) + 4h(4P_e + y_0, r_*, -2)
\end{aligned} \tag{4.273}$$

Before unpacking all these terms, let us analyze their general form at the leading order in the $P_e \to \infty$ limit:

$$\begin{aligned} h\left(nP_e \pm y_0, r_*, 1\right) &\approx \frac{\left(1+2(nP_e \pm y_0)e^{-2P_e}\right)}{(nP_e \pm y_0)^2} e^{-(nP_e \pm y_0)} \\ &\approx \frac{1}{(nP_e \pm y_0)^2} e^{-(nP_e \pm y_0)} \end{aligned} \tag{4.274}$$

$$h\left(nP_e \pm y_0, r_*, 0\right) \approx \frac{1}{nP_e \pm y_0} e^{-(nP_e \pm y_0)} \tag{4.275}$$

$$\begin{aligned} h\left(nP_e \pm y_0, r_*, -1\right) &\approx e^{-(nP_e \pm y_0)} \left(-\gamma - \log(nP_e \pm y_0) - \log(2) + 2P_e + 2(nP_e \pm y_0)e^{-2P_e}\right) \\ &\approx 2P_e e^{-(nP_e \pm y_0)} \end{aligned} \tag{4.276}$$

$$\begin{aligned} h\left(nP_e \pm y_0, r_*, -2\right) &\approx e^{-(nP_e \pm y_0)} \Bigg(\frac{e^{-(nP_e \pm y_0)2e^{-2P_e}}}{2e^{-2P_e}} \\ &\quad - (nP_e \pm y_0)\left(-\gamma - \log(nP_e \pm y_0) - \log(2) + 2P_e + 2(nP_e \pm y_0)e^{-2P_e}\right) \Bigg) \\ &\approx e^{-(nP_e \pm y_0)} \left(\frac{\left(1 - (nP_e \pm y_0)2e^{-2P_e}\right)e^{2P_e}}{2} - (nP_e \pm y_0)\left(2P_e\right) \right) \\ &\approx e^{-(nP_e \pm y_0)} \left(\frac{e^{2P_e}}{2} - 2P_e(nP_e \pm y_0) \right) \end{aligned} \tag{4.277}$$

where n is assumed to be a positive integer. As we can see, the leading order terms arise from $h\left(2P_e \pm y_0, r_*, -1\right)$ and $h\left(4P_e \pm y_0, r_*, -2\right)$. Unpacking these expressions, we have:

$$\begin{aligned} I_R &\approx 2h\left(2P_e - y_0, r_*, -1\right) - 2h\left(2P_e + y_0, r_*, -1\right) \\ &\quad - 4h\left(4P_e - y_0, r_*, -2\right) - 4h\left(4P_e + y_0, r_*, -2\right) \\ &\approx 2\left(2P_e e^{-2P_e}\left(2\sinh(y_0)\right)\right) \\ &\quad + 4e^{-4P_e}\left(\left(\frac{e^{2P_e}}{2} - 4P_e^2\right)\left(2\sinh(y_0)\right) - 2P_e y_0\left(-2\cosh(y_0)\right)\right) \\ &\approx 8P_e \sinh(y_0) e^{-2P_e} \end{aligned} \tag{4.278}$$

Since the terms in I_R are leading the terms in I_L, we can omit I_L altogether. The final expression for $k_{d,1}$ becomes:

$$\begin{aligned} k_{d,1} &= \frac{v_R^2 e^{-y_0}}{2D_R}\left(I_L + I_R\right) \\ &\approx \frac{v_R^2 e^{-y_0}}{2D_R}\left(8P_e \sinh(y_0) e^{-2P_e}\right) \\ &= \frac{2P_e v_R^2 e^{-2P_e}}{D_R}\left(1 - e^{-2y_0}\right) \\ &= \frac{L v_R^3 e^{-\frac{v_R L}{D_R}}}{D_R^2}\left(1 - e^{-\frac{v_R x_0}{D_R}}\right) \end{aligned} \tag{4.279}$$

Finally, combining the zeroth and first-order terms of the death rate, we obtain the following approximate expression in limit $L \to \infty$:

$$\begin{aligned} k_d &= \langle \frac{1}{\tau} \rangle \\ &\approx k_{d,0} + k_{d,1} \\ &= \frac{e^{-\frac{v_R x_0}{D_R}}\left(2D_R + v_R x_0\right)}{x_0^2} + \frac{L v_R^3 e^{-\frac{v_R L}{D_R}}}{D_R^2}\left(1 - e^{-\frac{v_R x_0}{D_R}}\right) \end{aligned} \tag{4.280}$$

4.6.6 Stochastic simulation of the 1D biased random walk in a finite domain

To assess the accuracy of our estimate for the mean first-passage time $\langle \tau \rangle$ and the mean death rate $\langle \frac{1}{\tau} \rangle$ in the finite domain case, we performed stochastic simulations of the first-passage problem with the following parameter values:

$$
\begin{aligned}
v_R &= 0.1 \frac{\mu m}{\text{min}} \\
D_R &= 0.5 \frac{\mu m}{\text{min}} \\
x_0 &\in \{1, 1.1, \ldots, 5\} \mu m \\
L &\in \{5, 5.1, \ldots, 10\} \mu m
\end{aligned}
$$

which were chosen in the physiological range of the class IV neuron tip growth. Using the simulation results, we calculate estimates of $\langle \tau \rangle$ and $\langle \frac{1}{\tau} \rangle$ and compare them against our theoretical expressions (eqs. (4.234) and (4.280)) as shown in fig. 4.7. The theoretical estimates are in good agreement with the calculations from the stochastic simulations. However, the theoretical estimate for $\langle \frac{1}{\tau} \rangle$ deviates from the simulation when $L < 7.5 \, \mu m$. This is expected since our approximation relies on the large L limit, which is evidently not satisfied as L approaches 0. Indeed, we find a complete agreement when we calculate a more accurate estimate of the death rate by numerically integrating the full expression of the Laplace transform (see eq. (4.245) and blue line in fig. 4.7).

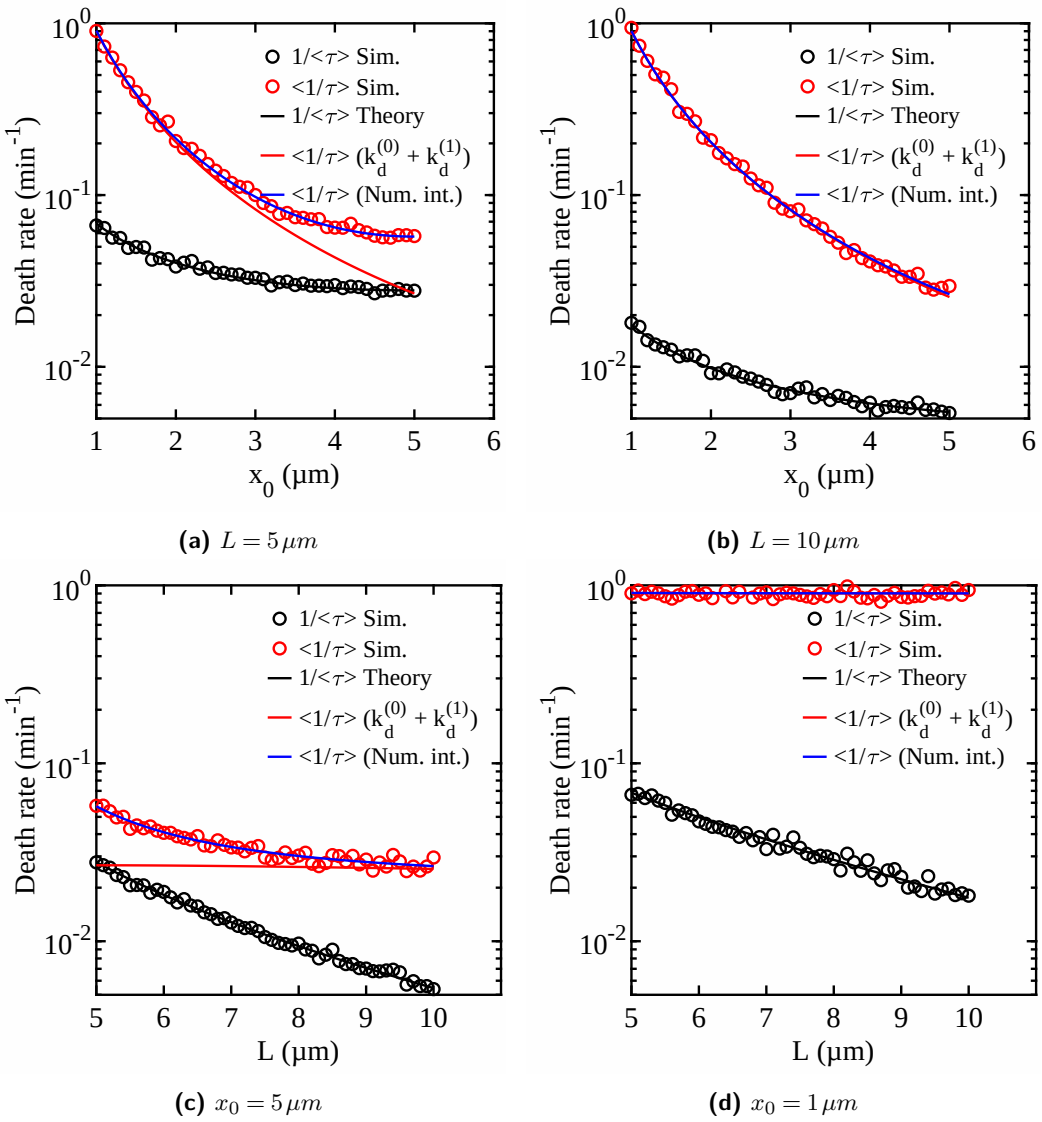

(a) $L = 5\,\mu m$ **(b)** $L = 10\,\mu m$

(c) $x_0 = 5\,\mu m$ **(d)** $x_0 = 1\,\mu m$

Figure 4.7 – Death rate estimates from first-passage stochastic simulations
Each data point corresponds to an average of $N = 1000$ simulations. The results of the simulations for the two different averages are plotted as open circles. The solid line corresponds to the theoretical estimates calculated above.

Moreover, we also find that $\frac{1}{\langle\tau\rangle} < \langle\frac{1}{\tau}\rangle$ for the cases analyzed above. This is due to the fact that short-lived particles have much a bigger impact on $\langle\frac{1}{\tau}\rangle$ in comparison to $\frac{1}{\langle\tau\rangle}$. One can see this in the simulation estimates as well where the difference between $\frac{1}{\langle\tau\rangle}$ and $\langle\frac{1}{\tau}\rangle$ increases when x_0 approaches the absorbing boundary at $x = 0$. This inequality is in fact true in general and is a particular case of Jensen's inequality

[28]. Given a convex function $f(x)$ and a random variable X, Jensen's inequality states the following:

$$f(\langle X \rangle) \leq \langle f(X) \rangle \tag{4.281}$$

In our case, $f(x) = \frac{1}{x}$ is indeed convex in the domain $x \in [0, \infty)$, which is the relevant domain for the first-passage time since $\tau \geq 0$.

4.7 Predictions of the 2-species mean-field model

In summary, the 2-species model consists of the following two differential equations:

$$\frac{\partial U}{\partial t} = v_R R - c_{RU} RU \tag{4.282}$$

$$\frac{\partial R}{\partial t} = -v_r \frac{\partial R}{\partial r} + D_r \frac{\partial^2 R}{\partial r^2} - k_d(U) R + k_b U \tag{4.283}$$

where $k_d(U) = k_{d,0} + k_{d,1}(U)$ is the tips death rate, which is a non-linear function of U, $v_r = c_1 v_R, D_r = c_2 D_R$ are the drift velocity and diffusion constants along the radial direction, and $c_1 = \langle \cos(\psi) \rangle, c_2 = \langle \cos(\psi)^2 \rangle$ account for the orientation of the branches (see section 4.4.1).

The beauty of the mean-field model is that it connects the microscopic parameters of the tip dynamics to the macroscopic properties of the tree. The microscopic parameters are given by the average tip growth parameters v_R, D_R, the transition rates k_{ij}, the average state velocities v_S, v_G, the growth orientation parameters c_1, c_2, the branching rate k_b and the death rate k_d. The macroscopic properties are given by the expansion velocity of the tree V and the steady-state densities of dendrites and branch tips U_{ss}, R_{ss}.

4.7.1 Parameters summary

As a result of our analysis of the tip growth, we obtain quantitative measurements of the microscopic parameters that describe tip growth at 24, 48 and 96 hr AEL. These parameters are summarized in table 4.1.

Parameters\Stage	24 hr AEL	48 hr AEL	96 hr AEL
k_{SP} (min^{-1})	0.204 ± 0.0188	0.200 ± 0.0156	0.428 ± 0.0306
k_{SG} (min^{-1})	0.489 ± 0.0417	0.394 ± 0.0287	0.566 ± 0.0387
k_{PS} (min^{-1})	0.672 ± 0.0578	0.553 ± 0.0467	0.239 ± 0.0131
k_{PG} (min^{-1})	0.465 ± 0.0385	0.366 ± 0.0302	0.248 ± 0.0142
k_{GS} (min^{-1})	0.609 ± 0.0562	0.706 ± 0.0540	0.845 ± 0.0519
k_{GP} (min^{-1})	0.0875 ± 0.00681	0.120 ± 0.00788	0.265 ± 0.0146
v_S ($\mu m\,\text{min}^{-1}$)	0.648 ± 0.0210	0.499 ± 0.0166	0.343 ± 0.00798
v_G ($\mu m\,\text{min}^{-1}$)	0.772 ± 0.0210	0.917 ± 0.0166	0.456 ± 0.00798
k_b ($\text{min}^{-1}\mu m^{-1}$)	0.00937 ± 0.000543	0.00129 ± 0.000104	0.00115 ± 0.000228
c_1	0.411 ± 6.76e-06	0.295 ± 3.19e-06	0.222 ± 7.66e-07
c_2	0.551 ± 3.85e-06	0.537 ± 1.67e-06	0.526 ± 3.90e-07
v_R ($\mu m\,\text{min}^{-1}$)	0.0343 ± 0.000592	0.0200 ± 0.000304	0.00161 ± 0.000451
$v_{R,r}$ ($\mu m\,\text{min}^{-1}$)	0.0141 ± 0.000243	0.00592 ± 8.98e-05	0.000358 ± 0.000100
D_R ($\mu m^2\,\text{min}^{-1}$)	0.354 ± 0.0156	0.258 ± 0.0187	0.0858 ± 0.00293
$D_{R,r}$ ($\mu m^2\,\text{min}^{-1}$)	0.195 ± 0.00859	0.139 ± 0.0101	0.0451 ± 0.00154
$D_{R,\theta}$ (min^{-1})	0.159 ± 0.00700	0.120 ± 0.00867	0.0407 ± 0.00139

Table 4.1 – Model parameters in the 2-species mean-field model
k_{ij} are the tip transition rates determined experimentally (see fig. 3.5), v_S, v_G are the average speed of of the tip in the shrinking and growing state (see fig. 3.3), k_b is the branching rate measured in experiments (see fig. 3.12b), c_1, c_2 are estimated from the branch orientation (see fig. 3.36), v_R, D_R are determined by the track displacement fits (see fig. 4.3), $v_{R,r}$ is determined by eq. (4.68), $D_{R,r}$ is determined by eq. (4.69) and $D_{R,\theta}$ is determined by eq. (4.70)

Moreover, we almost use macroscopic measurements to infer other microscopic parameters. First, we use the expansion velocity of the tree, which is estimated by fitting the neuron size with a spline (see fig. 4.8a). The spline fit's zero is constrained at 14 hr AEL since it corresponds to the start of morphogenesis. Using the fit, we evaluate its derivative to estimate the velocity at each developmental stage (see fig. 4.8b) where the error of the velocities are calculated by bootstrapping the fit. The values of the velocities are shown in table 4.2.

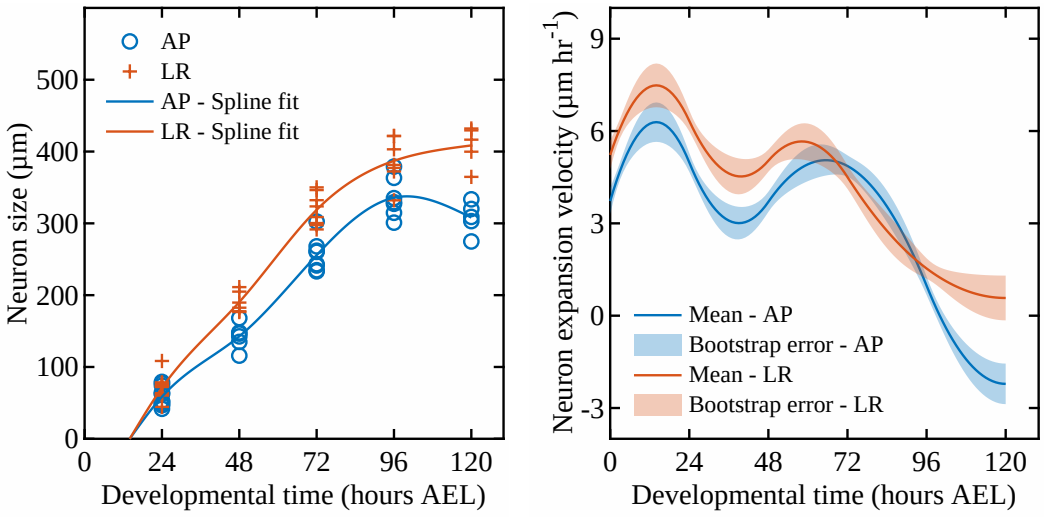

(a) Spline fit of the neuron size **(b)** Spline fit of the neuron expansion velocity

Figure 4.8 – Measurement of the expansion velocity along the AP and LR dimension

	24 hr AEL	48 hr AEL	96 hr AEL
$V_{\text{uni, AP}}$ $(\mu m\,\text{hr}^{-1})$	4.98 ± 0.310	3.70 ± 0.328	0.977 ± 0.299
$V_{\text{uni, LR}}$ $(\mu m\,\text{hr}^{-1})$	6.33 ± 0.343	5.04 ± 0.359	1.53 ± 0.329
$\frac{1}{2}(V_{\text{uni, AP}} + V_{\text{uni, LR}})$ $(\mu m\,\text{hr}^{-1})$	5.65 ± 0.327	4.68 ± 0.366	1.26 ± 0.314

Table 4.2 – Neuron expansion velocity along the AP and LR axes

The other macroscopic properties that we use are the average dendrites and branch tips density as shown in fig. 3.48. These estimates are summarized in table 4.3.

	24 hr AEL	48 hr AEL	96 hr AEL
U_{ss} (μm^{-1})	0.169 ± 0.00906	0.131 ± 0.00259	0.0990 ± 0.00435
R_{ss} (μm^{-2})	0.0212 ± 0.00231	0.0110 ± 0.000375	0.00648 ± 0.000503

Table 4.3 – Average dendrites and branch tips density over development

4.7.2 Numerical integration

To get more insights into the dendritic tree growth predicted by the mean-field model, we numerically integrate the spatio-temporal differential equations. To demonstrate an example of the predicted growth, we use the parameter values measured at 24 hr

AEL. In addition, we specify the death rate k_d using the steady-state approximation, i.e. $k_{d,ss} = \frac{k_b U_{ss}}{R_{ss}}$.

For the boundary conditions, we use Dirichlet boundary conditions since there are no indications that fluxes of particles vanish at the origin $r = 0$. On the left boundary $r = 0$, the species density is set to the steady-state value U_{ss}, R_{ss} that we measured previously (see fig. 3.48), while the density vanishes on the right boundary:

$$\begin{aligned} U(\vec{x} = 0, t) &= U_{ss} \\ R(\vec{x} = 0, t) &= R_{ss} \\ U(|\vec{x}| = L, t) &= 0 \\ R(|\vec{x}| = L, t) &= 0 \end{aligned} \tag{4.284}$$

For the initial conditions, we set the initial density profiles to a peaked profile localized near the origin. The shape of the profile is sigmoidal and decays away from the origin:

$$\begin{aligned} f(x) &= \frac{1}{1 + e^x} \\ U(\vec{x}, 0) &= U_{ss} f\left(\frac{|\vec{x}| - L_0}{\sigma_0}\right) \\ R(\vec{x}, 0) &= R_{ss} f\left(\frac{|\vec{x}| - L_0}{\sigma_0}\right) \end{aligned} \tag{4.285}$$

where L_0 and σ_0 modulate the shape of the sigmoidal. In our integrations, we choose $L_0 = 10\,\mu m$ and $\sigma_0 = 2\,\mu m$. With these boundary conditions and parameters, we integrate the dynamical system to obtain their radial density profiles as shown in fig. 4.9.

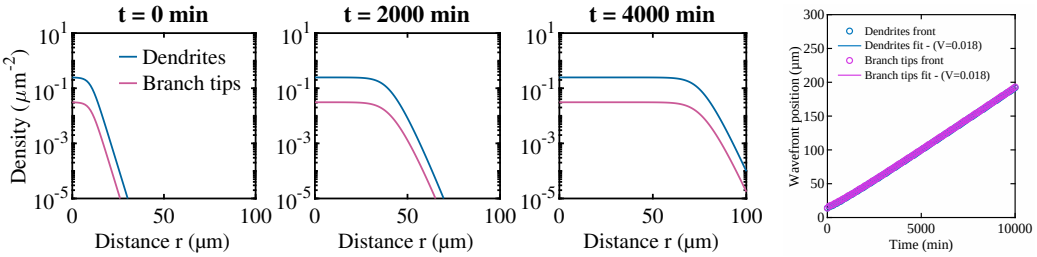

Figure 4.9 – Temporal dynamics of the 2-species mean-field model at 24 hr AEL

As one can see, there are three main features exhibited in the temporal dynamics: 1) the species densities gradually invade space at a constant speed, 2) the densities reach a steady state after passage of the front and 3) the shape of the density fronts is constant over time. In other words, the numerical solution indicates that the dendritic tree proliferates by the propagation of a density front that leaves a steady state behind. This is in agreement with what he have observed in real neurons when we examined the species density over development (see fig. 3.44, fig. 3.45, fig. 3.46).

4.7.3 Marginal stability analysis of the growth front

Motivated by the observation of a front propagation in the numerical results, we derive an expression of the front speed as a function of the microscopic parameters using marginal stability analysis [85]. Recall the differential equations of the 2-species model that govern the temporal change of the dendrites line density U and branch tips point density R:

$$\frac{\partial U}{\partial t} = v_R R - c_{RU} RU \tag{4.286}$$

$$\frac{\partial R}{\partial t} = -v_r \frac{\partial R}{\partial r} + D_r \frac{\partial^2 R}{\partial r^2} - k_d(U)R + k_b U \tag{4.287}$$

where $k_d(U) = k_{d,0} + k_{d,1}(U)$ is the tips death rate, which is a non-linear function of U. To find the marginally stable velocity, we seek traveling wave solutions of the

form $\{U(r,t), R(r,t)\} = \{U(r-Vt), R(r-Vt)\}$ where V is the wavefront velocity. Moreover, we assume that the waveform decays exponentially from the center to the forefront of the wave with a decay length of $1/q$. This leads us to the following ansatz for U, R:

$$U(r,t) = U_0 e^{-q(r-Vt)} \tag{4.288}$$

$$R(r,t) = R_0 e^{-q(r-Vt)} \tag{4.289}$$

Linearizing the equations in terms of U, R and substituting the traveling wave ansatz, we get:

$$VqU_0 = v_R R_0 \tag{4.290}$$

$$VqR_0 = \left(qv_r + q^2 D_r - k_{d,0}\right) R_0 + k_b U_0 \tag{4.291}$$

Eliminating U_0, R_0, we obtain the following equation for V:

$$qV - \frac{v_R k_b}{qV} + k_{d,0} = qv_r + q^2 D_r \tag{4.292}$$

where all terms that depend on V are on the left-hand side. This first equation can be understood as finding the intersection between two functions of q for a given V, namely:

$$f_1(q) = f_2(q) \tag{4.293}$$

$$f_1(q) = qV - \frac{v_R k_b}{qV} + k_{d,0} \tag{4.294}$$

$$f_2(q) = qv_r + q^2 D_r \tag{4.295}$$

Note that $f_1(q)$ is a monotonic function of q ($\forall q,\, f_1'(q) > 0$) and $f_2(q)$ is a quadratic function of q with no constant term. At small values of q, $f_1(q)$ is negative, while $f_2(q)$ approaches zero from the positive side. In this regime, there are no solutions that satisfy the equation. On the other hand, once q passes a certain threshold from

below, namely $qV > \frac{-k_{d,0}+\sqrt{k_{d,0}^2+4v_R k_b}}{2}$, $f_1(q)$ becomes positive, which implies that $f_2(q)$ will have two points that intersect with $f_1(q)$. At the crossing between these two regimes, $f_1(q) = f_2(q)$ admits a single solution (q_m, V_m), which corresponds to the marginally stable solution [85].

The solution is still underdetermined as there is one equation for two unknowns q, V. The additional constraint arises from the stability condition of the velocity, namely, $\left.\frac{dV}{dq}\right|_{q=q_m} = 0$. Using this fact and taking a q derivative on both sides of eq. (4.293), we find:

$$\frac{\partial f_1(q,V)}{\partial q} + \frac{\partial f_1(q,V)}{\partial V}\frac{dV}{dq} = \frac{\partial f_2(q,V)}{\partial q} + \frac{\partial f_2(q,V)}{\partial V}\frac{dV}{dq} \tag{4.296}$$

$$\Rightarrow \left.\frac{\partial f_1(q,V)}{\partial q}\right|_{q=q_m} = \left.\frac{\partial f_2(q,V)}{\partial q}\right|_{q=q_m} \tag{4.297}$$

In other words, at the marginally stable point (q_m, V_m), the slopes of the two intersecting functions must also match. This last condition adds another constraint that determines the marginal stability solution completely. The two constraint equations are:

$$q_m V_m - \frac{v_R k_b}{q_m V_m} + k_{d,0} = q_m v_r + q_m^2 D_r \tag{4.298}$$

$$V_m + \frac{v_R k_b}{q_m^2 V_m} = v_r + 2q_m D_r \tag{4.299}$$

Multiplying the second equation by q_m and adding the first equation, we find the following relation between V_m and q_m:

$$3D_r q_m^2 + 2(v_r - V_m)q_m - k_{d,0} = 0 \tag{4.300}$$

Removing the dependence on q_m, we obtain an equation for V_m:

$$k_c^2\left(4V_m\left(V_m-v_r\right)^3+18k_{d,0}D_rV_m\left(V_m-v_r\right)-27D_r^2k_c^2\right)$$
$$+k_{d,0}^2V_m^2\left(\left(V_m-v_r\right)^2+4k_{d,0}D_r\right)=0 \tag{4.301}$$

where $k_c=\sqrt{v_Rk_b}$ is the effective dendrites growth rate, akin to the rate constant of the Fisher-Kolmogorov–Petrovsky–Piskunov equation [14, 34]. As we can see, k_c arises from the combination of both tip growth (v_R) and branching (k_b). To simplify the equation for V_m, we use the following dimensionless parameters:

$$u_m=\frac{V_m}{v_r} \tag{4.302}$$
$$\epsilon=\frac{\sqrt{D_rk_c}}{v_r} \tag{4.303}$$
$$\delta=\frac{k_{d,0}}{k_c} \tag{4.304}$$

where ϵ controls the strength of the two growth modes (diffusion or drift) and δ is the tip death rate in proportion to the effective dendrite's growth k_c. With these substitutions, we have the following equation for u_m:

$$4u_m\left(u_m-1\right)^3+\delta^2u_m^2\left(\left(u_m-1\right)^2+4\delta\epsilon^2\right)+18\delta\epsilon^2u_m\left(u_m-1\right)-27\epsilon^4=0 \tag{4.305}$$

Solving this equation for u_m amounts to finding the roots of a quartic polynomial. In general, for $\delta>0,\epsilon>0$, this polynomial has two imaginary and two real roots. For this analysis, we will focus on finding the positive real root, which is associated with the right-moving front.

Since the u_m polynomial has two parameters (ϵ,δ), there are four limits to study. First, ϵ controls whether the growth is dominated by the tips' radial drift ($\epsilon\ll1$) or radial diffusion ($\epsilon\gg1$). Second, δ controls the tip's death rate $k_{d,0}$ in comparison to the birth rate k_c. Expanding the real solutions for u_m in terms of δ and ϵ, we get the following expressions in each of the four limits:

- Drift dominated growth, low relative death rate ($\epsilon \ll 1, \delta \ll 1$)

$$u_m = 1 + \left(\frac{27}{4}\right)^{\frac{1}{3}} \epsilon^{\frac{4}{3}} - \delta \left(\frac{1}{2}\right)^{\frac{1}{3}} \epsilon^{\frac{2}{3}} + O(\delta^2, \epsilon^2) \tag{4.306}$$

$$V_m \approx v_r + \left(\frac{27}{4}\right)^{\frac{1}{3}} \left(\frac{D_r^2 k_c^2}{v_r}\right)^{\frac{1}{3}} - \frac{k_{d,0}}{2^{\frac{1}{3}} k_c} \left(D_r k_c v_r\right)^{\frac{1}{3}} \tag{4.307}$$

In this regime, the growth of the tree is dominated by the radial drift motion of the tips, which is dependent upon the tip transition dynamics and velocities. The expansion velocity is then equal to the tip's radial drift velocity to leading order in ϵ, δ. At the next order, the diffusion of the tips increases the expansion velocity, while the death rate $k_{d,0}$ slows down the propagation of the front.

- Drift dominated growth, high relative death rate ($\epsilon \ll 1, \delta \gg 1$)

$$u_m = \frac{3\sqrt{3}\epsilon}{2\delta^{3/2}} + \frac{9}{4\delta^2} + O(\frac{1}{\delta^3}, \frac{1}{\epsilon}) \tag{4.308}$$

$$V_m \approx \frac{3\sqrt{3}\sqrt{D_r k_c}}{2} \left(\frac{k_c}{k_{d,0}}\right)^{3/2} + \frac{9 v_r k_c^2}{4 k_{d,0}^2} \tag{4.309}$$

In this regime, the asympotic behavior of the expansion velocity depends on the relative value of ϵ and δ. For $\epsilon < \frac{1}{\sqrt{\delta}}$, the second term becomes dominant and $u_m \sim \frac{1}{\delta^2}$. In this regime, the growth of the tree is driven by the drift v_r although it is heavily damped by the death rate $k_{d,0}$. For $\epsilon > \frac{1}{\sqrt{\delta}}$, the first term becomes dominant over the second term, which leads to $u_m \sim \frac{1}{\delta^{\frac{3}{2}}}$. In this regime, diffusion dominates, but it is again heavily damped by $k_{d,0}$. Moreover, the existence of these two regimes may not be physically achievable. Recall that $k_{d,0}$ also depends on the drift velocity v_R and D_R. When the drift is high compared to diffusion ($\epsilon \ll 1$), the tip quickly escapes the absorbing boundary and therefore has a low death rate $k_{d,0}$. Depending on the value of k_b, this means that $\delta \gtrsim 1$ for $\epsilon \ll 1$.

- Diffusion dominated growth, low relative death rate ($\epsilon \gg 1, \delta \ll 1$)

$$u_m = \left(\frac{27}{4}\right)^{\frac{1}{4}} \epsilon + \frac{3}{4} - \delta \left(\frac{\sqrt{3}}{4} \left(\frac{27}{4}\right)^{\frac{1}{4}} \epsilon + \frac{\sqrt{3}}{8} \right) + O(\delta^2, \frac{1}{\epsilon}) \tag{4.310}$$

$$V_m \approx \left(\frac{27}{4}\right)^{\frac{1}{4}} \sqrt{D_r k_c} + \frac{3}{4} v_r - \frac{k_{d,0}}{k_c} \left(\frac{\sqrt{3}}{4} \left(\frac{27}{4}\right)^{\frac{1}{4}} \sqrt{D_r k_c} + \frac{\sqrt{3}}{8} v_r \right) \tag{4.311}$$

  In this regime, the growth is dominated by the combined effect of branching and the diffusion of the tips. In this case, at the leading order, the front velocity is proportional to $\sqrt{D_r k_c}$, which is reminiscent of the Fisher's equation front velocity. At the next order, increasing the radial drift velocity v_R increases the expansion velocity, while increasing the zeroth-order death rate $k_{d,0}$ decreases the expansion velocity.

- Diffusion dominated growth,high relative death rate ($\epsilon \gg 1, \delta \gg 1$)

$$u_m = \frac{3\sqrt{3}\epsilon}{2\delta^{3/2}} + \frac{9}{4\delta^2} + O(\frac{1}{\delta^3}, \frac{1}{\epsilon}) \tag{4.312}$$

$$V_m \approx \frac{3\sqrt{3}\sqrt{D_r k_c}}{2} \left(\frac{k_c}{k_{d,0}}\right)^{3/2} + \frac{9 v_r k_c^2}{4 k_{d,0}^2} \tag{4.313}$$

  In this regime, the expansion velocity has the same asymptotic expression as in the case $\epsilon \ll 1, \delta \gg 1$. However, in this regime, there is no ambiguity regarding the dominance of each term: the first term is leading. Therefore, the expansion velocity is dominated by the combined effect of branching and diffusion and dampened by the death rate.

By using eq. (4.305) and the measured expansion velocities, we evaluated the growth regimes of the neuron at the sampled developmental stages as shown in table 4.4. At 24 hr AEL, the growth is dominated by diffusion with a high relative death rate ($\epsilon \gg 1, \delta \gg 1$), while at 48 and 96 hr AEL the growth is still dominated

by diffusion but the death rate is relatively low ($\epsilon \gg 1, \delta \gg 1$). However, since the values of δ are not significantly different than 1, the δ expansion may not be accurate in physiological conditions.

Predictions\Stage	24 hr AEL	48 hr AEL	96 hr AEL
$\epsilon = \frac{\sqrt{D_r k_c}}{v_r}$	3.45	3.93	19.7
$\delta = \frac{k_0}{k_c}$	1.84	0.667	0.531
Growth regime	Diffusion dominated	Diffusion dominated	Diffusion dominated

Table 4.4 – Marginal stability parameters at different developmental stages
Note that δ is evaluated using eq. (4.305) and the average value of $k_{d,0}$ inferred from the measured expansion velocities V_{AP}, V_{LR} (see table 4.2)

Finally, to test the validity of these approximations, we compare them graphically against the exact u_m solution found numerically (see fig. 4.10). As depicted, at small and large δ, the asymptotic expansions are good approximations of the exact solution obtained by numerically solving the quartic equation in u_m.

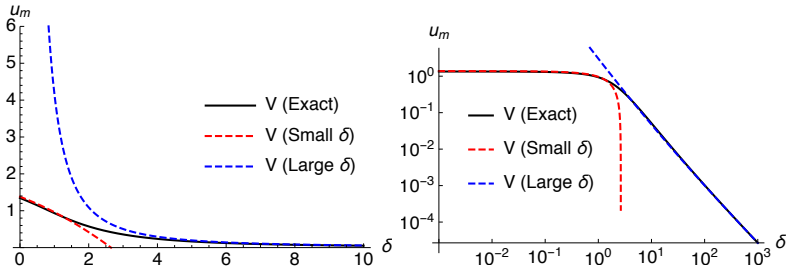

(a) Drift dominated growth, $\epsilon = 0.3$

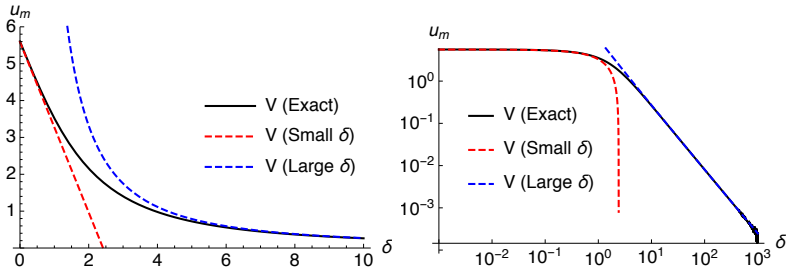

(b) Diffusion dominated growth, $\epsilon = 3$

Figure 4.10 – Approximations of the expansion velocity using marginal stability
The exact value of u_m is calculated numerically by solving for the u_m roots in eq. (4.305). The small and large δ behavior are calculated using the approximate formula derived above.

By rearranging the marginal stability equations, the model can make also predictions on the decay length of the density front, $\lambda_\rho = \frac{1}{q}$, given an estimate of the expansion velocity V_m. More precisely, by eliminating the dependence on the zeroth-order death rate $k_{d,0}$, one finds the following constraint equation for q in terms of the microscopic parameters and the expansion velocity:

$$2D_r V_m q^3 - q^2\left(V_m^2 - v_r V_m\right) - v_R k_b = 0 \tag{4.314}$$

Since the growth of the tree is different along AP and LR axis, we make separate predictions of the decay length λ_ρ along each of these dimensions for each measured developmental stage. The resulting predictions are compared with our measurements of the dendrites density front decay length in fig. 4.11. As shown, the predicted AP decay length is overestimated at 24 and 48 hr AEL, while the LR decay length is overestimated only at 48 hr AEL.

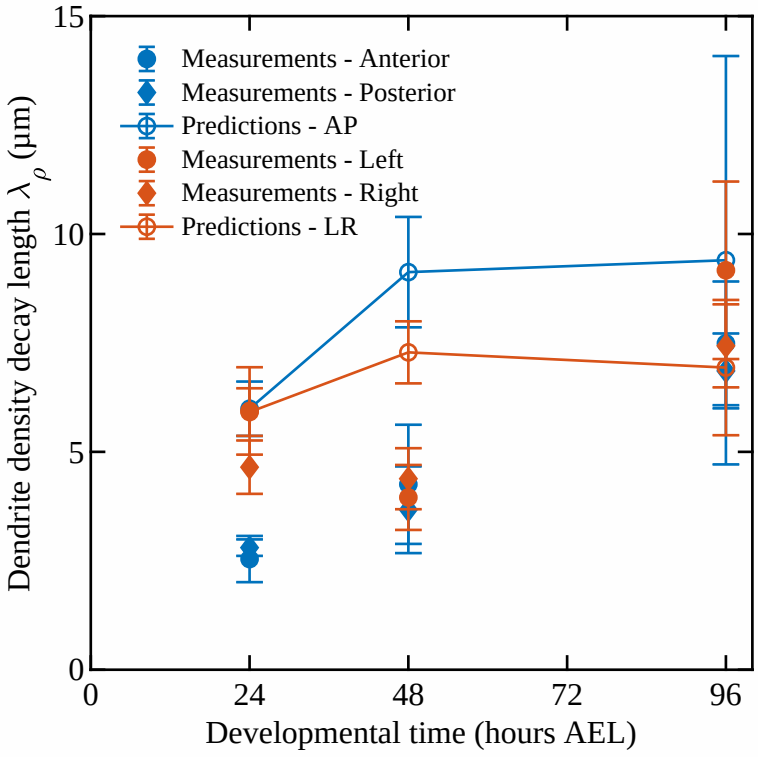

Figure 4.11 – Mean-field predictions of the density front decay length λ_ρ

4.7.4 Predictions of the microscopic parameters c_{RU}, k_d, L_0

In addition to making predictions on the large-scale dendritic growth, the mean-field theory also makes quantitative predictions on the microscopic growth parameters using the macroscopic morphometrics. More precisely, using measurements of the steady-state densities U_{ss}, R_{ss} and the expansion velocity $V_{\text{uni, AP}}, V_{\text{uni, LR}}$ at each developmental stage, we infer the contact inhibition parameter c_{RU}, the death rate k_d and the initial branch length L_0.

First, we make predictions on the contact inhibition parameter c_{RU}. Using the steady-state equation of the mean-field model, we estimate the value of c_{RU} from U_{ss}, R_{ss} and v_R:

$$c_{RU,ss} = \frac{v_R}{U_{ss}} \tag{4.315}$$

Alternatively, recall that we also estimate c_{RU} by treating the effect of contact inhibition as a modification of the k_{GS} or k_{GP} rate, which induces a perturbation of the tip transition steady state as derived in eq. (4.158) and eq. (4.165). The resulting three estimates are compared in fig. 4.12. First, note that all three estimates are within a factor of two of one another, which is already a success for a mean-field approximation. Furthermore, note that the k_{GP} perturbation prediction is consistently smaller than the k_{GS} perturbation prediction. This is consistent with the intuition that contacts that promote transitions to the shrinking state are more prohibitive than contacts that promote transitions to the paused state. In other words, one expects that contact inhibition will be more severe on the growth of the dendrite if the tips retract instantly after collision as opposed to pausing. In addition, if we treat the predictions from the density steady state as a ground truth, the fact that it is bounded by the k_{GS} and k_{GP} perturbations indicates that the effect of contacts is in between pure retraction and pure pausing. This is also consistent with what we find in experimental observations where branch tips make several contacts

with other dendrites before retraction is initiated and contacts have a non-zero duration as shown in fig. 3.8.

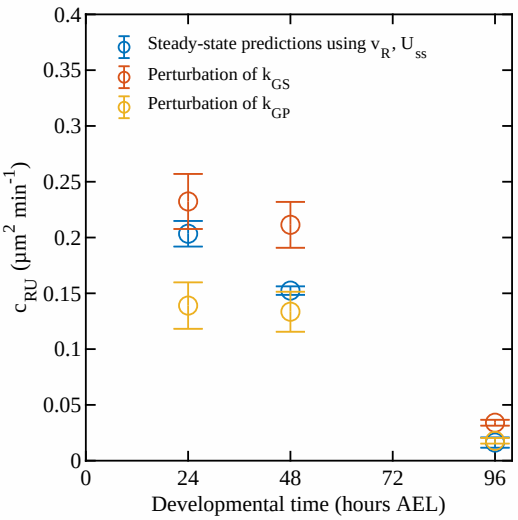

Figure 4.12 – Mean-field predictions of the contact inhibition parameter c_{RU}

Second, we make predictions on the branch tip death rate k_d using three different methods. In the first method, we use the steady-state density equations to estimate k_d:

$$k_{d,ss} = \frac{k_b U_{ss}}{R_{ss}} \tag{4.316}$$

Since we expect that the dendritic densities reach a steady state near the soma, this estimate assumes that most of the branch deaths occur in the bulk of the tree.

In the second method, we predict k_d using the formula of the average death rate $\langle k_d \rangle$ from the first-passage time analysis (see eq. (4.245)). Since we do not have a closed form of the full death rate, we evaluate the integral numerically with the respective microscopic parameters at each developmental stage. This estimate has one free parameter, the initial length of the branch L_0. To make predictions, two values of L_0 that are proportional to the inverse dendrites density U_{ss}^{-1} are used.

Indeed, we expect that $L_0 \lessapprox U_{ss}^{-1}$ since U_{ss}^{-1} is the length scale of the average space between the dendrites.

Finally, the third estimate of k_d is derived from the marginal stability equation and the measurement of the tree expansion velocity $V_{\text{uni, AP}}$ or $V_{\text{uni, LR}}$. More precisely, with a given expansion velocity, we use the marginal stability equation eq. (4.301) to solve for the positive quadratic root of $k_{d,0}$. However, this prediction underestimates the death rate since it omits the non-linear dependence on U, i.e. the deaths due to contacts.

The comparison of these three estimates with the measured value of the death rate is shown in fig. 4.13a. First, similar to the predictions of c_{RU}, the death rate predictions and measurements are all within a factor of two of one another, except for the marginal stability predictions, which is expected since they underestimate the death rate. Furthermore, the steady-state predictions are in agreement with the measurements, which implies, as explained above, that branches die mostly within the bulk of the tree. Moreover, the first-passage predictions are also consistent with the measurements. Indeed, since we expect that $L_0 \lessapprox U_{ss}^{-1}$, the first-passage estimate that uses $L_0 = U_{ss}^{-1}$ should be a lower bound of the death rate, which is what we observe. In addition, the 24 hr AEL measurement is in between the $L_0 = U_{ss}^{-1}$ and $L_0 = 0.5 U_{ss}^{-1}$ estimates, while the 48 hr measurement is smaller than the $L_0 = U_{ss}^{-1}$ estimate. This indicates that branches at the earlier stage initially grow to longer lengths (in proportion to U_{ss}^{-1}) before they die compared to the later stages. Finally, at 96 hr AEL, the estimates are not in agreement with the measurements, but the closest prediction is the $L_0 = 0.5 U_{ss}^{-1}$ first-passage time estimate. This discrepancy may be a consequence of the fact that the mean-field model does not take the effect of the segment boundary into account. Indeed, as shown in the numerical integration, the tree's expansion is unbounded. This is a good approximation at the earlier stage where the neuronal boundaries have not been established. However,

at the later stages, the boundaries may have considerable effects on the densities, which will affect the steady state, first-passage and marginal stability predictions.

Parallel to the predictions of the death rate, we also examine the value of the initial branch length L_0 as inferred from the marginal stability equation and the measured expansion velocities $V_{\text{uni, AP}}, V_{\text{uni, LR}}$. The predictions are shown in fig. 4.13b. Again, since the marginal stability analysis only accounts for the zeroth-order death rate, the predictions of L_0 from these expressions will be overestimated. This is indeed what we observe as the predictions are comparable or greater than U_{ss}^{-1}, which is the upper bound of L_0.

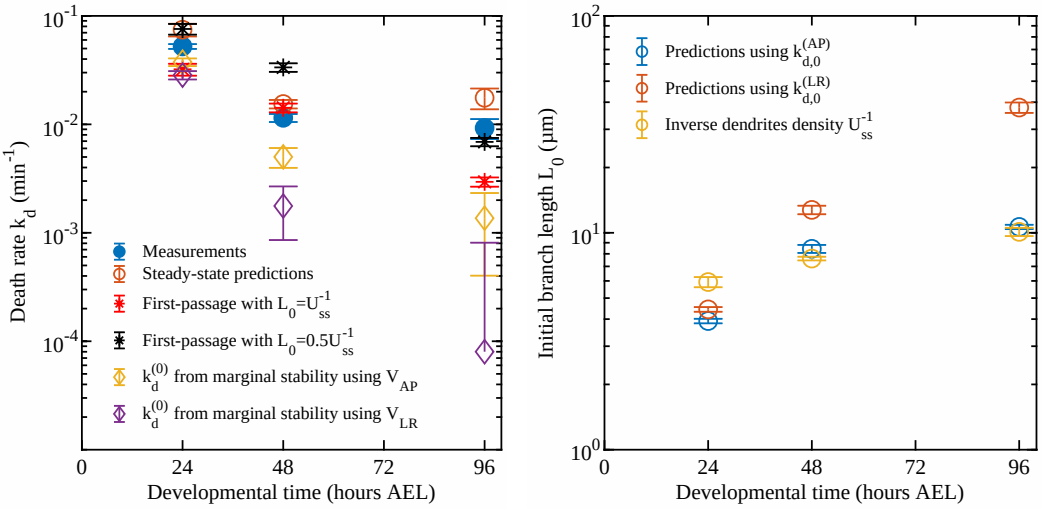

(a) k_d **(b)** L_0

Figure 4.13 – Mean-field predictions of the death rate k_d and initial branch length L_0

4.8 Conclusions

- We propose a model of dendritic morphogenesis cast into a set of reaction-diffusion equations, which uses the mean-field approximation to model the interaction between the active and passive elements of the growth process.

- The model predicts that the dendritic tree expands from the combined effect of tip growth and branching akin to the propagating wavefront in Fisher's equation.

- The model makes quantitative predictions on the microscopic growth parameters, such as the death rate and the contact inhibition, which are in agreement with the measured values at the early stage of development.

5 Agent-based Models of Class IV Neuron Morphogenesis

In this chapter, we formulate a computational model of morphogenesis using stochastic processes that reproduce the growth of dendritic tips. After constraining the model parameters with our measurements, we show that it recapitulates some of the morphometrics of class IV neurons. Finally, we explore the effect of the free parameters on the tree morphology and investigate an alternate model of the branching process.

The initial design of the agent-based model was performed in collaboration with Sujoy Ganguly and Hugo Bowne-Anderson [15]. Subsequent modifications of the model were inspired by the analysis of the tip dynamics provided by Sabyasachi Sutradhar. Finally, model predictions of various morphometrics is compared against physiological values that were measured using images and movies of class IV neurons provided by Sonal Shree.

5.1 Agent rules of morphogenesis

An agent-based model is a model where agents are given a set of rules that control their behavior within their environment. In this case, the agents are the branch tips, which are the main contributors to the growth of the dendritic tree. We identify

three main rules of dendritic tip growth based on the observed growth dynamics: 1) tip growth, 2) branching, 3) contact inhibition. The implementation of these rules is described in the following sections.

5.1.1 Tip growth

One of the main rule of morphogenesis governs how the tip grows. Following the analysis of the tip dynamics (see section 3.1), we model tip growth as a 3-state Markov process whose states define the velocity of the tip. First, the transition dynamics of the tip state is governed by the 3-state Markov process whose transition rates are given by the measured values.

First, each new tip is initialized in the growing state G and the duration of this initial phase of growth is determined by a free parameter of the model, T_0. Once the initial phase is complete, the next state of the tip is determined by the measured transition probability. Specifically, the next state is shrinking if a Bernouilli trial succeeds with a success rate of $p = \frac{k_{GS}}{k_{GS}+k_{GP}}$, while a failure indicates that the next state is paused. Once the next state is determined, denoted as m, the duration of this phase of growth is determined by sampling an exponential distribution with an average of $\frac{1}{k_m}$ where $k_m = \sum_j k_{mj}$ is the exit rate of state m as determined by the transition rates k_{mj}. Finally, the velocity of the tip in each state is determined by sampling the m^{th} component of the velocity distribution mixture model fit.

The subsequent transitions of the tip are processed in a similar manner. In general, let $s_i(t) \in \{S, P, G\}$ correspond to the state of the i^{th} tip at time t in the simulation and assume that a transition occurs. The next state is determined by a Bernouilli trial with a success rate of $p = \frac{k_{s_i(t)m}}{\sum_j k_{s_i(t)j}}$ where success indicates that the next state is m and failure indicates that the next state is the last choice that remains after excluding state m and state $s_i(t)$. Once the next state is determined, the duration and velocity of this new phase are determined as explained previously by

sampling an exponential distribution with an average of $\frac{1}{k_m}$ and the m^{th} component of the velocity distribution mixture model fit.

Moreover, the transition rates and velocity fit parameters change continuously over the course of the simulation. The temporal evolution of the parameters is determined by a linear interpolation of the measured values within the measured temporal range. Outside the measured range, the dynamics parameters are extrapolated constantly from the closest measured value.

As a result of the tip dynamics, the length of branches changes. Let Δt and δ correspond to the time scale of the simulation and the spatial sampling interval of the branch path, respectively. Moreover, let $v_i(t)$ correspond to the velocity of the i^{th} tip at time t in the simulation and let $L_i(t)$ correspond to the length of its associate branch. Then, the change in length of the i^{th} branch $\Delta L_i(t)$ is given by the following expression:

$$L_i(t+\Delta t) = L_i(t) + \Delta L_i(t) \tag{5.1}$$

$$\Delta L_i(t) = v_i(t)\Delta t \tag{5.2}$$

Once the change in length is calculated, the number of steps of length δ taken by the tip is determined by the following formula:

$$N_i(t) = \left\lfloor \frac{\Delta L_i(t) + \Delta \tilde{L}_i(t)}{\delta} \right\rfloor \tag{5.3}$$

$$\Delta \tilde{L}_i(t) = L_i(t) - L_i(t-\Delta t) - \delta N_i(t-\Delta t) \tag{5.4}$$

where $\Delta \tilde{L}_i(t) \geq 0$ corresponds to the amount of length that is not accounted for by the finite amount of steps in the previous iteration. Accounting for $\Delta \tilde{L}_i(t)$ ensures that the finite sampling interval of the branches δ does not cause rounding errors in the length of the branch. Moreover, using a finite stepsize δ ensures that branches

are discretized uniformly and therefore have the same smoothness irrespective of the magnitude of the growth steps that they have taken in the past.

Once the number of steps is determined, the two-dimensional position of the tip $\vec{x}_{\text{Tip},i}$ is updated. There are three cases to consider: $N_i(t) > 0, N_i(t) = 0, N_i(t) < 0$.

- $N_i(t) > 0$

  In this case, the branch grows in a direction that is determined by the persistence length L_p, which is a free parameter of the simulation. More specifically, the change of the growth direction $\Delta\theta_{i,j}$ at each step j is determined by sampling a normal distribution with a mean of 0 and a variance of $\frac{2\delta}{L_p}$:

$$\forall 1 \leq j \leq N_i(t), \quad \Delta\theta_{i,j} \sim \mathcal{N}\left(0, \frac{2\delta}{L_p}\right) \tag{5.5}$$

  where $\mathcal{N}(\mu, \sigma^2)$ denotes a normal distribution with mean μ and variance σ^2. The new tip position is then given by:

$$\vec{x}_{\text{Tip},i}(t + \Delta t) = \vec{x}_{\text{Tip},i}(t) + \delta \sum_{j=1}^{N_i(t)} \hat{t}(\theta_{i,j-1} + \Delta\theta_{i,j}) \tag{5.6}$$

$$\hat{t}(\phi) = (\cos(\phi), \sin(\phi)) \tag{5.7}$$

$$\theta_{i,j} = \theta_{i,0} + \sum_{k=1}^{j} \Delta\theta_{i,k} \tag{5.8}$$

  where $\theta_{i,0}$ corresponds to the growth angle of the tip at the beginning of the iteration.

- $N_i(t) = 0$

  In this case, the tip doesn't move:

$$\vec{x}_{\text{Tip},i}(t + \Delta t) = \vec{x}_{\text{Tip},i}(t) \tag{5.9}$$

- $N_i(t) < 0$

  When a negative number of steps is calculated, it implies that the branch has retracted caused by a negative tip velocity. Consequently, the new position of the tip will correspond to one of the point that discretizes the branch path. Let $\{\vec{y}_j | 0 \leq j \leq n, n = \left\lfloor \frac{L_i(t)}{\delta} \right\rfloor\}$ correspond to the ordered set of two-dimensional points $\vec{y}_j$ that discretize the path of the branch of length $L_i(t)$ such that $\vec{y}_0$ corresponds to the branch point position and $\vec{y}_n$ corresponds to the branch tip position. The new tip position is then given by:

$$\vec{x}_{\text{Tip},i}(t + \Delta t) = \vec{y}_{\tilde{j}} \tag{5.10}$$

$$\tilde{j} = \left\lfloor \frac{L_i(t + \Delta t)}{\delta} \right\rfloor \tag{5.11}$$

  Note that since $L_i(t + \Delta t) < L_i(t)$, $\tilde{j} < n$, which implies that $\vec{y}_{\tilde{j}}$ is well-defined provided $L_i(t + \Delta t) \geq \delta$. If $L_i(t + \Delta t) < \delta$, this implies that the branch tip has retracted back to the branch point. In this case, the tip or agent is deleted and cannot grow any further. This models the branch annihilation process.

5.1.2 Branching

At any given time during the simulation, new branch tips or agents are spawned from existing branches in the dendritic tree. The rate at which each branch gives birth to a new branch tip is proportional to its length as found previously in the analysis of the branching process (see section 3.2). In other words, the longer a branch becomes, the more likely it is to give birth to a new branch tip during the time step of the simulation Δt. This probabilistic event is modeled as a Poisson process whose rate is proportional to the branching rate k_b. Namely, the probability

$P(L, \Delta t)$ that a branch of length L gives birth to a new branch tip in a time Δt is given by:

$$P(L, \Delta t) = 1 - e^{-k_b L \Delta t} \tag{5.12}$$

$$\overset{\Delta t \ll 1}{\approx} k_b L \Delta t \tag{5.13}$$

Once a new branch tip is born, its position along its parent branch is sampled uniformly with some restrictions. This rule is chosen in order to preserve the exponential distribution of branch lengths (see fig. 3.29). The candidate branch points are restricted to be a distance of at least $2\epsilon = 0.8\,\mu m$ from existing branch points to ensure that the new branch tip does not collide prematurely with the high density of dendrites near branch points.

Once the tip is born, the orientation of its growth with respect to its parent is determined by sampling a normal distribution with an average of $99.03°$ and a standard deviation of $30.36°$. These parameters correspond to the average and standard deviation of all measured branching angles pooled together (see section 3.2.4). Furthermore, the branching angle is restricted to the range $[30, 150]°$ to prevent the tip from colliding with its parent branch.

Finally, at birth, tips are initialized in the growing dynamical state and the duration of the initial growing state is determined by the free parameter T_0 as mentioned in the previous section.

5.1.3 Contact inhibition

As a tip grows following the prescribed tip dynamics, it may contact other dendrites in the tree. The third main rule of the dendritic tips determines the changes that follow contacts, which model the growth inhibition process mediated by Dscam1.

First, a tip collides with another branch when it is in close proximity with one of its branch nodes. Specifically, the tip is deemed in contact with another branch when it is within a distance $\epsilon = 0.4\,\mu m$ from the branch. This value loosely corresponds to the branch thickness at the tip. Once a contact occurs, the state of the tip changes to the paused state and its duration is determined by sampling an exponential distribution with an average of $2.5\,\text{min}$. This value is chosen based on the analysis of the contact duration (see fig. 3.8).

Once the tip exits the paused state, its growth dynamics changes compared to its dynamics prior to contact. More specifically, the transition rate parameters of the Markov process are changed to the post-collision transition rates as measured previously at 18 hr AEL (see fig. 3.9). Moreover, since the velocity of the tip measured at 18 hr AEL is not representative of the tip velocity throughout development, only the transition rates are modified upon collision while the the state velocity parameters remain the same. As shown in fig. 5.1, the post-collision transition rates favor the shrinking state as the average tip velocity becomes negative after contact.

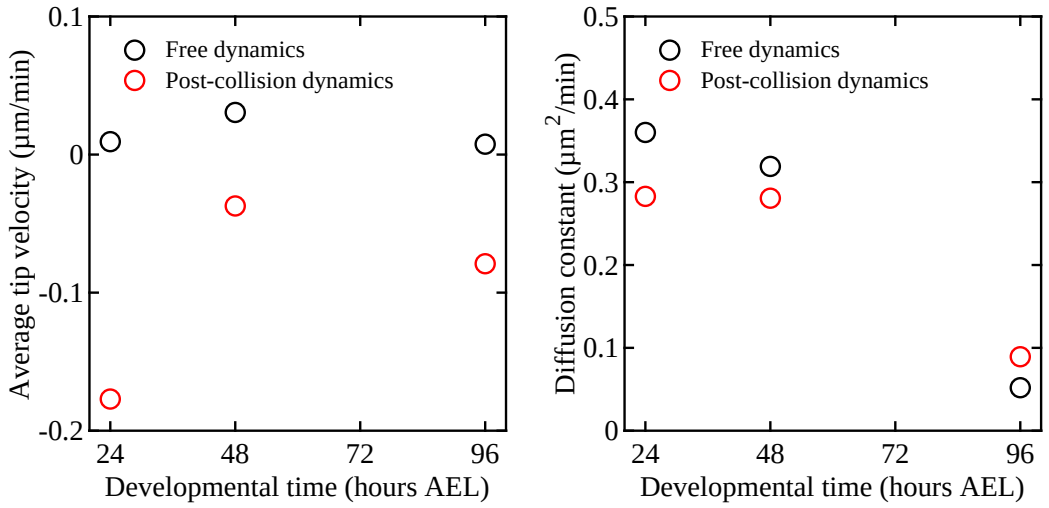

Figure 5.1 – Comparison of the free and post-collision dynamics *in silico*
The average velocity is measured from the transition rates steady state and the average state velocities while the diffusion constant is calculated using the Green-Kubo relation described in section 4.4.3.

Finally, the post-collision dynamics is transient and its duration is determined by the free parameter α. More specifically, once the tip enters into the post-collision dynamics, it transits from one state to another according to the post-collision transition rates for a duration α, after which the values of the transition rates are reverted back to the free tip transition rates, i.e. the transition rates that determine the tip dynamics before collision.

5.2 Initial and boundary conditions

In addition to the agent rules, additional modeling choices are made to define the initial and boundary conditions of the simulated morphogenesis.

For the initial conditions, the simulation starts at 14 hr AEL, which corresponds to the start of morphogenesis, and ends at 120 hr AEL. Initially, 3 agents are positioned at the soma located at the origin $(0,0)$ and their initial growth direction is given by $0, 120, 240°$, respectively. Moreover, to ensure that the initial branches do not retract prematurely due to randomness, their velocity is set to $1\,\mu m\,\text{min}^{-1}$ for the first 25 minutes of the simulation. Moreover, branching is not allowed during this period to prevent premature collisions of the soma branches with secondary branches.

For the boundary conditions, the growth of dendrites is restricted to a rectangular boundary to model the tiling phenotype of the class IV neurons. The sizes of the boundary are determined by a linear fit to the corrected segment size measurements (see fig. 3.25) and remain constant after 96 hr AEL. Also, when a dendritic tip collides with the boundary, their state changes to the paused state preventing them from crossing.

5.3 Parameter summary

The agent-based model has many parameters that define the growth rules of the agent. Some parameters change over the course of the simulation and are summarized in table 5.1. In particular, the transition rates and velocity parameters are linear interpolated between the measured developmental times. In addition, the constant parameters are summarized in table 5.2 and the free parameters are given in table 5.3.

Parameters	Symbol (Units)	24 hr AEL	48 hr AEL	96 hr AEL
Shrinking-to-paused transition rate	k_{SP} (min^{-1})	0.204	0.200	0.428
Shrinking-to-growing transition rate	k_{SG} (min^{-1})	0.489	0.394	0.566
Paused-to-shrinking transition rate	k_{PS} (min^{-1})	0.672	0.553	0.239
Paused-to-growing transition rate	k_{PG} (min^{-1})	0.465	0.366	0.248
Growing-to-shrinking transition rate	k_{GS} (min^{-1})	0.609	0.706	0.845
Growing-to-paused transition rate	k_{GP} (min^{-1})	0.0875	0.120	0.265
Shrinking state velocity avg.	$\langle v_S \rangle$ ($\mu m\,\text{min}^{-1}$)	0.648	0.499	0.343
Shrinking state velocity std.	std(v_S) ($\mu m\,\text{min}^{-1}$)	0.482	0.494	0.324
Paused state velocity avg.	$\langle v_P \rangle$ ($\mu m\,\text{min}^{-1}$)	0	0	0
Paused state velocity std.	std(v_P) ($\mu m\,\text{min}^{-1}$)	0.082	0.045	0.053
Growing state velocity avg.	$\langle v_G \rangle$ ($\mu m\,\text{min}^{-1}$)	0.772	0.917	0.456
Growing state velocity std.	std(v_G) ($\mu m\,\text{min}^{-1}$)	0.504	1.603	0.655
Branching rate	k_b ($\text{min}^{-1}\mu m^{-1}$)	fit (see fig. 3.12b)		
Segment size	$D_{\text{AP}}, D_{\text{LR}}$ (μm)	fit (see fig. 3.25)		

Table 5.1 – Dynamic simulation parameters

Parameters	Symbol (Units)	Value
Timestep	Δt (min)	0.1
Stepsize	δ (μm)	0.1
Collision distance	ϵ (μm)	0.4
Contact duration average	t_{contact} (min)	2.5
Post-collision shrinking-to-paused transition rate	k^*_{SP} (min^{-1})	0.097
Post-collision shrinking-to-growing transition rate	k^*_{SG} (min^{-1})	0.540
Post-collision paused-to-shrinking transition rate	k^*_{PS} (min^{-1})	1.015
Post-collision paused-to-growing transition rate	k^*_{PG} (min^{-1})	0.406
Post-collision growing-to-shrinking transition rate	k^*_{GS} (min^{-1})	0.946
Post-collision growing-to-paused transition rate	k^*_{GP} (min^{-1})	0.079
Branching angle average	μ_{θ_b} (°)	99.03
Branching angle standard deviation	σ_{θ_b} (°)	30.36
Simulation start time	t_{start} (hr AEL)	14
Simulation end time	t_{end} (hr AEL)	120
Branching start time	$t_{\text{branching}}$ (hr AEL)	14.4167
Initial number of branches	$N_{b,\text{soma}}$	3
Initial branches velocity	V_{soma} ($\mu m\,\text{min}^{-1}$)	1

Table 5.2 – Constant simulation parameters

Parameters	Symbol (Units)	Value
Growth persistence length	L_p (μm)	100
Initial growth duration	T_0 (min)	1.5
Post-collision dynamics duration	α (min)	10

Table 5.3 – Free simulation parameters

5.4 Morphogenesis of class IV neuron *in silico*

Using the dendritic growth rules and parameters mentioned above, a series of 12 stochastic simulations is generated and the morphology is recorded throughout the development of the tree *in silico*. Examples of simulated trees are shown in fig. 5.2 at the 24, 48, 72, 96 and 120 hr AEL and compared against examples of experimental neurons. As depicted, the morphology of the simulated neurons are qualitatively similar to the real class IV neurons. Moreover, the accuracy of the agent-based model is assessed with various quantitative metrics as shown in fig. 5.3. For each of these

metrics, the average and standard deviation of the metric value is calculated using the 12 simulations generated with the same parameter set.

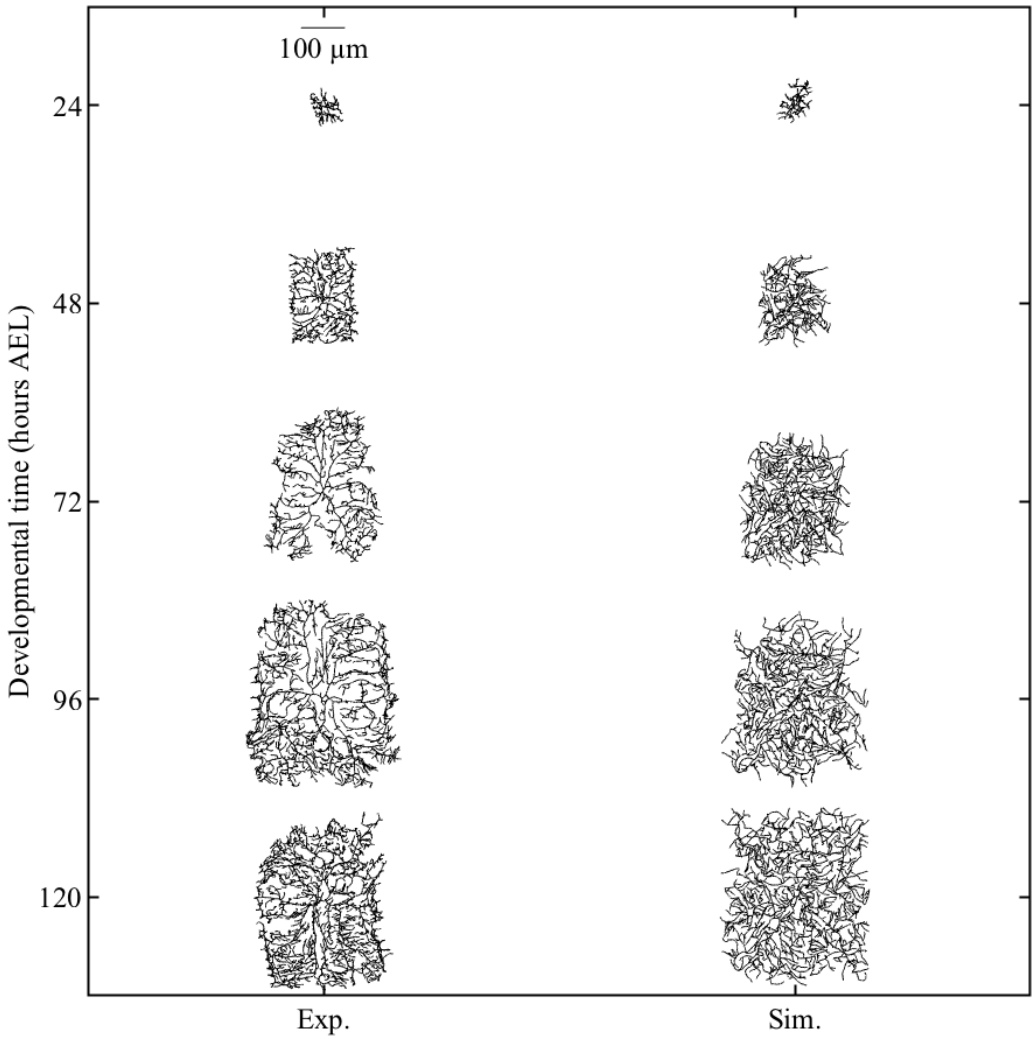

Figure 5.2 – Comparison of experimental and simulated trees

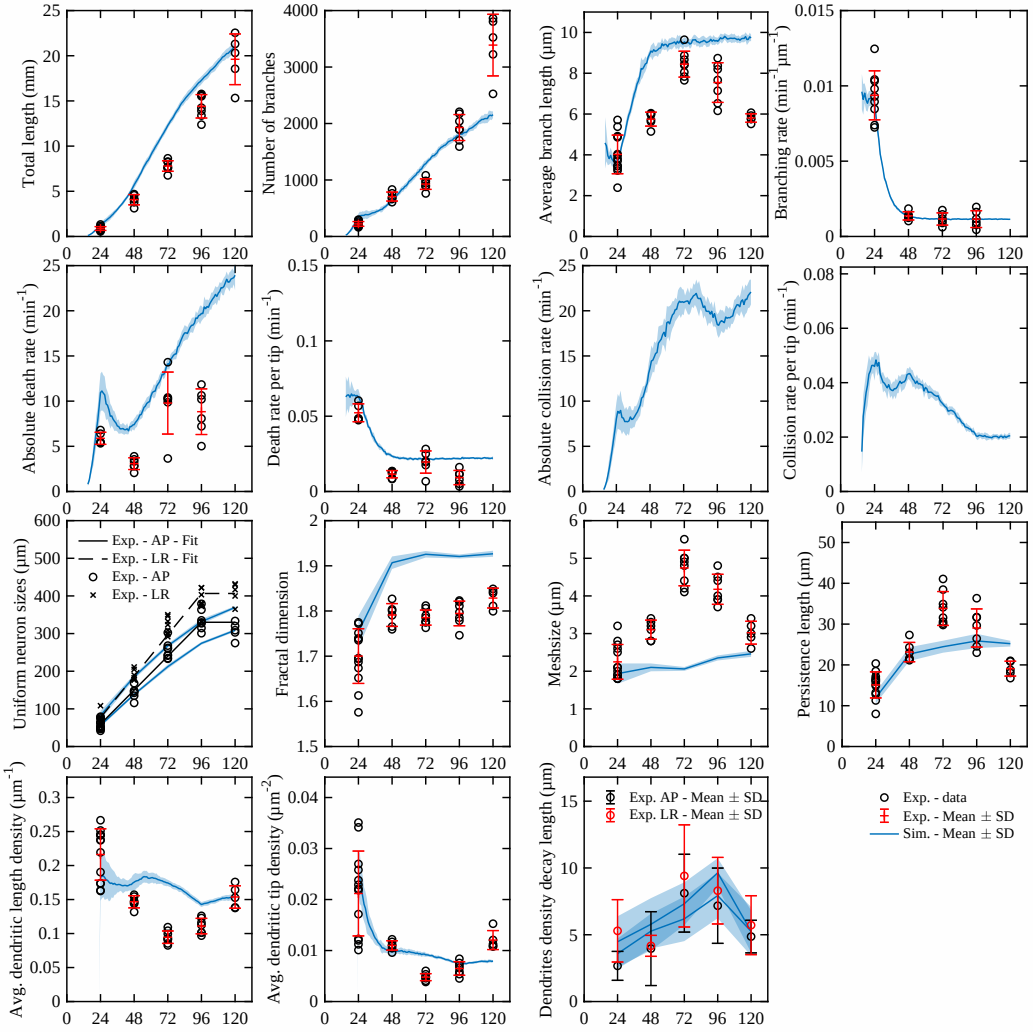

Figure 5.3 – Simulated morphometrics over development
The horizontal axis corresponds to the developmental time in hr AEL.

First, topological metrics such as the total branch length, the number of branches and the mean branch length are compared. Note that these metrics are not independent since the mean branch length corresponds to the ratio of the total branch length and the number of branches. Although the total branch length of simulated and real neurons are in agreement throughout development, the number of branches differ significantly at 120 hr AEL. This discrepancy is potentially due to an overestimation of the number of branches by the skeletonization algorithm. Alternatively, the difference in the number of branches at the later stages could also indicate that

branches disappear too quickly in simulated morphogenesis, which could be caused by a highly dynamic branch tip or a rescue mechanism that is not captured by the model. Finally, the output branching rate per unit length is calculated to verify that the branching process is indeed extensive. Agreement of the branching rate between simulated and real neurons is expected since the input branching rate is determined by the fit to the measured values.

Next, various rates are quantified over the development of the dendritic tree. First, the rate at which branch tips die or annihilate is measued as explained previously in section 3.2.5. Both the absolute death rate over the entire neuron and the death rate normalized by the number of tips are calcualted. As shown, the death rate is slightly lower than the physiological value at 24 hr AEL, but is overestimated almost two-fold from 48 hr AEL onward. Moreover, the temporal evolution of the death rate per unit tip matches the evolution of the branching rate as expected from the fact that more branch births leads to a proportionally higher death rate. This is also consistent with the mean-field model, which predicts that the ratio $\frac{k_b}{k_d}$ is set by the density ratio $\frac{U_{ss}}{R_{ss}}$ once the steady-state is established (see section 4.7). To get more insights into the cause of the branch death, the rate at which branch tips collide with other dendrites or the boundary is also recorded, which is not measured experimentally. The absolute collision rate and the collision rate per unit tip are calculated in a manner similar to the death rate. As shown, the absolute collision rate increases until 72 hr AEL, but subsequently decreases until 96 hr AEL and increases again from 96 to 120 hr AEL. This non-monotonic variation of the collision rate is a signature of the change in the tip dynamics, which becomes less active or more immobile at 96 hr AEL compared to the previous stages. Hence, the probability that a tip collides with other dendrites decreases accordingly. Finally, the collision rate per unit tip shows a rather peculiar behavior. After an initial sharp increase, it reaches a plateau until 48 hr AEL. Then, it decreases linearly with time until 96 hr AEL and remains constant from this point until the end of the simulation. The linear

decrease of the collision rate is likely caused by the linear interpolation of the tip dynamics parameters, which decreases the mobility of the branch tip from 48 to 96 hr AEL. Also, at 96 hr AEL, the collision rate per unit tip reaches a steady-state since the tip dynamics parameters remain constant from that point forward.

Moreover, metrics that assess the space-filling ability of the shape are considered. First, the simulated neuron size is calculated (as explained in section 3.3.1) on the anterior-posterior (AP) or the left-right (LR) dimension. As depicted, the sizes of the neuron are under-estimated compared to the measurements indicating that the mass of the simulated neurons is more concentrated near the soma than the physiological neurons. In addition, the fractal dimension (as explained in section 3.3.5) and the mesh size (as explained in section 3.3.6) are also compared. As indicated by both metrics, the density of the simulated trees is initially in agreement with the real neurons at 24 hr AEL, but the simulated tree becomes significantly denser from 48 hr AEL onward. Indeed, after 48 hr AEL, the fractal dimension is overestimated by at least 1 standard deviation indicating that the shape is closer to filling two-dimensional space compared to real neurons. Moreover, the meshsize is underestimated by at least 2 standard deviations (worst at 72 hr AEL) indicating that holes in the dendritic tree are significantly smaller than real class IV neurons. Finally, the average persistence length of the branches is used to assess the morphological shape of the branches. As shown, the persistence length is in agreement with the real neurons throughout most of the development. Note that the persistence length of the growth process, set to $100\,\mu m$, is different than the persistence length of the branches. This is due to the combined effect of branching and branch annihilation, which effectively segments branches into a set of short connected segments whose orientation changes abruptly from one segment to the next. These abrupt changes in the branch path reduces its straightness, which explains why the output persistence length is much smaller than the persistence length of the growth process.

Finally, the density profiles of the dendrites and dendritic tips are quantified using the average species density and the density decay length as explained in section 3.3.8. Regarding the average dendrites density, the simulated neurons are similar to the real neurons with the highest discrepancy observed at 72 hr AEL. This is explained by the fact, at 72 hr AEL, the neuron size is underestimated and the total branch length is overestimated, which both contribute to increasing the average dendrites density. Furthermore, the dendritic tips density of the simulated neurons is also in agreement with the measured values where the highest discrepancy occurs at 120 hr AEL, which again may be due to the over-estimation of the number of branches by the skeletonization algorithm. Since the neuron size and the total number of branch tips are both underestimated, this indicates that although the simulated trees do not extend as far as the real trees, their spatial distribution of branch tips normalized over the tree area is similar. Finally, the decay length of the dendrite density profiles at the periphery is examined. As this measure is inherently noisy, agreement between the model and real neurons is difficult to assess. Nevertheless, the metric value of the simulated neurons is within a standard error of the measured values. In addition, note that the decay length along the AP and LR directions are similar, since the boundary conditions are uniform across all four boundaries. This is a limitation of the agent-based model since the AP boundary *in vivo* is known to be more sharply defined than the LR boundary.

5.4.1 Successes and failures

Using three simple rules of dendritic morphogenesis, which include 1) stochastic branch growth, 2) extensive branching and 3) contact-based growth inhibition, the agent-based model succeeds at capturing the qualitative features of the dendritic tree morphology as exemplified by the simulated trees shown in fig. 5.2. Moreover, the model also succeeds at reproducing coarse-grained morphometrics such as the total branch length, the neuron size or the dendrites density.

However, the agent-based model is unable to capture some key processes of morphogenesis. One of the biggest failure, which has a major impact on the tree morphology is the branch death rate. Indeed, in simulations, the death rate is almost twice as high as the measured death rate indicating that branches annihilate too quickly which over-prunes the tree. Two reasons may explain a high death rate. First, the average initial branch length T_0 may be too small to allow branches to survive to fluctuations of the tip growth. Indeed, as was found in the analysis of the mean-field death process, a higher initial branch length leads to a higher probability that the branch tip does not return to its native branch point where it annihilates. Second, the duration of the post-collision dynamics may be too long, which increases the probability that the tip retracts back to its branch point since the post-collision dynamics is skewed towards the shrinking state. Finally, another failure of the model is its inability to reproduce the low density of dendrites near the soma that is observed at the late stages. This indicates that the assumption of a spatially uniform branching rate may be incorrect. Alternatively, there could also be a non-uniform death process whereby old branches, which are predominantly closer to the soma, are more likely to die than younger branches, which are located mostly at the periphery of the neurons.

5.5 Free parameter exploration

In order to assess the importance of the free parameters of the model, the parameter space is explored and the effect of the parameters on the morphology is quantified using the morphometrics. The agent-based model has 3 free parameters: the persistence length of the growth L_p, the duration of the post-collision dynamics α and the duration of the initial branch growth phase T_0. To analyze their effect, multiple series of 12 simulations are generated where each series possess a different set of free parameter values. To simplify the parameter exploration, the exploration

of each free parameter is performed independently from the other free parameters. When a free parameter is not explored, its value is fixed to the value given in table 5.3. These base values were selected because they are physiologically plausible and because they generated realistic morphologies as shown in section 5.4 in preliminary explorations.

5.5.1 Persistence length L_p

First, the effect of the persistence length on the morphology is analyzed. More specifically, the following values of the growth persistence length are considered:$25, 50, 100, 200\,\mu m$. Examples of simulated trees generated with each of these four persistence length values are compared with the experimental trees in fig. 5.4. As expected, increasing the persistence length increases the straightness of the branches. Moreover, the morphometrics are compared against the experimental measurements as shown in fig. 5.5.

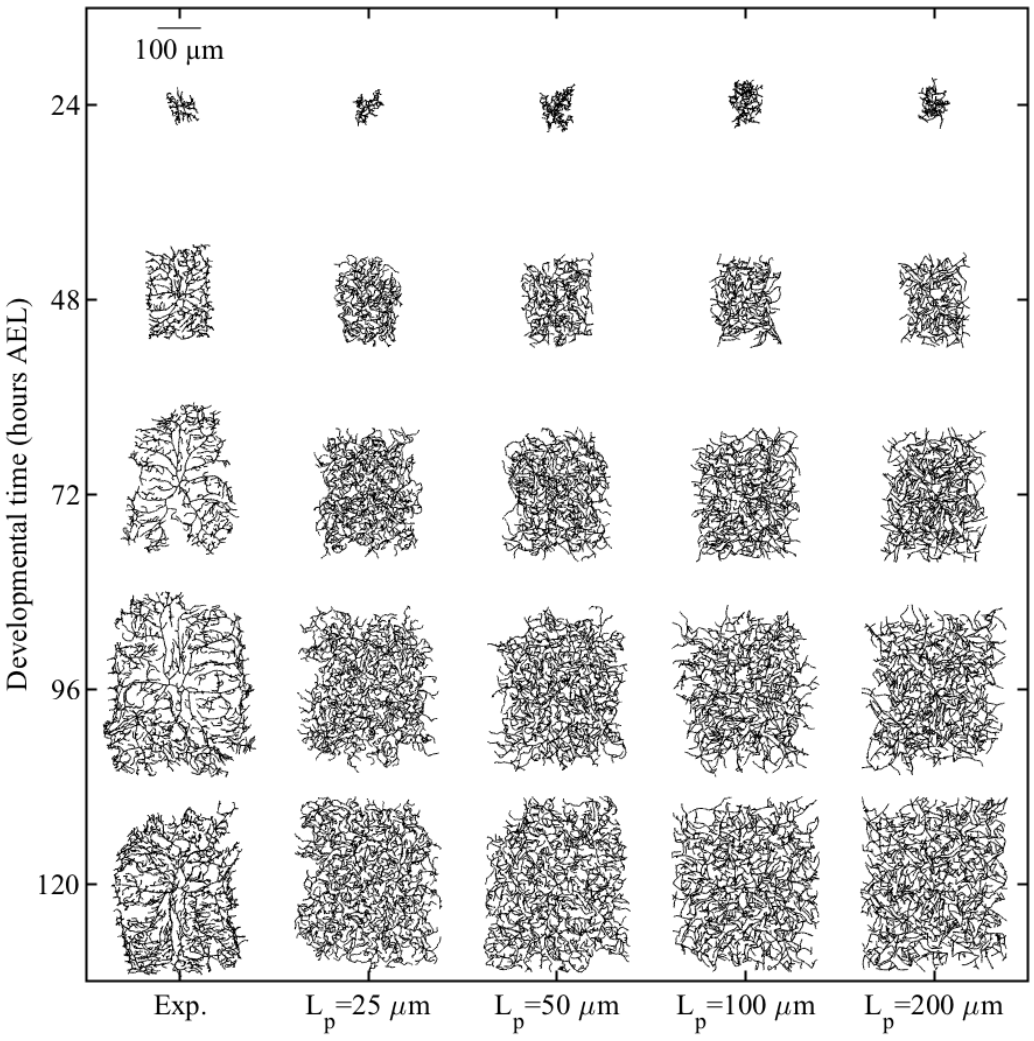

Figure 5.4 – Simulated trees with variable persistence length L_p

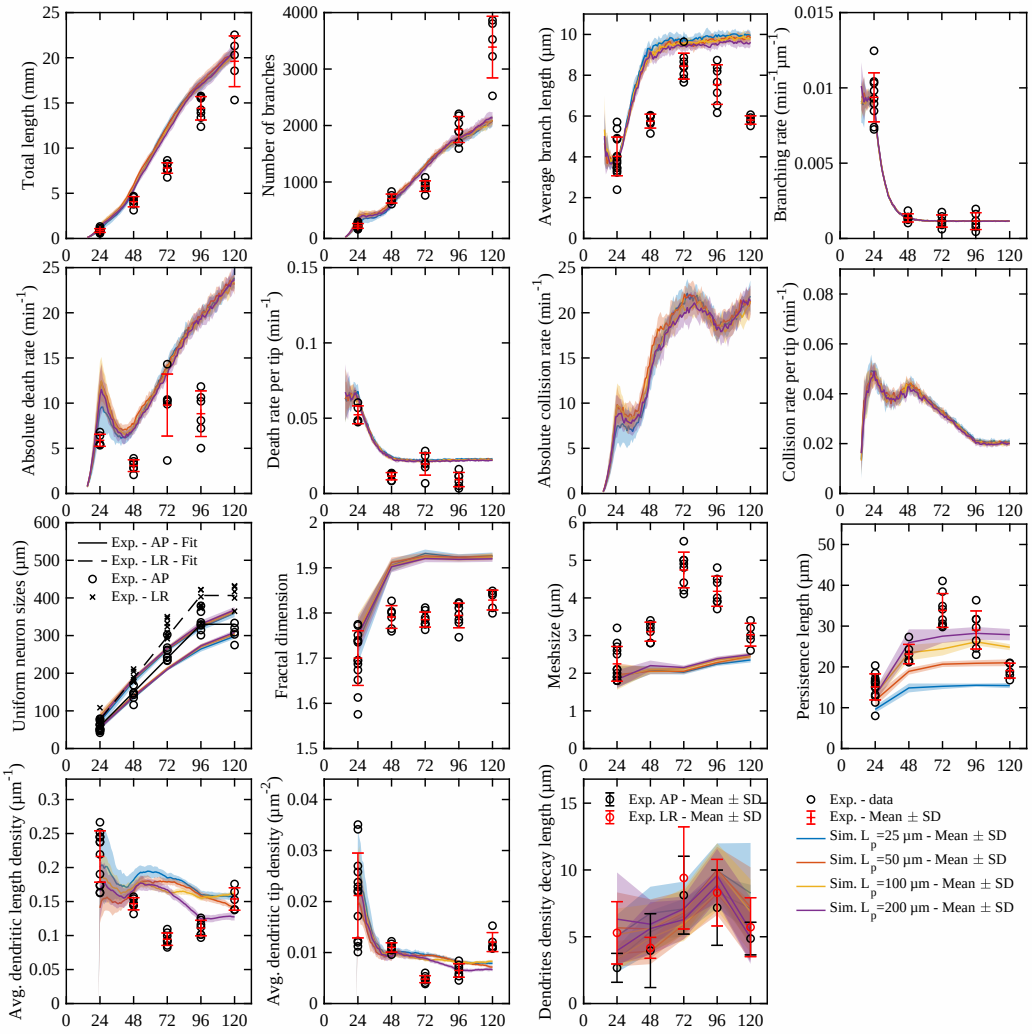

Figure 5.5 – Simulated morphometrics with variable persistence length L_p
The horizontal axis corresponds to the developmental time in hr AEL.

As depicted, the value of the persistence length does not have a considerable effect on most of the morphometrics. The morphometrics that are the most affected are the branch persistence length and the dendrites average density. As expected, the branch persistence length decreases as the growth persistence length decreases, since the growth persistence length is an upper bound of the persistence length of the branch path. Moreover, the dendrites density decreases as the input persistence length increases because increasing the growth persistence length decreases the ability of branches to explore and fill space. The fact that the persistence length

has a small effect on the overall tree morphology is potentially a consequence of the uniform branching rate. Indeed, since branching can occur everywhere and since it scales with the local density of dendrites, the branching process is efficient at exploring and filling space and henceforth branches may not require a suitable persistence length to explore their neighborhood.

5.5.2 Post-collision dynamics duration α

The second free parameter that is explored is the duration of the post-collision dynamics α. In this exploration, α takes the following values: $1, 5, 10, 50, 100$ min. Examples of simulated trees for each of these values are depicted in fig. 5.6 and the morphometrics comparison is shown in fig. 5.7.

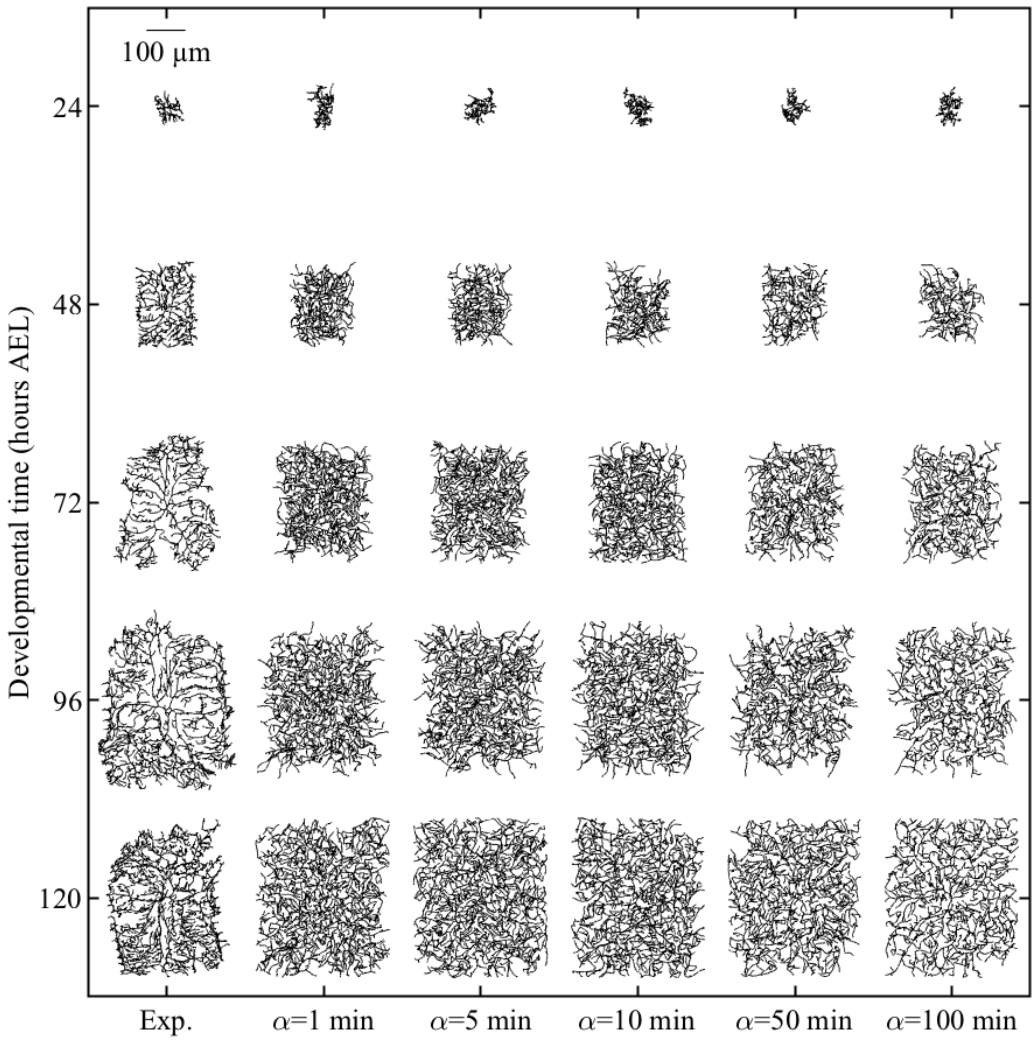

Figure 5.6 – Simulated trees with variable post-collision dynamics duration α

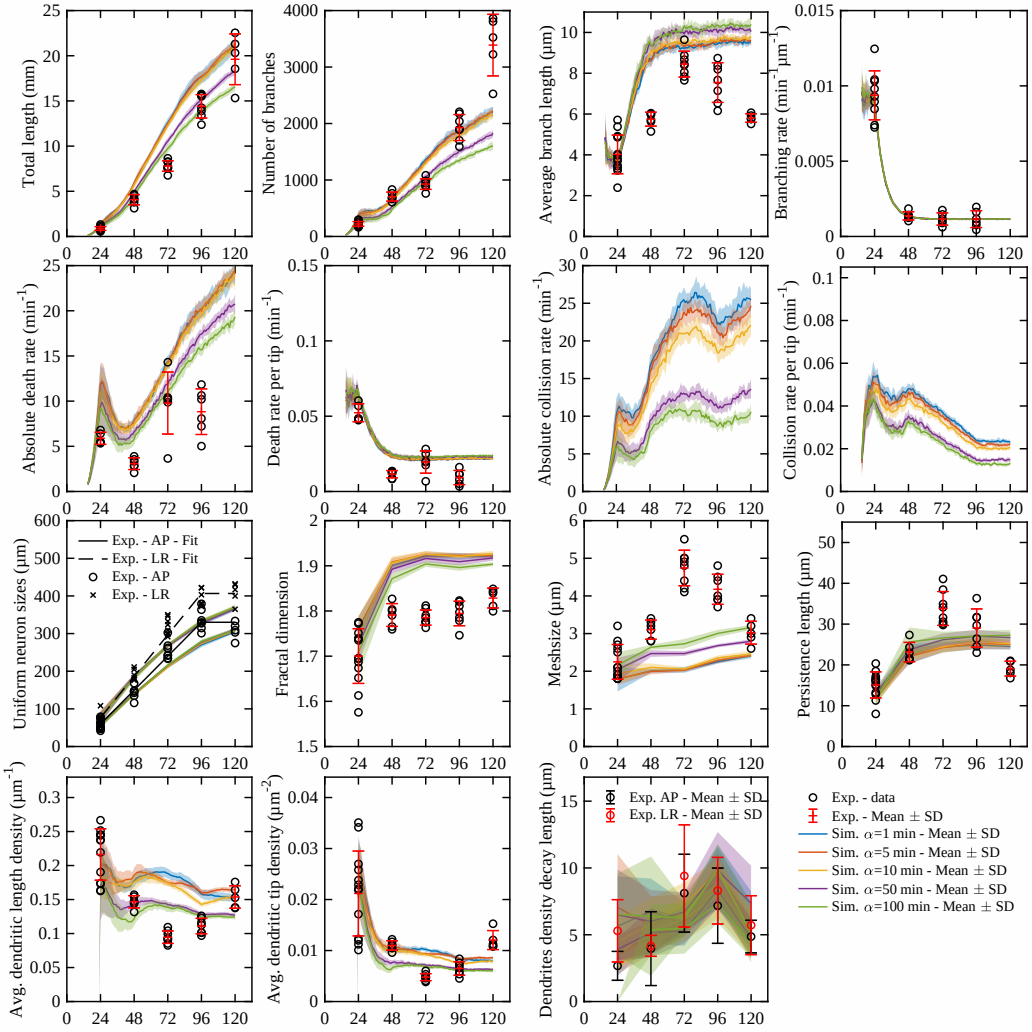

Figure 5.7 – Simulated morphometrics with variable post-collision dynamics duration α
The horizontal axis corresponds to the developmental time in hr AEL.

In general, the metrics portray what one would expect by increasing the duration of the repulsive post-collision dynamics, i.e., increasing α increases the pruning of the tree. This intuition is demonstrated in several ways.

First, the total branch length and the number of branches decrease as α increases, while the mean length remains relatively constant over the range of the explored values. Moreover, the collision rate per unit tip decreases as α increases since the branch tip spends more time in a repulsive state. Surprisingly, increasing

α decreases the absolute death rate while the death rate per unit tip is almost unaffected. This can be explained by the compound effect of branching and tip growth. As branch tips spend more time in the shrinking state, the total branch length increases at a slower rate, which leads to fewer new branches, since the branching process is extensive. Fewer branch births therefore leads to fewer branch deaths, since the death rate scales with the birth rate.

In addition, the metrics of density are also consistent with the idea that increasing α increases pruning. Indeed, the meshsize increases and the dendrites and dendritic tips densities decrease when α increases. However, the fractal dimension is almost unaffected by α and slightly decreases by increasing α to $100\,\text{min}$. Finally, α has also no effect on the uniform neuron size.

5.5.3 Initial growth duration T_0

The third free parameter that is explored is the duration of the initial growth phase of the branch tip T_0. For this exploration, the value of T_0 is set to $0.5, 1, 1.5, 2\,\text{min}$. Examples of simulated trees for each of these values are depicted in fig. 5.8 and the morphometrics comparison is shown in fig. 5.9.

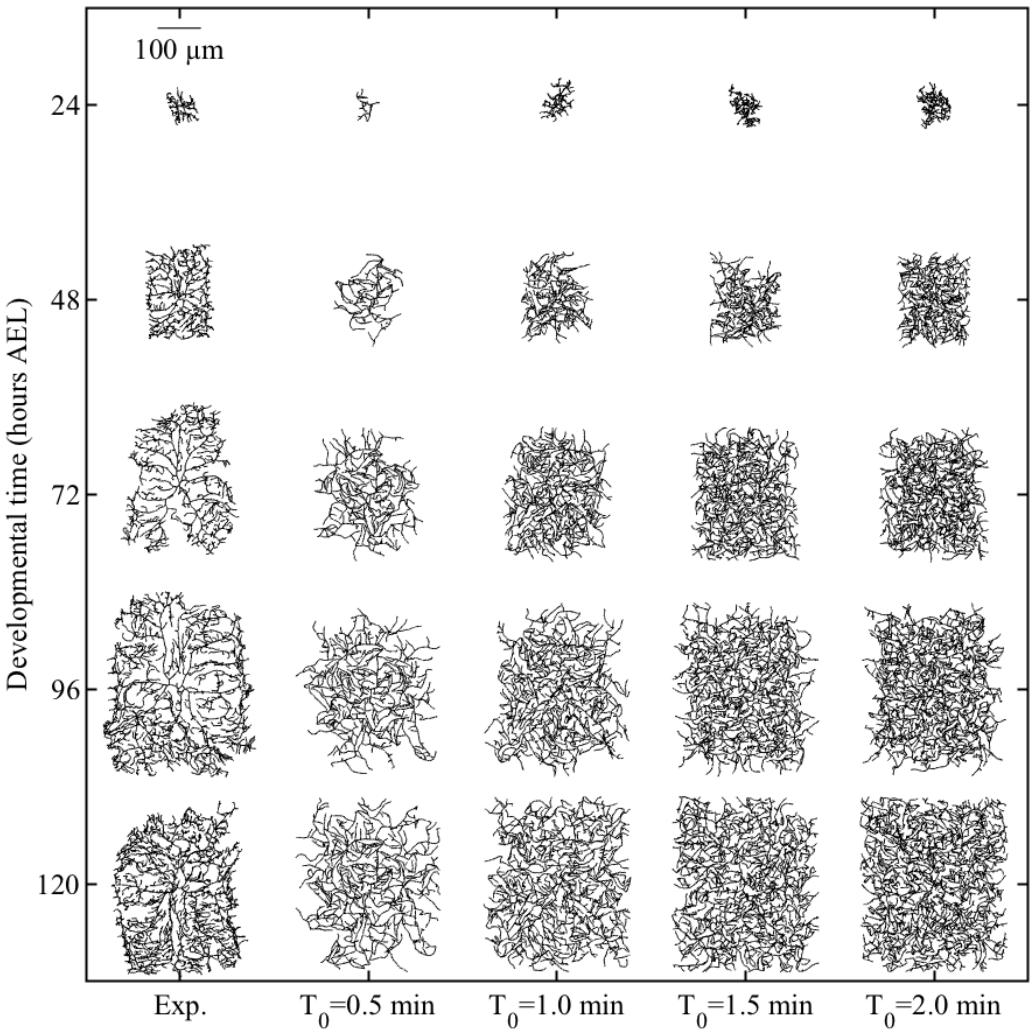

Figure 5.8 – Simulated trees with variable initial growth duration T_0

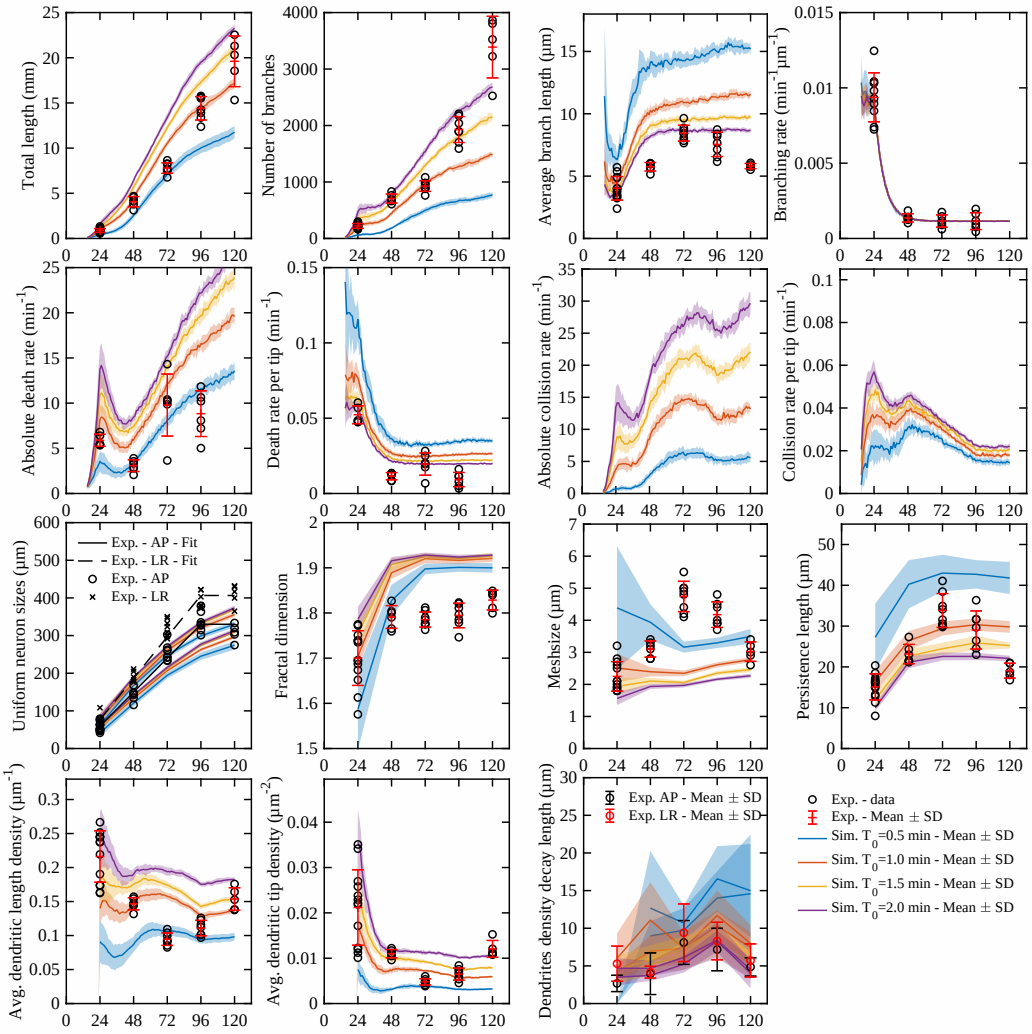

Figure 5.9 – Simulated morphometrics with variable initial growth duration T_0
The horizontal axis corresponds to the developmental time in hr AEL.

The duration of the initial growth phase T_0 is the free parameter that has the most prominent effect on the morphology. In general, the change in the metrics are consistent with the idea that increasing T_0 leads to a higher branch survival, which increases the dendrites mass and density. Indeed, as T_0 increases, both the total branch length and number of branches increases, and the mean branch length decreases since more branches survive. Furthermore, the collision rate increases for increasing T_0 and the density metrics also indicate that the tree becomes denser with a higher value of T_0.

One unexpected observation is the fact that the persistence length of the branches decreases as T_0 increases. This maybe caused by the fact that, when the value of T_0 is small, the tree is sparse and therefore branches collide less often and their persistence length is closer to the persistence length of the growth, which is given by $L_p = 100\,\mu m$ in this exploration.

Another surprising observation is the *increase* of the absolute death rate as T_0 increases. This is again a signature of the compound effect of branch growth and extensive branching as mentioned in the α exploration. However, when normalizing by the number of branch tips, the death rate decreases as T_0 increases consistent with the first-passage analysis presented in the mean-field model (see section 4.6). Moreover, the death rate per unit tip does not decrease linearly as T_0 increases linearly. This is again consistent with the first-passage analysis that shows that the death rate depends non-linearly on the initial branch length.

Interestingly, looking at the uniform neuron size and the decay length of the density fronts, two predictions of the mean-field model are confirmed as established by the marginal stability analysis of the front (see section 4.7.3). First, as T_0 increases, the zeroth-order death rate $k_{d,0}$ decreases since the branch has a higher survival probability. This allows for the density front to propagate faster as shown by the increase in the uniform neuron size for increasing T_0. Second, as T_0 increases, the agent-based model predicts that the density front decay length decreases. Indeed, this is consistent with the marginal stability analysis of the mean-field model since a lower value of $k_{d,0}$ is associated with a sharper density front as a higher branch survival leads to a more quickly filled boundary.

5.6 Non-uniform branching exploration

Motivated by the failure of the agent-based model to recover the low dendrites density near the soma, the effect of a non-spatially uniform branching rate is also explored. For this new branching rule, branches that are closer to the periphery of the neuron are more likely to give birth to new branch tips. More specifically, the probability that any branch node of length δ at position $\vec{x}_i$ gives birth to a new branch tip is given by the following formula:

$$P_B(\vec{x}_i) = \frac{\exp\left[\frac{-(R_g - |\vec{x}_i|)}{\lambda}\right]}{\sum_j \exp\left[\frac{-(R_g - |\vec{x}_j|)}{\lambda}\right]} \tag{5.14}$$

where R_g is the radius of gyration of the tree, $(0,0)$ corresponds to the position of the soma as mentioned before and λ is a free parameter that determines the spatial extent of the non-uniform branching rate. In this modified branching rule, the number of new branch tips at the given time t is first determined by sampling a Poisson distribution with an average of $k_b(t)L_{\text{Tot}}(t)\Delta t$, where $L_{\text{Tot}}(t)$ corresponds to the total branch length. Then, the new branch tips are spatially distributed according to eq. (5.14).

Using this new branching rule, multiples series of simulations are generated by changing the value of λ to $12.5, 25, 50, 100\,\mu m$. Examples of simulated trees are compared with the experimental trees in fig. 5.10 and the associated morphometrics are given in fig. 5.11.

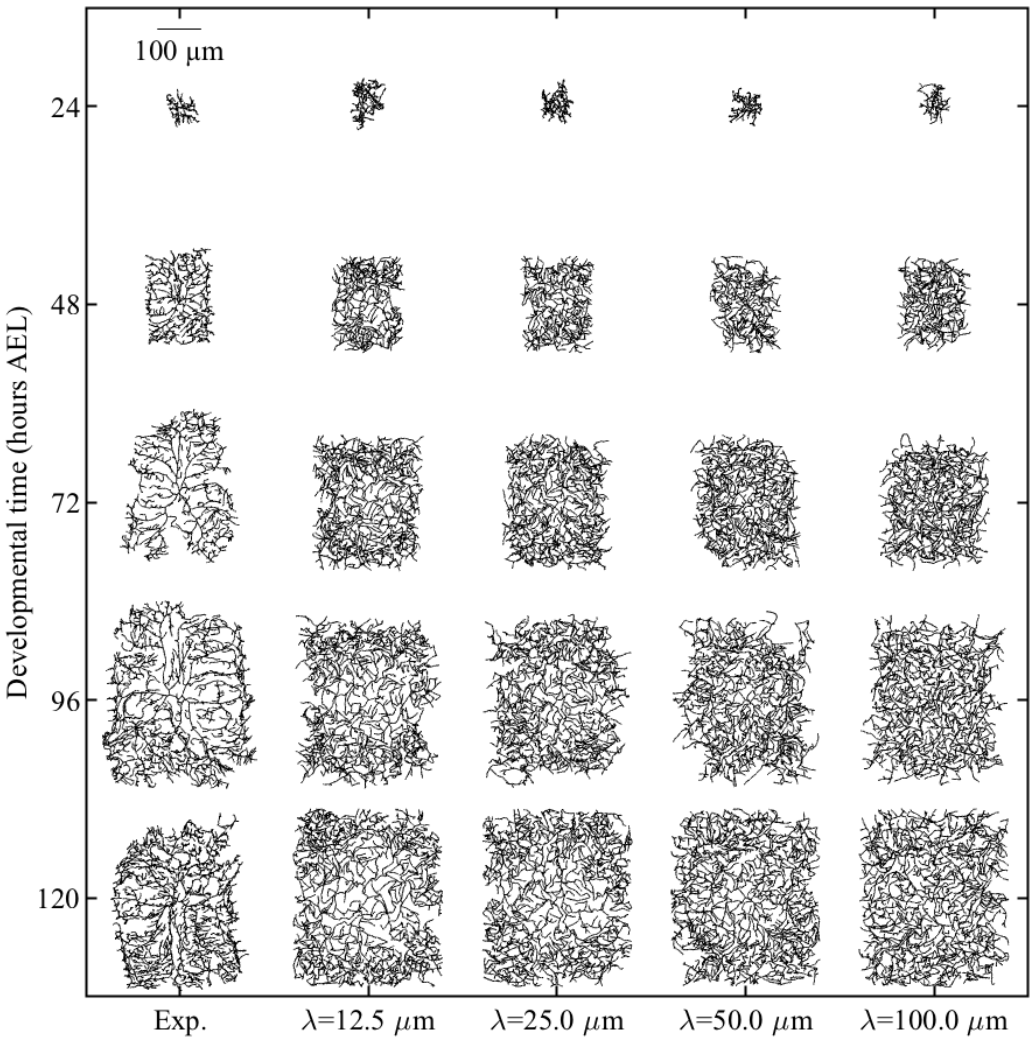

Figure 5.10 – Simulated trees with variable branching rate decay length λ

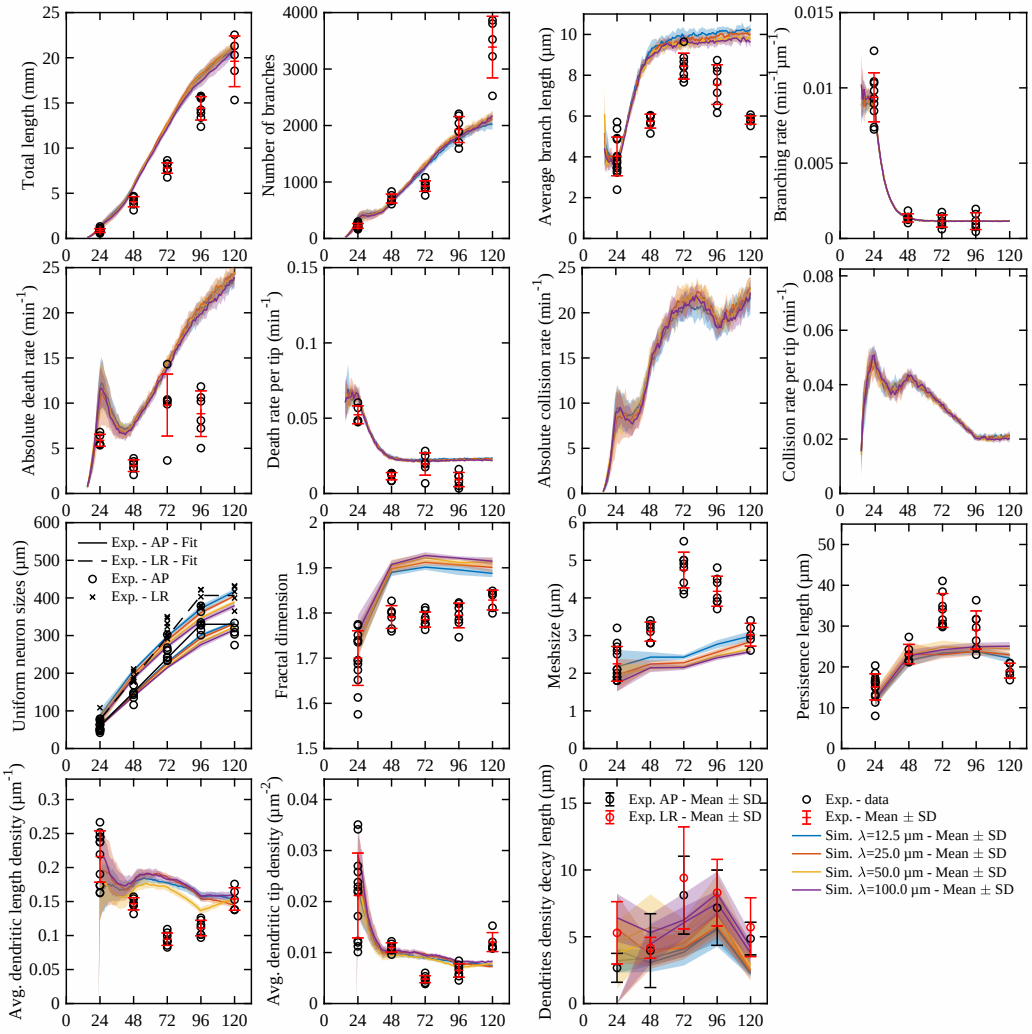

Figure 5.11 – Simulated morphometrics with variable branching rate decay length λ
The horizontal axis corresponds to the developmental time in hr AEL.

As shown by the simulated tree examples, the tree density is slightly lower near the soma as the branching rate is more biased towards the periphery of the neuron (smaller values of λ). Although changing the branching rate decay length has a noticeable effect on the branching pattern, the morphometrics are only slightly affected. The uniform neuron size increases slightly as λ decreases since the mass distribution of the tree has a higher variance in this case. Moreover, the changes in the fractal dimension and the meshsize indicate that the tree is sparser as λ decreases, but the differences of these metrics at different values of λ are not significant. In

addition, the decay length of the density profile increases proportionally with the decay length of the branching rate. This is expected since a higher branching rate at the boundary (small λ) leads to denser dendrites at the front, and hence the density profile decays more sharply.

Based on the results of this exploration, a non-uniform branching rate with a decay length of $12.5\mu m$ could explain the sparser density of dendrites near the soma. However, this modified branching rule does not significantly affect most morphometrics.

5.7 Effect of the segment boundary condition

Finally, to asses the effect of the boundary condition on the morphology of the tree, another set of simulations is generated using a repulsive boundary. More specifically, in this model, branch tips that collide with the boundary go directly to the shrinking state, as opposed to going to the paused state as used previously. Examples of simulated trees for a repulsive boundary are depicted in fig. 5.12 and compared against the pausing boundary used in the base simulations. The morphometrics comparison is shown in fig. 5.13 and demonstrates that the boundary condition has no significant effects on the morphology.

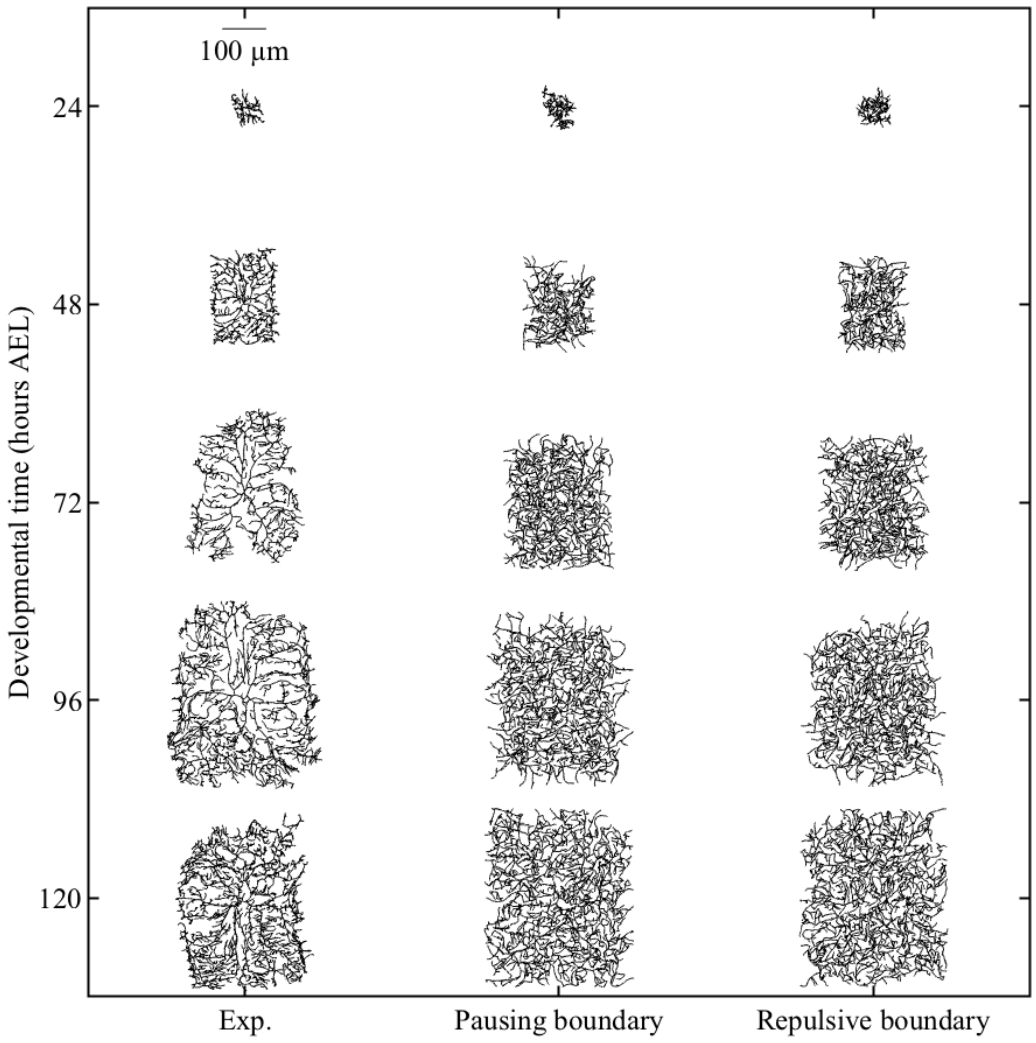

Figure 5.12 – Simulated trees with a repulsive boundary

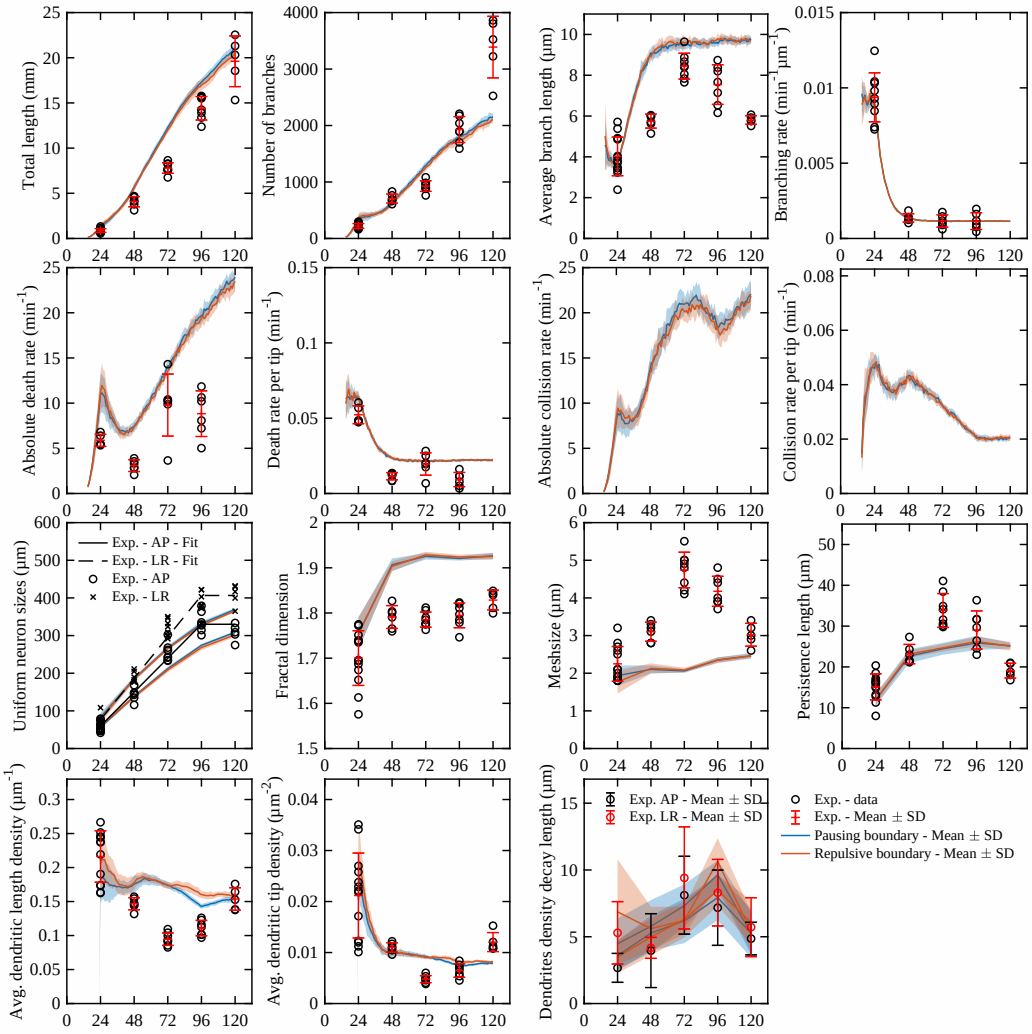

Figure 5.13 – Simulated morphometrics with a repulsive boundary
The horizontal axis corresponds to the developmental time in hr AEL.

5.8 Caveats and limitations

The agent-based model succeeds at reproducing qualitative and quantitative features of dendritic morphogenesis. However, the model makes several assumptions that may limit the range of its application and the accuracy of the predicted morphology. This section lists some of these limitations.

First, the tip dynamics parameters at 72 hr AEL are not constrained by experimental measurements, but are determined by the linear interpolation of the 48 and 96 hr AEL parameters. Large differences between the interpolated and measured values could incur significant changes in the morphology on and after 72 hr AEL.

Second, the transition rates of the post-collision dynamics do not change throughout development. Depending on the variation of the post-collision dynamics during development, this assumption could cause discrepancies in the morphology leading to either denser or sparser trees.

Third, the model assumes that the substrate, i.e. the epithelium, has no effect on the growth. The main assumption is that neurons are slipping onto the substrate, which was warranted by the non-extension of the non-terminal branches (see fig. 3.28). However, this assumption is potentially incorrect as interactions of the dendrites with the epithelium may play a functional role in the expansion of the dendritic tree. Indeed, recent work has shown that proximal dendrites of da neurons in *Drosophila* are enclosed in epithelial cells, which inhibits branching and growth, and the enclosure is mediated by membrane-associated proteins [81]. Moreover, if dendrites gradually attach to the substrate as they are growing, older dendritic branches may be more affected by the epithelium compared to newer branches. This mechanism could explain the sparser number of branches observed near the soma at the later stages.

Finally, the model completely neglects the effect of neuronal activity on the development. This is in part due to the fact that neuronal activity was not measured in this first attempt to characterize class IV neuron development. It is imaginable and likely possible that the sensory stimulation of class IV neurons plays a significant role in the development of its dendritic tree.

5.9 Conclusions

- We propose an agent-based model of dendritic morphogenesis that generates synthetic class IV neuron dendritic trees using three stochastic rules of growth constrained by experimental measurements: 1) stochastic branch growth, 2) extensive branching and 3) contact-based growth inhibition.

- The model predicts that coarse-grained morphometrics such as the total branch length and the number of branches are in agreement with the measurements, but the dendrites density and the branch death rate are overestimated.

- The model has three free parameters: 1) the persistence length of the growth, 2) the duration of the post-collision dynamics and 3) the duration of the initial branch growth phase. Among these parameters, the duration of the initial growth phase of the branch has the strongest impact on the tree morphology whereby increasing this duration leads to denser dendritic trees.

6 Conclusions and Outlook

Dendrites are essential for neurons to receive information from their external environment. The shape of dendritic trees comes in various forms and their development ensues from a complex cellular machinery that assembles the dendritic arbor through a multitude of microscopic molecular mechanisms. How these mechanisms cooperate with one another to form the observed dendritic morphologies remains misunderstood. This lack of knowledge and the beauty of this complex multi-scale process has motivated us to investigate the causal relationships between the molecular processes of dendritic growth and the emergent cellular morphology. Our study of the class IV neuron dendritic growth in *Drosophila melanogaster* larvae has led us to characterize dendritic growth using common and novel metrics and build multi-scale models of dendritic morphogenesis that improved upon previous proposals.

6.1 Contributions

To investigate the dendritic growth of class IV neurons, we have used analytical tools, theoretical models and stochastic simulations to quantify the microscopic and macroscopic aspects of the growth. Our contribution to the research of neuronal growth is multi-faceted.

In chapter 2, we described how we made our observations of the class IV dendritic growth *in vivo*. To process our images, we designed a novel image stitching

algorithm using non-rigid displacement fields. We also designed a skeletonization algorithm based on a previous algorithm that traces neurons by scooping pixels [70].

In chapter 3, we characterized the dendritic development into three main processes: 1) stochastic tip growth, 2) extensive branching and 3) contact-based growth inhibition. First, we found that the class IV dendritic tip growth can be described by a 3-state Markov process whose state determines the velocity of the tip. Second, we discovered that the branching process is spatially uniform with a rate that scales with the total amount of dendrites in the tree. Third, we found that the duration of the branch tip contacts are exponentially distributed and the post-collision dynamics favors tip retraction. Finally, we described the morphology using established and novel metrics and concluded that the density of the tree is initially dense, but subsequently becomes sparser and reaches a steady-state at later stages.

In chapter 4, we formulated a mean-field model of dendritic growth following the ideas of previous models [21, 78] and using the insight that we gained from our analysis of the dendritic growth process. Our framework constructs mathematical relationships between the local growth processes and the macroscopic growth. In particular, we succeed at predicting the parameter values of the microscopic processes using the large-scale morphometrics henceforth establishing a link between the sub-cellular processes and the morphology. In addition, we predict that the dendritic tree expands from the motion of a solitary wave of dendritic tips that travel at a constant speed. The wave velocity results from the combined effect of tip growth, branching and contact inhibition, akin to the propagating wavefront in Fisher's equation and the Hannezo *et al.* model of the ductal network morphogenesis in mammary glands [21].

In chapter 5, we implemented an agent-based model of branching morphogenesis similar in idea to the proposal of Palavalli *et al.* [61]. However, our model is more strongly constrained by our measurements of the growth processes leaving only three parameters free. Moreover, the agent-based model can recapitulate the dendritic morphology of the three larval stages, while the Palavalli *et al.* model recovers only the first 10 hours of development. By exploring the parameter space, we also find that the initial branch growth duration is a strong determinant of the morphology, while the effect of the growth persistence length and the duration of the post-collision dynamics on the morphology are nominal. Our fine-grained computational model improves our understanding of branching morphogenesis by providing a mechanistic foundation for the development of the class IV neuron morphology. Combined with the mean-field model, the agent-based model strengthens our hypothesis that dendritic morphogenesis is an emergent phenomenon of the local growth processes.

In summary, we characterized the class IV growth processes throughout the larval development and constructed multi-scale theoretical and computational models of dendritic growth constrained by our analysis. Our models improve upon previous approaches by providing a mechanistic framework to understand dendritic growth. The mean-field model establishes a direct connection between the microscopic growth mechanisms and the large-scale features, which improves the Sugimura *et al.* [78] model as it better represents the stochastic growth process of class IV neurons. Moreover, the microscopic growth mechanisms that build the foundations of both models help us the cellular processes that drive neuronal growth at the large scale. This connection is an improvement of the proposal by Cuntz *et al.* [9] model, since their model disregards constraints imposed by the cellular processes when optimizing the dendritic network. Finally, our results demonstrate that the sub-cellular growth processes of class IV neurons are sufficient to produce

a self-organized dendritic arbor leading us to answer our original question in the following way:

How do neuronal dendrites grow?

The growth of the class IV neuron dendritic tree is autonomous and self-organizes through contact-based retraction.

6.2 Future work

Our characterization of dendritic growth and our proposed multi-scale models opens many avenues that will shine new light on dendritic morphogenesis in class IV neurons.

Our analysis of the tip growth dynamics characterizes the growth as a Markov process with specific transition rates and associated velocities. Our samples of the tip dynamics allowed us to calculate the dynamics parameters with certainty at each developmental stage. However, the sparsity of the dataset prohibited an in-depth analysis of the spatial dependence of tip dynamics. With a denser sampling of the tip dynamics, one could study the variability of the tip dynamics throughout the arbor with the following questions: How does the tip dynamics change spatially? Specifically, how do the average growth velocity and diffusion constant change as a function of the distance from the soma? Is the dynamics more or less active at the periphery? A non-uniform dynamics would indicate that spatial cues are potentially at play during the development while a uniform dynamics would indicate that such spatial cues are either spatially uniform or inconsequential to the large scale of the tree. Alternatively, non-uniformities in the dynamics could also provide evidence

on intracellular transport constraints that module the growth of tips throughout the tree.

Another aspect of the tip dynamics that raises new questions is the Markov property. As explained earlier, we found mixed evidence that the tip growth process is truly Markov. One could further test this result with more data or by using the agent-based model as a testbed for the effects of non-Markovianness on the morphology. Furthermore, the agent-based model assumes that the state duration is uncorrelated with the state velocity. However, our preliminary analysis has shown the presence of some correlation between the duration of the velocity. Including these correlations in the agent-based model would be the first strategy to probe their effect.

The predictions of the mean-field model also suggest new investigations. One of the major caveats of the mean-field model is the absence of the boundary effects, which arise from the tiling of the class IV neurons *in vivo*. As such, the model predicts a forever expanding tree constrained solely by the tip dynamics and branching process. One could easily implement the boundary constraints numerically using a moving boundary whose velocity is set by the growth of the body segment size. The results of this model would provide answers to these questions: how does the boundary condition change the density front profile? How far do these changes propagate towards the bulk of the profile?

Moreover, the validity of the mean-field model could be further assessed by measuring the distribution of the branch lifetimes over development. The model makes quantitative predictions on the shape of the lifetime distribution by modeling the tip death process as a first-passage problem. Discrepancies between the predicted and measured distribution would suggest the presence of additional mechanisms that influence tip growth. A measured lifetime that is higher than predicted would indicate that there are rescue mechanisms that promote regrowth or prevents certain

death, while a shorter measured lifetime would suggest that the contact growth inhibition promotes persistent changes in the tip dynamics that accelerate the death process. Related to this question, one could also use the agent-based model to test the mean-field predictions of the contact inhibition parameter c_{RU} and the death rate k_d. In particular, c_{RU} was predicted from a first-order perturbation of the tips steady-state. How important is the next leading order in this perturbation? Simulations could help put a bound on the error of the perturbation or elucidate second-order effects due to contacts.

Finally, this thesis establishes a connection between the dendritic tip growth processes and the morphology of the resulting tree. However, this relationship provides only a partial answer to the broader question of the emergence of morphology from molecular mechanisms. Establishing the other half of this connection requires a consideration of the molecular constraints on the growth of the dendritic tips. To build this connection, one could use stochastic simulations framed within the agent-based model to implement the molecular constraints on the growth. First, one could model the transport of the membrane and cytoskeletal elements by sectioning the dendrite branches into finite elements with transport properties that depend on the density of molecular motors. Then, the tip could be treated as an independent agent that moves based on the local dynamics and density of the cytoskeleton (actin and microtubules). Furthermore, the effect of the stabilization of microtubules on the establishment of the branch could be studied by modeling the acetylation and tyrosination of the microtubule bundles. In addition, one could model local sources of proteins (eg. Golgi outposts) and study how their distribution throughout the arbor influences the growth of the dendritic tips. Based on recent findings [56], the microtubule and actin density are strong predictors of the morphology, hence modeling the cytoskeleton dynamics could be sufficient to predict the morphology from the molecular processes.

Bibliography

[1] A. Akhmanova and M. O. Steinmetz, "Microtubule End Binding: EBs Sense the Guanine Nucleotide State", en, Current Biology **21**, R283–R285 (2011) (cit. on p. 11).

[2] F. R. Amthor and C. W. Oyster, "Spatial organization of retinal information about the direction of image motion", eng, Proceedings of the National Academy of Sciences of the United States of America **92**, 4002–4005 (1995) (cit. on p. 15).

[3] M. Ashburner, *Drosophila: A laboratory handbook*, Drosophila / Michael Ashburner (Cold Spring Harbor Laboratory, 1989) (cit. on pp. 8, 72).

[4] S. R. Y. Cajal, "La rétine des vertébrés", Cellule **9**, 119–255 (1893) (cit. on p. 15).

[5] S. Cajal, *Histology of the Nervous System of Man and Vertebrates: General principles, spinal cord, spinal ganglia, medulla & pons*, Histology of the Nervous System of Man and Vertebrates (Oxford University Press, 1995) (cit. on p. 17).

[6] J. Canny, "A Computational Approach to Edge Detection", IEEE Transactions on Pattern Analysis and Machine Intelligence **PAMI-8**, 679–698 (1986) (cit. on p. 45).

[7] J. Cardy and U. C. Täuber, "Theory of Branching and Annihilating Random Walks", Physical Review Letters **77**, 4780–4783 (1996) (cit. on p. 23).

[8] M. M. Corty, B. J. Matthews, and W. B. Grueber, "Molecules and mechanisms of dendrite development in Drosophila", Development **136**, 1049–1061 (2009) (cit. on p. 10).

[9] H. Cuntz, F. Forstner, A. Borst, and M. Häusser, "One rule to grow them all: A general theory of neuronal branching and its practical application", PLoS Computational Biology **6**, edited by A. Morrison, e1000877 (2010) (cit. on pp. 17, 18, 241).

[10] R. Dominguez and K. C. Holmes, "Actin Structure and Function", Annual review of biophysics **40**, 169–186 (2011) (cit. on p. 10).

[11] K. Emoto, Y. He, B. Ye, et al., "Control of Dendritic Branching and Tiling by the Tricornered-Kinase/Furry Signaling Pathway in Drosophila Sensory Neurons", en, Cell **119**, 245–256 (2004) (cit. on p. 16).

[12] K. Emoto, J. Z. Parrish, L. Y. Jan, and Y.-N. Jan, "The tumour suppressor Hippo acts with the NDR kinases in dendritic tiling and maintenance", en, Nature **443**, 210–213 (2006) (cit. on p. 16).

[13] K. Falconer, *Fractal geometry: Mathematical foundations and applications* (Wiley, 2013) (cit. on p. 108).

[14]R. A. Fisher, “The Wave of Advance of Advantageous Genes”, Annals of Eugenics **7**, 355–369 (1937) (cit. on p. 195).

[15]S. Ganguly, O. Trottier, X. Liang, H. Bowne-Anderson, and J. Howard, “Morphology of Fly Larval Class IV Dendrites Accords with a Random Branching and Contact Based Branch Deletion Model”, ArXiv **1611.05918**, 1–12 (2016) (cit. on p. 205).

[16]F.-B. Gao, M. Kohwi, J. E. Brenman, L. Y. Jan, and Y. N. Jan, “Control of Dendritic Field Formation in Drosophila: The Roles of Flamingo and Competition between Homologous Neurons”, en, Neuron **28**, 91–101 (2000) (cit. on p. 16).

[17]P. Grassberger and I. Procaccia, “Measuring the strangeness of strange attractors”, en, Physica D: Nonlinear Phenomena **9**, 189–208 (1983) (cit. on p. 108).

[18]W. B. Grueber, B. Ye, A. W. Moore, L. Y. Jan, and Y. N. Jan, “Dendrites of Distinct Classes of Drosophila Sensory Neurons Show Different Capacities for Homotypic Repulsion”, Current Biology **13**, 618–626 (2003) (cit. on p. 15).

[19]W. B. Grueber, L. Y. Jan, and Y. N. Jan, “Tiling of the Drosophila epidermis by multidendritic sensory neurons.”, Development (Cambridge, England) **129**, 2867–78 (2002) (cit. on pp. 7, 8, 15).

[20]C. Han, D. Wang, P. Soba, et al., “Integrins Regulate Repulsion-Mediated Dendritic Patterning of Drosophila Sensory Neurons by Restricting Dendrites in a 2D Space”, en, Neuron **73**, 64–78 (2012) (cit. on pp. 6, 7, 15).

[21]E. Hannezo, C. L. Scheele, M. Moad, et al., “A Unifying Theory of Branching Morphogenesis”, Cell **171**, 242–255.e27 (2017) (cit. on pp. 23, 24, 26, 240).

[22]S. E. Hill, M. Parmar, K. W. Gheres, et al., “Development of dendrite polarity in Drosophila neurons”, Neural Development **7**, 34 (2012) (cit. on p. 11).

[23]N. Hirokawa, S. Niwa, and Y. Tanaka, “Molecular Motors in Neurons: Transport Mechanisms and Roles in Brain Function, Development, and Disease”, en, Neuron **68**, 610–638 (2010) (cit. on p. 10).

[24]J. Howard and A. A. Hyman, “Dynamics and mechanics of the microtubule plus end”, en, Nature **422**, 753–758 (2003) (cit. on p. 10).

[25]M. E. Hughes, R. Bortnick, A. Tsubouchi, et al., “Homophilic Dscam Interactions Control Complex Dendrite Morphogenesis”, en, Neuron **54**, 417–427 (2007) (cit. on p. 15).

[26]R. Y. Hwang, L. Zhong, Y. Xu, et al., “Nociceptive Neurons Protect Drosophila Larvae from Parasitoid Wasps”, en, Current Biology **17**, 2105–2116 (2007) (cit. on p. 7).

[27]Y.-N. Jan and L. Y. Jan, “Branching out: mechanisms of dendritic arborization”, en, Nature Reviews Neuroscience **11**, 316–328 (2010) (cit. on pp. 6, 8, 33).

[28]J. L. W. V. Jensen, “Sur les fonctions convexes et les inégalités entre les valeurs moyennes”, FR, Acta Mathematica **30**, 175–193 (1906) (cit. on p. 188).

[29]S. Jinushi-Nakao, R. Arvind, R. Amikura, et al., “Knot/Collier and Cut Control Different Aspects of Dendrite Cytoskeleton and Synergize to Define Final Arbor Shape”, en, Neuron **56**, 963–978 (2007) (cit. on p. 12).

[30]L. C. Kapitein and C. C. Hoogenraad, "Building the Neuronal Microtubule Cytoskeleton", en, Neuron **87**, 492–506 (2015) (cit. on p. 11).

[31]K.-M. Kim, K. Son, and G. T. R. Palmore, "Neuron Image Analyzer: Automated and Accurate Extraction of Neuronal Data from Low Quality Images", en, Scientific Reports **5**, 17062 (2015) (cit. on p. 45).

[32]M. E. Kim, B. R. Shrestha, R. Blazeski, C. A. Mason, and W. B. Grueber, "Integrins Establish Dendrite-Substrate Relationships that Promote Dendritic Self-Avoidance and Patterning in Drosophila Sensory Neurons", en, Neuron **73**, 79–91 (2012) (cit. on p. 15).

[33]H. Kimura, T. Usui, A. Tsubouchi, and T. Uemura, "Potential dual molecular interaction of the Drosophila 7-pass transmembrane cadherin Flamingo in dendritic morphogenesis", en, Journal of Cell Science **119**, 1118–1129 (2006) (cit. on p. 16).

[34]A Kolmogorov, I Petrovskii, and N Piscounov, "A study of the diffusion equation with increase in the amount of substance, and its application to a biological problem.", Bull. Moscow Univ. Math. Mech. **1**, 1 (1937) (cit. on p. 195).

[35]V. A. Kulkarni and B. L. Firestein, "The dendritic tree and brain disorders", en, Molecular and Cellular Neuroscience **50**, 10–20 (2012) (cit. on p. 31).

[36]Y.-W. Kuo, O. Trottier, and J. Howard, "Predicted Effects of Severing Enzymes on the Length Distribution and Total Mass of Microtubules", English, Biophysical Journal **117**, 2066–2078 (2019) (cit. on p. 12).

[37]Y.-W. Kuo, O. Trottier, M. Mahamdeh, and J. Howard, "Spastin is a dual-function enzyme that severs microtubules and promotes their regrowth to increase the number and mass of microtubules", en, Proceedings of the National Academy of Sciences **116**, 5533–5541 (2019) (cit. on p. 12).

[38]M. Landgraf, V. Jeffrey, M. Fujioka, J. B. Jaynes, and M. Bate, "Embryonic Origins of a Motor System: Motor Dendrites Form a Myotopic Map in Drosophila", en, PLOS Biology **1**, e41 (2003) (cit. on p. 15).

[39]T. C. Lee, R. L. Kashyap, and C. N. Chu, "Building Skeleton Models via 3-D Medial Surface Axis Thinning Algorithms", en, CVGIP: Graphical Models and Image Processing **56**, 462–478 (1994) (cit. on p. 45).

[40]T. Lee and L. Luo, "Mosaic Analysis with a Repressible Cell Marker for Studies of Gene Function in Neuronal Morphogenesis", en, Neuron **22**, 451–461 (1999) (cit. on p. 8).

[41]J. L. Lefebvre, J. R. Sanes, and J. N. Kay, "Development of Dendritic Form and Function", Annual Review of Cell and Developmental Biology **31**, 741–777 (2015) (cit. on p. 33).

[42]d. V. Leonardo 1452-1519, *The notebooks of Leonardo da Vinci* (New York : Dover Publications, 1970., 1970) (cit. on p. 105).

[43]K. Li, *The image stabilizer plugin for ImageJ*, Feb. 2008 (cit. on p. 37).

[44]S. Liu, D. Zhang, S. Liu, et al., "Rivulet: 3D Neuron Morphology Tracing with Iterative Back-Tracking", Neuroinformatics **14**, 387–401 (2016) (cit. on p. 45).

[45]M. H. Longair, D. A. Baker, and J. D. Armstrong, "Simple Neurite Tracer: open source software for reconstruction, visualization and analysis of neuronal processes", Bioinformatics **27**, 2453–2454 (2011) (cit. on p. 45).

[46]W. Lu, P. Fox, M. Lakonishok, M. W. Davidson, and V. I. Gelfand, "Initial Neurite Outgrowth in Drosophila Neurons Is Driven by Kinesin-Powered Microtubule Sliding", en, Current Biology **23**, 1018–1023 (2013) (cit. on p. 13).

[47]B. B. Mandelbrot, *The fractal geometry of nature*, First (W.H. Freeman, 1982) (cit. on p. 113).

[48]C.-X. Mao, Y. Xiong, Z. Xiong, et al., "Microtubule-severing protein Katanin regulates neuromuscular junction development and dendritic elaboration in Drosophila", en, Development **141**, 1064–1074 (2014) (cit. on p. 12).

[49]MATLAB, *Version 9.6.0 (R2019a)* (The MathWorks Inc., Natick, Massachusetts, 2019) (cit. on p. 45).

[50]B. J. Matthews and W. B. Grueber, "Dscam1-Mediated Self-Avoidance Counters Netrin-Dependent Targeting of Dendrites in Drosophila", en, Current Biology **21**, 1480–1487 (2011) (cit. on p. 15).

[51]B. J. Matthews, M. E. Kim, J. J. Flanagan, et al., "Dendrite Self-Avoidance Is Controlled by Dscam", English, Cell **129**, 593–604 (2007) (cit. on pp. 13, 15).

[52]R. Milo and R. Phillips, *Cell biology by the numbers* (CRC Press, 2015) (cit. on p. 10).

[53]T. Mitchison and M. Kirschner, "Dynamic instability of microtubule growth", en, Nature **312**, 237–242 (1984) (cit. on p. 10).

[54]A. Mukherjee, P. S. Brooks, F. Bernard, A. Guichet, and P. T. Conduit, "Microtubules originate asymmetrically at the somatic golgi and are guided via Kinesin2 to maintain polarity within neurons", eLife **9**, edited by Y. M. Yamashita and K VijayRaghavan, e58943 (2020) (cit. on p. 11).

[55]D. Myatt, T. Hadlington, G. Ascoli, and S. Nasuto, "Neuromantic – from Semi-Manual to Semi-Automatic Reconstruction of Neuron Morphology", English, Frontiers in Neuroinformatics **6** (2012) (cit. on p. 45).

[56]S. Nanda, S. Bhattacharjee, D. N. Cox, and G. A. Ascoli, "Distinct Relations of Microtubules and Actin Filaments with Dendritic Architecture", en, iScience **23**, 101865 (2020) (cit. on pp. 12, 244).

[57]M. M. Nguyen, C. J. McCracken, E. S. Milner, et al., "γ-Tubulin controls neuronal microtubule polarity independently of Golgi outposts", Molecular Biology of the Cell **25**, 2039–2050 (2014) (cit. on p. 12).

[58]V. Nithianandam and C.-T. Chien, "Actin blobs prefigure dendrite branching sites", en, The Journal of Cell Biology **217**, 3731–3746 (2018) (cit. on p. 12).

[59]R. Norkett, U. del Castillo, W. Lu, and V. I. Gelfand, "Ser/Thr kinase Trc controls neurite outgrowth in Drosophila by modulating microtubule-microtubule sliding", eLife **9**, edited by S. R. Pfeffer and J. G. DeLuca, e52009 (2020) (cit. on p. 13).

[60]K. M. Ori-McKenney, R. J. McKenney, H. H. Huang, et al., "Phosphorylation of β-Tubulin by the Down Syndrome Kinase, Minibrain/DYRK1a, Regulates Microtubule Dynamics and Dendrite Morphogenesis", Neuron **90**, 551–563 (2016) (cit. on p. 11).

[61]A. Palavalli, N. Tizón-Escamilla, J.-F. Rupprecht, and T. Lecuit, "Deterministic and Stochastic Rules of Branching Govern Dendrite Morphogenesis of Sensory Neurons", en, Current Biology **31**, 459–472.e4 (2021) (cit. on pp. 27, 28, 241).

[62]J. Z. Parrish, P. Xu, C. C. Kim, L. Y. Jan, and Y. N. Jan, "The microRNA bantam Functions in Epithelial Cells to Regulate Scaling Growth of Dendrite Arbors in Drosophila Sensory Neurons", en, Neuron **63**, 788–802 (2009) (cit. on p. 16).

[63]H. Peng, Z. Ruan, F. Long, J. H. Simpson, and E. W. Myers, "V3D enables real-time 3D visualization and quantitative analysis of large-scale biological image data sets", en, Nature Biotechnology **28**, 348–353 (2010) (cit. on p. 45).

[64]M. Pool, J. Thiemann, A. Bar-Or, and A. E. Fournier, "NeuriteTracer: A novel ImageJ plugin for automated quantification of neurite outgrowth", en, Journal of Neuroscience Methods **168**, 134–139 (2008) (cit. on p. 45).

[65]S. Preibisch, S. Saalfeld, and P. Tomancak, "Globally optimal stitching of tiled 3D microscopic image acquisitions", en, Bioinformatics **25**, 1463–1465 (2009) (cit. on p. 40).

[66]W. Rall, "Electrophysiology of a Dendritic Neuron Model", Biophysical Journal **2**, 145–167 (1962) (cit. on p. 17).

[67]C. R. Rao, *Linear statistical inference and its applications*, English (Wiley, New York, 2002) (cit. on p. 154).

[68]S. Redner, *A guide to first-passage processes*, A Guide to First-Passage Processes (Cambridge University Press, 2001) (cit. on p. 170).

[69]J. L. Robertson, A. Tsubouchi, and W. D. Tracey, "Larval Defense against Attack from Parasitoid Wasps Requires Nociceptive Neurons", PLoS ONE **8**, edited by E. M. C. Skoulakis, e78704 (2013) (cit. on p. 7).

[70]A. Rodriguez, D. B. Ehlenberger, P. R. Hof, and S. L. Wearne, "Three-dimensional neuron tracing by voxel scooping", Journal of Neuroscience Methods **184**, 169–175 (2009) (cit. on pp. 43, 240).

[71]C. Santiago and G. J. Bashaw, "Transcription factors and effectors that regulate neuronal morphology", en, Development **141**, 4667–4680 (2014) (cit. on p. 33).

[72]D. Satoh, D. Sato, T. Tsuyama, et al., "Spatial control of branching within dendritic arbors by dynein-dependent transport of Rab5-endosomes", en, Nature Cell Biology **10**, 1164–1171 (2008) (cit. on p. 12).

[73]P. Soba, S. Zhu, K. Emoto, et al., "Drosophila Sensory Neurons Require Dscam for Dendritic Self-Avoidance and Proper Dendritic Field Organization", Neuron **54**, 403–416 (2007) (cit. on pp. 13, 15).

[74]P. Soba, C. Han, Y. Zheng, et al., "The ret receptor regulates sensory neuron dendrite growth and integrin mediated adhesion", eLife **2015**, 1–21 (2015) (cit. on p. 15).

[75]O. Steward and E. M. Schuman, "Compartmentalized Synthesis and Degradation of Proteins in Neurons", en, Neuron **40**, 347–359 (2003) (cit. on p. 11).

[76]M. C. Stone, F. Roegiers, and M. M. Rolls, "Microtubules Have Opposite Orientation in Axons and Dendrites of Drosophila Neurons", Molecular Biology of the Cell **19**, 4122–4129 (2008) (cit. on p. 11).

[77]M. C. Stone, K. Rao, K. W. Gheres, et al., "Normal Spastin Gene Dosage Is Specifically Required for Axon Regeneration", en, Cell Reports **2**, 1340–1350 (2012) (cit. on p. 12).

[78]K. Sugimura, K. Shimono, T. Uemura, and A. Mochizuki, "Self-organizing mechanism for development of space-filling neuronal dendrites", PLoS Computational Biology **3**, 2143–2154 (2007) (cit. on pp. 19, 21, 22, 240, 241).

[79]N. T. Sweeney, W. Li, and F.-B. Gao, "Genetic Manipulation of Single Neurons in Vivo Reveals Specific Roles of Flamingo in Neuronal Morphogenesis", en, Developmental Biology **247**, 76–88 (2002) (cit. on p. 16).

[80]N. T. Sweeney, J. E. Brenman, Y. N. Jan, and F.-B. Gao, "The Coiled-Coil Protein Shrub Controls Neuronal Morphogenesis in Drosophila", en, Current Biology **16**, 1006–1011 (2006) (cit. on p. 13).

[81]C. M. Tenenbaum, M. Misra, R. A. Alizzi, and E. R. Gavis, "Enclosure of dendrites by epidermal cells restricts branching and permits coordinated development of spatially overlapping sensory neurons", Cell reports **20**, 3043–3056 (2017) (cit. on p. 237).

[82]S.-I. Terada, D. Matsubara, K. Onodera, et al., "Neuronal processing of noxious thermal stimuli mediated by dendritic Ca2+ influx in Drosophila somatosensory neurons", eLife **5**, edited by L. C. Griffith, e12959 (2016) (cit. on p. 7).

[83]J. P. Thirion, "Image matching as a diffusion process: an analogy with Maxwell's demons", Medical Image Analysis **2**, 243–260 (1998) (cit. on p. 41).

[84]A. M. Turing, "The Chemical Basis of Morphogenesis", Philosophical Transactions of the Royal Society B: Biological Sciences **237**, 37–72 (1952) (cit. on p. 19).

[85]W. Van Saarloos, "Front propagation into unstable states: Marginal stability as a dynamical mechanism for velocity selection", Physical Review A **37**, 211–229 (1988) (cit. on pp. 192, 194).

[86]T. Vercauteren, X. Pennec, A. Perchant, and N. Ayache, "Diffeomorphic demons: Efficient non-parametric image registration", NeuroImage, Mathematics in Brain Imaging **45**, S61–S72 (2009) (cit. on p. 41).

[87]H. Wassle and B. B. Boycott, "Functional architecture of the mammalian retina", Physiological Reviews **71**, 447–480 (1991) (cit. on p. 15).

[88]H. Wässle, L. Peichl, and B. B. Boycott, "Dendritic territories of cat retinal ganglion cells", en, Nature **292**, 344–345 (1981) (cit. on p. 15).

[89]Q. Wen and D. B. Chklovskii, "A cost-benefit analysis of neuronal morphology.", Journal of neurophysiology **99**, 2320–8 (2008) (cit. on p. 8).

[90]M. Winding, M. T. Kelliher, W. Lu, J. Wildonger, and V. I. Gelfand, "Role of kinesin-1–based microtubule sliding in Drosophila nervous system development", en, Proceedings of the National Academy of Sciences **113**, E4985–E4994 (2016) (cit. on p. 13).

[91]Y. Xiang, Q. Yuan, N. Vogt, et al., "Light-avoidance-mediating photoreceptors tile the Drosophila larval body wall", en, Nature **468**, 921–926 (2010) (cit. on p. 7).

[92]H. Xiao and H. Peng, "APP2: automatic tracing of 3D neuron morphology based on hierarchical pruning of a gray-weighted image distance-tree", eng, Bioinformatics (Oxford, England) **29**, 1448–1454 (2013) (cit. on p. 45).

[93]X. Xu, J. L. Brechbiel, and E. R. Gavis, "Dynein-Dependent Transport of nanos RNA in Drosophila Sensory Neurons Requires Rumpelstiltskin and the Germ Plasm Organizer Oskar", en, Journal of Neuroscience **33**, 14791–14800 (2013) (cit. on p. 76).

[94]B. Ye, Y. Zhang, W. Song, et al., "Growing Dendrites and Axons Differ in Their Reliance on the Secretory Pathway", en, Cell **130**, 717–729 (2007) (cit. on p. 11).

[95]T. Zhao, J. Xie, F. Amat, et al., "Automated Reconstruction of Neuronal Morphology Based on Local Geometrical and Global Structural Models", Neuroinformatics **9**, 247–261 (2011) (cit. on p. 45).

[96]Y. Zheng, J. Wildonger, B. Ye, et al., "Dynein is required for polarized dendritic transport and uniform microtubule orientation in axons", en, Nature Cell Biology **10**, 1172–1180 (2008) (cit. on p. 10).

[97]S. Zipursky and W. B. Grueber, "The Molecular Basis of Self-Avoidance", Annual Review of Neuroscience **36**, 547–568 (2013) (cit. on pp. 13, 14, 33).

List of Figures

List of Tables

A

Abbreviations

AEL	after egg-lay
AP	anterior-posterior
LR	left-right
da	dendritic arborization
F-actin	filamentous actin
MT	microtubules
SD, STD	standard deviation
SEM	standard error of the mean
SEV	standard error of the variance

ProQuest Number: 28322428

INFORMATION TO ALL USERS
The quality and completeness of this reproduction is dependent on the quality
and completeness of the copy made available to ProQuest.

Distributed by ProQuest LLC (2021).
Copyright of the Dissertation is held by the Author unless otherwise noted.

This work may be used in accordance with the terms of the Creative Commons license
or other rights statement, as indicated in the copyright statement or in the metadata
associated with this work. Unless otherwise specified in the copyright statement
or the metadata, all rights are reserved by the copyright holder.

This work is protected against unauthorized copying under Title 17,
United States Code and other applicable copyright laws.

Microform Edition where available © ProQuest LLC. No reproduction or digitization
of the Microform Edition is authorized without permission of ProQuest LLC.

ProQuest LLC
789 East Eisenhower Parkway
P.O. Box 1346
Ann Arbor, MI 48106 - 1346 USA